The Buckling of Capillaries in Tumours

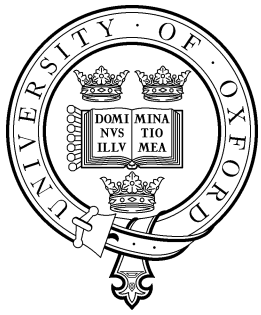

James MacLaurin

Keble College

University of Oxford

A thesis submitted for the degree of

Doctor of Philosophy

Trinity 2011

Contents

List of Figures

This thesis is dedicated to

my parents

with much love

Abstract

Capillaries in tumours are often severely buckled (in a plane perpendicular to the axis) and / or chaotic in their direction. We develop a model of these phenomena using nonlinear solid mechanics. Our model focusses on the immediate surrounding of a capillary. The vessel and surrounding tissue are modelled as concentric annulii. The growth is dependent on the concentration of a nutrient (oxygen) diffusing from the vessel into the tumour interstitium. The stress is modelled using a multiplicative decomposition of the deformation gradient $\mathbf{F} = \mathbf{F}_e\mathbf{F}_g$. The stress is determined by substituting the elastic deformation gradient $\mathbf{F}_e$ (which gives the deformation gradient from the hypothetical configuration to the current configuration) into a hyperelastic constitutive model as per classical solid mechanics. We use a Blatz-Ko model, parameterised using uniaxial compression experiments. The entire system is in quasi-static equilibrium, with the divergence of the stress tensor equal to zero. We determine the onset of buckling using a linear stability analysis. We then investigate the post-buckling behaviour by introducing higher order perturbations in the deformation and growth before using the Fredholm Alternative to obtain the magnitude of the buckle.

Our results demonstrate that the growth-induced stresses are sufficient for the capillary to buckle in the absence of external loading and / or constraints. Planar buckling usually occurs after $2 - 5$ times the cellular proliferation timescale. Buckles with axial variation almost always go unstable after planar buckles. Buckles of fine wavelength are initially preferred by the system, but over time buckles of large wavelength become energetically more favourable. The tumoural hoop stress $T_{\Theta\Theta}$ is the most invariant (Eulerian) variable at the time of buckling:

it is typically of the order of the tumoural Young's Modulus when this occurs.

Acknowledgements

I am very grateful for the help of my supervisors Dr Tiina Roose and Professor S. Jon Chapman. Dr Roose proposed this project and has shown immense patience and kindness to me throughout my DPHIL. Prof. Chapman has helped me a lot and provided encouragement when it was most needed.

I am also very grateful to Dr Gareth Wyn Jones, who helped me get started in nonlinear solid mechanics and has provided many useful insights throughout the course of my research (as well as reading through my entire thesis).

A big thanks to my examiners Prof. Alain Goriely and Prof. Mark Chaplain. They gave me a lot of constructive feedback which has improved this thesis. Finally, I would like to thank the following people I have discussed my work with over the years: Dr Derek Moulton, Dr Peter Howell, Prof. Sir John Ball, Prof L. Mahadavan, Dr Philippe Kuhl and last but not least my helpful and friendly officemates (Henry,Hermes, Guido and Ornella).

Chapter 1

Introduction and Literature Review

It has been hypothesised for a long time that intratumoural blood vessel abnormalities can impair blood flow into the tumour, and consequently decrease the effectiveness of chemotherapeutic treatment [83, 126]. Tumour blood vessels can have many types of abnormality, including chaotic direction and entanglement, a high level of branching, overly porous capillary walls and chaotic blood flow. One particular type of abnormality is vascular buckling and collapse. The aim of this thesis is to develop a mathematical model of this phenomenon.

There are two broad types of vascular buckling we consider in this thesis: planar buckling and axial buckling. Planar buckling occurs when most of the non-cylindrical deformation is in a plane perpendicular to the vessel's axis. Axial buckling involves a significant non-cylindrical deformation in a direction parallel to the axis of the vessel. Of course these two categories are not entirely distinct: some buckles may possess significant planar and axial components.

Planar vascular buckling has been well-documented by experimentalists. Goldacre and Sylven investigated this phenomenon by injected dyes into the bloodstream of mice [62]. They determined that the dye (and therefore the blood) was generally less penetrative for older and larger tumours. Since older and large tumours tend to have a greater density of tumour cells, they conjectured that tumour cell growth was a major cause of the collapse

of the tumour vasculature. Boucher and Jain reaffirmed this hypothesis [26]. They discovered that the elevated interstitial fluid pressure of tumours was matched by an elevated microvascular blood pressure. Therefore they conjectured that vascular collapse was not caused by an imbalance in fluid pressure but by the pressure of the growing tumour cells. Griffon-Etienne *et al* have observed that drug-induced apoptosis around a collapsed lumen caused the lumen to reopen [66]. Stoll [129] and Padera *et al* observed similar results [111]. Stoll also observed an increased density of cells around collapsed lumen [129]. This research suggests that the collapsed lumen may have been caused by an increase in the density of the surrounding tumour cells.

The high degree of tortuosity of the tumour vasculature has also been well-documented by experimentalists. In normal tissue, the vasculature is typically a well-ordered network reaching all parts of the tissue. However in cancer tissue the capillaries often follow chaotic directions and are highly entangled. Nagy *et al* conjecture that vessel tortuousity is primarily due to excessive lengthening of the growing capillary [105], so that if the ends of the capillary are fixed it is forced to coil to accommodate the extra length.

In this thesis we investigate whether the planar buckling of tumour blood vessels and the high degree of vessel tortuosity can be partly explained in terms of a mechanical instability resulting from the proliferating tumour cells.

1.1 The Mechanical Structure of Blood Vessels

In this section we provide an overview of the mechanical structure of capillaries, arteries and veins. At the end of this section we look at the distinctive features of blood vessels in cancer tumours.

There is comparatively little data on the mechanical structure of capillaries. From the mechanical point of view there are three major components to the capillary wall. These are the endothelial layer (on the inside), the basement membrane (in the middle) and, in some tissues, pericytes (on the outside). The endothelial cells are extremely thin (as little as 200 nm in height) [24]. The basement membrane is a fine network of reticular collagen fibers (mostly type IV collagen). Its thickness is typically about 50 - 100 nm [85]. The pericytes

are thought to play a contractile role similar to the smooth muscle cells of arteries [25]. Unlike the arteries, in capillaries there is no well-defined adventitia.

We could not locate any data on the mechanical properties of capillary endothelial cells, however there is data on other types of endothelial cell. The Young's Modulus in all cases was typically 10^3 to 10^4 Pascals. Sato *et al* found the Young's Modulus of human umbilical vein endothelial cells to be typically 5×10^3 Pa [124]. Mathur *et al* similarly found a range from 1400 to 6800 Pascals in their measurement of the the Young's Modulus of human umbilical vein endothelial cells [99]. Pesen *et al* found bovine pulmonary artery endothelial cells to typically have a Young's modulus of 200 to 2000 Pascals [112]. The endothelial cell layer also has viscoelastic properties, although these are negligible on the growth timescale [145, 16].

There has been very little experimental work to investigate the mechanical behaviour of the basement membrane. Although many connective tissues, such as cartilage, consist of similar molecules (collagenous fibres), there is still much room for the basement membrane to have substantially different behaviour due to the different composition and crosslinks of its molecules [31]. In common with other collagenous biomaterials, the basement membrane displays strain stiffening properties [89]. In other words, as the membrane is stretched, it becomes stiffer. Several experimentalists have measured the elastic properties of capillaries by isolating them from the surrounding tissue and varying the transmural pressure. The Young's modulus is inferred through observing the dilation of the capillary. In obtaining the Young's Modulus it was assumed the basement membrane bore all the load. In the work of Lee *et al* on rat skeletal muscle capillaries the completely relaxed basement membrane had a Young's Modulus of approximately 10^5 Pa [89]. It increased approximately linearly with strain to a value of approximately 10^6 Pa at a strain of 1. In the work of Smaje *et al* on the cat mesentery, the Young's modulus of capillaries was determined to be approximately 1.8×10^6 Pa and the Young's modulus of the venules to be approximately 5.4×10^6 Pa. It can be seen that the Young's Modulus of the basement membrane is approximately 100 times the Young's modulus of the endothelial cells.

Tumour angiogenesis results from the unbalanced release of cytokines, particularly vascular endothelial growth factor (VEGF) [105]. This process can result in a variety of different

Property	Value	Units	Source
Endothelial Cell Layer Young's Modulus	0.2 to 10	kPa	[16, 124, 99, 112, 145]
Endothelial Cell Layer Thickness	0.2 to 0.5	μm	[24, 140]
Basement Membrane Young's Modulus	0.1 to 4	MPa	[89, 127, 31]
Basement Membrane Thickness	50 to 100	nm	[85]

Table 1.1: A summary of the data on the mechanical structure of the capillary. These are only approximate values.

types of blood vessel. We provide an overview of these, drawing on the review of Nagy *et al* [105]. *Mother vessels* begin to develop hours after injection of vascular endothelial growth factor into mice. They are characterised by an enlarged radius, degraded basement membrane and detached pericytes. Mother Vessels can evolve into normal capillaries through intraluminal bridging. Nagy *et al* [105] report that they are particularly prone to collapse. *Glomeruloid microvascular proliferations* are hyperpermeable and characterised by abnormal layers of basement membrane. Some mother vessels evolve into *vascular malformations*, retaining their large radius and acquiring a smooth coating of muscle cells. Abnormal levels of VEGF can also stimulate the abnormal growth of arteries and veins. Tumour blood vessels often follow highly tortuous paths. Nagy *et al* conjecture that this is due to the vessels lengthening despite being fixed at either end: they must coil to accommodate the extra length [105].

The mechanical properties of arteries and veins have been modelled in considerable detail. We give a brief overview. Arteries and veins have a considerably more complicated structure than capillaries, with three concentric layers: the intima, media and adventitia. These layers contain a mixture of collagenous fibres, elastin, endothelial cells and muscle. Most models of their elastic response to *stretching* in the longitudinal and azimuthal directions use a strain energy function that is of the form [56]

$$\psi = c\left(e^{Q(\mathbf{E}_{ZZ},\mathbf{E}_{Z\Theta},\mathbf{E}_{\Theta\Theta})} - 1\right), \tag{1.1}$$

for some constant c and function Q. The function Q is usually carefully parameterised and takes into account the reorientation of the collagen and elastin fibres at high levels of strain.

1.2 The Mechanical Structure of Tumours

Tumours are composite entities and therefore exhibit a variety of mechanical behaviours. Broadly speaking, there are three mechanically relevant components to tumour tissue: cells, the extracellular matrix and interstitial fluid. Each of these contributes to the mechanical behaviour of tumours. We provide an overview of the basic structure of these components and of experimental efforts to measure their mechanical properties. There are two basic types of experiment: those which measure the behaviour of the individual constituents and those which measure the macroscopic behaviour of the tumour as a whole. There have been many models which attempt to synthesise these together [120]. For a more detail review refer to Roose *et al* or Chaplain *et al* [121, 37]. We firstly outline the properties of the individual constituents.

Typical cells consist of a membrane, a cytoplasm (consisting of a fluid-like cytosol, structural cytoskeleton and dispersed organelles), and a nucleus which contains the chromosomal DNA. The cytosol means that cells often exhibit fluid-like effects: they exhibit stress relaxation, they may flow irreversibly and they may be highly deformable. However the cytoskeleton provides considerable structural support to the cell, so that cells also exhibit behaviour characteristic of elastic solids. The cytoskeleton is composed primarily of actin filaments, intermediate filaments and microtubules. The actin filaments link points of adhesion of the cell to the extracellular matrix. They assert a contractile force which assists in the cell retaining its rounded shape. Microtubules are the 'supporting struts' of cells: they provide compression resistance. The interaction of the various components of the cell results in a complicated mechanical behaviour, as evidenced for example in the 'tensegrity' models of Ingber and co-workers [80, 142]. For a review of the mechanics of cells, refer to Lim *et al* [94].

The extracellular matrix is a network of proteins (including elastin, collagen and fibronectin), glycosaminoglycans (GAGs) and water. The proteins provide most of the structural support. In particular, elastin is the most linearly elastic material known [56]. For elastin, the stress / strain relationship remains linear for strains of up to 60 per cent. Cell adhesion to the ECM occurs primarily via integrins, a family of heterodimers that bond

to external ligands (for example collagen and fibronectin) in the ECM. Cell adhesion is a time-dependent process, as the adhesive components are not fully developed until several hours after the cell initially binds with the ECM.

We now give an overview of recent experimental investigation of the mechanical structure and interaction of the cells and extracellular matrix. The most common method to measure the elastic properties of individual cells is atomic force microscopy [99]. A rigid probe is pushed into the side of a cell and the indentation measured. Typically the Hertz Model is applied to deduce the Young's Modulus of the cell. The Hertz model approximates the experiment as the indentation of a rigid probe into a semi-infinite linear elastic material. As the cell itself is mostly fluid and is therefore almost incompressible, the Poisson's ratio is assumed to be 0.5. There is usually significant variation in the measured Young's Modulus depending on the proximity of the probe to the nucleus or cytoskeleton. Mathur *et al* summarise experimental measurements for a range of endothelial cells and typically find a Young's Modulus on the order of 0.5 - 10 kPa [99]. Canetta *et al* apply a more sophisticated Oldroyd-B model to their experiments and also obtain results in this range [32]. The adhesive interactions between cell membrane receptors and extracellular matrix (ECM) ligands have been measured in various experiments, as reviewed by Christ *et al* [41]. As Christ notes in his review, various experiments indicate that the ligand-receptor bond strengthens over time. The time it takes for the bond to reach its full potential appears to be on the order of a day [41]. Perhaps the most reliable measurement of the receptor-ligand bond strength is the following hydrodynamic flow experiment. Fluid is flowed over cells cultured on a substrate in the bottom of a channel. The shear stress exerted on the cells was calculated using a (low Reynolds number) fluid mechanics model. In the experiments of Christ *et al*, the strength of the bond of NIHT3 fibroblasts was found to be typically 50-100 Pa [42]. These measurements were taken after the cells had been cultured for several hours and the bonds allowed to strengthen. Lu *et al* measured the adhesive strength of WTNR6 fibroblasts using a similar experimental technique and found the adhesive strength to be approximately 200-267 Pa [95]. However the cells had only been cultured for half an hour and presumably the adhesive bonds were not at their full potential. Recent work by Legant *et al* used a linear elastic model to infer the force exerted by cells on a substrate [90].

In the preceding paragraphs we provided a brief overview of the mechanical structure of the individual constituents (chiefly the cells and extracellular matrix) or tumours. We now give an overview of experimental investigation of the macroscopic (or aggregate) mechanical behaviour of tumours.

Netti *et al* performed confined compression tests on various tumours to investigate their resistance to compression [106]. A slice of tumour was placed in a confined environemnt and uniaxially compressed. There was initially a large pressure in response to the compression, however this decayed over time to typically at most 10 per cent of its initial value. This relaxation is partly due to the squezing out of the interstitial fluid over time (as the compression was performed under drained conditions), and probably partly due to the fact that the cells have a large fluid component, and are therefore able to realign themselves in response to the pressure gradient over time [80]. In the softer carcinomas, with a relatively less-developed extracellular matrix, Netti *et al* found that the stress completely relaxed to zero for small strain compressions. They rightly conclude from this that these tumour lines are dominated by fluid like behaviour. In the linear limit, these tumours could probably be modelled using the viscoelastic Maxwell model (although the authors do not do this). In the tumour lines U87 (human glioblastoma), and HSTS6 (Human Soft Tissue Sarcoma), however, a gradient in the stress remained even for small strains. In the linear limit, each of these tumours could probably be modelled as a viscoelastic Kelvin-Voigt material. The experiments of Netti *et al* outlined above demonstrate that the solid phase of a tumour is compressible, under drained conditions, due to the intercellular fluid being squeezed out of the pore spaces. The compressibility of tumours has also been demonstrated through Helmlinger's growth of tumour spheroids in an agarose gel [75, 106]. When the spheroids were removed from the agarose gel their volume expanded, which suggests that while they were in the gel they were residually stressed. The nature of the transmission of the macroscopic stress (experienced by the aggregate material) to the cellular and ECM level is poorly understood [120].

Many tumours grow in collagenous substances in which the extracellular matrix does most of the load-bearing, such as the skin or brain. The high collagen content means that these substances behave elastically for high levels of stress and strain (as was demonstrated

in the experiments of Netti *et al* [106]). We therefore given an overview of the mechanical properties of skin and and brain tissue as this will be of assistance in the construction of our model. Arumugan *et al* performed experiments to measure the elastic response of skin [15]. Goat skin was stretched in one direction and the stress (tension) measured. Initially, up to a strain of approximately 25 per cent, the stress vs strain curve was convex (superlinear). Such convex curves are a hallmark of elastic rubber-like materials [56]. After this, the stress still increased with respect to strain, but the curve inflected to a concave shape. The authors argue that the concavity indicates the onset of irreversible plastic damage to the skin. The stress at which this occured was approximately twice the initial linear Young's Modulus *et al* [15]. Franceschini *et al* performed similar experiments on segments of brain tissue, investigating the elastic response and onset of fracturing [52]. The stress / stretch curves had a similar shape to those from the experiments of Arumugam *et al* outlined above. At low levels of stretch the curvature of the stress/stretch curve was positive, as the brain tissue 'hardened' in response to increasing stretch. At a stretch of typically about 1.9, the shape of the curve inflected to negative curvature, which (in the authors' opinion) indicates the onset of damage to the tissue [52]. Complete fracture of the tissue occurred typically at a stretch of 2.66 [52].

1.3 The Growth and Treatment of Vascular Tumours

There are many factors which affect the growth of tumours. The effect of oxygen, glucose and pH on the growth of multicellular tumour spheroids has been studied in detail by Freyer *et al*, Casciari *et al* and others [54, 53, 34, 35]. Their experiments indicate that the rate of proliferation of tumour cells increases in response to an increase in the oxygen concentration or glucose concentration. The rate of uptake of oxygen or glucose increases in response to an increase in the concentration of either of these. The rate of proliferation decreases in response to an increase in acidity. Casciari *et al* fit Michaelis-Menten type dynamics to model the rate of proliferation of tumours cells / the rate of uptake of nutrient: such that the proliferation and growth are initially linear for small concentrations, but asymptote to a limit for large concentrations. Furthermore Freyer and Sutherland have demonstrated

that the cellular glucose consumption rate increases with decreasing oxygen concentration [54]. Similarly, the cellular oxygen consumption rate increases with decreasing glucose concentration. Tumours tend to have elevated levels of lactic acid [138, 81]. The rate of production of lactic acid is linked to the glucose levels as lactic acid is a byproduct of glycolysis. If the lymphatic system in a tumour is poorly developed, then the lactic acid levels will build up because it won't be removed as efficiently.

In recent years there has been a renewed interest in the effect of mechanical compression on the growth of tumours. In the landmark experiments of Helmlinger *et al*, tumour spheroids were cultured in an agarose gel and the net growth was found to be less in the gels of greater stiffness [75]. Cheng *et al* performed similar experiments [40]. In both papers, the conclusion drawn by the authors was that the growth was inhibited by the stress field. They conclude that cells will duplicate only if they have sufficient energy to overcome this yield stress and displace their neighbours. This was also evident in the modelling of the growth of EMT6-R0 tumour spheroids by Casciari *et al* [34]. They developed a very carefully paremeterised model of tumour growth involving oxygen, glucose and pH levels, yet there was still a substantial difference between their model predictions and experimental results. They rightly hypothesise that growth inhibitory effects (both due to chemicals and intercellular contact) are necessary for a more accurate model.

Since tumours are complex heterogeneous structures, mechanical forces can affect the growth in a number of ways [37]. Cells actively monitor their environment and respond to mechanical stimuli and strains. For example mechanical strain (tension) can increase production of ECM [139], and applying tensile forces often strengthens adhesive bonds over time [39]. In normal cells growth is inhibited when the cells are densely packed: a phenomenon known as contact inhibition of growth. Contact initiates the formation of intercellular junctions through a complicated cascade of proteins which is initiated by adjacent cells [45, 135]. Compressed cells are more prone to enter the quiescent phase of the cell cycle - where they absorb less nutrient and do not proliferate [54]. For example in the experiments of Tsukatani *et al*, the density of normal breast epithelial cells in a nutrient rich but confined environment asymptoted to a limit after about 10 days. Conversely the disruption of these intercellular junctions can lead to deregulated growth. This is thought

by some to be a fundamental cause of avascular tumours [36]. It has also been demonstrated cell proliferation can be increased by tension [38, 39].

1.4 Mathematical Models of the Mechanics of Growing Tumours

Thus far we have seen that tumours exhibit a variety of mechanical and fluid behaviours. Not surprisingly there is a corresponding variety of models which attempt to capture this behaviour.

There are two basic types of model of the mechanical response of tumours to growth: the multiphase model and the single-constituent solid mechanics model. A detailed review is provided in Roose *et al* [121]. Both approaches assume that the tumour can be approximated as a continuum: with solid-like and / or fluid-like behaviour.

One type of model is to consider the tumour as a multiphase substance consisting of (for example) extracellular matrix, cells and interstitial fluid [28, 9, 13, 14, 122, 30, 116, 37]. The phases are governed by a balance of momentum, mass, energy and thermodynamics. Growth is typically modelled as the conversion of interstitial fluid and nutrients into the solid phase. The stress tensor giving the total mechanical stress is a sum of the stress tensors from the different phases. In most models the constitutive relations for the stress in each phase are determined by the volume fraction, deformation gradient and a viscoelastic component proportional to the relative velocity of the phases. The equations of mechanical equilibrium thus have an elastic and viscoelastic component. In most models the extracellular matrix is an elastic solid, and the tumour cells are an elastic fluid. As such, the cells are able to 'flow' through the extracellular matrix and exhibit viscoelastic behaviour. The experiments of Netti *et al* [106] and Pioletti *et al* [113] found a viscoelastic timescale on the order of 1000 seconds. In recent models by Chaplain *et al* [37] and Ambrosi and Preziosi [9], the tumour cells behave as an elastic solid up to a certain yield stress, after which there is plastic flow. This latter model thus provides a means of stress relaxation at high pressures and accounts for the complicated adhesion mechanics of cell-cell and cell-ECM interactions.

1.4.1 Elastic Models of Growth

There are many ways classical single-phase solid mechanics has been used to model growth. Perhaps the most familiar is to decompose the strain tensor *additively* into a growth deformation and an elastic response. This approach is analogous to the modelling of thermoelastic stress [23]. A linear constitutive law is almost always used in conjunction with this, i.e. the stress is modelled as being linearly proportional to the strain. This model is accurate for small deformations only. It has been applied to the growth of tumours by Jones *et al* and Araujo and McElwain [84, 12, 11]. Ambrosi and Preziosi [8], use a linear viscoelastic constitutive law, with the elastic response depending on both the deformation and the rate of deformation. For a review of the application of this model to tumours refer to Roose *et al* [121].

Another more comprehensive approach is to decompose the deformation gradient *multiplicatively* into a growth deformation followed by an elastic response deformation. This is the approach we will adopt in this thesis. It was first used for volumetric growth by Rodriguez *et al* [119]. Let B_0 be the reference configuration of the body and B_2 the current configuration.[1] We decompose the deformation gradient (which is a map from the tangent space of B_0 to the tangent space of B_2) into a deformation due to cellular growth $\mathbf{F}_g$ followed by an *elastic* deformation $\mathbf{F}_e$, i.e.,

$$\mathbf{F} = \mathbf{F}_e \cdot \mathbf{F}_g. \tag{1.2}$$

We define a hypothetical unstressed intermediate configuration B_1, such that we may obtain B_1 by elastically de-stressing each point in B_2. We need not assume that B_1 is compatible: i.e. we do not expect there to exist a continuously differentiable bijection from B_1 to B_2. However this is not a problem because we only require that for each point $\mathbf{X}_1 \in B_1$ with corresponding point x_1 in B_2, there exists a tangent space map $\mathbf{F}_e$ from the tangent space of X_1 to the tangent space of x_1. We may equivalently think of B_1 as the structure obtained by letting each point in the reference configuration grow in an uninhibited way, such that the local deformation gradient from B_0 to B_1 is $\mathbf{F}_g$. We assume that the grown material is hyperelastic, so that there exists a function $\psi_g(\mathbf{F}_e)$ which gives the strain energy per unit

[1] Refer to Section A in the Appendix for an introduction to the mathematics of differential geometry and nonlinear elasticity.

volume of B_1. It is difficult to sensibly define the stress tensors over B_1; so we prefer to work with the first Piola-Kirchhoff stress tensor $\mathbf{P}$ over B_0. Since $\mathbf{P} = \frac{\partial \psi}{\partial \mathbf{F}}$ (where $\psi = \eta^{-1}\psi_g$ is the strain energy density function corresponding to B_0), we find

$$\mathbf{P} = \eta \frac{\partial \psi_g}{\partial \mathbf{F}_e} \mathbf{F}_g^{-T}. \tag{1.3}$$

If the system is in mechanical equilibrium, then $\nabla \cdot \mathbf{P} = \mathbf{0}$.

It can be seen that with this construction, internal stress can develop due to differential growth despite the absence of external loading. It was the existence of such *residual stresses* in organic tissue which motivated the development of the theory in the first place. This second approach is nonlinear and is generally used for modelling large deformations. It was applied to tumour growth by Ambrosi and co-workers, who employed a Blatz-Ko constitutive law [6, 5].[2] For a fuller discussion of the methodology refer to Rodriguez *et al* [119], Goriely *et al* [64], Himpel and Kuhl [58] or Lubarda *et al* [96]. This has become the dominant method for modelling growth-induced stress [64], with applications in the areas of tumour growth [6, 5, 9], shell deformation [4], cardiac hypertrophy [119], plant growth [136], airway wall remodelling [104] arterial wall stress [131, 79] and many others.

1.4.2 Effect of Stress on Growth

As outlined in the introduction, there is strong experimental evidence that the rate of cellular proliferation decreases in response to compression of the tumour. There have been several models of this in recent years. There is a lack of quantified experimental data, which means these models cannot be precise.

Chaplain *et al* [37] and Ambrosi *et al* [9] model the inhibition of growth due to compression using a monotonic mollifier of the step function. If the overall volume fraction occupied by the cells and extracellular matrix surpasses a certain limit, then the growth is zero. If the volume fraction is zero, the growth is uninhibited. Between these two limits, the level of growth depends linearly on the volume fraction. Galle *et al* have a similar set-up in their stochastic model [59, 60]. Byrne and Preziosi [30] model the growth rate per tumour mass as proportional to $(1 + \sigma\Sigma(\phi_T))^{-1}$, where $\Sigma(\psi_T)$ gives the attractive / repulsive force

[2] We define this constitutive law in the Appendix, in equation (2.51).

experienced by the cells and σ is a constant. In their modelling of stress-modulated growth in arteries, Taber and co-workers postulate that the rate of growth is proportional to the stress [131, 130]. In their modelling of tumour spheroid growth, Ambrosi and Mollica multiply the growth rate by $\exp\left(-\left(\mathrm{tr}(\mathbf{P})/s_0\right)^2\right)$, where s_0 is a constant [7]. They are only able to motivate this in the sense that it satisfies their phenomenological requirement that stress always inhibits growth. It is interesting to notice that their model implies that tensile stress inhibits growth, whereas the experimental evidence outlined in Section 1.3 only concerns the inhibitory affect of compressive stress on growth. Araujo and McElwain model the effect of the prevailing stress field on the *direction* of growth, rather than the total *amount* of growth [11].

1.5 The Mathematics of Buckling

In this section we give a brief introduction to the mathematics of buckling. The subject is best introduced through an example: the Euler Strut. In this problem, a pressure P is applied to an upright thin elastic rod. We wish to determine when the rod buckles. We give an overview of the solution to this without providing too many details. In doing this we are following in the footsteps of Euler, who first solved this problem in 1757. To answer this question we must first apply an appropriate constitutive theory which relates the elastic deformation of the rod to the pressure using the material properties. We assume that the bending moment is proportional to the curvature of the rod (a standard assumption in the mathematics of rods) and that the rod is inextensible. Let s be an arclength parameterisation of the undeformed rod, and y the horizontal deflection from its resting position. It follows that up to linear order, the bending moment is

$$EI\frac{d^2y}{ds^2}, \tag{1.4}$$

where EI is a constant. The pressure P, which is assumed to be constant down the rod, also applies a bending moment of the form $-Py$ (to first order accuracy). Since the net moment must be zero,

$$EI\frac{d^2y}{ds^2} + Py = 0. \tag{1.5}$$

The transverse displacement at either end of the rod is zero, i.e.

$$y = 0, \tag{1.6}$$

at $x = 0$ and $x = L$. The general solution of the ordinary differential equation is

$$y = A \sin\left(\sqrt{\frac{P}{EI}} s\right) + B \cos\left(\sqrt{\frac{P}{EI}} s\right). \tag{1.7}$$

In order that the boundary conditions are satisfied, we require $B = 0$ and

$$\sqrt{\frac{P}{EI}} L = m\pi, \tag{1.8}$$

i.e.

$$P = \frac{EIm^2\pi^2}{L^2}. \tag{1.9}$$

This is the *critical pressure* at which the system *bifurcates* from the trivial solution to a buckled solution with wavenumber m. The point of this toy example is to illustrate the approach mathematicians often take to buckling. The system is assumed to adopt an unbuckled *fundamental* solution in quasistatic equilibrium. A critical parameter is identified, and we search for values of the parameter such that there is a solution to the linearised equations of equilibrium (this approach is known as a linear stability analysis). The evolution of the buckled state must then be solved for using the full nonlinear version of the constitutive theory. (Note that in the constitutive theory outlined above we only kept linear terms and so cannot accurately model the nonlinear behaviour).

1.6 Vascular Buckling in Tumours

The buckling of capillaries in cancer tumours has been modelled in two major ways in the literature. One way is to consider the capillary wall as a thin cylindrical shell subject to a constant net external pressure. The buckling of a thin circuluar ring (such as this) under a constant external pressure has been extensively analysed [10, 49, 132, 114, 103, 71]. We provide a brief overview of this analysis; refer to Tadjbakhsh and Odeh [132] for more details. The ring is typically modelled as a circular one-dimensional inextensible rod[3], so that it

[3]Known as a Special Cosserat Rod.

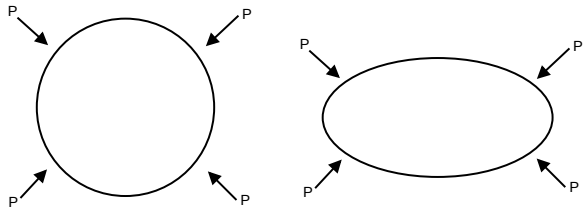

Figure 1.1: The buckling of a thin ring under a constant external hydrostatic pressure P. On the left is the reference configuration and on the right is the Mode 2 buckled (current) configuration. Our solutions (to be derived in the next few chapters) for the buckled shape of a capillary look similar to the shape of a buckled ring such as this.

could represent, for example, the cross-section of a long cylinder: see Figure 1.1. In this model there is a net external pressure p which everywhere exerts a constant force normal to the ring. The pressure does not exert any shear force on the ring. The constitutive relations for the mechanical response of the ring are given by the bending moment m being linearly proportional to the change in curvature. The ring is considered to be inextensible, so that there is no stretch. A force balance yields a second order boundary value problem in the curvature κ, relative to the arclength parameter s, which can be accurately solved numerically.

Such a model has been applied to the buckling of capillaries in tumours by Stoll [129] and Mollica [102]. It was tested experimentally on veins isolated from surrounding tissue by Moreno *et al* [103] and the theory agreed closely with the experiment. More complicated models, such as by Heil and Pedley [74], take into account the viscous effects of fluid flow on the stability of elastic shells. Despite these successes, there are several weaknesses with this model. It is accurate for fluid-pressure induced buckling, but is less accurate for solid-growth induced buckling. Experimental evidence suggests that it is the compression resulting from the growing tumour cells which is the major reason for vascular collapse, as the microvascular pressure and interstitial fluid pressure tend to be approximately equal in tumours with collapsed capillaries [26]. Thus we cannot just consider the mechanical behaviour of the capillary wall, but we must also consider the mechanical behaviour of the tissue surrounding the wall. Indeed Fung has found, both experimentally and analytically, that the surrounding tissue provides strong support for a capillary, preventing it from buckling in normal cases [56].

The second type of model of vascular collapse concerns the macroscopic response of the entire spheroid and is due to Araujo and McElwain [12, 11]. They model the tumour as a continuous spheroid, with the growth and elastic response radially symmetric. The strain tensor is decoupled additively into a growth component and the standard linear strain tensor. The growth depends on the concentration of a single generic nutrient, and is preferentially directed in the direction of least stress. As growth occurs the hoop stress $\sigma_{\theta\theta}$ (the stress in the direction normal to the radius of the spheroid) becomes more and more compressive (i.e. more and more negative). It is assumed that vascular collapse occurs once the hoop stress falls below a certain threshold. This second model occurs on a different scale to the first model. The spheroid is modelled as a continuum: there are no 'cavities' corresponding to blood vessels like with the first model. This model does not attempt to predict the shape of the individual collapsed blood vessels; rather it assumes vessels are either functioning normally or completely collapsed and nonfunctional. A strength of this model is that it links vascular collapse and necrosis to give novel predictions concerning the macroscopic behaviour of a growing tumour. However this model does not attempt to elucidate the local mechanics governing the buckling of individual capillaries.

1.7 Modelling of Buckling of Related Phenomena

The buckling of structures with a cylindrical geometry has been extensively studied. We provide an overview of some this work, with an emphasis on the biomechanical literature. Haughton and Ogden [71, 72] consider the buckling of a cylindrical annulus, loaded both axially and with internal / external pressures. They determine the conditions under which buckling occurs by finding the parameters for which there is a nontrivial solution to the equilibrium equations. They find that 'prismatic buckling' (i.e. with nontrivial deformation only in the plane perpendicular to the cylinder's axis) only occurs when the cylinder is loaded with an external pressure. In this situation the second mode is always the first to buckle. Vandiver and Goriely [136] have modelled the growth-induced buckling of cylindrical structures. They consider the effect of differential bulk growth on the 'Euler Buckling' of cylindrical columns submitted to an external pressure (i.e. with nontrivial axial deforma-

tion, similar to the Euler strut example discussed earlier). The growth induced collapse of airway walls has been modelled by Moulton *et al* [104] and Li *et al* [92, 93]. Both authors model the airway as an elastic cylinder undergoing volumetric growth. They both use an incompressible neo-Hookean strain energy function to provide the constitutive relations. Moulton *et al* investigate the stability of the airway to an external pressure and obtained mixed results: the stability of the airway sometimes improves and sometimes weakens according to the growth profile. Li *et al* find that initially the system prefers fine wrinkling with a small wavelength. However as the growth increases, the system increasingly prefers longer wavelengths, so that the buckle becomes dominated by several large folds. This phenomenon is known as *period-doubling* and will be observed in our results as well. Li *et al* also find that stiffening of the inner mucosal layer induces a preference for the buckling of smaller modes, with a larger deformation, so that the overall obstruction of the airway is greater. The collapse of fluid-lined lung airways has been modelled by (amongst others) Heil, Hazel and Rosenzweig [74, 73, 123]. The basement membrane surrounding the airway is typically modelled as a nonlinearly-elastic shell, and the fluid layer on the inside is modelled using free surface Navier-Stokes equations. The net pressure on the shell is equal to the difference between the external pressure and the surface tension of the fluid. Buckling results from complicated solid-fluid interactions.

The buckling of arteries and veins has been extensively modelled in recent years. Han and co-workers model the artery wall using a Fungian exponential strain energy function, and the surrounding substrate as a linear elastic material [68, 69, 70, 88]. They perform a linear stability analysis to determine the onset of buckling and find that the two major factors contributing to axial buckling are an increased internal hydrostatic pressure (exerted by the blood) or decreased axial stretch. They conjecture that mechanical buckling is a major reason behind high levels of arterial tortuousity and kinking. Goriely and Vandiver similarly perform a linear stability analysis to determine an onset of buckling, however their constitutive relations also take into account the anisotropic elastic response of the artery wall [65].

1.8 The Goals of This Thesis

We develop a model of the elastic deformation and buckling of a capillary caused by tumoural growth in its immediate vicinity. Our model is at a scale between the models of Stoll [129] and Araujo and McElwain [12, 11]. Our model will predict the final buckled shape of the capillary like the thin shell model of Stoll, but also incorporate the elastic behaviour of the growing tissue like Araujo and McElwain. Our model focusses on growth in the tissue in the immediate surrounding of the capillary: our aim is to investigate how far buckling can be explained by the local nutrient profile (from a single capillary), growth and residual stress as opposed to macroscopic factors which can only be explained through a model of the entire tumour.

We investigate the effect of the mechanical stress / compression in the tumour as a whole on the growth and buckling in the immediate vicinity of a capillary. We thus will consider a variety of mechanical boundary conditions at the interface of our model geometry with the ambient tumour. The size of the 'immediate vicinity' of the capillary can vary considerably, as demonstrated by the huge range in the intercapillary distances measured by Konerding *et al* [87]. It is clear that we cannot expect to accurately model every scenario: the stress within some tumours can only be accurately modelled through a consideration of the entire structure and its interaction with the host environment. For example the ambient environment might possess a highly heterogeneous stress field. Our fundamental aim is not to model every single possible cause of vascular buckling, but to investigate the conditions under which buckling can occur as a result of growth and elastic deformation in the immediate surrounding of a single capillary only.

We investigate both planar and axial buckling of the capillary (or a combination of the two). Planar buckling is of therapeutic interest because it restricts blood flow. Axial buckling of the capillary is also of therapeutic interest because it potentially contributes to the high degree of tortuousity often exhibited by bloods vessels in tumours. Although Nagy conjectures that capillary tortuosity is primarily due to its excessive lengthening with constrained ends [105], we investigate the possibility that a contributing factor could be a mechanical instability resulting from the proliferating tumour cells.

We investigate the effect of chemotherapy and radiotherapy on the mechanical stability of tumours. The chemotherapeutic drugs to be considered are cisplatin and tirapazamine. The distribution of both of these is dominated by diffusion. The latter is of interest because its metabolism is oxygen-dependent: its metabolism is low in oxygen-rich regions and high in hypoxic regions. We also consider the effect of radiotherapy on the mechanical stability of the system. We investigate whether the application of these treatments can destabilise existing capillaries, and also whether these treatments can reopen already-buckled vessels as reported in Padera *et al* [111].

As with many biological models, there is some uncertainty over parameter values. Some parameters have not been accurately measured by experimentalists, and other parameters have been measured, but vary a lot amongst different tumours and sometimes also within individual tumours. The general methodology of our results will be to vary the parameters over their physically realistic range (this range might have to be estimated) and investigate the effect of this on the mechanical stability of the system.

1.9 The Structure of this Thesis

In Chapter 2 we develop a mathematical model for the growth of a tumour in the immediate surrounding of a capillary, and the resulting elastic deformation. As there is some uncertainty in this modelling, we develop a wide array of model variants to test out in our results chapters.

In Chapter 3 we solve our model in the radially symmetric case. We eliminate the model variants which make unrealistic predictions.

In Chapter 4 we apply a linear stability analysis to a simplified version of our model without a distinct capillary wall structure. At the time of buckling, we perform a perturbation expansion to determine the magnitude and stability of the buckle. We continue this analysis in Chapter 5, but this time we include a distinct capillary wall structure.

We perform a boundary layer analysis in Chapter 6 to investigate the buckled patterns as the wavenumber n asymptotes to infinity. The critical times cluster, and asymptote to a finite constant. We outline our method of numerical solution in Chapter 7.

We present results for the onset of buckling in the system without a distinct capillary wall structure in Chapter 8. We present more results for the onset of buckling in the system with a distinct capillary wall structure in Chapter 9. In these chapters we achieve our goal of explaining the buckling of a tumoural capillary through reference to its immediate surrounding only. We investigate the nature of the buckling, and its sensitivity to various parametric regimes.

Chapter 2

Mathematical Model of Tumoural Growth and Deformation Around a Capillary

In this chapter we develop a model for the growth and elastic deformation in the immediate surrounding of a capillary in a tumour.

2.1 Mechanical Model

We model our system as being in a *quasi-steady-state*. This means that inertial and viscoelastic forces are negligible in our mechanical equation of equilibrium, and that fluid flux is negligible. The characteristic timescale of our model is the average time it takes a cell to multiply in a nutrient rich environment (i.e. the 'cellular proliferation timescale'). This varies considerably, with a minimum of approximately 11 hours [34]. We justify these assumptions further below.

We choose to work within the framework of nonlinear solid mechanics, rather than multiphase theory. These two models are summarised in Section 1.4. The fundamental reason for this is that in the quasi-steady state approximation the multiphase model is little different from the single-phase model, except the latter is better parameterised. Although we may measure the mechanical properties of the individual cells / ECM components /

interstitial fluid, it is difficult to model their interaction, and in particular to develop a model of the entire heterogeneous multiphase tumour.

As the tumour is compressed, borrowing ideas from the modelling of fluid-filled cellular structures, we expect a complicated interaction of the phases [61]. At the initial stage of compression we expect the pore volume to be reduced as the cells flow into the pore space and remain relatively unstressed. Indeed this was demonstrated in the experiments of Netti *et al* which were summarised in Section 1.2. In these experiments, the stress in the tumours without well-developed extracellular matrices decayed almost to zero for small strains - implying that the cellular phase was unstressed [106]. In tumours with well-developed extracellular matrices we expect the initial stress to be mostly borne by the extracellular matrix. It is only when the level of compression greatly increases, such that the interstitial fluid fractional volume approaches zero, that we expect the compression of the cellular phase to make a significant contribution to the stress. Since the cells are largely composed of fluid, they are almost incompressible, and would provide considerable resistance to compression as the pore volume is squeezed.

Furthermore we do not need to model the aspect of tumours where the theoretical advantages of the multiphase model are greatest - the viscoelastic interaction of each of the phases. The reason is that we are interested in the behaviour of the material on the long-term growth timescale, where inertial and viscoelastic effects are negligible. We are justified in doing this because, as will be seen, the viscoelastic and poroelastic timescales are much less than the growth timescale. This is known as the quasi-steady state approximation. Thus we set the viscoelastic terms to zero, and find that the equations of equilibrium for each phase typically reduce to the divergence of the elastic component of the stress tensor being zero (see in particular [8, 30, 13, 9]). Under the assumption of constituent separation, the elastic stress tensor for each phase depends only on the volume fraction and deformation gradient of that phase. Thus the structure of the equations of mechanical equilibrium is similar to that of the single-phase model, except there are additional unknown variables (the volume fractions). However given the similarity in the structure of the equations of equilibrium, we prefer the single-phase model, which is better parameterised (from the experiments of Netti, Roose and co-workers outlined in the introduction). While the properties of the

individual constituents of a tumour have been measured, there are very few experiments quantifiably indicating how the constituents combine and interact to explain the behaviour of the macroscopic homogeneous tumour. It is difficult also to obtain accurate experimental data governing the growth of the extracellular matrix.

However it needs to be acknowledged that the multiphase model perhaps has a better theoretical motivation. The multiphase model can account for some of the variety of behaviour arising from cell-cell and cell-ECM adhesive forces [37, 116, 9]. In particular, it can account for the migration of cells from areas of high density and pressure to areas of low density and pressure. This plastic flow of cells can provide a means of stress relaxation, offsetting the problem of implausibly high compressive stresses in nonlinear elastic models of tumour growth [141, 9]. Although we assume in our model that the cells do not move relative to the extracellular matrix, in Section 2.5.3 we incorporate local settling and rearrangement of the cellular phase through modelling the local direction of growth to be dependent on the prevailing stress field.

In the following section we will restrict the tumour geometry to an annulus that is cocentric with the capillary. The geometry is thus similar to that of a tumour cord - a cylindrical shell of tumour cells growing around a blood vessel, usually surrounded by necrotic tissue [133]. The cellular kinetics of tumour cords has been modelled in detail by Bertuzzi and co-workers [21, 19, 20]. In general, their models bear considerable similarities to ours: typically, the cord is in quasi-steady-state equilibrium and cellular proliferation is chiefly governed by the oxygen concentration (which in turn is chiefly governed by diffusion from the capillary). However they typically assume that the cells are *motile* and as such are able to relieve stress by migrating radially outward in a fluid-like manner. Thus their models are not intended to be accurate for elastic tumours, as ours is.

The yield stress for when plastic flow occurs is determined by the stress required to overcome intercellular or cell-ECM adhesive bonds. In the multiphase elasto-plastic model of Ambrosi *et al* the yield stress was in terms of the cellular stress only [9]. It is difficult to model this effect using the single-phase model because it requires knowledge of the stress being borne by the cells, whereas the single phase model only gives the stress of the mixture (which includes the ECM) as a whole. As we noted at the start of this section, we

cannot assume a simple linear decomposition of the stress because in the initial phase of compression we expect the majority of the stress to be borne by the extracellular matrix while the cellular phase locally flows into the pore spaces. The confined compression tests of Netti *et al* only exert *uniaxial* compressive forces on the tumour: since lateral movement is not possible, there is no absolute assurance that the cells would not flow if the lateral confinement were removed. We state our yield criteria mathematically in Section 2.5.1.

We will parameterise our elastic model by fitting a constitutive relation to data from confined compression tests similar to Netti *et al* [106]. They compressed tumour materials in a confined environment and determined the long-term elastic behaviour once viscoelastic and poroelastic effects had subsided (refer to Appendix B.0.12 for the parameterisation of our elastic constitutive relations). We thus will not need to worry about poroelastic effects because these processes occur on a timescale much faster than the growth timescale (this argument is spelled out in more detail in Section 2.3). Thus we may model the stress using the First Piola-Kirchhoff stress tensor $\mathbf{P}$ (we outline constitutive relations for this further below).

We model the growth of the tissue to be dependent on the concentration of a nutrient (oxygen) diffusing from the capillary out into the tumour. The capillary is assumed to be far enough from the edge of the tumour that the effect of oxygen diffusing from healthy tissue into the tumour is negligible. We assume that the flux of the interstitial fluid is negligible, so that the concentration profile of the nutrient is due to diffusion rather than convection. This assumption is justified by the fact that the lymphatic system of growing tumours is often severely dysfunctional [26, 91], which means that the flux of fluid from the capillaries to lymph nodes is often negligible, and hence there is no convection. We do not incorporate the effects of other nutrients, such as glucose, into our model. The fundamental reason for this is that we expect the glucose distribution to be driven by diffusion just like the oxygen, so that including the effects of glucose would have little qualitative effect on the growth profile. Instead of including other nutrients, we will investigate the effects of altering the parameters governing the distribution of oxygen. So, for example, we could simulate a glucose-rich environment by increasing the oxygen rate-of-uptake parameters and increasing the rate of cellular proliferation. The effect of our oxygen-diffusion driven model of tumour

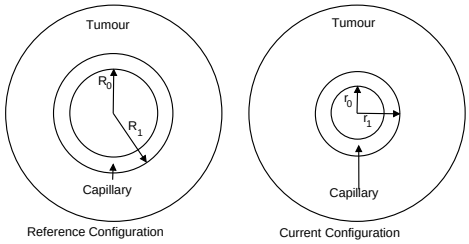

Figure 2.1: The geometry of our model. In the reference geometry the basement membrane and tumour are concentric annuli. The outer radius of the tumour is given by R_2, the outer radius of the capillary by R_1 and the inner radius of the capillary by R_0. Growth in the tumour causes the capillary wall on the inside to buckle in the current configuration. In most of our model variants the displacement at R_2 is set to zero.

cell growth is that the growth will be greatest near the edge of the capillary.

2.2 Model Geometry and Boundary Conditions

We assume the capillaries are (locally) cylindrical. That is, if Z_0 is the axial length of the capillary over which it is approximately cylindrical, we assume Z_0 is much greater than the average capillary radius. We take Z_0 to be approximately of the order of the mean interbranch distance. Konerding *et al* measured the capillary radii, intervessel distances and interbranch distances in human colon adenocarcinomas [87]. In their results the ratio of the mean interbranch distance to the mean capillary radii is approximately 9 in the control tissue and in the tumour centre. The ratio is approximately 5 at the periphery of the tumour.

We assume the nutrient concentration, growth and tissue strain are constant along lines parallel to the axis of the capillary (prior to buckling). Thus the nutrient flux and nontrivial deformation occurs in a plane perpendicular to the cylinder's axis. In effect, we have reduced the geometry of our model to a 2-dimensional planar cross-section of the capillary and surrounding tissue. The outer radius of the capillary wall is R_1 in material coordinates and r_1 in spatial coordinates. The inner radius of the capillary wall is R_0 in material coordinates and r_0 in spatial coordinates. The assumption that the only nonzero deformation occurs in a plane perpendicular to the axis is known as *plane strain*. We note

that this model may not be accurate for tumours with very chaotic vasculature, because the curvature of the capillary with respect to the Z-axis would become significant. It needs to be noted that in our plane strain model, even though the axial displacement u_z is zero, the stress in the axial direction, i.e. P_{ZZ}, will grow to be negative with time due to the compressive stress resulting from the multiplying cells.

Although the displacement is initially assumed to be planar before buckling, we are interested in finding buckles with both planar and axial variation. We stipulate that the axial component of the displacement (u_z) is zero at either end of the annulus (i.e. at $Z = 0$ and $Z = Z_0$). The rationale for this boundary condition is that the buckle is 'axially confined' at branching points.

We consider models which both include and do not include the capillary wall as a distinct elastic structure. Not including the capillary wall is of heuristic value. It is also of practical value because as we saw in Section 1.1 some blood vessels, such as mother vessels, have severely degraded basement membranes. In this case, the 'capillary' is merely an annular cavity in the tumour (from a mechanical point of view). We denote the tumour body by V_m and the capillary wall - if it exists as a distinct mechanical structure - by V_c.

We consider a variety of boundary conditions and geometries: both finite and infinite. Our aim is to develop a model which explains buckling through a consideration of the immediate surrounding of the capillary only. Of course we do not expect to be able to model every scenario: for example there could be a large heterogeneous stress field across the entire tumour. We neglect nonradially symmetric inhomogeneities, which might result, for example, from neighbouring capillaries.

We begin by discussing models with a finite tumour size. In this case, it makes sense to restrict V_m to an annulus surrounding the capillary. The radius (in material coordinates we designate this as R_2) is fixed to be half the average intercapillary distance.

We expect the flux of nutrient at a point midway between two neighbouring capillaries to be zero. This condition is extrapolated around the entire outside of the annulus so that

$$\frac{\partial c}{\partial R} = 0, \text{at } R = R_2. \tag{2.1}$$

There are several options we consider for the mechanical outer boundary condition at R_2. To an extent, we expect the mechanical behaviour here to depend on the macroscopic behaviour of the tumour as a whole, and so it is difficult to determine a 'one-size-fits-all' boundary condition. One outer boundary condition we use is null-displacement: $\mathbf{u} = 0$ at $R = R_2$. This corresponds to the situation of a tumour growing in a confined environment. Another situation we consider is that the tumour can freely expand, so that the boundary condition at R_2 is null-stress: $\mathbf{P} \cdot \mathbf{n} = \mathbf{0}$. For the purposes of testing, another model to be considered is that the tumour is embedded in an infinite linear elastic medium (which is not growing). We equate the traction and displacement at the interface, i.e.

$$\begin{aligned} \mathbf{u}|_- &= \mathbf{u}|_+, \\ \mathbf{P}|_- \cdot \mathbf{n} &= \mathbf{P}|_+ \cdot \mathbf{n}, \text{ where } \mathbf{n} \text{ is the unit normal.} \end{aligned} \tag{2.2}$$

Another possibility is to consider the external medium to exert a radially-inwards pressure at R_2. To motivate this boundary condition, we recall that the no-flux nutrient outer boundary condition is equivalent to stipulating that the nutrient concentration has a minimum halfway between adjacent capillaries. We may arrive at an analogous mechanical boundary condition by arguing that the compressive stress on a line joining two capillaries should be minimal halfway between them. Extrapolating this over the entire outer boundary of the annulus, we find in cylindrical coordinates

$$\frac{\partial(\mathbf{n}^T \cdot \mathbf{P} \cdot \mathbf{n})}{\partial R} = \frac{\partial P_{RR}}{\partial R} = 0, \tag{2.3}$$

where $\mathbf{n} = \mathbf{e}_R$ is the unit normal. This is a very unorthodox boundary condition and we need to be very careful in our interpretation of it. In particular, the buckling analysis to be carried out in the following chapters requires the existence of an energy potential for the entire system, and on first appearances an energy potential for (2.3) cannot be found. However we may circumvent these problems by interpreting (2.3) as a stress boundary condition, i.e.

$$\mathbf{P} \cdot \mathbf{n} = \mathbf{P}^{(I)} \tag{2.4}$$

at $R = R_2$, where $\mathbf{P}^{(I)}$ is defined to be the radial stress at R_2 such that $\frac{\partial P_{RR}}{\partial R} = 0$. We

will see in the following chapters that there exists an energy potential for this system. We could have alternatively interpreted the above as a displacement boundary condition. However it is more natural to interpret (2.3) as a stress boundary condition because the original motivation is that the *stress* is at a minimum halfway between two capillaries. We only require the symmetry condition (2.3) to hold for the radial deformation of the fundamental solution. We do not require it to hold for the incremental (buckled) solution to be obtained in the following chapter because there is no reason to insist that buckling must occur simultaneously in neighbouring capillaries.

We also consider applying the symmetry condition to the displacement u_0, giving us the boundary condition $\frac{\partial u_0}{\partial R} = 0$. For this boundary condition, it seems most natural to interpret this as a fixed displacement, i.e.

$$\mathbf{u} = \mathbf{u}^{(I)} \tag{2.5}$$

at $R = R_2$, where $\mathbf{u}^{(I)}$ is the displacement such that $\frac{\partial u_0}{\partial R} = 0$. The incremental buckled displacements would then have zero displacement.

We now turn to consideration of an infinite geometry. In these models, the tumour is of infinite size and the capillary is an annulus embedded within it. On first appearances this geometry might seem unrealistic, however it has several advantages in comparison to the finite models. We recall that one of the aims of this thesis is to assess the degree to which capillary buckling may be attributed to the profile of the growth gradient in the immediate vicinity of the capillary, as opposed to compressive forces resulting from the confined growth of the tumour as a whole. With the exception of the null-stress boundary condition, in all of the finite-geometry models the pressure at R_2 is *compressive*. Buckling is a consequence of both the growth gradient and the compressive pressure essentially resulting from growth occurring in a confined environment. However with the infinite geometry models, the geometry is not confined and buckling can only occur as a consequence of the growth gradient. Thus the infinite geometry models are in part a mathematical idealisation with heuristic value.

In the first of the infinite geometry models, we insist that the nutrient, growth and

deformation all decay to zero as the radius $R \to \infty$. This model can be obtained from any of the finite geometry models by taking $R_2 \to \infty$. Since the annulus has only one lengthscale (R_1), the equations of mechanical equilibrium over V_m are not directly affected by changes in R_1 (when the deformation is radially symmetric and independent of Z). The lengthscale only affects our problem indirectly through affecting the nutrient distribution. This model seems especially realistic in cases when the distances between capillaries is large - for example Konerding *et al* find that the distance between two capillaries can be as much as 500 times the average capillary radius [87].

The second infinite geometry model we consider is of an annulus in an infinite 'growing' medium. We set the derivative of the nutrient concentration to be zero at outer radius $r = r_1 + r_a$ (in spatial coordinates), where r_a is half the average intercapillary distance. In effect we are insisting that there is zero nutrient flux at points midway between two capillaries, and then extrapolating this condition around the entire boundary of the annulus. For $r > r_1 + r_a$ we insist that the nutrient concentration is constant and equal to its value at $r_1 + r_a$. The rate of mass growth per material volume, r_g, is determined by the nutrient concentration and is also constant throughout this domain. We define r_g more rigorously later on in the chapter. In effect our model is of a capillary in an infinite growing tumour, where the growth for large values of r is equal to the growth midway between two capillaries. For the large r mechanical behaviour, we insist that the stress decays to 0, i.e.

$$\mathbf{P} \to \mathbf{0} \text{ as } r \to \infty. \tag{2.6}$$

The second infinite geometry model is more ad-hoc than the first, however its strength is that it can make sense of the fact that the entire geometry is growing. We further discuss the strengths and weakness of each of the boundary conditions in Chapter 8.

For the internal boundary condition we need to consider whether or not we are including a distinct capillary wall structure in the model. If we include the capillary wall structure, we set the displacement of the tumour at R_1 equal to the displacement of the capillary at R_1 and the normal traction $\mathbf{P}|_+ \cdot \mathbf{n}$ of the tumour equal to the normal traction $\mathbf{P}|_- \cdot \mathbf{n}$ of the capillary (here $\mathbf{n} = -\mathbf{e}_R$ is the unit outward normal at R_1 in material coordinates).

Key	Geometry	Description
A	Finite	Null Displacement and zero nutrient flux at $R = R_2$.
B	Finite	Null Stress and zero nutrient flux at $R = R_2$.
C	Infinite	$[R_2, \infty)$ is linearly elastic, zero nutrient flux at $R = R_2$.
D	Finite	$\frac{\partial \mathbf{P}_{RR}}{\partial R} = 0$ and zero nutrient flux at $R = R_2$.
E	Finite	$\frac{\partial u_0}{\partial R} = 0$ and zero nutrient flux at $R = R_2$.
F	Infinite	Nutrient Distribution and Displacement decay to 0 as $R \to \infty$.
G	Infinite	$\frac{\partial c}{\partial R} = 0$ at $R = R_2$ and $c(R) = c(R_2)$ (for $R > R_2$). $\mathbf{P} \to \mathbf{0}$ as $R \to \infty$.

Table 2.1: We summarise the various boundary conditions and geometries.

If we do not include a distinct capillary wall structure, we set the traction at R_1 equal to zero, i.e. $\mathbf{P} \cdot \mathbf{n} = \mathbf{0}$. The reason we do not set this to (say) the blood pressure is that we expect the interstitial fluid pressure to approximately match the blood pressure, so that the net fluid pressure is close to zero [26]. We assumed in Section 2.3 that the stress can be linearly decomposed into a solid component and a fluid component, and it follows from this assumption that the solid stress must be zero at R_1.

In Chapter 8 we critically evaluate these boundary conditions and discard the ones which produce unrealistic results.

2.3 Interstitial Fluid Pressure

Tumours are characterised by an elevated interstitial fluid pressure gradient [33, 26]. Boucher and Jain found that the elevated interstitial fluid pressure is usually accompanied by an elevated microvascular fluid pressure of similar magnitude [26]. They reasoned therefore that it was unlikely the difference in fluid pressures either side of the capillary wall could be a reason for vascular collapse. However it is still possible that the interstitial fluid pressure gradient within the tumour itself could affect the stress and the distribution of the growth. We assess the significance of this below.

The lymphatic systems of tumours often function poorly, or are nonexistent [26, 91]. Leu *et al* conjecture that this is due to vascular collapse [91]. Thus in tumours the hydrostatic pressure difference between the capillaries and the lymphatic vessels is often much less than in normal tissue. We assume that this pressure difference, and any net flux of fluid due to it, is negligible. This means that the distribution of oxygen, and by implication

the distribution of growth, is *diffusion*-dominated rather than *advection*-dominated. We outline the implications of this in the next section. However in the meantime we must still consider the possibility that there exists an internal hydrostatic pressure gradient which has a significant effect on the stress. In particular, it might be the case that differential growth and deformation throughout the tumour has a significant effect on the hydrostatic pressure gradient. We use linear poroelasticity theory to assess this possibility.

In standard linear poroelasticity theory the interstitial fluid pressure is modelled as resulting in an additional body force of $\alpha\nabla p$, where α is a constant known as Biot's Coefficient. In other words, there is a body force exerted which is proportional to the gradient of the interstitial fluid pressure. Let $\mathbf{v}$ be the velocity of the fluid. We follow the discussion of Mahadevan [97] to assess the relative importance of ∇p. Assuming the body force is $\alpha\nabla p$, the force equilibrium (A.59) implies

$$\alpha\nabla^{\phi}p = \nabla^{\phi}\cdot\mathbf{T}. \tag{2.7}$$

From Darcy's law we find the fluid flux $\mathbf{v}$ is $-K_H\nabla^{\phi}p$, where K_H is the hydraulic conductivity [51]. We wish to find the timescale $[t]$ over which $\nabla^{\phi}p$ has a significant effect on $\nabla\cdot\mathbf{T}$. We let $[r]$ be the natural length scale of (2.7). We set the lengthscale to be approximately the mean intercapillary distance, i.e. $[r] = 10^{-4}$m [87]. The natural scale of $\nabla^{\phi}\cdot\mathbf{T}$ is $K/[r]$, where K is the bulk modulus. This means the natural scale of the left hand side of (2.7) is $\frac{\alpha[r]}{K_H[t]}$ after we substitute $\nabla^{\phi}p = -\frac{1}{K_H}\mathbf{v}$. Balancing the scales of the left and right hand sides of (2.7) leads us to the following expression for the timescale $[t]$ over which the fluid induced body force influences the mechanics, i.e.

$$[t] = \frac{[r]^2\alpha}{K_H K}. \tag{2.8}$$

This gives us the timescale over which there is significant flux of fluid (i.e. the poroelastic relaxation timescale). For the tumours we will be studying, $K\times K_H$ is approximately $10^{-8}-10^{-9}m^2s^{-1}$ [106]. On substitution into (2.8) we find $[t]$ is at most approximately 10α seconds. Since α is order 1, the timescale $[t]$ is a matter of seconds [122]. On the other hand the timescale over which growth is significant is at least a couple of days. For times much

greater than $[t]$ (such as the timescale of our growth model), the fluid flux $\mathbf{v}$ is negligible, which in turn implies the hydrostatic pressure gradient is negligible. Hence we conclude that over the growth timescale poroelastic effects are negligible and we neglect them in our model. In sum, in our model we are assuming the tumour behaves as a nonlinear-elastic material.

2.4 Growth Distribution

There are many variables which influence the tumour growth. These include nutrients, such as oxygen and glucose, chemical growth factors and solid stress [75]. In our model we will simplify the rate of growth to be dependent on the concentration of one nutrient only (oxygen).

The oxygen levels in tumours are usually much lower than normal tissue [137]. For example in some cervical cancers, the median of oxygen partial pressure readings taken throughout the tumour fell to 5 mmHG at the advanced stages of tumour growth, compared to a median of 36 mmHG for normal tissue. There is considerable variation in the oxygenation of tumours. In individual tumours, some areas are saturated with oxygen and others are hypoxic. Vaupel conjectures that the major reason for this is the heterogeneity of the tumour vasculature, so that some areas of tumours are hypoxic due to their great distance from the capillaries [137]. Tannock demonstrated that oxygen concentration is a key factor behind differential growth rates in tumours [134]. Our model builds on the work of these two by modelling the growth to be primarily determined by the oxygen concentration, and the oxygen concentration in turn is primarily determined by proximity to the nearest capillary.

We model the growth using the multiplicative decomposition of the deformation gradient method outlined in Section 1.4.1, i.e.

$$\mathbf{F} = \mathbf{F}_e \cdot \mathbf{F}_g. \tag{2.9}$$

That is, the growth is supposed to result in a hypothetical intermediate configuration V_m^h which is unstressed but potentially incompatible. Refer to Appendix A for an overview of

the mathematics of nonlinear elasticity. We now set up the required formalism, with the ultimate aim of determining an expression for $\mathbf{F}_g$ in terms of the nutrient distribution and stress. Let r_g be the rate of mass growth, per unit mass. That is, suppose that a small section δV_0 of the reference configuration has mass δM_0 at time t. The mass occupying δV_0 at time $t + \delta t$, where $\delta t \ll 1$ is approximately $\delta M_0(1 + r_g \delta t)$.

We now determine an equation relating the growth dilation $\eta = |\mathbf{F}_g|$ (where $|.|$ is the determinant of a matrix) to the mass growth r_g. This is necessary because in Section 2.5 we determine $\mathbf{F}_g$ from η. Let ρ be the mass density per current volume. The continuity equation in material coordinates is

$$\frac{d}{dt}(\rho J) = \rho r_g J, \tag{2.10}$$

since ρJ is the mass density per reference volume. We recall that the growth can be decomposed into two stages. There is an initial isotropic expansion, followed by an elastic deformation. We assume that the growth (i.e. from $V_m \to V_m^h$) preserves the structure and density of the tumoural material. This means that the mass per unit grown volume over V_m^h is constant. Since the mass per unit grown volume is ρJ_e (where $J_e = |\mathbf{F}_e| = J\eta^{-1}$), we find

$$\frac{d}{dt}(\rho J_e) = 0. \tag{2.11}$$

Since $J = J_e \eta$, we may simplify (2.10) to

$$\frac{d\eta}{dt} = r_g \eta. \tag{2.12}$$

Note that we can equivalently think of r_g as

$$r_g = \frac{\partial ln(\phi_s)}{\partial t}, \tag{2.13}$$

where $\phi_s(t)$ is equal to the number of grown cells occuping a small reference volume element δV_0 at time t, divided by the original number of cells occupying δV_0 at $t = 0$. This is because

$$\rho J = \rho_0 \phi_s, \tag{2.14}$$

where ρ_0 is the density at time $t = 0$. We have assumed that the cellular fraction of V_m^h is

preserved over time. We obtain (2.13) by taking the logarithm of (2.14) and differentiating with respect to time. On a comparision of (2.13) and (2.12) we find

$$\eta = \phi_s, \tag{2.15}$$

after making use of the fact that both these quantities must be equal to 1 at $t = 0$.

We will determine constitutive relations for r_g in terms of the oxygen concentration, and in turn we will use r_g to determine the components of the growth dilation tensor $\mathbf{F}_g$. However before doing this we must first model the distribution of oxygen.

2.4.1 Mass Growth and Nutrient Diffusion

We denote the concentration of oxygen per unit current volume by c and model it using a reaction-diffusion equation over current coordinates

$$\frac{\partial c}{\partial t} = D\nabla^2 c - \Gamma_c \text{ on } B_0, \tag{2.16}$$

where Γ_c is the rate of uptake of oxygen per volume of tumour and D is the diffusion coefficient. Following our argument in Section 2.3, we have assumed that fluid flux is negligible. Thus the distribution of oxygen is diffusion dominated, rather than advection dominated (as in ordinary tissue). We will see that this leads to a more accentuated growth profile in tumour tissue: with the growth at the edge of a capillary much higher than the growth at a point halfway between capillaries. One of the fundamental aims of this thesis is to investigate the effect of this growth profile on the mechanical stability of tumours.

We may approximate the nutrient time derivative over the annulus to be zero because the diffusive timescale is much less than the growth timescale. This is known as the quasi-steady-state assumption, and is common in the modelling of nutrient-diffusion-modulated tumour growth: see for example Ambrosi *et al* [6]. The diffusive timescale $[t]_d = [R]^2/D$ gives the timescale over which diffusion is significant. The diffusion coefficient is approximately $10^{-9}m^2s^{-1}$ [122]. From Konerding *et al* the length scale (i.e. half the average intercapillary distance) is approximately $[R] = 10^{-4}m$ [87]. Hence we find the diffusive timescale over this distance is of the order of 10 seconds. Since the growth timescale is a matter of days,

we may model the oxygen concentration as having reached equilibrium, i.e.

$$D\nabla^2 c - \Gamma_c = 0. \tag{2.17}$$

We note that the nutrient concentration profile varies with respect to time as the tumour grows and individual points move further away from the capillary. In material coordinates this is

$$\nabla_0 . \left(J\mathbf{F}^{-1}\mathbf{F}^{-T}\nabla_0 c \right) = \frac{J}{D}\Gamma_c, \tag{2.18}$$

where the divergence and gradient are taken with respect to material coordinates. We obtained this expression by noting that the nutrient flux vector $D\nabla c$ in reference coordinates is $D\mathbf{F}^{-T}\nabla_0 c$.[1] In addition, if $\mathbf{m}$ is a vector field in the current configuration, then $\nabla \cdot \mathbf{m} = J^{-1}\nabla_0 . \left(J\mathbf{F}^{-1}\mathbf{m} \right)$. These identities can be obtained through the use of Reynold's Transport Theorem [110]. The nutrient boundary conditions are

$$\begin{aligned} c &= c_0 \text{ at } R = R_1, \\ \frac{\partial c}{\partial R} &= 0 \text{ at } R = R_2. \end{aligned} \tag{2.19}$$

The rate of uptake per volume of tissue is modelled using Michaelis-Menten kinetics, [122, 143, 34]. Justification for this model can be found in the experiments of Freyer *et al* and Casciari *et al* [54, 34]. Freyer and Sutherland demonstrated that the uptake of oxygen per volume by (oxygen saturated) EMT6/Ro tumour spheroids is approximately independent of the oxygen concentration [54]. Casciari *et al* demonstrated that the uptake per volume depends approximately linearly on the oxygen concentration for hypoxic spheroids [34]. We thus find

$$\Gamma_c = \frac{\lambda_n c}{k_n + c} \tag{2.20}$$

where λ_n and k_n are constants determined from the experiments.

[1] Note that technically $\mathbf{D}$ is a (2,0) tensor, except we assume the diffusion is isotropic so it may be written as a scalar multiple D of the identity (metric) tensor).

2.4.2 Constitutive Relations for Mass Growth

We model the rate of growth, per mass, through Michaelis-Menten type kinetics (2.20), using parameters outlined in [34]. Hence our expression for the rate of growth is

$$r_g = \frac{\lambda_c c}{k_c + c} - k, \tag{2.21}$$

where k is the cell death rate due to treatment. Note that the experiments of Casciari *et al* give the *net* rate of growth of the tumour cells, which means that we do not need to include any terms accounting for apoptosis.

2.4.3 Effect of Compression on Mass Growth

As discussed in Section 1.2, increased cell-cell contact reduces the rate of cell-proliferation through initiating quiescence in cells. We outlined some phenomenologically-motivated models that have been used by others in this section, however none of these are well-parameterised. Since there is a lack of experimental evidence giving a clear indication of the mathematical behaviour of this effect, we keep our model as simple as possible. We multiply the growth rate and the nutrient uptake rate by a factor H accounting for contact inhibition. The reason we multiply the nutrient uptake by H is that compressed cells become quiescent, and therefore do not require as much nutrient [37, 54, 53]. There are two types of model for contact inhibition of growth that we consider: a model in terms of cellular density, and a model in terms of stress. We now outline these models.

One possible model for H is to follow Chaplain *et al* and Ambrosi *et al* by modelling contact inhibition of growth via the cellular density ψ (the number of cells per current volume) [37, 9]. We multiply r_g by the factor H (so that $r_g \to H r_g$), where

$$H = \frac{\psi_2}{\psi_1 + \psi}, \tag{2.22}$$

and ψ_1 and ψ_2 are constants. We divide the numerator and denominator of the above expression by the cellular density at time 0, ψ_0. We know from (2.15) that

$$\frac{\psi}{\psi_0} = \frac{\eta}{J} = |\mathbf{F}_e|^{-1}, \tag{2.23}$$

since η gives the ratio of the number of cells in the grown configuration V_m^h to the reference configuration (as shown in (2.15)), and J gives the ratio of volumes. We recall that $|\mathbf{F}_e|$ gives the local change in volume from the grown (unstressed) configuration V_m^h to the current configuration. We insist that $H = 1$ at time $t = 0$, so that there is no growth inhibition initially. We may thus use (2.23) to rewrite (2.22) as

$$H = (1 + H^*)\frac{|\mathbf{F}_e|}{1 + H^*|\mathbf{F}_e|}, \tag{2.24}$$

where H^* is a parameter we fit in Appendix B.

Another possible way to model H is via the stress, as done by Roose *et al* and Byrne *et al* [122, 30]. The heuristic for this model is that H is inversely proportional to the increment in stress necessary for the production of an unstressed cell. We implement this model using the bulk modulus. The bulk modulus is defined to be the ratio of an increment in the mean hydrostatic stress to an increment in the dilatation (the trace of the strain, which is equal to the fractional increase in volume). It measures the resistance to expansion / compression in the material for small displacements. At any given time, the bulk modulus is equal to

$$K(t) = \frac{1}{9}\frac{\partial P^{ii}}{\partial F_{jj}}, \tag{2.25}$$

and we sum over i and j. In other words, an 'hydrostatic' increment in the deformation gradient of the form $\frac{1}{3}\omega\mathbf{I}$ results in the following increment in the 'mean hydrostatic stress' ($\frac{1}{3}P^{ii}$, summed over i): $\omega K(t)$. At time $t = 0$, when the material is unstressed, $K(t) = K$, which is a measurable material parameter. Following Roose *et al*, we model H as the ratio of the stress needed to double the size of the cells in the unstressed configuration (at zero time) to the stress needed to double the size of the cells in the stressed configuration [122]. The stress is estimated by linearising about the stressed state: i.e. it is expressed in terms of the bulk-modulus. The increments in volume, given by $\frac{\partial J}{\partial \mathbf{F}} : (\frac{1}{3}\omega\mathbf{I}) = \frac{1}{3}\omega J\text{tr}(\mathbf{F}^{-T})$ must be the same in both cases. In the unstressed configuration this is equal to ω. We must also scale by the relative cell density: it can be seen from (2.15) that this is equal to η. We therefore find

$$H = \frac{K(0)Jtr(\mathbf{F}^{-T})}{3\eta K(t)}, \tag{2.26}$$

2.4.4 Cell Death

In this Section we consider radiotherapy-induced and chemotherapy-induced cell death.

Radiotherapeutic Cell Death

We consider the effect of radiotherapy. We model the surviving fraction of tumour cells using a Linear-Quadratic model. This states that for a radiation dosage D (in Grays), the surviving fraction of tumour cells is

$$\exp(-\alpha D - \beta D^2), \tag{2.27}$$

for constants α and β. However there is considerable evidence that the effectiveness of radiotherapy is dependent on the level of oxygen. We thus adapt the relative influence of the dosage in the above model [2, 55], i.e.

$$\exp(-\alpha_h.OER.D - \beta_h(OER.D)^2), \tag{2.28}$$

where OER is the oxygen enhancement ratio. We model the dependence on the oxygen concentration c as

$$OER = \frac{mc + K_m}{c + K_m}, \tag{2.29}$$

where m is the maximum oxygen enhancement ratio and K_m is the oxygen concentration at the point of inflexion of the OER curve. We assume that a dose of $2Gy$ is applied daily. Since the timescale under which apoptosis occurs is also approximately a day, we assume that the cellular kill rate is constant with respect to time and equal to (2.28).

If the cell density per material volume is ϕ, and the cell density per material volume at time 0 is ϕ_0, then from (2.13) we see that

$$\phi = \phi_0 \exp\left(\int_0^t r_g dt\right). \tag{2.30}$$

If we were to apply a single dose D of radiotherapy, then we must multiply (2.30) by (2.28)

to obtain the new cell density, which becomes

$$\phi_n = \phi_0 \exp\left(\int_0^t r_g dt - \alpha_h OER.D - \beta_h (OER.D)^2\right). \tag{2.31}$$

Let us assume the dose D is applied regularly at time intervals $\triangle T$. This allows us to approximate the (discontinuous) cell density function above, with the following continuous function

$$\phi_n = \phi_0 \exp\left(\int_0^t r_g - (\triangle\ T)^{-1}\left(\alpha_h OER.D + \beta_h (OER.D)^2\right) dt\right), \tag{2.32}$$

where we have assumed the treatment was begun at time $t = 0$. The above expression implies that the cell death rate k (as defined in (2.21)) is

$$(\triangle\ T)^{-1}\left(\alpha_h OER.D + \beta_h (OER.D)^2\right). \tag{2.33}$$

Chemotherapeutic Cell Death

The distribution of chemotherapeutic drugs in cancer tends to be dominated by diffusion rather than convection [82, 100]. This is for the same reason that the distribution of oxygen is diffusion dominated: the lymphatic systems of tumours tend to be poor, lessening the capillary-to-lymphatic vessel fluid pressure gradient. There is a paucity of data on the pharmacokinetic properties of chemotherapeutic drugs (i.e. diffusion coefficients and uptake parameters). Therefore we limit ourselves to modelling three well-parameterised ones: Vinblastine, Cisplatin and Tirapazamine.

We model the treatment of the tumour by a chemotherapeutic drug diffusing from the capillary into the tumour. We model the diffusion and uptake of the drug concentration d using a reaction-diffusion equation analogous to oxygen, i.e.

$$\frac{\partial d}{\partial t} = D_d \nabla^2 d - \Gamma_d \text{ on } B_0, \tag{2.34}$$

where Γ_d is the rate of uptake of the drug per volume of tumour and D_d is the diffusion coefficient. As before, we find the diffusive timescale is very small compared to the growth timescale, so that we may approximate the time derivative as zero. In material coordinates

the steady state diffusion equation becomes

$$\nabla_0 \cdot \left(J\mathbf{F}^{-1} \cdot \mathbf{F}^{-T} \cdot \nabla_0 d \right) = \frac{J}{D_d} \Gamma_d, \tag{2.35}$$

The boundary conditions are

$$\begin{aligned} d &= d_0 \text{ at } R = R_1, \\ \frac{\partial d}{\partial R} &= 0 \text{ at } R = R_2. \end{aligned} \tag{2.36}$$

The rate of uptake per volume (i.e. Γ_d), and toxicity of drugs have been modelled in a variety of ways. The general model we consider is of the form [77, 76],

$$\Gamma_d = k_{met} d + \frac{\lambda_{drug} d}{k_{drug} + d} \tag{2.37}$$

for constant λ_{drug}, k_{drug} and k_{met}. The functional form above was fitted by Hicks *et al* to a range of tirapazamine chemotherapeutic drugs. Notice that it contains a linear term and a Michaelis-Menten type term. These drugs are of interest because they selectively target hypoxic regions in tumours. We also use the above form to fit for the uptake of Vinblastine and cisplatin. The parameters for these assume $k_{met} = 0$. For some tirapazamine chemotherapeutic drugs the cell-kill rate is dependent on the level of oxygen ([125, 77, 76]), i.e.

$$k = p_1 \Gamma_d \frac{K0}{K0 + c}. \tag{2.38}$$

Here $K0$ is the oxygen concentration at which the kill rate is half of its maximum potential. For other tirapazimine drugs, as well as Vinblastine and Cisplatin, the cell kill rate is

$$k = p_1 \Gamma_d. \tag{2.39}$$

In both cases, the cell kill rate is proportional to the rate of uptake of the drug.

Chemotherapeutic Treatment Regimes

There is a variety of treatment methods for chemotherapy.

The concentration of cisplatin in the blood following a single injection may be modelled

by the three-compartment equation [47]. The concentration is given by

$$\sigma(t)/\sigma(0) = \left[\frac{(k_{21}-\sigma_a)(k_{31}-\sigma_a)}{(\sigma_b-\sigma_a)(\sigma_c-\sigma_a)} e^{-\sigma_a t} + \right. \\ \left. \frac{(k_{21}-\sigma_b)(k_{31}-\sigma_b)}{(\sigma_a-\sigma_b)(\sigma_c-\sigma_b)} e^{-\sigma_b t} + \frac{(k_{21}-\sigma_c)(k_{31}-\sigma_c)}{(\sigma_a-\sigma_c)(\sigma_b-\sigma_c)} e^{-\sigma_c t} \right], \quad (2.40)$$

where $\{\sigma_a, \sigma_b, \sigma_c\}$ are the half-lives of the three stages of elimination of the drug. The treatment varies according to the type of cancer. For testicular cancer dosage is of the order of a single bolus injection of 20mgm^{-2}. For ovarian cancer, it is $75 - 100\text{mgm}^{-2}$. For bladder cancer it is $50 - 70\text{mgm}^{-2}$.

Tirapazamine is a recently developed drug which selectively targets hypoxic cells [118, 29, 77, 76]. Its metabolism is low in oxygen-rich regions and high in hypoxic regions. This means it is more capable of diffusing to hypoxic regions than many chemotherapeutic agents. As such it is often used in combination with radiotherapy and cisplatin, as it remedies the weakness of these treatments against hypoxic cells. The dosage varies from approximately 160-300 mgm^{-2}.

2.5 Growth Induced Stress Response in Tumour

We assume there is a strain energy function ψ_g giving the stored mechanical energy per unit volume of the grown configuration V_m^h. The strain energy per reference volume ψ may be obtained by multiplying ψ_g by the determinant of $\mathbf{F}_g$ (i.e. η). As the tumour is modelled to be in a quasi-steady state, the strain energy is assumed to be a function of the deformation gradient and the growth only. It is not dependent on the time-derivatives of either of these. This means in particular that we neglect any *viscoelastic* effects. This is justified by the fact that the timescale for viscoelastic relaxation is on the order of 1000 seconds [50, 113], which is negligible compared to the growth timescale (which is on the order of a day). As we have already argued in Section 2.3, the poroelastic relaxation timescale is much less than the growth timescale, so we may similarly neglect the interstitial fluid pressure from our model of the tumour mechanics.

We recall from (2.12) that

$$\frac{d\eta}{dt} = r_g \eta. \tag{2.41}$$

We use this to find an expression for $\mathbf{F}_g$. We assume that the rate of growth of $\mathbf{F}_g$ is diagonal with respect to the axes of the three principal stresses. In subsequent chapters we will see that the system can be in one of two different types of state. In the first state (the 'base state') the system undergoes a purely radial expansion. The second state (State II) is buckled, and not radially symmetric. We will determine the form of $\mathbf{F}_g$ in the base state below, and will determine $\mathbf{F}_g$ for State II in Chapter 4.

The principal stresses of the base state are in the direction of the three cylindrical basis vectors.[2] We may therefore decompose $\mathbf{F}_g$ into its three components $\{\zeta_R, \zeta_\Theta, \zeta_Z\}$ with respect to the cylindrical basis vectors. We substitute $\eta = \zeta_R \zeta_\Theta \zeta_Z$ into (2.12) and find

$$\zeta_R^{-1}\frac{d\zeta_R}{dt} + \zeta_\Theta^{-1}\frac{d\zeta_\Theta}{dt} + \zeta_Z^{-1}\frac{d\zeta_Z}{dt} = r_g. \tag{2.42}$$

We define r_α to be the fractional rate of increase of ζ_α, i.e.

$$r_\alpha = \zeta_\alpha^{-1}\frac{d\zeta_\alpha}{dt}, \tag{2.43}$$

so that upon integration,

$$\zeta_\alpha = \exp\left(\int_0^t r_\alpha dt\right). \tag{2.44}$$

We have made use of the fact that there is no growth at zero time, i.e. $\zeta_\alpha = 1$ when $t = 0$. We observe that

$$r_g = \sum_\alpha r_\alpha, \tag{2.45}$$

so that r_α may be thought of as the mass growth in the direction $\mathbf{e}_\alpha$. We define $\{G_\alpha\}$ to be the multipliers governing the relative growth in the three principal directions, i.e.

$$r_\alpha = G_\alpha r_g, \tag{2.46}$$

[2]For a discussion of the symmetrisation of the growth tensor, refer to Hoger *et al* [78]. The Cauchy stress tensor is diagonalisable because it is symmetric. In the case of the radially symmetric deformation, the principal directions of the stress tensor align with the principal directions of the deformation gradient. The coaxiality of the deformation gradient and stress tensor is a proven result in isotropic hyperelasticity, however this cannot be assumed with anisotropic growth in general because the elastic response is not isotropic. This means that if one were to model growth anisotropy using the principal strains, as suggested by Skalak [126], then in many circumstances the principal axes would be different (although in our particular case they would remain the same).

such that $\sum_\alpha G_\alpha = 1$. We recall from (1.3) that the first Piola-Kirchhoff Stress tensor is

$$\mathbf{P} = \eta \frac{\partial \psi_g}{\partial \mathbf{F}_e} \mathbf{F}_g^{-T}. \tag{2.47}$$

We assume inertial terms are negligible and that the tumour is in mechanical equilibrium, i.e.

$$\nabla \cdot \mathbf{P} = \mathbf{0}. \tag{2.48}$$

2.5.1 Yield Criterion for Irreversible Tissue Damage

In the introduction we noticed that if the tensile forces are sufficiently great, the intercellular and cell-ECM bonds rupture and the tissue is irreversibly damaged. In this section we derive a yield criterion governing when this occurs, so that we may have conditions for when our elastic model ceases to be physically realistic. We assume that the onset of fracture for the entire composite system (cells and ECM) is governed by a yield stress $\tau > 0$. We will not attempt to model what happens beyond this critical threshold. However it suffices to note that we would expect considerable stress relaxation. In this situation we expect buckling to be much less likely to occur. We employ the Tresca yield criterion, i.e. the material yields when one of the following three conditions is reached,

$$\frac{1}{2} |T_{\gamma\gamma} - T_{\delta\delta}| = \tau, \tag{2.49}$$

for some $\gamma \neq \delta$. Here $\{T_{\gamma\gamma}\}$ are the three principal stresses. Sometimes there are tensile (positive) forces if the growth is so great that the tumour material towards the outer end of the annulus is forced to stretch to accommodate the swelling of the annulus. We therefore employ additional yield criteria of the form

$$T_{\gamma\gamma} = \tau, \text{ for some } \gamma. \tag{2.50}$$

The set of yield criteria given by (2.49) and (2.50) are intended to only give an approximate indication of when fracture occurs. We have restricted ourselves to determining when either

the pure shear or pure normal force exceeds the yield stress. We obtain an estimate for τ in Appendix B.0.12.

2.5.2 Tumour Elastic Constitutive Relations

To model the mechanical response of the tumour we use a general compressible non-linear elastic model: the Blatz-Ko Material. This was used by Ambrosi *et al* to model stress-modulated growth in tumours [6, 7]. The strain energy for a Blatz-Ko material is [18]

$$\psi(I_1, I_2, I_3) = \frac{Gf}{2}\left(I_1 - 3 - \frac{2}{q}\left(I_3^{\frac{q}{2}} - 1\right)\right) + \frac{G(1-f)}{2}\left(\frac{I_2}{I_3} - 3 - \frac{2}{q}\left(I_3^{\frac{-q}{2}} - 1\right)\right), \quad (2.51)$$

where $\{I_1, I_2, I_3\}$ are the three principal invariants of $\mathbf{C} = \mathbf{F}^T \cdot \mathbf{F}$, G is the shear modulus and $q < 0$ is a parameter. We will obtain estimates for the parameters q and f by fitting the data from confined compression tests to the model.[3]

We determine the stress tensor for a growing material as follows. We take the three invariants in (2.51) to be the invariants of the grown strain tensor $\mathbf{C}_e = \mathbf{F}_e^T \mathbf{F}_e$. With this understanding, we may now differentiate (2.51) with respect to $\mathbf{F}_e$ (as explained in Section 1.4), and obtain the first Piola-Kirchhoff Stress tensor using (2.47), i.e.

$$\mathbf{P} = \eta G_t f\left(\mathbf{F}\mathbf{F}_g^{-2} - \eta^{-q} J^q \mathbf{F}^{-T}\right) - \eta G_t (1-f)\left(\mathbf{F}^{-T}\mathbf{F}_g^2\mathbf{F}^{-1}\mathbf{F}^{-T} - \eta^q J^{-q}\mathbf{F}^{-T}\right). \quad (2.52)$$

We have made use of the fact $\mathbf{F}_g = \mathbf{F}_g^T$.

2.5.3 Growth Multiplier Constitutive Relations

Drawing on the literature review in Section 1.3, we motivate our model of anisotropic growth. After mitosis, the adhesion of the daughter cells to the extracellular matrix is at first weak, but strengthens over time [39]. As the adhesion strengthens, we expect the cells to stretch in response to the stress field. We also expect increased deposition of extracellular matrix in response to the stress field, and a strengthening of adhesive bonds which are under tension [139]. All these factors indicate that the growth is preferentially directed in the direction of least compressive stress. In fact it is impossible to fully separate

[3]The confined compression data is sourced from Roose (personal communication).

the growth from the deformation. As the tumour grows, the natural configuration evolves as the adhesive bonds and cellular shape alter in response to the stress field.

Perhaps the best experimental evidence of this is the work of Helmlinger *et al* and Cheng *et al* [75, 40]. Helmlinger *et al* cultured LS174T tumour multicell spheroids in an agarose gel contained in a cylinder [75]. As the spheroids grew, the gel was more compressed in the plane of the cylinder, and therefore compressive planar forces were greater than the force in the direction parallel to the cylinder's axis. In response to this orthotropic stress field, the spheroids grew more in the longitudinal direction than in the planar direction. Cheng *et al* obtained similar results.

These experiments demonstrate that the shape of the spheroid is dictated by the stress field. However it is not immediately clear the extent to which the ellipsoidal shape is due to anisotropic growth, or to anisotropic deformation. If for example the growth was purely isotropic, then our model developed thus far would predict the spheroid to elastically deform into the ellipsoidal shape in response to the elevated planar stress, and the deformed spheroid would be residually stressed. However there are two factors which suggest that there is little residual stress, and that the ellipsoidal shape is mostly due to anisotropic growth. Helmlinger *et al* imply that the spheroids maintained their ellipsoidal shape initially after they were cut out of the gel and placed in free suspension. If the growth was isotropic, we would expect the ellipsoids to elastically deform back towards a spheroidal shape once freed from the gel. Secondly the uniaxial compression experiments outlined above demonstrated that at low levels of compression LS174T monolayers cannot sustain a stress gradient over time (i.e. there is viscoelastic relaxation). We therefore expect considerable reorientation of the natural state in response to the growth.[4]

However even if the shape of the spheroid is mostly due to anisotropic growth, it it still very difficult to construct a model for the relationship between stress and growth from the data. Helmlinger *et al* acknowledge that there is substantial uncertainty in their calculation of the stress. Furthermore the stress field is not constant: initially the spheroid is

[4]Note that we do not expect our model to be accurate for carcinomas (i.e. the constituent of LS174T spheroids) for precisely this reason: the lack of elastic behaviour at small levels of stress. We nevertheless study Helmlinger's experiments in the hope that the relationship between growth and stress is broadly consistent for all types of material in the body.

unstressed, with the compressive stresses growing in response to the increasing compression. We conclude that it is impossible to to deduce the *rate* of growth from the data provided.

We must therefore make a sensible estimate for the form of the growth multipliers $\{G_{\alpha\alpha}\}$, with an emphasis on simplicity due to the paucity of data. We firstly outline our requirements for the growth multipliers. We assume that there is no resorption, so that $G_{\alpha\alpha} \geq 0$. We stipulated earlier that the growth multipliers do not affect the *net* amount of growth, so that $\sum_\alpha G_{\alpha\alpha} = 1$. We also require that there is no growth in the direction $\mathbf{e}_\alpha$ if the level of compression in this direction is infinite (i.e. $G_{\alpha\alpha} \to 0$ as $T_{\alpha\alpha} \to -\infty$ and the other components of $\mathbf{T}$ are fixed), and that if there is ininite tension in the direction $\mathbf{e}_\alpha$ then all of the growth is in this direction (i.e. $G_{\alpha\alpha} \to 1$ as $T_{\alpha\alpha} \to \infty$). There are two models for the growth multipliers we consider: one motivated by consideration of the strain energy, and one motivated by anisotropic growth in the human aorta.

In the first model, we motivate the functional form of G_α by considering the growth to (locally) minimise the strain energy. In other words, one can think of the anisotropic growth as a local means of stress relaxation. After mitosis, we assume the new tumour cells align in response to the local mechanical forces in such a way that the strain energy is minimised. We use the principal stretch formalism to write the strain energy, per unit volume of the hypothetical intermediate grown configuration, as

$$\psi_g(\lambda_1, \lambda_2, \lambda_3), \tag{2.53}$$

where $\{\lambda_j\}$ are the eigenvalues of $\mathbf{F}_e$.[5] We observe that $\lambda_\alpha = F_{\alpha\alpha}\zeta_\alpha^{-1}$, as the cylindrical basis vectors comprise the principal axes of each of $\{\mathbf{F}, \mathbf{F}_e, \mathbf{F}_g\}$. Consider a small increment of grown mass $\delta t G_\alpha r_g \mathbf{e}_\alpha$ in V_m^h from time $t \to t + \delta t$ (summed over α). This induces an increment in the strain energy per current volume of the form

$$\delta t \frac{\partial \psi_g}{\partial t} = -r_g \delta t \left(\frac{\partial \psi_g}{\partial \lambda_\alpha} \lambda_\alpha G_\alpha \right), \tag{2.54}$$

where we have used the fact

[5] We may employ the principal stretch formalism because the material is isotropic relative to the V_m^h. Indeed the Blatz-Ko constitutive relations (2.51) implicitly assume that the response relative to V_m^h is isotropic. Refer to Appendix A.1.4 for an explanation of the principal stretch formalism.

$$\begin{aligned}\frac{\partial \lambda_\alpha}{\partial t} &= \frac{\partial \lambda_\alpha}{\partial \zeta_\alpha}\frac{\partial \zeta_\alpha}{\partial t} \\ &= -\zeta_\alpha^{-2} F_{\alpha\alpha}\left(\zeta_\alpha r_g G_\alpha\right) \\ &= -\lambda_\alpha r_g G_\alpha. \end{aligned} \tag{2.55}$$

However $\frac{\partial \psi_g}{\partial \lambda_\alpha}\lambda_\alpha$ is merely the principal value of the Cauchy Stress multiplied by η. We may therefore write $\delta t \frac{\partial \psi_g}{\partial t}$ as

$$-\delta t r_g \eta T_{\alpha\alpha} G_\alpha, \tag{2.56}$$

where we sum over α. At the start of this section we noted that we require the growth multipliers to be such that $G_\alpha \geq 0$ and

$$\sum_\alpha G_\alpha = 1. \tag{2.57}$$

The above equation (2.56) demonstrates that the Cauchy Stress governs the topology of the strain energy function relative to the directional growth. As explained earlier, our motivation is to choose the growth multipliers so that they minimise the increment in the strain energy. However since (2.56) is linear in the growth multipliers, and the constraint is linear, the minimum may be obtained by setting $G_\beta = 1$ where $T_{\beta\beta}$ is the maximal principal Cauchy Stress. In other words, we are lead to the conclusion that the tumour is most inclined to grow in the direction where the stress field is most expansive and least compressive. This seems physically plausible. A problem however is that it implies our growth function is too discontinuous. If, for example, in some parts of the tumour the radial direction has the greatest Cauchy Stress and in other parts the axial direction has the greatest Cauchy Stress, then this criterion might suggest G_R switches from 1 to 0 at the interface of these two regions (and G_Z does the opposite).

We wish to find a continuous weighting function which approximates the above discontinuous step function. We therefore propose the following means of weighting the growth multipliers,

$$G_{jj} = \exp\left(AK_t^{-1}\mathbf{T}_{jj}\right) G_\Sigma^{-1}, \tag{2.58}$$

$$G_\Sigma = \exp\left(AK_t^{-1}\mathbf{T}_{RR}\right) + \exp\left(AK_t^{-1}\mathbf{T}_{\Theta\Theta}\right) + \exp\left(AK_t^{-1}\mathbf{T}_{ZZ}\right), \tag{2.59}$$

where K_t is the bulk modulus[6] and A is a constant. We have scaled by the bulk modulus because this represents the compressibility of the material. It can be seen that (2.59) satisfies all of the phenomenological requirements outlined above.

It is very difficult to motivate a value for A from the experimental literature. Perhaps our best hope are the experiments of Helmlinger *et al* outlined above. The ellipsoids have a long axis which is roughly 2.2 times as long as the short axis. We estimate that the stress in the long axis is approximately the same as the surface stress of a fully grown isotropic spheroid, which they report to be -105 mmHg (roughly 6 times the bulk modulus, using the value for the bulk modulus we obtain in Chapter 1). There is no way of estimating the stress in the direction of the short axis, although we expect this to be considerably more compressive than the long axis. Furthermore there is the problem mentioned above that the stress fields change over time as the compressive force of the gel gets greater in response to the growth of the spheroid. We guess from these experiments that A is $O(1)$, but cannot conclude much more.

Our other model of the growth multipliers is motivated by consideration of the modelling of anisotropic growth in the human aorta by Taber and co-workers [131, 130, 1]. Taber models the rate of growth in a principal direction as being proportional to the difference between the principal stress in that direction and a constant 'homeostatic' stress. We are not aware of any experimental evidence of such a homeostatic stress in tumours, but since there is such a paucity of experimental data we will nevertheless consider this model. We write this as

$$G_\alpha = \frac{T_{\alpha\alpha} - T_0}{T_{\beta\beta} - 3T_0}, \tag{2.60}$$

where we sum over β and $T_0 < 0$ is a constant. We have normalised so that $\sum_\alpha G_\alpha = 1$. This model is only accurate for $T_{\alpha\alpha} \geq T_0$, because otherwise G_α would be negative (contradicting our assumption that there is no resorption). In our results we investigate both models for $\{G_\alpha\}$ that we have motivated in this section (i.e. (2.59) and (2.60)).

[6]This is the bulk modulus, i.e. $K_t = \frac{2G_t(1+\nu_t)}{3(1-2\nu_t)}$.

2.6 Capillary Mechanics

We have already seen in Section 1.1 that the general consensus amongst experimentalists is that the basement membrane bears most of the load, much more than the endothelial layer and the pericytes. We model the pericytes as being of the same substance as the tumour and therefore do not consider them as a distinct mechanical structure. In fact we may also neglect the endothelial layer and for the purposes of our model only include the basement membrane.

We argue that the stored elastic energy of the endothelial layer is negligible compared to the stored elastic energy of the basement membrane. We justify this as follows. We begin by comparing the geometry of the two layers. From Table 1.1 the radius of the basement membrane is approximately 6 - 15 μm, the thickness of the basement membrane is approximately 0.05 to 0.1 μm and the thickness of the endothelial layer is approximately 0.2 to 0.5 μm. Although there is considerable variance amongst different capillaries, the experimental data suggests these values correlate quite strongly, so that capillaries with a greater radius typically have a thicker basement membrane and thicker endothelial layer. We let h_e and h_{BM} be the respective thicknesses of the two layers, and R_e and R_{BM} be the respective radii of the two layers. From the data we obtain the following approximate ratios

$$\frac{h_{BM}}{R_{BM}} = \frac{1}{125} \ , \ \frac{h_e}{R_{BM}} = \frac{1}{25} \ , \ \frac{h_e}{h_{BM}} = 5. \tag{2.61}$$

For both layers, the ratio of the thickness over the radius is relatively small. This means we may approximate the radii as being equal, to leading order. We are now lead to make the key assumption that the displacement gradient $\mathbf{F} - \mathbf{I}$ over the basement membrane is of the same order as the displacement gradient $\mathbf{F} - \mathbf{I}$ over the endothelial layer. We denote the leading order magnitude of the displacement gradient by γ. Thus the leading orders of the basement membrane elastic energy and the endothelial layer elastic energy are respectively

$$E_{BM} h_{BM} R_{BM} \gamma \text{ and } E_e h_e R_{BM} \gamma. \tag{2.62}$$

We use the data in Table 1.1 to estimate the ratio of the Young's Moduli to be 10^{-3}. Accordingly we find the ratio of the stored energy in the endothelial layer to the stored

energy in the basement membrane to be approximately

$$\frac{E_e h_e}{E_{BM} h_{BM}} \approx 0.005. \tag{2.63}$$

Since this is much less than one, we may neglect the endothelial layer from our model.

It needs to be noted that our assumption that the leading order of the elastic energies have the form of (2.62) is not trivial. In Stoll's model of the capillary wall as a flexural inextensible ring, the elastic energy is dominated by the change in curvature and the energy due to the strain (i.e. the 'tangential stretch') is neglected [129] (due to the assumption of inextensionality). Furthermore the elastic energy is proportional to the bending moment, which is proportional to the cube of the thickness. However we argue in Section 9.3 that the inextensible flexural ring is not appropriate for our model, chiefly because we expect the capillary wall to be extensible and pre-stressed at the time of buckling. Refer to this section for a more detailed discussion.

2.6.1 Constitutive Relations for the Basement Membrane

In Chapter 1 we saw that the mechanical behaviour of blood vessels has been modelled in a variety of ways. We choose to model the basement membrane as a neo-Hookean material. However before we detail this model we first explain why we did not choose the Fungian exponential strain energy function. In this strain energy function, the stress is proportional to the exponential of a quadratic form in the strain variables $E_{\alpha\beta}$. It has been used to model blood vessels, particularly arteries and veins, many times. However we do not use it for the following reasons. The basement membrane has a different composition to arteries and membranes: there are insufficient parameters in the experimental literature for a Fungian strain energy function as the only parameter in the literature is the Young's Modulus. The basement membrane is relatively stiff (i.e. it has a high Young's Modulus) and we therefore expect it to be resistant to compression in the radial and azimuthal directions. However most Fungian strain energy functions are only intended to model *stretching* in the azimuthal and longitudinal directions. They do not model compression, and do not model strain in the radial direction.

We will use a simple model for the capillary basement membrane: an incompressible Neo-Hookean material, with strain energy $\psi_{NH} = \frac{G_c}{2}(I_1 - 3)$, where I_1 is the first invariant of $\mathbf{C}$ and G_c is the Shear Modulus of the basement membrane. To model the incompressibility constrain, we must include a term of the form $-p(J-1)$, where p is a Lagrange Multiplier corresponding to the incompressibility constraint $J = 1$, i.e.

$$\psi = \psi_{NH} - p(J-1). \tag{2.64}$$

On differentiating, we obtain the following expression for the first Piola-Kirchhoff Stress, i.e.

$$\mathbf{P} = G_c\mathbf{F} - p\mathbf{F}^{-T}. \tag{2.65}$$

The strength of this model is that the only unknown parameter is one for which we have a good estimate from experimental data: the shear modulus G_c. The incompressibility assumption seems to be well-established experimentally [56]. Indeed Holzapfel uses such a model to model the isotropic response of larger arteries at low strain [79]. Holzapfel remarks that the Neo-Hookean model is accurate at low strain because the collagenous fibres have not been able to orient themselves along their principal axes.

2.7 Model Summary and Nondimensionalisation

We summarise the model developed over this chapter. We recall our key variables: t is the time, $\mathbf{u}$ is the growth induced displacement from the reference state to the current state, c is the concentration of nutrient and ζ is the growth dilation. The deformation gradient $\mathbf{F}$ is equal to $\mathbf{I} + \nabla\mathbf{u}$ and $J = |\mathbf{F}|$. Our model is formulated in *material* coordinates. The parameters used in the model are outlined and justified in Appendix B.

We adopt the following scaling. The lengthscale is R_1 (the radius of the capillary wall), the timescale is the inverse of the drug proliferation rate λ_c^{-1}, the nutrient scale is the nutrient concentration at R_1 (i.e. c_0) and the drug scale is the drug concentration at R_1 (i.e. d_0). Scaled variables are denoted with an asterix.

2.7.1 Nondimensionalisation of Growth and Diffusion Equations

After adopting the above scaling, we obtain the following nondimensional parameters and equations,

$$\begin{aligned} k_n^* =& \frac{k_n}{[c]}, & k_c^* =& \frac{k_c}{[c]}, \\ K0^* =& \frac{K0}{[c]}, & \alpha =& \frac{[R]^2\lambda_n}{D[c]}, \\ k_d^* =& \frac{k_{drug}}{[d]}, & \alpha_d =& \frac{[R]^2\lambda_{drug}}{D_d[d]}, \\ t^* =& t\lambda_c, & k_{met}^* =& k_{met}\frac{[R]^2}{D_d}, \\ \mu^i =& p_1 k_{met}\lambda_c^{-1}[d], & \mu^{ii} =& p_1\lambda_{drug}\lambda_c^{-1}. \end{aligned} \tag{2.66}$$

The growth dilation in a direction $\alpha \in \{R, \Theta, Z\}$ is

$$\zeta_\alpha = \exp\left(\int_0^t r_\alpha dt\right), \tag{2.67}$$

where

$$r_\alpha = G_\alpha H\left(\frac{c^*}{c^* + k_c^*} - \mu\right). \tag{2.68}$$

The nutrient and drug distributions are governed by the equations,

$$\nabla\cdot\left(J\mathbf{F}^{-1}\mathbf{F}^{-T}\nabla c^*\right) = \frac{H\alpha J c^*}{k_n^* + c^*}, \tag{2.69}$$

$$\nabla\cdot\left(J\mathbf{F}^{-1}\mathbf{F}^{-T}\nabla d^*\right) = HJk_{met}^* d^* + \frac{HJ\alpha_d d^*}{k_d^* + d^*}. \tag{2.70}$$

with $c^* = 1$ and $d^* = d_0(t^*)$ at $R = R_1$. If we are employing a finite geometry, $\frac{\partial c^*}{\partial R} = \frac{\partial d^*}{\partial R} = 0$ at $R = R_2$. If we are modelling a 'growing' infinite medium (model G), $\frac{\partial c^*}{\partial R} = \frac{\partial d^*}{\partial R} = 0$ at $R = R_2$ and $\{c(R) = c(R_2),\ d(R) = d(R_2)\}$ if $R > R_2$. If our model is that of a 'decaying' infinite medium (model variant F), $c^* \to 0$ and $d^* \to 0$ as $R \to \infty$. In the case

of chemotherapy, depending on the type of drug we have

$$\mu = \mu^i d^* + \mu^{ii} \frac{d^*}{k_d^* + d^*}, \tag{2.71}$$

$$\mu = \left(\mu^i d^* + \mu^{ii} \frac{d^*}{k_d^* + d^*} \right) \frac{K0^*}{K0^* + c^*}. \tag{2.72}$$

In the case of radiotherapy, we have

$$\mu = \frac{1}{\lambda_c \triangle T} \left(\alpha_h OER_\alpha \cdot D + \beta_h \left(OER_\beta \cdot D \right)^2 \right), \tag{2.73}$$

where

$$OER_\alpha = \frac{c^* m_\alpha + K_m^*}{c^* + K_m^*}, \tag{2.74}$$

$$OER_\beta = \frac{c^* m_\beta + K_m^*}{c^* + K_m^*}. \tag{2.75}$$

The types of growth inhibition we consider are respectively cell-contact and bulk modulus, i.e.

$$H = (1 + H^*) \frac{|\mathbf{F}_e|}{1 + H^* |\mathbf{F}_e|}, \tag{2.76}$$

$$H = \frac{K(0) J tr(\mathbf{F}^{-T})}{3\eta K(t)}. \tag{2.77}$$

Our default model of the growth multipliers is

$$G_{jj} = \exp\left(A K_t^{-1} \mathbf{T}_{jj} \right) G_\Sigma^{-1}, \text{ where} \tag{2.78}$$

$$G_\Sigma = \exp\left(A K_t^{-1} \mathbf{T}_{RR} \right) + \exp\left(A K_t^{-1} \mathbf{T}_{\Theta\Theta} \right) + \exp\left(A K_t^{-1} \mathbf{T}_{ZZ} \right). \tag{2.79}$$

We also consider growth multipliers of the form

$$G_{\gamma\gamma} = T_{\gamma\gamma}^* / \sum_\alpha T_{\alpha\alpha}^*, \tag{2.80}$$

where $T_{\alpha\alpha}^* = T_{\alpha\alpha} - T_0$ and T_0 is a constant.

2.7.2 Summary of Mechanical Model

The tumour is in mechanical equilibrium, such that

$$\nabla \cdot \mathbf{P} = \mathbf{0} \text{ on } V_m, \tag{2.81}$$

where $\mathbf{P}$ is the 1st Piola-Kirchhoff stress tensor. The yield criteria, governing the onset of irreversible tissue damage, are

$$\begin{aligned} &\frac{1}{2}\left|T_{RR} - T_{\Theta\Theta}\right| = \tau \ \ , \ \ \frac{1}{2}\left|T_{RR} - T_{ZZ}\right| = \tau, \\ &\frac{1}{2}\left|T_{ZZ} - T_{\Theta\Theta}\right| = \tau \ \ , \ \ T_{RR} = \tau, \\ &T_{\Theta\Theta} = \tau \ \ , \ \ T_{ZZ} = \tau. \end{aligned} \tag{2.82}$$

If the geometry is finite, the mechanical boundary condition at R_2 could be one of the following, depending on the model variant,

$$\begin{aligned} \mathbf{u} &= \mathbf{0} \text{ for model A}, \\ \mathbf{P} \cdot \mathbf{n} &= \mathbf{0} \text{ for model B}, \\ \mathbf{P}|_- \cdot \mathbf{n} &= \mathbf{P}|_+ \cdot \mathbf{n} \text{ and } \mathbf{u}|_- = \mathbf{u}|_+ \text{ for model C}, \end{aligned} \tag{2.83}$$

$$\begin{aligned} \frac{\partial P_{RR}}{\partial R} &= 0 \text{ for model D}, \\ \frac{\partial u_R}{\partial R} &= 0 \text{ for model E}. \end{aligned} \tag{2.84}$$

In model C, the stress $\mathbf{P}|_+$ and displacement $\mathbf{u}|_+$ are that of an infinite linear medium in quasistatic equilibrium. In models F and G, the geometry is infinite, and

$$\mathbf{u} \to \mathbf{0} \text{ as } R \to \infty. \tag{2.85}$$

The boundary condition at $R = R_1$ varies according to whether we are including a distinct capillary wall structure in our model or not. If we are not including the capillary wall structure, the boundary condition is

$$\mathbf{P} \cdot \mathbf{n} = \mathbf{0}. \tag{2.86}$$

If we are including a distinct capillary wall structure then we must ensure the continuity of the traction and displacement at the interface of the tumour and capillary wall, i.e.

$$\mathbf{P}|_{-} \cdot \mathbf{n} = \mathbf{P}|_{+} \cdot \mathbf{n}, \tag{2.87}$$

$$\mathbf{u}|_{-} = \mathbf{u}|_{+}, \tag{2.88}$$

at $R = R_1$. At $R = R_0$,

$$\mathbf{P} \cdot \mathbf{n} = \mathbf{0}. \tag{2.89}$$

We outline the method of solution of our model in the following chapter.

Chapter 3

Radially Symmetric Solution for Model

In this chapter we determine the radially symmetric solution of our model. We denote this the *fundamental* solution. This is the state the system is assumed to adopt before buckling; in subsequent chapters we will perform a linear stability analysis over this state to determine the onset of buckling. We work in cylindrical coordinates, so that the displacement is of the form $\mathbf{u} = u_0(R,t)\mathbf{e}_R$, and all of the other variables are independent of the cylindrical coordinates Θ and Z. The thrust of this chapter is to determine which of the model variants outlined in Chapter 2 are physically realistic. There are seven different boundary conditions (outlined in Table 3), two different models of growth inhibition (as well as no

Key	Tumour Geometry	Description
A	Finite	Null Displacement and zero nutrient flux at $R = R_2$.
B	Finite	Null Stress and zero nutrient flux at $R = R_2$.
C	Infinite	$[R_2, \infty)$ is linearly elastic, zero nutrient flux at $R = R_2$.
D	Finite	$\frac{\partial \mathbf{P}_{RR}}{\partial R} = 0$ and zero nutrient flux at $R = R_2$.
E	Finite	$\frac{\partial u_0}{\partial R} = 0$ and zero nutrient flux at $R = R_2$.
F	Infinite	Nutrient Distribution and Displacement decay to 0 as $R \to \infty$.
G	Infinite	$\frac{\partial c}{\partial R} = 0$ at $R = R_2$ and $c(R) = c(R_2)$ (for $R > R_2$). $\mathbf{P} \to \mathbf{0}$ as $R \to \infty$.

Table 3.1: The various boundary conditions and geometries. The radius of the cavity (which represents the capillary) is R_1. If the geometry is finite, the outer radius of the tumour annulus is R_2. At $R = R_1$, the boundary condition is always that of null stress $\mathbf{P} \cdot \mathbf{n} = \mathbf{0}$ and fixed nutrient concentration $n = 1$.

growth inhibition) and two different models of the anisotropic response of growth to stress (as well as isotropic growth). We eliminate the model variants which predict physically unrealistic behaviour. We will see that each of the model variants have strengths and weaknesses, however the model variant we most prefer is model F (that of a capillary in an infinite medium with decaying nutrient). In model F we require the growth to be anisotropic in order that the model predictions seem physically realistic. Of the finite geometry models, we most prefer model A. We assume throughout this chapter that the tumour is not being treated, so that $\mu = 0$. For convenience, we drop the asterisks from our scaled variables.

There are four main sections to this chapter. In the first section we state the equations governing the radially symmetric solution of our model. In the second section we linearise the system and obtain an exact analytic solution. This will be of assistance in our obtaining a numerical solution for the infinite medium models, and it also sheds light on the qualitative behaviour of our model. In the third section we outline our numerical method for solving the radially symmetric model. In the last section, we outline results for the system without a distinct capillary wall structure.

3.1 The Equations Governing the Radially Symmetric Model

In this section we obtain explicit expressions governing the radially symmetric solution of our model. We write the nutrient distribution as a radially symmetric function of R, $c_0(R)$. Its governing equation is

$$\nabla \cdot \left(J_0 \mathbf{F}_0^{-1} \mathbf{F}_0^{-T} \nabla c_0 \right) = \frac{H_0 J_0 \alpha c_0}{k_n + c_0}, \tag{3.1}$$

where $c_0 = 1$ at $R = R_1$ and H_0 is the growth inhibition factor (as given in (2.77)). Since the azimuthal equation is identically zero as a consequence of the radial symmetry, this reduces to the following ordinary differential equation

$$F_{0,RR}^{-1} F_{0,\Theta\Theta} \frac{\partial^2 c_0}{\partial R^2} + \frac{\partial c_0}{\partial R} \left[R^{-1} - F_{0,\Theta\Theta} F_{0,RR}^{-2} u_0'' \right] - \frac{H_0 J_0 \alpha c_0}{k_n + c_0} = 0, \tag{3.2}$$

where $J_0 = |\mathbf{F}_0|$ and $F_{0,RR} = 1 + \frac{\partial u_0}{\partial R}$ and $F_{0,\Theta\Theta} = 1 + \frac{u_0}{R}$ are respectively the radial and azimuthal components of the deformation gradient. If the geometry is finite, the boundary

condition at $R = R_2$ is $\frac{\partial c_0}{\partial R} = 0$. In model F, $c_0 \to 0$ as $R \to \infty$.

The diagonal components of the growth dilation are given by

$$\zeta_\alpha = \exp(\bar{r}_\alpha), \tag{3.3}$$

where the directional mass growth is

$$\bar{r}_\alpha = \int_0^t \left(H_0 G_{\alpha,0} \frac{c_0}{k_c + c_0} - \mu_0 \right) d\tau. \tag{3.4}$$

Here $\{G_{\alpha,0}\}$ are the directional growth multipliers. We refrain from writing explicit expressions for $G_{\alpha,0}$ and H_0, as they depend on the model variant, but merely note that they are functions of the growth and deformation gradient.

The tumour is in mechanical equilibrium, such that

$$\nabla \cdot \mathbf{P}_0 = \mathbf{0} \text{ over } V_m, \tag{3.5}$$

where $\mathbf{P}_0$ is the first Piola-Kirchhoff Stress. This amounts to a second order differential equation in $u_0(R)$ of the form

$$\begin{aligned}
&G_t \eta u_0'' \left(f(\zeta_R^{-2} + (1-q) J_0^q \eta^{-q} F_{0,RR}^{-2}) - (1-f)(-3\zeta_R^2 F_{0,RR}^{-4} + (q+1) J_0^{-q} \eta^q F_{0,RR}^{-2}) \right) \\
&\quad + \eta' G_t \left(f(F_{0,RR}\zeta_R^{-2} - J_0^q \eta^{-q} F_{0,RR}^{-1}) - (1-f)(\zeta_R^2 F_{0,RR}^{-3} - J_0^{-q}\eta^q F_{0,RR}^{-1}) \right) \\
&\quad + \eta G_t \Big(f(-2F_{0,RR}\zeta_R' \zeta_R^{-3} + q J_0^q \eta^{-q-1} F_{0,RR}^{-1} \eta' - q J_0^q \eta^{-q} F_{0,RR}^{-1} F_{0,\Theta\Theta}^{-1} F_{0,\Theta\Theta}') \\
&\qquad -(1-f)\left(2F_{0,RR}^{-3}\zeta_R \zeta_R' - q J_0^{-q} \eta^{q-1} F_{0,RR}^{-1} \eta' + q J_0^{-q-1} \eta^q F_{0,\Theta\Theta}' \right) \Big) \\
&\quad + \eta G_t R^{-1} \Big(f(F_{0,RR}\zeta_R^{-2} - F_{0,\Theta\Theta}\zeta_\Theta^{-2}) + f J_0^q \eta^{-q} \left(F_{0,\Theta\Theta}^{-1} - F_{0,RR}^{-1} \right) \\
&\quad + (1-f)\left(\zeta_\Theta^2 F_{0,\Theta\Theta}^{-3} - \zeta_R^2 F_{0,RR}^{-3} \right) + (1-f) J_0^{-q} \eta^q \left(F_{0,RR}^{-1} - F_{0,\Theta\Theta}^{-1} \right) \Big) = 0.
\end{aligned} \tag{3.6}$$

If we are not including a distinct capillary wall structure in our model, then $\mathbf{P} \cdot \mathbf{e}_R = \mathbf{0}$ at $R = R_1$. Since $P_{\Theta R} = P_{ZR} = 0$ (as a consequence of the deformation being radially symmetric), this reduces to the nonlinear equation $P_{RR}|_{R=R_1} = 0$. If we are including a distinct capillary wall structure in our model, then we find $P_{RR}|_- = P_{RR}|_+$ and $u_0|_- = u_0|_+$ at $R = R_1$, and $P_{RR}|_{R=R_0} = 0$. The explicit forms of these boundary conditions may be

inferred from the constitutive equations defining the stress, i.e. (2.52) and (2.65).

Over the capillary wall V_c, the system is in mechanical equilibrium and is incompressible, so that $\nabla \cdot \mathbf{P}_0 = \mathbf{0}$ and $J_0 = 1$. We may use the identities in Appendix C.0.14 to simplify these expressions. If we write the Lagrange Multiplier (which is radially symmetric) as $p_0(R)$, these two equations simplify to

$$\frac{\partial^2 u_0}{\partial R^2} + \frac{1}{R}\frac{\partial u_0}{\partial r} - \frac{u_0}{R^2} - \frac{\partial p_0}{\partial R}\left(1 + \frac{u_0}{R}\right) G_c^{-1} = 0. \tag{3.7}$$

$$\frac{\partial u_0}{\partial R} = -\frac{u_0}{R + u_0}. \tag{3.8}$$

3.2 Linearised System

In this section we linearise the equations governing the fundamental (radially symmetric) state and obtain an analytic solution. We denote variables corresponding to the fundamental state with a subscript 0. This linearised solution is of assistance in our numerical solution of the models with an infinite geometry (C, F and G). The reason for this is that many of the variables asymptote to a constant as $R \to \infty$, so that the linearisation is increasingly accurate as $R \to \infty$. Broadly speaking, our method of solution is to initially integrate numerically when R is small, but once R is sufficiently great we stipulate that the numerical solution corresponds to the analytic solution.

We now outline the linearisation of the model outlined in Chapter 2. The variables $\{c_0, u_0, (\zeta_\alpha - 1)\}$ are considered small over this domain. The growth multipliers $\{G_\alpha\}$ are all equal to leading order. This means that to linear order the growth is isotropic and equal to $\zeta_\alpha = 1 + \gamma$, where $\gamma(t) = \int_0^t \frac{1}{3}\left(\frac{1}{k_c}c_0\right) dt$, at time t. For the linearisation to be accurate we require $\frac{t}{3k_c}c_0$ to be small. This gives the order of magnitude of the growth. The nutrient distribution c_0 in this case is governed by

$$\frac{\partial^2 c_0}{\partial R^2} + \frac{1}{R}\frac{\partial c_0}{\partial R} - \frac{\alpha}{k_n}c_0 = 0. \tag{3.9}$$

The linearised stress tensor is

$$\mathbf{P}_0 = 2G_t\epsilon_0 + \left(K_t - \frac{2G_t}{3}\right)\mathrm{tr}(\epsilon_0)\mathbf{I} - 3K_t\gamma\mathbf{I}, \tag{3.10}$$

where K_t and G_t are the bulk and shear moduli of the tumour and

$$\epsilon_0 = \frac{1}{2}\left(\nabla \mathbf{u}_0 + \nabla \mathbf{u}_0^T\right), \tag{3.11}$$

is the linearised strain tensor. It can be seen that the incremental stress tensor $\frac{\partial \mathbf{P}_0}{\partial \mathbf{F}}$ is constant in the linear regime. The equation of mechanical equilibrium has the same form, i.e. $\nabla \cdot \mathbf{P}_0 = \mathbf{0}$.

3.2.1 Analytic Solution of Linearised System

The domain over which we solve the linearised system is an annulus of infinite outer radius. We require the displacement, nutrient distribution and growth $(\zeta_\alpha - 1)$ to asymptote to 0 as $R \to \infty$. We do not worry about implementing the internal boundary condition because we only need to match the linearised solution to the nonlinear solution for large R. We begin by finding the radially symmetric fundamental solution for the displacement, growth and nutrient distribution.

The general solution of the linearised nutrient equations may be expressed as a linear combination of modified Bessel functions of the first and second kind. Since we require the nutrient concentration to asymptote to 0 as $R \to \infty$, the coefficient of the first modified Bessel function must be zero. Thus

$$c_0(R) = C_n(t) K_0\left(\sqrt{\frac{\alpha}{k_n}} R\right), \tag{3.12}$$

where $C_n(t)$ is undetermined. We note that the derivative of c_0 is $\frac{\partial c_0}{\partial R} = -C_n \sqrt{\frac{\alpha}{k_n}} K_1\left(\sqrt{\frac{\alpha}{k_n}} R\right)$. To solve the equation of mechanical equilibrium we assume that the growth γ is negligible, so that the displacement is governed by the equation

$$R^2 \frac{\partial^2 u_0}{\partial R^2} + R \frac{\partial u_0}{\partial R} - u_0 = 0. \tag{3.13}$$

We explain why we assume the growth is negligible further below in Section 3.3.1. The general solution of (3.13) which decays as $R \to \infty$ is

$$u_0 = C_u R^{-1} \tag{3.14}$$

where C_u is an undetermined constant.

3.3 Method of Numerical Solution

We now outline our method of numerical solution. The fundamental variable we solve for is the mass growth $\{r_\alpha\}$. To represent the mass growth we construct a mesh over the the spatial domain (in the reference coordinates). We interpolate these points with cubic splines to determine the mass-growth between nodes. We use not-a-knot boundary conditions, so that the order of accuracy of our interpolation is of the order of the fourth power of the mesh spacing.

The mass growth at each mesh point is determined by integrating (3.4) at that point. It can be seen that the integrand is determined by the nutrient distribution and displacement: we outline our method for determining these variables using the mass growth further below. The integration of the mass growth (3.4) is performed using a variable order Adams-Bashforth-Moulton multistep solver. A multistep solver is appropriate because the derivative of the mass-growth is particularly expensive to calculate (it will be seen that we must solve two boundary value problems at every step), but we expect the mass-growth distribution to be relatively smooth. The implementation of the Adams-Bashforth-Moulton solver that we use is the ODE113 solver of MATLAB.

We determine r_α at any particular time by solving for the displacement and nutrient distribution. It is assumed that we already have a solution for $\bar{r}_\alpha$ at this time using the method of integration outlined above. We can obtain ζ_α directly from $\bar{r}_\alpha$ using (3.3). We use this solution for ζ_α to determine u_0 (and p_0 if we are including a distinct capillary wall), which is governed by a boundary value problem with field equations (3.6)-(3.8). In turn we use this solution for u_0 to solve for the nutrient distribution, which is also governed by a boundary value problem with field equation (3.2).

For each of the boundary value problems in the displacement and nutrient distribution, one boundary condition is stipulated at R_1. In the model variants with a finite geometry we stipulate the other boundary condition at R_2. Refer to Table 3 for a summary of the

various boundary conditions. In model variant F we require

$$\mathbf{u} \to \mathbf{0} \text{ and } c \to 0 \text{ as } R \to \infty. \tag{3.15}$$

In model variant G we require $P_{RR} \to 0$ as $R \to \infty$. We employ the shooting method to solve these boundary value problems. In brief, the shooting method involves successively solving the system using finite difference integration until both boundary conditions are satisfied (we provide further details below). The reason we do not employ a variational method (such as the finite element method) is that the shooting method is typically more efficient than this when the system is of low dimension and the solution is highly unstable [128]. The boundary value problems governing the displacement and nutrient distribution are solved in C++ because this code is frequently used and needs to be as efficient as possible.

We now outline in more detail our method of solution for the infinite and finite geometries.

3.3.1 Solution over Infinite Geometry

In this section we outline our method of solution for the model variants with an infinite geometry (models C,F and G).

We begin with model F, where the nutrient distribution c_0 decays to zero as $R \to \infty$. We already have analytic solutions to the linearised equations governing u_0 and c_0 from Section 3.2. We use these analytic solutions to obtain a condition on the behaviour of these variables for large R. We require that u_0 and its derivative correspond to the linear analytic solution, once u_0 and u_0' are sufficiently small. Since there is one unknown constant in the linear analytic solution, this amounts to a one dimensional linear outer boundary condition once the unknown constant is eliminated. The same method can be applied to obtain the solution of c_0. We are not strictly required to match the linearised equations: we could have simply used the leading order of the boundary condition, i.e. $u_0 = 0$ and $c = 0$ for R large enough. However the numerical convergence is much faster when we match to linear order.

We recall the linearised solutions for c_0 and u_0 are

$$c_0(R) = C_n K_0\left(\sqrt{\frac{\alpha}{k_n}}R\right) \quad , \quad u_0 = C_u R^{-1}, \tag{3.16}$$

where $\{C_n, C_u\}$ are undetermined constants. On inspection of (3.16), we must distinguish three different length scales in our infinite medium model: $R_\zeta < R_u < R_{inc}$. The shortest length scale is the diffusion lengthscale R_ζ. This is the value of R for which the nutrient is sufficiently small that our linearisation is accurate to the required tolerance. Since the total mass growth r_g is essentially determined by the nutrient concentration, this is also the lengthscale over which the growth is nontrivial. For the nutrient linearisation to be accurate we require

$$\frac{c_0}{k_n} = O\left(\sqrt{\epsilon_c}\right), \tag{3.17}$$

where ϵ_c is the error tolerance for c_0. We arrived at (3.17) through Taylor expanding the rate of uptake term in the nutrient governing equation (3.2), i.e.

$$\frac{\alpha c_0}{k_n + c_0} = \alpha\frac{c_0}{k_n} - \alpha\left(\frac{c_0}{k_n}\right)^2 + \text{h.o.t.} \tag{3.18}$$

For our linearisation to be accurate, we require the quadratic term to be of the order of the nutrient tolerance ϵ_c. The reason R_ζ is very small is that the nutrient decays exponentially. The can be seen from the linearised solution, as the modified Bessel Function $K_m(x)$ is of asymptotic order

$$K_m(x) \simeq \sqrt{\frac{\pi}{2x}}\exp(-x), \tag{3.19}$$

for large x. In fact R_ζ is essentially determined by the initial nutrient distribution at time $t = 0$. This is because, as time progresses, the nutrient concentration at any particular *material* point monotonically decreases. This is a result of the fact that as the tumour swells and grows, any particular material point moves further and further from the capillary. This is evident in the results of the following chapter (for example in Figure 3.7). Thus we are justified in using a fixed mesh (in Lagrangian coordinates) over $[R_1, R_\zeta]$ to interpolate the growth. At $R = R_\zeta$ we apply the linear boundary condition

$$\frac{\partial c_0}{\partial R}K_0\left(\sqrt{\frac{\alpha}{k_n}}R\right) + c_0\sqrt{\frac{\alpha}{k_n}}K_1\left(\sqrt{\frac{\alpha}{k_n}}R\right) = 0, \tag{3.20}$$

which is obtained by eliminating C_n from (3.16).

The length R_u is the value of R for which the displacement is well inside the linear regime. Technically we only require the deformation gradient $\mathbf{F}_0$ to be in the linear regime since the nutrient equation (3.2) and incremental equations (which are defined in subsequent chapters) are functions of $\mathbf{F}_0$, i.e.

$$\left|\frac{u_0}{R}\right|, \left|\frac{\partial u_0}{\partial R}\right| = O(\sqrt{\epsilon_u}), \tag{3.21}$$

where ϵ_u is the error tolerance for the displacement. We generally do not need to worry about nonlinear contributions from the growth, because the growth decays exponentially and therefore at R_u the magnitude of the growth is typically much less than the deformation gradient. This is why we neglected the contribution of the linearised growth γ in our determination of the linearised expression for u_0 in (3.14). The boundary condition is obtained as follows. The displacement and traction on either side of R_u are equal, i.e.

$$u_0|_- = u_0|_+ \ , \ P_{RR}|_- = P_{RR}|_+. \tag{3.22}$$

The linearised stress is

$$P^+_{RR} = \left(K_t + \frac{4G_t}{3}\right)\frac{\partial u_0}{\partial R} + \left(K_t - \frac{2G_t}{3}\right)\frac{u_0}{R}. \tag{3.23}$$

We may thus eliminate the unknown constant C_u from (3.14) and (3.22) to obtain

$$P_{RR} + 2G_t\frac{u_0}{R_u} = 0 \text{ at } R = R_u. \tag{3.24}$$

The length scale R_{inc} is the value of R for which the linear approximation in the incremental displacement equations is valid. In Section 7.1.2 we will see this is approximately

$$R_{inc} = O\left(\sqrt{|C_u|\epsilon^{-1}_{inc}}\right), \tag{3.25}$$

where ϵ_{inc} is the desired error tolerance for the incremental displacement equations.

We now turn to discussing the large R behaviour of the 'growing' infinite medium model (model G). In this model there is zero nutrient flux at some fixed outer radius $r - r_1 = r_c$ (where $r = R + u_0$ is the spatial radius coordinate), i.e. $\frac{\partial c}{\partial r} = 0$. We let $R_c = r_c - u_0(R_c)$

be the material radius corresponding to this. For $R > R_c$, the nutrient concentration is set to be equal to its value at R_c. However we cannot assume the growth ζ_α is constant for $R > R_c$ because if we are employing growth inhibition or growth anisotropy the stress will probably be anisotropic for $R > R_c$. We therefore construct the mesh for the mass growth $\{r_\alpha\}$ over the domain $R \in [R_1, R_\zeta]$, where R_ζ is sufficiently great that the relative differences in the directional mass growth are less than our error tolerance ϵ_ζ, i.e.

$$\frac{|r_\beta - r_\alpha|}{r_\alpha} < \epsilon_\zeta. \tag{3.26}$$

We note that $\sum r_\alpha = r_g$ is constant for all $r > r_c$ when there is no growth inhibition. In solving for the displacement u_0, we expect the radial and azimuthal stress to asymptote to zero as $R \to \infty$, i.e.

$$P_{RR} \to 0 \text{ and} \tag{3.27}$$

$$P_{\Theta\Theta} \to 0. \tag{3.28}$$

The growth dilation variables $\{\zeta_R, \zeta_\Theta, \zeta_Z\}$ all asymptote to the same constant as $R \to \infty$. It follows from (3.27) and (3.28) that the radial and azimuthal strains asymptote to the same constant D (this is a different constant to the constant governing the radiotherapy cell death), i.e.

$$\frac{u_0}{R} \to D \text{ and } \frac{\partial u_0}{\partial R} \to D, \tag{3.29}$$

so that $u_0 = (D-1)R + o(R)$. Thus for large R we use the following condition to solve for u_0 using the shooting method,

$$\frac{u_0}{R} - u_0' = 0. \tag{3.30}$$

Note that it can be shown that (3.30) implies (3.27) and (3.28) in the large R asymptotic limit.

3.3.2 Solution Over Finite Annulus

The outer boundary condition in the finite annulus models is straightforward. The finite annulus has outer radius R_2. The nutrient boundary condition is $\frac{\partial c_0}{\partial R} = 0$ at $R = R_2$. The mechanical boundary condition at R_2 depends on the model variant: the conditions for

variants A,B,C,D and E, are respectively

$$u_0 = 0, \quad \frac{\partial u_0}{\partial R} = 0, \quad P_{RR} + 2G_t \frac{u_0}{R} = 0, \quad \frac{\partial P_{RR}}{\partial R} = 0 \text{ and } \frac{\partial u_0}{\partial R} = 0. \tag{3.31}$$

These equations provide the boundary condition required for us to implement the shooting method.

3.3.3 Numerical Implementation of Shooting Method

We use the shooting method to solve for the nutrient and displacement. These are both governed by second order boundary value problems. For economy of discussion we consider R_2 to be the outer radius, even though in the case of the infinite medium the outer radius could be one of $\{R_\zeta, R_u\}$ depending on the model variant. We outline our method for u_0; the nutrient equation is solved similarly.

We begin by outlining our method of solution of the composite model with a distinct capillary wall structure. We integrate the differential equation from R_0 to R_2 using a Runge-Kutta Fehlberg method, using the code provided by the GNU Scientific Library. The ordinary differential equation does not exhibit any sign of stiffness so an ordinary explicit solver is sufficient. The fundamental unknown we are solving for is the displacement u_0 at R_0. Our method of solution is to integrate the governing ordinary differential equation from R_0 to R_2, successively refining our estimate of u_0 until the boundary condition at R_2 is satisfied. The two variables we integrate over V_c (i.e. from R_0 to R_1) are u_0 and p_0. Their evolution is governed by (3.7) and (3.8). The starting value of p_0 at R_0 is obtained from the boundary condition $P_{RR} = 0$, i.e. $p_0 = G_c \left(1 + \frac{\partial u_0}{\partial R}\right)^2$, where $\frac{\partial u_0}{\partial R}$ is obtained using the incompressibility condition (3.8). Once we have integrated from R_0 to R_1, we must continue the integration from R_1 to R_2. The two variables we integrate over V_m are u_0 and u_0'. The governing equation is given by (3.6). We obtain u_0 at R_1^+ using the continuity requirement $u_0|_- = u_0|_+$, and we obtain u_0' at R_1^+ by solving the nonlinear equation $P_{RR}|_- = P_{RR}|_+$. We use the Brent algorithm, which is essentially a modification of the bisection method [115], to do this. The boundary condition at R_2 is given by (3.31). If we are not including a distinct capillary wall structure, then the unknown we solve for is $u_0(R_1)$. The rest of the

Dim. Parameter	Value	Description
R_2	$10^{-4}m$	Outer Radius of Annulus (for finite geometries).
R_1	1.5×10^{-5}	Inner Radius of Annulus.
q	-7.9	Tumour Elastic Parameter.
f	0.2	Tumour Elastic Parameter.
λ_n	$0.01mMs^{-1}$	Rate of Uptake of Oxygen.
k_n	$4.6 \times 10^{-3}mM$	Michaelis Constant for Oxygen Uptake.
k_c	$8.3 \times 10^{-3}mM$	Michaelis Constant for Cell Growth.
D	$1.5 \times 10^{-9}m^2s^{-1}$	Diffusion Coefficient of Oxygen in Tumour.
c_0	$0.1mM$	Oxygen Concentration at R_1.
Nond. Parameter	Value	Description
α	0.015	$\lambda_n R_1^2/D$
k_n^*	0.046	k_n/n_0
k_c^*	0.083	k_c/n_0
R_2^*	6.6667	R_2/R_1.

Table 3.2: The default parameter values we use in our results, unless otherwise indicated. In our nondimensionalisation the lengthscale is R_1, the nutrient scale is the concentration at R_1 and the timescale is the average time it takes for a tumour cell to proliferate. We do not provide a value for the characteristic proliferation rate because it does not affect our results. The tumoural elastic modulii (f and q) are for glioblastoma. Refer to Appendix B for an explanation of these parameters and the papers from which they are sourced.

method is exactly the same.

3.4 Results

We now outline the radially symmetric results. Our aim is to assess the various model variants outlined in the previous chapter, and eliminate the physically unrealistic ones. The seven different boundary conditions and geometries we consider are outlined in Table 3. We must also consider two different models of growth anisotropy and two different models of growth inhibition, which are outlined in Section 2.7. We neglect the capillary wall as a distinct mechanical structure because our aim is to investigate the growth models and outer boundary condition. The default parameter values are outlined in Table 3.4.

3.4.1 Criteria Against Which We Assess our Results

Since we are modelling an *in vivo* phenomenon, there is a paucity of data against which we may evaluate our models. However the following criteria are of use in guiding our evaluation. It is important to note that we can not prove any of these criteria, and indeed

occasionally we expect many of them may not hold. However we expect them to hold in most circumstances.

We expect the stress to not grow too quickly, so that it is below the yield level at $t = 1$. (3.32)

We expect the displacement to be negative at R_1. The reason for this is that we expect the growing tumour to exert a compressive, not expansive, force on the capillary wall. (3.33)

The displacement u_0 and the material derivative $\dfrac{Du_0}{dt}$ should be positive for large R, since we expect the distance between existing capillaries to increase as the tumour grows. (3.34)

For large R, T_{RR} should be negative. This is because the growing tumour must displace material as it radially expands, which should result in a compressive radial stress. (3.35)

For our restriction to an annulus to be accurate, we require that the nonlinear behaviour at R_2 is minimal. (3.36)

Model variants which satisfy all of the above criteria must give similar predictions. (3.37)

We now provide further justification for perhaps the most contentious of these criteria: (3.32) and (3.33). We are not aware of any experiments which prove these assumptions, and it is certainly possible that at least one of them is wrong.

We begin by providing further justification for (3.32). Because the stresses tend to be greatest at R_1, we only investigate yielding here. At $R = R_1$, $P_{RR} = 0$, and therefore the shear stress yield criterion is

$$\frac{1}{2}\left|P_{\Theta\Theta}\right| = \tau, \tag{3.38}$$

where τ is the yield stress. In Appendix B, we estimate that the yield stress is approximately $5-25$ times the Young's Modulus E_t for brain tissue, and approximately 2 times the Young's Modulus for skin. When $0.5\left|P_{\Theta\Theta}\right|$ exceeds the yield stress, we expect the tissue to start

fracturing, if buckling does not occur first. Our general expectation is that the stress does not reach the yield level before one cycle of cell-proliferation has passed: it seems implausible that the growing tumour would fracture through its own growth so readily.

We now discuss (3.33) in further detail. Our best motivation for this assumption is that, when we include the capillary wall, we expect the normal traction T_{RR} at the wall-tumour interface to be compressive. Most authors appear to share our assumption [129, 12, 26]. However it is important to note, according to our model, (3.33) is not necessary for buckling to occur. We will see in our results in Chapter 9 that the tumour dominates the energy landscape, and the buckling is driven more by the tangential (to the capillary wall) forces $T_{\Theta\Theta}$ and T_{ZZ} in the tumour than the stress in the capillary wall. Thus the system can still buckle if u_0 is positive at R_1. However this does not hold in the thin-ring model of Stoll [129]. In this model, since the tumour is an 'elastic fluid', the stability of the system derives from the strength of the capillary wall rather than the tumour, so that we expect that buckling would *never* occur if the normal traction is expansive (just as one does not expect an inflated balloon to buckle). For further discussion of this point refer to Section 9.3.

We discuss (3.36) and (3.37) in more detail in Section 3.4.4.

3.4.2 Isotropic Growth Results

In this section we analyse the various outer boundary conditions with respect to the simplest model of growth: isotropic, with $\zeta_R = \zeta_\Theta = \zeta_Z$. We begin with model A, which is plotted in Figure 3.1(II). The null-displacement model represents situations where the growing tumour is strongly constrained, so that the mean intercapillary distance does not increase (note that we do not expect this to hold in general circumstances as it violates criterion number (3.34)). Its strength is its relative simplicity. However it violates two of the criteria of Section 3.4.1: the stress grows too rapidly (violating (3.32) and the stress and displacement are in the nonlinear regime at $R = R_2$ (violating (3.36)).

One of the advantages of models F (infinite medium, plotted in Figure 3.2) and B (null-pressure, plotted in Figure 3.1(I)) over A (null-displacement) is that they allow u_0 to be positive at R_2 (thus satisfying criterion number (3.34)). However a weakness of these models

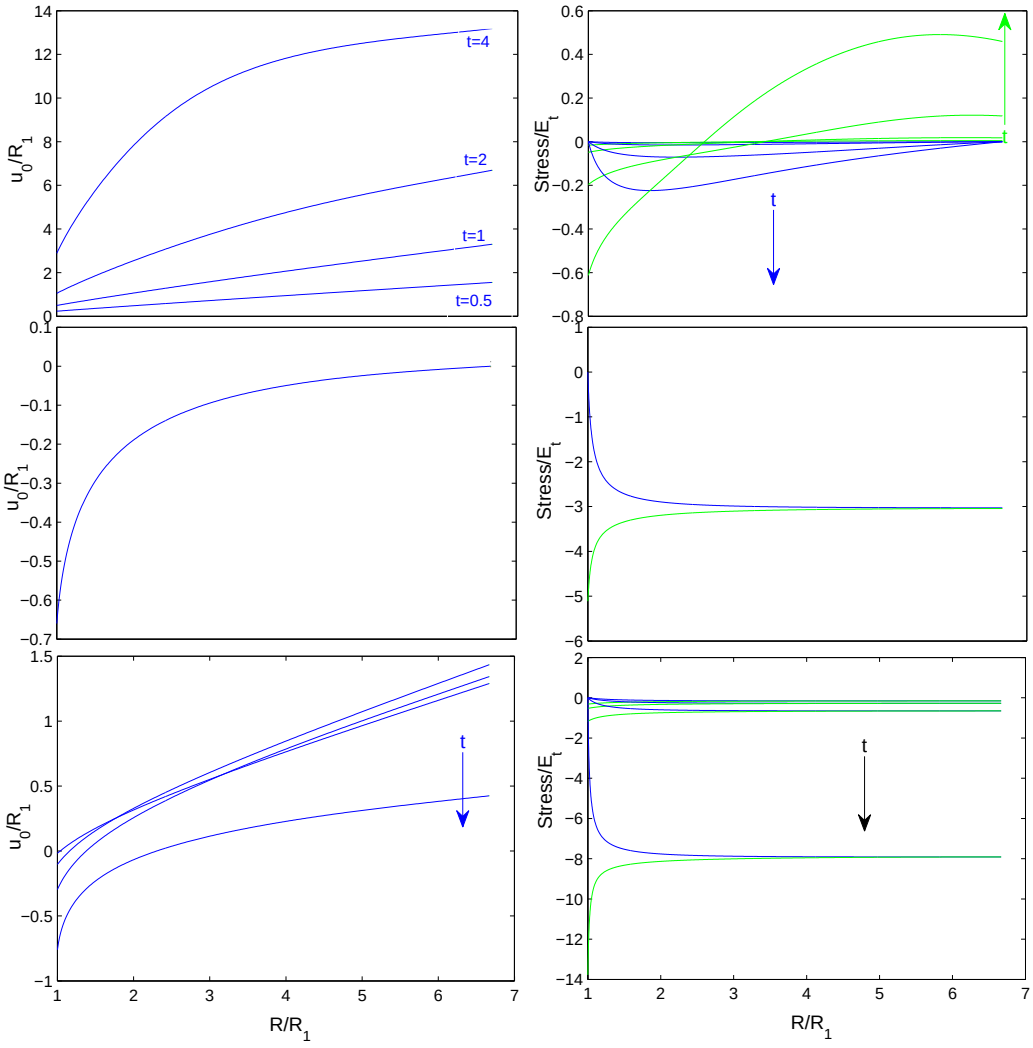

Figure 3.1: The displacement (left) and stress distribution (right) in the growing tumour, relative to the reference configuration. In the top figures we implement the null-stress outer boundary condition (model B), and the times are $t = \{0.5, 1, 2, 4\}$. In the middle figures we implement the null-displacement outer boundary condition (model A), and the time is $t = 0.5$. In the bottom figures we implement the boundary condition $\frac{\partial P_{RR}}{\partial R} = 0$ (model D), and the times are $t = \{0.5, 0.6, 0.7, 0.8\}$. In the stress figures, the blue line represents P_{RR} and the green line $P_{\Theta\Theta}$.

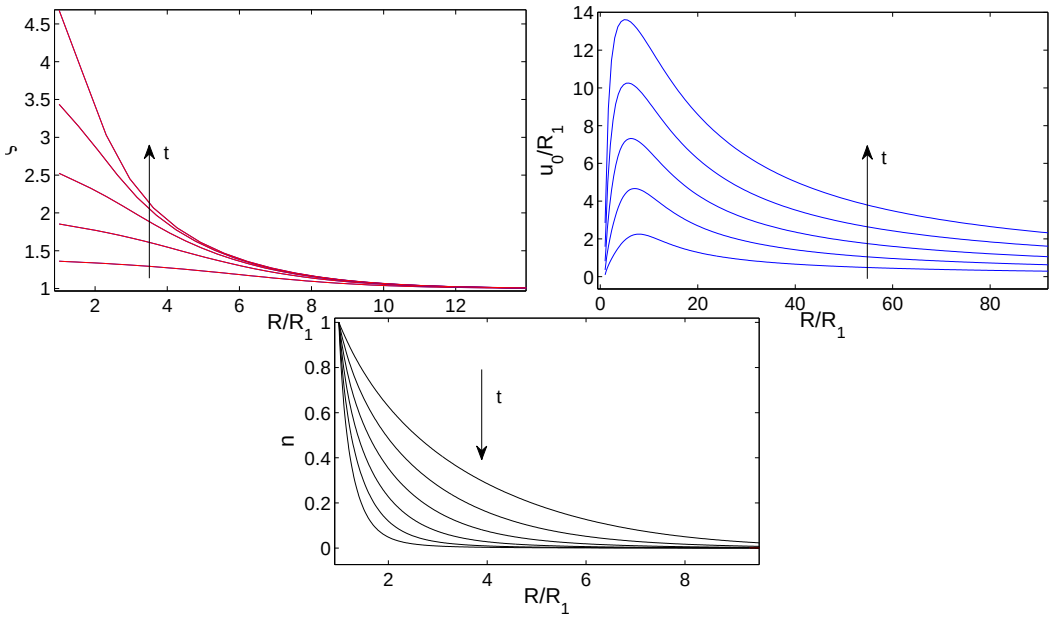

Figure 3.2: The growth (left), radial displacement (right) and nutrient distribution (bottom) in model F, relative to the reference configuration. The plots represent the solution at $\{1, 2, 3, 4, 5\}$ times the proliferation timescale. The displacement and growth increase as time progresses. The nutrient decreases because points in the tumour become further and further from the capillary as the tumour grows. There is no growth-inhibition. The behaviour as $R \to \infty$ is as predicted by our linearised solution: u_0 is $O(R^{-1})$ and ζ and n_0 decline exponentially.

is that the displacement at the inner boundary ($R = R_1$) is positive (violating criterion number (3.33)). The reason the displacement is positive is that the growing tumour's need to relieve the enormous hoop stress at R_1 encourages the entire annulus to expand, because increasing the diameter of a hoop relieves the compression. Because there is no fixed outer boundary condition, there is not sufficient 'resistance' to this effect, and so the entire annulus expands. This result is akin to the expansion of a tightly-screwed jar lid by running hot water over it.

One way we attempt to remedy this problem is the incorporation of growth-inhibition into our model. The growth remains isotropic, but is now a function of the cellular density per volume or the compressive stress (according to the model variant being used). Thus the growth at R_1 is lessened due to the large compression. We plot the fundamental solutions with growth inhibition in Figure 3.3, using model variant F. In the top two figures we implement 'cell-density' growth inhibition, and in the bottom two figures we implement 'compressive-stress' growth inhibition. Observe that the displacement and the stress is less with growth inhibition, as expected. However the model still suffers from the fundamental problem that the displacement at R_1 is positive. Generally, the qualitative differences arising from the inclusion of either type of growth inhibition are not massive. Since the growth inhibition is not well parameterised, it unnecessarily complicates our model and we do not incorporate it again.

Models D and E have some strengths, but also fatal weaknesses. In Figure 3.1(III) we plot results for model D, with no growth inhibition. This boundary condition is superior to model F insofar as it satisfies criterion (3.33). However it violates criterion (3.32), and, more importantly, it violates criterion (3.34): the displacement at R_2 at $t^* = 0.8$ is *less* than the displacement at R_2 at $t^* = 0.7$, which means the overall volume of tumour tissue is *less* at $t = 0.8$ than at $t = 0.7$. Model E suffers from the same defect (although the results are not plotted). We consider these weaknesses to be fatal, and do not consider these model variants again.

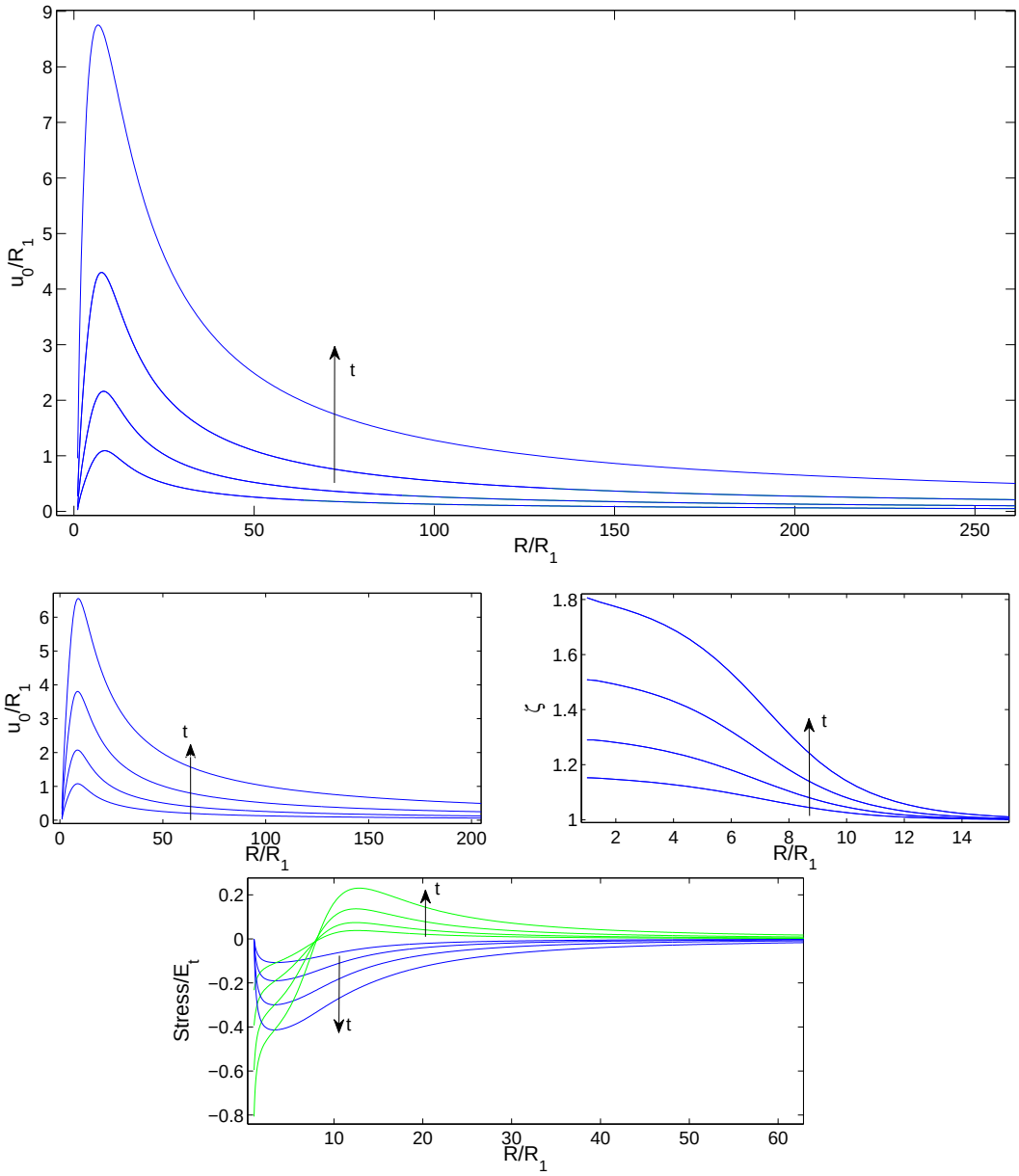

Figure 3.3: The stress distribution (left) and displacement (right) in the growing tumour, relative to the reference configuration, for model F. The plots are at times $t = \{0.5, 1, 2, 4\}$. In the top figure, we implement the 'cell-density' model of growth inhibition, with parameter $h^* = -0.3$ (not to be confused with the capillary wall thickness), and in the bottom three figures we implement the 'compressive-stress' form of growth inhibition. In the stress figure, the blue line represents P_{RR} and the green line $P_{\Theta\Theta}$. In each of the plots, the stress, displacement and growth all increase in magnitude over time.

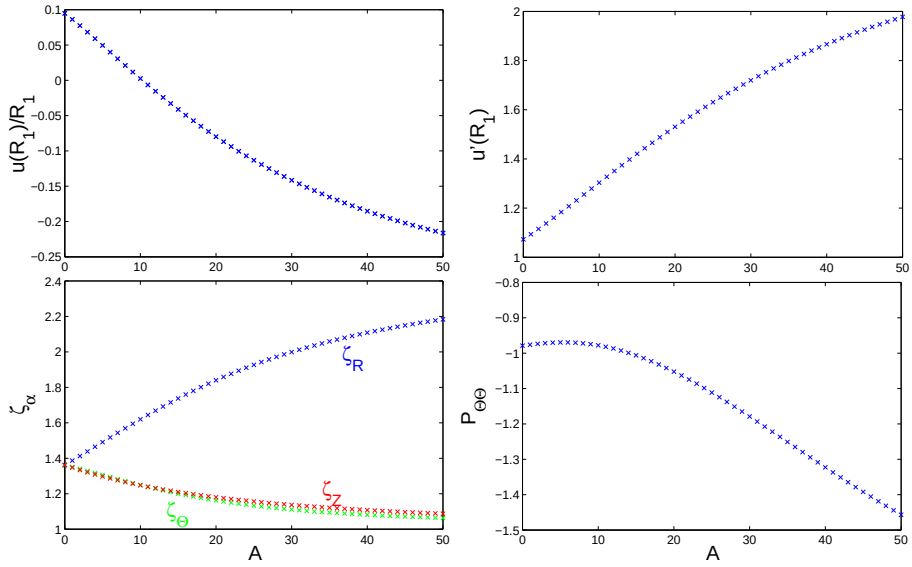

Figure 3.4: In the above simulations we varied the growth anisotropy coefficient A from 0 to 50 (with increment 1) and plotted data at $t = 1$. We use model F. At the top is the displacement and the displacement derivative at R_1 (the radius of the cavity). At the bottom is the growth dilation and azimuthal stress at R_1. Observe that as A gets larger, the differences in growth become more pronounced and the displacement at R_1 is more negative.

3.4.3 Anisotropic Growth

We saw in the previous section that with isotropic growth the displacement at R_1 is usually positive in model F, which violates criterion number (3.33). We therefore investigate whether the incorporation of anisotropic growth multipliers into our model may help correct this problem. As we explained in Section 2.5.3, there is excellent experimental evidence that growth can be anisotropic in response to anisotropic stress. However it is very difficult to model and parameterise the growth anisotropy as there is little experimental data. We therefore investigate two different models of growth anisotropy and a range of parameter values to find the model and parameter value which seems the most realistic.

In Figure 3.4 we employ the growth multipliers

$$G_{jj} = \exp\left(AK_t^{-1}\mathbf{T}_{jj}\right) G_\Sigma^{-1} \text{ where} \tag{3.39}$$

$$G_\Sigma = \exp\left(AK_t^{-1}\mathbf{T}_{RR}\right) + \exp\left(AK_t^{-1}\mathbf{T}_{\Theta\Theta}\right) + \exp\left(AK_t^{-1}\mathbf{T}_{ZZ}\right), \tag{3.40}$$

where we recall that K_t is the bulk modulus and A is a constant which cannot be easily

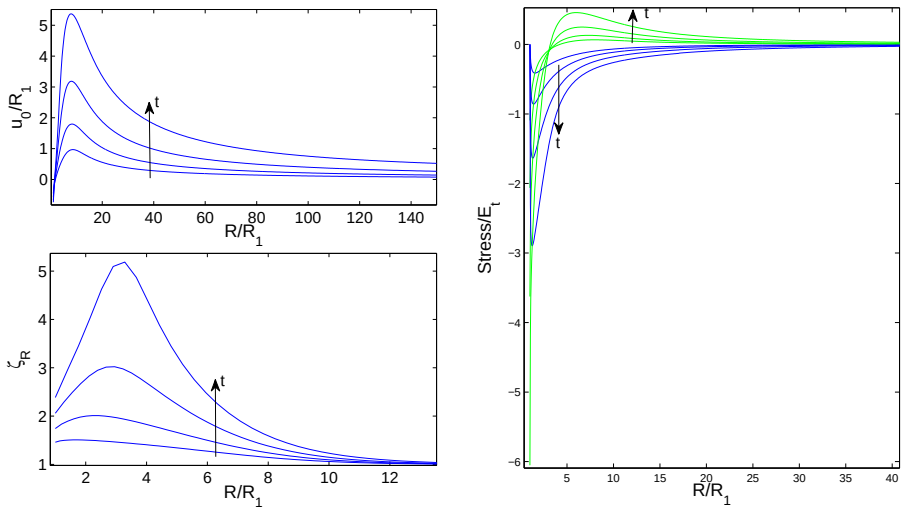

Figure 3.5: In this simulation the growth is entirely radial, so that $\zeta_\Theta = \zeta_z = 1$ throughout the tumour. We have employed the bulk-modulus growth inhibition as well. We use model F. The radial stress P_{RR} is plotted in blue and the hoop stress $P_{\Theta\Theta}$ is plotted in green. The times are $t = \{1, 2, 3, 4\}$.

parameterised from the literature and must be estimated. We varied A from 0 to 50. When $A = 0$ the growth is isotropic. As A increases, the multipliers are more sensitive to differences in the stress. Growth is preferentially directed towards tensile stress and away from compressive stress. It can be seen that the displacement at R_1 is negative for A large enough. In other words, incorporating anisotropic growth remedies the principal weakness of model F, as long as A is sufficiently large. We now briefly survey the other model variants incorporating anisotropic growth.

We investigate a 'radial' growth function (with $G_{RR} = 1$ and $G_{\Theta\Theta} = G_{ZZ} = 0$) for model F in Figure 3.5. The displacement at R_1 is sufficiently negative. However it seems physically unrealistic that the growth would be entirely radial when the hoop stress is less compressive than the radial stress, as is the case towards the outside of the annulus.

In Figure 3.6 the growth multipliers are proportional to the principal stress minus a homeostatic stress T_0, i.e.

$$G_\alpha = \frac{T_\alpha - T_0}{T_\beta - 3T_0}, \tag{3.41}$$

where we sum over β. We used model F. It can be observed that we encounter the same problem: the displacement at R_1 is always positive (violating criterion number (3.33). It might seem that if we were to extrapolate the results, the displacement at R_1 might become

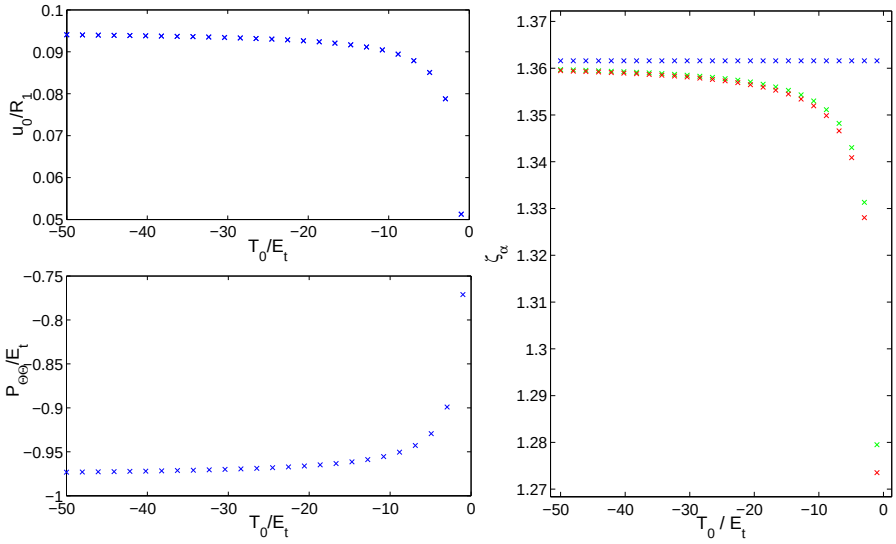

Figure 3.6: In this simulation the rate of growth in a direction $\mathbf{e}_\alpha$ is proportional to $T_{\alpha\alpha} - T_0$, where $T_{\alpha\alpha}$ is the principal component of the Cauchy Stress in this direction and T_0 is a 'homeostatic' stress. We use model F. The stress and growth are at R_1, with ζ_R in blue, ζ_Θ in green and ζ_Z in red. We plot the first Piola-Kirchhoff hoop stress, which is of the same order of magnitude as the Cauchy Stress.

negative for $|T_0|$ small enough. However this would be physically unrealistic because this model is only well defined for $|T_{jj}| > |T_0|$, so if $|T_0|$ is too small the stress would rapidly fall below T_0.

We conclude that the most preferable model for the growth multipliers in model F is the first type (3.39). As explained in Section 2.5.3, the experimental data is insufficient for us to find a value for A. We therefore estimate $A = 10$. We plot the solution for $A = 10$ in Figure 3.7. It can also be observed from a comparison with Figure 3.1 that the stress grows much more slowly than model A (which we consider to be the strongest of the models with a finite geometry).[1] In this respect model F seems more realistic than model A.

We now briefly investigate the realism of the remaining model variants: B and G (discussion of model variant C is deferred until later). We investigate model B (with a null-stress outer boundary condition) in Figure 3.8, employing growth multipliers of the form (3.39). We varied the growth multiplier constant A from 0 to 2000 (this upper limit seems much greater than what would be physically realistic, despite our lack of hard experimental data

[1] Although the growth is isotropic in Figure 3.1, the stress still grows almost as rapidly when the growth is anisotropic. The fundamental reason for the high level of stress in model A is the geometric constraint on the growing tumour.

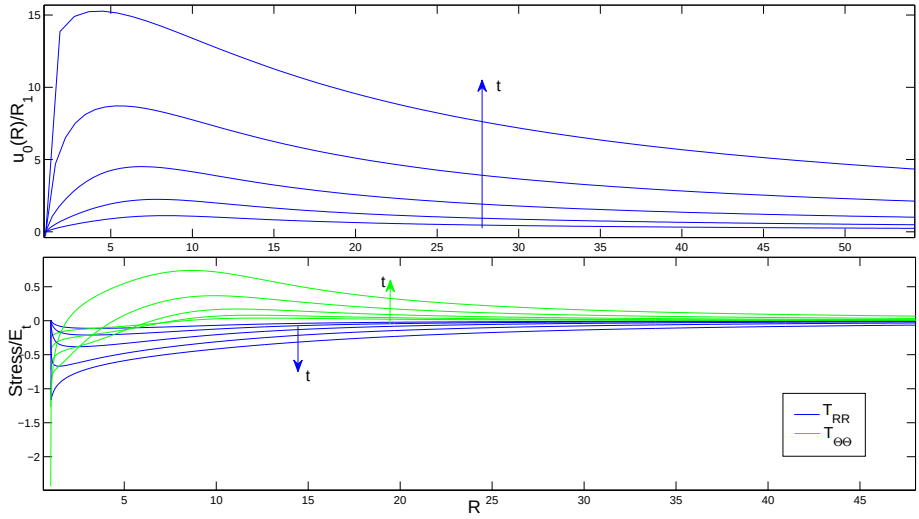

Figure 3.7: The solution at times $t = \{0.5, 1, 2, 4, 8\}$ over an infinite tumour. We employed the growth multipliers given in 3.39. The growth multiplier constant was $A = 10$. The plotted stress is the Cauchy Stress. These results should be compared to the results for the same model, but with isotropic growth (see 3.2).

for A). Observe that the inner displacement $u(R_1)$ is always positive, which means that even if the growth is highly anisotropic, criterion number (3.33) is not satisfied. This is a considerable weakness. Another weakness of model B is that it violates criterion number (3.35).

We implement model G in Figures 3.9 and 3.11. In Figure 3.9 the growth multiplier constant A is varied from 0 to 100. It can be seen that varying the growth multiplier has little qualitative effect on the solution. This is fundamentally different from the other model with infinite geometry (model F), where the displacement at the inner boundary switched from positive to negative as the growth multiplier increased. By contrast, in model G, for all values of A the displacement at R_1 is large and positive - violating criterion number (3.33). It is not surprising that the expansion is so great, because over the annulus $[R_2, \infty)$ the growth asymptotes to a nonzero constant, and hence there is much less resistance to expansion than in model F.

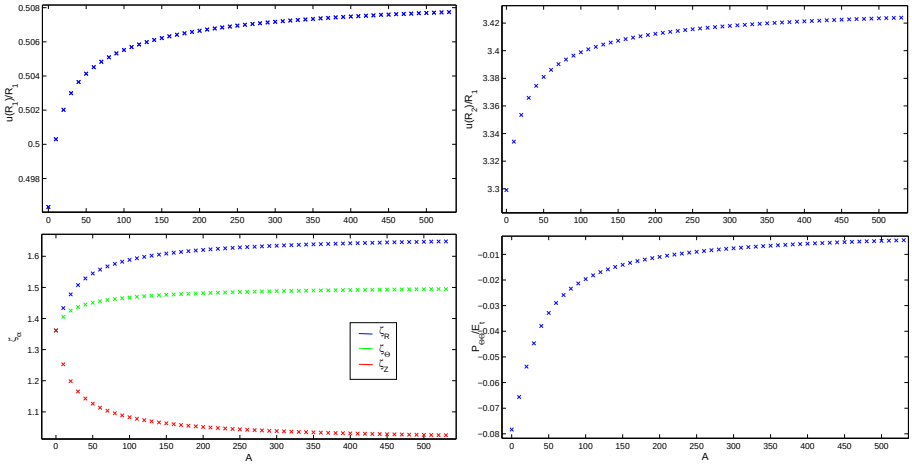

Figure 3.8: In this solution we implement the no stress outer boundary condition. We employed the growth multipliers given in (3.39), varying the constant A from 0 to 550. The stress $P_{\Theta\Theta}$ and growth multipliers $\{\zeta_\alpha\}$ are the values at $R = R_1$: ζ_R is in blue, ζ_Θ is in green and ζ_Z is in red.

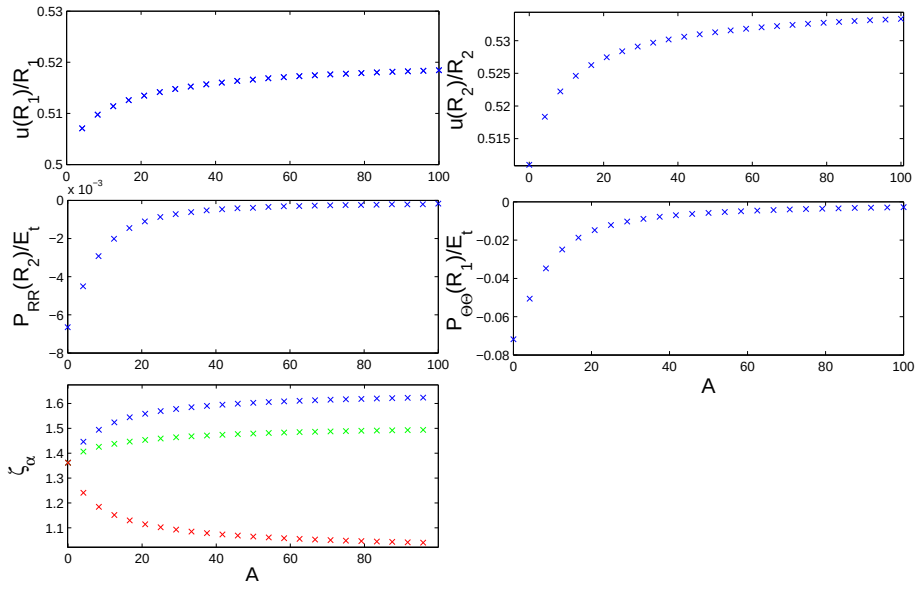

Figure 3.9: In this solution we implement model G (a 'growing' infinite medium), with the nutrient derivative equal to zero at $R = R_2$ and $n(R) = n(R_2)$ for $R > R_2$. We employed the growth multipliers given in (3.39), varying the growth multiplier constant A from 0 to 100.

3.4.4 The Compatibility of the Model Predictions with the Rest of the Tumour

One of the fundamental aims of this thesis is to explain buckling in terms of the microenvironment of a single capillary only. This aim is implicit to our model geometry insofar as there is only a single capillary. In this section we discuss how effective each of the model variants is in achieving this goal. It is important to do this because if, for example, a model variant predicts that neighbouring capillaries (and the associated nutrient distribution, growth and deformation) would have a nontrivial effect on the behaviour of the particular capillary in our model, then we have moved beyond the scope of accuracy of our model. In this situation we need to include more capillaries in the model to obtain accurate results. The conclusion we reach is that, although individual model variants have particular strengths, model F is the best.

We discuss model variant F first and shape our discussion of the other model variants around this. Let R_i be the distance of a particular capillary to its nearest neighbour. We now determine approximate criteria governing how large R_i must be for the results from model F to be compatible with the broader tumour environment. We proceed from the discussion of the asymptotic behaviour of model F for large R in Section 3.2. We noted that the nutrient distribution n and the growth $(\zeta_\alpha - 1)$ decay exponentially, but the asymptotic behaviour of the displacement is

$$u_0 \simeq C_u R^{-1}. \tag{3.42}$$

Since the displacement decays much more slowly than the growth and nutrient, the former is the key determinant of the compatibility of the fundamental solution with the wider tumour environment. The inverse-square decline in the strains $(\frac{\partial u_0}{\partial R}, \frac{u_0}{R})$ and the exponential decline in the growth $(\zeta_\alpha - 1)$ may be observed in Figures 3.5 and 3.7. We expect that if R_i is sufficiently large that $u_0(R_i)$ is in the regime of convergence of (3.42), then we may be confident that the results of model F are compatible with the rest of the tumour body. More precisely, we require that

$$\left(|u_0(R_i) - C_u R_i^{-1}|\right) / \left(C_u R_i^{-1}\right) \ll 1. \tag{3.43}$$

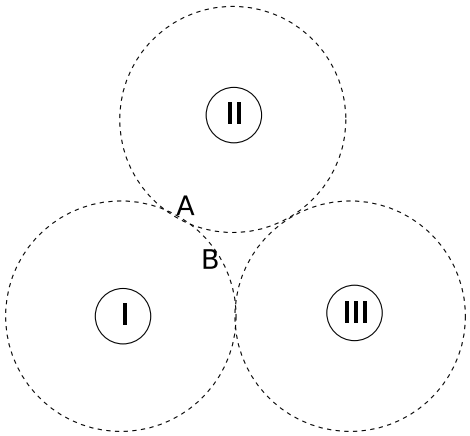

Figure 3.10: The distortion resulting from the restriction of the model geometry to an annulus surrounding the capillary.

We now discuss the accuracy of the models with a finite geometry (A,B,D and E). These converge to model F as $R_2 \to \infty$ (although it needs to be noted that we have already rejected models D and E as fundamentally flawed when R_2 is of the order of the intercapillary distance). If R_2 is sufficiently great that the displacement and nutrient distribution are in the linear regime at R_2, then we expect the behaviour of the finite geometry model to be essentially the same as model F. However if this is not the case then we expect the displacement (and possibly also the nutrient and growth) to be in the nonlinear regime at R_2 (which is defined to be R_i). It seems likely that the displacement fields resulting from the growth of neighbouring capillaries would also interact nonlinearly, which could potentially quite severely undermine the accuracy of the model. For example consider the simple situation of three neighbouring capillaries in Figure 3.10. Let us suppose we model the annulus around each capillary (indicated by the dashed lines) using model A. The assumption of null-displacement at the outer boundary of annulus I might seem justified at point A, but at point B we would expect the radial displacement to be positive (relative to capillary I). If in model A the stress and strain at the outer boundary is large (i.e. outside the linear regime), then we expect the distortion resulting from our restriction to an annulus surrounding the capillary to be substantial. It seems possible that buckling would occur much more readily - an effect which often accompanies symmetry breaking inhomogeneities in buckling analyses [10].

Most of the behaviour of the other models with an infinite geometry (C and G) is

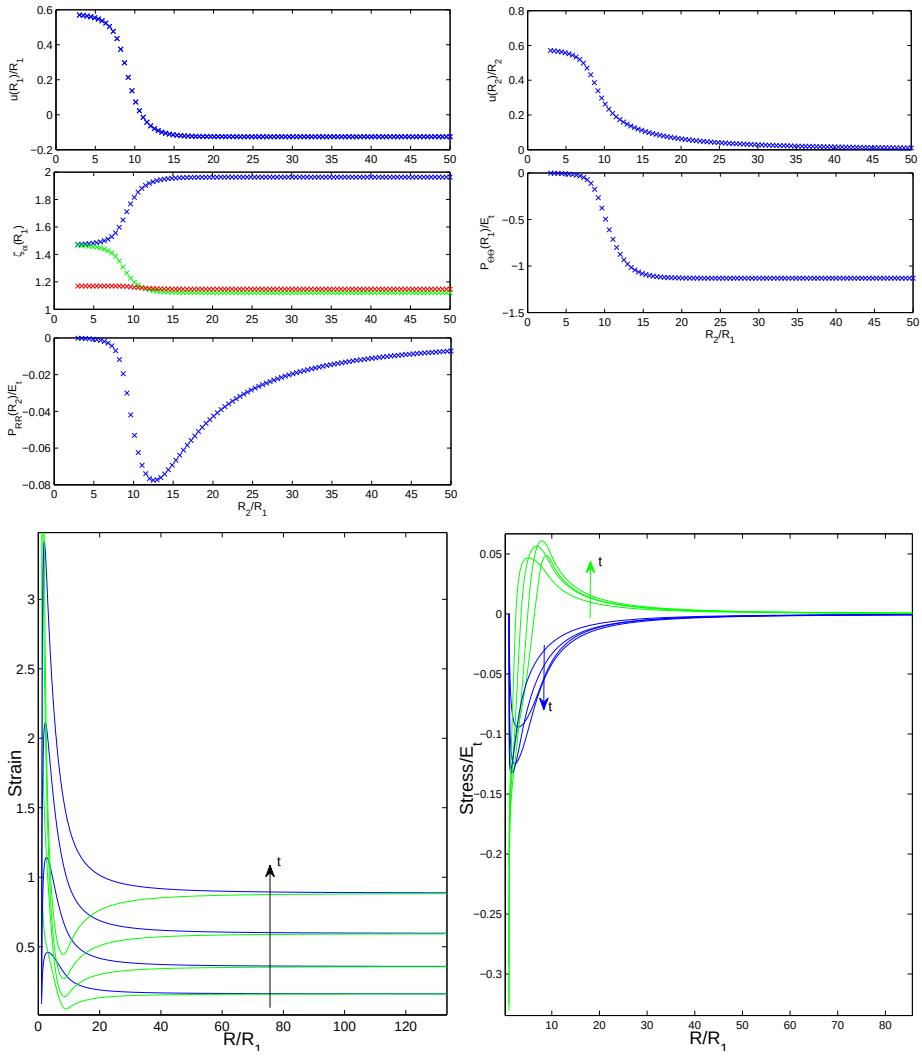

Figure 3.11: In this solution we implement the 'growing' infinite medium boundary condition (model G), with the same parameters as in Figure 3.9, except we fix the growth multiplier constant A to be 10. In the top five figures we vary R_2/R_1 from 3 to 50. As $R_2 \to \infty$, the model gets closer and closer to model F (compare this to Figures 3.4 and 3.7). In the bottom two figures we plot the strain and stress profiles for $R_2/R_1 = 10$, at times $t = \{0.5, 1, 2, 4\}$ the characteristic proliferation timescale. The azimuthal strain $\frac{u_0}{R}$ is in blue and the radial strain $\frac{\partial u_0}{\partial R}$ is in green. The radial stress P_{RR} is in blue and the azimuthal stress $P_{\Theta\Theta}$ is in green. Observe that the stress decays to zero as $R \to \infty$. The strains asymptote to the same nonzero constant.

captured by model F. Models C and G are 'hybrid' models insofar as they have an infinite geometry, but a 'finite lengthscale' R_2. They both converge to model F as $R_2 \to \infty$. The response of model G to the variance of R_2 is plotted in Figure 3.11. Observe that for $R_2/R_1 \geq 15$, the model has almost completely converged to model F: the variables at R_1 change very little as R_2 increases and the strain $\frac{u_0}{R}$ and stress P_{RR} at $R = R_2$ decay with order $O(R_2^{-2})$. Model G is very sensitive to values of R_2 less than 15. This is because as R_2 increases, the nutrient concentration at R_2 decreases, and so the growth in the region $R > R_2$ is less and the outer region is less expansive. This makes it more difficult for the growth at R_1 to expand the tumour radially outward because it must displace more tumour material to do so. However for $R_2/R_1 < 10$, the displacement at R_1 is positive, which we argued in the previous section is physically unrealistic. Thus the range of values of R_2 for which model G is physically realistic almost corresponds to the range of values of R_2 where the behaviour of model G is very similar to the behaviour of model F. A similar conclusion holds for model C. In other words, most of the useful results from models C and G can be obtained using model F (although we are still interested in performing a buckling analysis for model G and $R_2 < 15$).

3.5 Summary and Conclusions

In this chapter we outlined the radially symmetric solution of our model and the method of numerical solution. We explored a wide variety of model variants, so that we might investigate their physical realism. We concluded that model F, with anisotropic growth, is the most physically realistic. It has the following strengths:

- It is the most consistent in keeping with our aim of explaining buckling through reference to the microenvironment of a single capillary. If a model with finite geometry is substantially different from model F, then it is likely that the restriction to a finite annulus surrounding the capillary produces distorted results.
- It allows the intercapillary distance to naturally increase as the tumour grows.
- The stresses remain relatively low as the tumour grows. More precisely, for $t \leq 8$, the

stresses P_{RR} and $P_{\Theta\Theta}$ are generally of the order of the Young's Modulus (at most).

- The radial displacement at the capillary-tumour interface is negative when we incorporate growth anisotropy, which is consistent with our expectation that the growing tumour exerts a compressive force on the capillary wall.

Of the finite geometry models, we most prefer model A (with null-displacement outer boundary condition). It has the following strengths and weaknesses. Its strengths are that it is relatively simple, and the displacement at the capillary-tumour interface is negative. Its weaknesses are that stress seems to build up too rapidly, it cannot account for an increase in the distance between existing capillaries as the tumour grows (although perhaps we should expect this to be constant for highly constrained tumours), and when it differs from model F, we expect the restriction of the geometry to an annulus surrounding the capillary to distort the solution.

Chapter 4

Onset of Buckling in Model Without Differentiated Capillary Wall Structure

In this chapter we for the sake of simplicity neglect the capillary wall structure and consider the buckling of just a growing tumour cylindrical annulus. The capillary is represented as a cylindrical cavity in the tumour. We assume that initially the growth field, nutrient concentration and elastic deformation are all radially symmetric. The displacement in the axial direction is assumed to be zero. We denote this configuration State I.

We wish to determine when the system ceases to be radially symmetric and starts to buckle. To do this we linearise about State I and use the *Trefftz criterion* to investigate the stability of the system. For each azimuthal wavenumber n and axial wavenumber ω, we determine the critical time $t_{n,\omega}$ at which the system becomes unstable to a buckle with these wavenumbers. It is important to note that even though the critical parameter is time, the system is still in quasi-static equilibrium and we neglect inertial effects. In the subsequent sections we perform a perturbation expansion about the critical time to further investigate the buckle. We use the Liapunov-Schmidt reduction to determine its amplitude, before applying the energy criterion to investigate its stability.

We do not consider the model variants eliminated in the previous chapter. Thus we do

Key	Geometry	Description
A	Finite	Null-Displacement and zero nutrient flux at $R = R_2$.
C	Infinite	$[R_2, \infty)$ is linearly elastic, zero nutrient flux at $R = R_2$.
F	Infinite	Nutrient Distribution and Displacement decay to 0 as $R \to \infty$.
G	Infinite	$\frac{\partial c}{\partial R} = 0$ at $R = R_2$ and $c(R) = c(R_2)$ (for $R > R_2$). $\mathbf{P} \to \mathbf{0}$ as $R \to \infty$.

Table 4.1: The various boundary conditions and geometries. We do not consider the boundary conditions which were eliminated in Chapter 3. The radius of the cavity (which represents the capillary) is R_1. The axial displacement u_z is zero at $Z = 0$ and $Z = Z_0$. If the geometry is finite, the outer radius of the tumour annulus is R_2. At $R = R_1$, the boundary condition is always that of null stress $\mathbf{P} \cdot \mathbf{n} = \mathbf{0}$ and fixed nutrient concentration $n = 1$.

not incorporate growth inhibition into our model, and we assume the anisotropic growth multipliers are of the form in (2.59). Furthermore we only consider the four outer boundary conditions in Table 4.1. We drop the asterisks from the scaled variables for convenience.

4.1 Change in Stability of Tumour Matrix

In this section we outline the Trefftz Criterion for the onset of buckling and apply it to our model.

4.1.1 Trefftz Condition for a Change in Stability

We will investigate the stability of our system according to the *energy criterion* of Lagrange. According to the energy criterion, a system is stable at a certain configuration if the energy functional has a local minimum there [10]. Suppose that a mechanical system is in equilibrium in State I. We investigate the stability of this state by superimposing a small *virtual* displacement $\mathbf{u}$, thereby creating a second state II. In doing this we are employing the Calculus of Variations.

We recall V_m denotes the tumour body. The inner radius is R_1, and in the case of a finite geometry the outer radius is R_2. We fix the axial length of the two concentric cylinders to be Z_0. This corresponds to the buckling of a fixed length capillary anchored at either end.

We insist that the displacements in this thesis are members of the Sobolev space $W^{1,1}$, meaning that $\iiint_{V_m} \|\mathbf{u}\|^2 dV < \infty$ and $\iiint_{V_m} \|\nabla \mathbf{u}\|^2 dV < \infty$. The displacement gradient $\nabla \mathbf{u}$ is defined using the theory of distributions. Refer to Marsden for further explanation of this [98]. We define the set of all *admissible* displacements to be the subspace ${}^a\mathbb{U}$ of $W^{1,1}$

which satisfies the 'incremental' boundary conditions detailed below (for an explanation of the boundary conditions refer to Section 2.2). Intuitively, $\mathbf{u}$ must be such that $\mathbf{u}_0 + \mathbf{u}$ satisfies the boundary conditions (to linear order) if $\mathbf{u}_0$ does.

We now detail more precisely the boundary conditions $\mathbf{u}$ must satisfy to be admissible. It must satisfy the increment in the null-stress boundary condition at the inner boundary $R = R_1$, i.e.

$$\left(\frac{\partial \mathbf{P}}{\partial \mathbf{F}} : \nabla \mathbf{u}\right) \cdot \mathbf{n} = \mathbf{0} \text{ at } R = R_1. \tag{4.1}$$

Here, and henceforth, all gradients with respect fo $\mathbf{F}$ are evaluated at u_0. The displacement must satisfy

$$u_Z = 0 \text{ at } Z = 0 \text{ and } Z = Z_0. \tag{4.2}$$

For the models with an infinite geometry, we require $\mathbf{u} \to \mathbf{0}$ as $R \to \infty$ (refer to Table 4.1 for an explanation of the model variants). For model A, which has a finite geometry, the increment must have null-displacement at $R = R_2$, i.e.

$$\mathbf{u} = \mathbf{0}. \tag{4.3}$$

For model C, the increment in the traction and displacement must be equal either side of R_2, i.e.

$$\left(\frac{\partial \mathbf{P}}{\partial \mathbf{F}} : \nabla \mathbf{u}|_+\right) \cdot \mathbf{n} = \left(\frac{\partial \mathbf{P}}{\partial \mathbf{F}} : \nabla \mathbf{u}|_-\right) \cdot \mathbf{n} \tag{4.4}$$

$$\mathbf{u}|_+ = \mathbf{u}|_-. \tag{4.5}$$

The potential energy of state I is denoted by W_I and the potential energy of state II by W_{II}. The change in potential energy is

$$\triangle W = W_{II} - W_I. \tag{4.6}$$

We decompose the change in potential energy into terms which are linear in $\mathbf{u}$, quadratic in $\mathbf{u}$, and terms of higher order, i.e.

$$\triangle W = W_1 + W_2 + \ldots. \tag{4.7}$$

For state I to be in equilibrium it is necessary that

$$W_1 = 0, \tag{4.8}$$

for all admissible variations $\mathbf{u}$. We call the displacement $\mathbf{u}_0$ of State I, which must satisfy (4.8), the *fundamental solution*. It follows from Lagrange's energy criterion that the fundamental solution is stable if $W_2 > 0$ for all admissible variations $\mathbf{u}$, and it is unstable if $W_2 < 0$ for some admissible variation $\mathbf{u}$ [110].

In our investigation of the onset of buckling we do not consider a small increment in the other state variables: such as the nutrient distribution n and mass growth r_g. Our reason for this is that the elastic deformation timescale is much more rapid than the growth or diffusive timescales. The elastic timescale is estimated to be $\ll 1s$. The diffusive timescale is obtained by matching the dimensions of the diffusion equation, i.e.

$$[t]_D = [x]^2 D^{-1}, \tag{4.9}$$

where $[x]$ is the lengthscale and D is the diffusion coefficient. The lengthscale is that of the mean intercapillary distance, i.e. approximately 5×10^{-5}m. The diffusion coefficient of oxygen is approximately $1.5 \times 10^{-9} m^2 s^{-1}$. We thus find

$$[t]_D \simeq 2s. \tag{4.10}$$

The cell-doubling time varies from 10 to 600 hours.[1] It can be seen that the elastic deformation timescale is much more rapid that the growth or diffusive timescales.

Thus we assume that the initial perturbation in the deformation does not immediately affect the distribution of the nutrient or the growth. In other words we are only investigating the *mechanical* stability of the system. This means that we do not increment the equations governing the nutrient distribution or mass growth (i.e. (2.69) and (2.67)).

We wish to find when the equilibrium point (state I) goes unstable as the level of growth is increased. Initially, at low levels of growth, if the system is stable then W_2 must be positive definite. As the growth is increased, for the system to buckle eventually W_2 must become less than zero for some variation. At the point of transition, $W_2(\mathbf{u}) = 0$ for some $\mathbf{u} \neq 0$.

[1] We have used typical the parameter values outlined in Appendix B.

At this point of transition, $\mathbf{u}$ must be a local minimum of the quadratic functional $W_2(\mathbf{u})$. A necessary condition for this is the *Trefftz Condition*, i.e. the variation of $W_2(\mathbf{u})$ in the direction of $\mathbf{v}$ is zero for all admissible $\mathbf{v}$ [110],

$$\frac{\partial W_2}{\partial \mathbf{u}} \cdot \mathbf{v} = \mathbf{0}. \tag{4.11}$$

This yields a linear partial differential equation in $\mathbf{u}$ (known as the Euler-Lagrange equation). It is interesting to notice that from another perspective, the Trefftz Condition is merely the Inverse Mapping Theorem condition for a function to not be locally invertible [98]. To find the level of growth at which the equilibrium point becomes unstable we need to find the lowest level of growth such that there is a solution $\mathbf{u}$ to the Euler-Lagrange equations. The critical parameter modulating the growth is *time* (which can be seen from (2.67)). Thus our method is to integrate our system with respect to time until there exists a solution to (4.11). We term such a solution an *eigenmode*. It needs to be noted that this is not enough to prove the system is unstable either at this critical point, or for times beyond this critical point. To further analyse the stability at these points we need to consider the higher order variations of $\triangle W$, which we do later in the chapter.

4.1.2 Implementation of Trefftz Condition

We recall there are three configurations of interest. The reference configuration is the pre-growth configuration. In State I the tumour has undergone a purely radial deformation induced by the growth. State II corresponds to an incremental, nonradial, deformation from State I. To implement the Trefftz condition we find an expression for the change in energy from State I to State II in terms of the components of the displacement from State I to State II. We determine this from the tumour constitutive relations, which are expressed through $\psi(\mathbf{F}, \zeta)$ (which gives the strain energy per unit volume in the reference state).

We work in cylindrical coordinates and let $\mathbf{u} = u_r\mathbf{e}_R + u_\theta\mathbf{e}_\Theta + u_z\mathbf{e}_Z$ be an incremental admissible displacement from State I to State II (so $\mathbf{u}$ satisfies the boundary conditions outlined in the previous section). The vector $\mathbf{u}_0$ gives the purely radial displacement from the reference state to State I. Let $\mathbf{F}_0 = \mathbf{I} + \nabla\mathbf{u}_0$ be the deformation gradient corresponding

to the deformation from the reference configuration to State I and $\mathbf{F}$ be the deformation gradient corresponding to the deformation from the reference configuration to State II. Since the displacement from the reference configuration to State I is purely radial, the orthonormal cylindrical coordinate basis vectors are the same for both these states. Accordingly we may add the deformation gradients component-wise, i.e. $\mathbf{F} = \mathbf{F}_0 + \nabla\mathbf{u}$. We similarly let $\mathbf{P}_0$ be the stress field over State I. We provide a detailed overview of the cylindrical coordinate system in Appendix A.1.8.

The quadratic component W_2 of the energy is

$$W_2 = \frac{1}{2}\iiint_{V_m} \frac{\partial \mathbf{P}}{\partial \mathbf{F}} : \nabla\mathbf{u} : \nabla\mathbf{u} dV. \tag{4.12}$$

To implement the Trefftz condition, we must determine the first variation of (4.12). The first variation is

$$\begin{aligned}\frac{\partial W_2}{\partial \mathbf{u}} \cdot \tilde{\mathbf{u}} &= \iiint_{V_m} \frac{\partial \mathbf{P}}{\partial \mathbf{F}} : \nabla\mathbf{u} : \nabla\tilde{\mathbf{u}} dV \\ &= -\iiint_{V_m} \tilde{\mathbf{u}} \cdot \left(\nabla \cdot \left(\frac{\partial \mathbf{P}}{\partial \mathbf{F}} : \nabla\mathbf{u}\right)\right) dV + \iint_{\partial V_m} \tilde{\mathbf{u}} \cdot \left(\left(\frac{\partial \mathbf{P}}{\partial \mathbf{F}} : \nabla\mathbf{u}\right) \cdot \mathbf{n}\right) dA, \end{aligned} \tag{4.13}$$

where $\mathbf{n}$ is the unit outer normal. Since both $\mathbf{u}$ and $\tilde{\mathbf{u}}$ are admissible (which means they satisfy the increment in the boundary conditions outlined at the start of Section 4.1.1), the boundary integral in (4.13) is zero at the boundaries $R = R_1$ and $R = R_2$. The boundary integral in (4.13) is also zero at the boundaries $Z = 0$ and $Z = Z_0$, because at these boundaries

$$\left(\frac{\partial \mathbf{P}}{\partial \mathbf{F}} : \nabla\mathbf{u}\right)_{RZ} = \left(\frac{\partial \mathbf{P}}{\partial \mathbf{F}} : \nabla\mathbf{u}\right)_{\Theta Z} = 0, \tag{4.14}$$

although this fact will only become apparent in light of the Fourier decomposition to be performed below. This ensures that the boundary integral in (4.13) is zero over the axial boundaries. However we note that in order that (4.13) is zero for all admissible variations $\tilde{\mathbf{u}}$, the incremental displacement $\mathbf{u}$ over V_m must satisfy

$$\nabla \cdot \left(\frac{\partial \mathbf{P}}{\partial \mathbf{F}} : \nabla\mathbf{u}\right) = \mathbf{0}. \tag{4.15}$$

The above equation (4.15), together with the boundary conditions in Section 4.1.1 which

define the admissible displacements, constitute a linear boundary value problem which governs the mechanical stability of the system. The time at which a solution to this problem exists is the time at which the system bifurcates from stable to unstable.

Fourier Decomposition

We wish to investigate the stability of particular modes, so we must stipulate $\mathbf{u}$ to be of the following form. Let $\mathbf{u} = \mathbf{u}^{(n,\omega)} + \bar{\mathbf{u}}^{(n,\omega)}$, where

$$u_r^{(n,\omega)} = W_{n,\omega}(R)\cos(n\Theta)\cos(\omega Z)\,, \tag{4.16}$$

$$u_\theta^{(n,\omega)} = V_{n,\omega}(R)\sin(n\Theta)\cos(\omega Z)\,, \tag{4.17}$$

$$u_z^{(n,\omega)} = Z_{n,\omega}(R)\cos(n\Theta)\sin(\omega Z)\,, \tag{4.18}$$

$$\bar{u}_r^{(n,\omega)} = \bar{W}_{n,\omega}(R)\sin(n\Theta)\cos(\omega Z)\,, \tag{4.19}$$

$$\bar{u}_\theta^{(n,\omega)} = \bar{V}_{n,\omega}(R)\cos(n\Theta)\cos(\omega Z)\,, \tag{4.20}$$

$$\bar{u}_z^{(n,\omega)} = \bar{Z}_{n,\omega}(R)\sin(n\Theta)\sin(\omega Z)\,. \tag{4.21}$$

We insist that $n \in \mathbb{N}$ and ω is of the form $m\pi/Z_0$ for $m \in \mathbb{N}$, so that the condition $u_z = 0$ at $Z = 0$ and $Z = Z_0$ is satisfied. Let $U_{n,\omega}^{(1)}$ be the set of all admissible displacements of the form $\mathbf{u}^{(n,\omega)}$, and similarly let $U_{n,\omega}^{(2)}$ be the set of all admissible displacements of the form $\bar{\mathbf{u}}^{(n,\omega)}$. In fact there are two other subspaces the operator is also invariant over, however they do not satisfy the condition $u_z = 0$ at the axial boundaries. We nevertheless state them for future reference: $U_{n,\omega}^{(3)}$ is the set of all displacements of the form

$$u_r = W_{n,\omega}\sin(n\Theta)\sin(\omega Z)\,, \tag{4.22}$$

$$u_\theta = V_{n,\omega}\cos(n\Theta)\sin(\omega Z)\,, \tag{4.23}$$

$$u_z = Z_{n,\omega}\sin(n\Theta)\cos(\omega Z)\,, \tag{4.24}$$

and $U^{(4)}_{n,\omega}$ is the set of all displacements of the form

$$u_r = W_{n,\omega}\cos(n\Theta)\sin(\omega Z)\,, \tag{4.25}$$

$$u_\theta = V_{n,\omega}\sin(n\Theta)\sin(\omega Z)\,, \tag{4.26}$$

$$u_z = Z_{n,\omega}\cos(n\Theta)\cos(\omega Z)\,. \tag{4.27}$$

The reason for this particular splitting is that the operator in (4.15) is invariant over each of these subspaces.

In cylindrical coordinates the deformation gradient is

$$\nabla\mathbf{u} = \begin{pmatrix} \frac{\partial u_r}{\partial R} & \frac{1}{R}\left(\frac{\partial u_r}{\partial\Theta} - \hat{u}_\theta\right) & \frac{\partial u_r}{\partial Z} \\ \frac{\partial u_\theta}{\partial R} & \frac{u_r}{R} + \frac{1}{R}\frac{\partial u_\theta}{\partial\Theta} & \frac{\partial u_\theta}{\partial Z} \\ \frac{\partial u_z}{\partial R} & \frac{1}{R}\frac{\partial u_z}{\partial\Theta} & \frac{\partial u_z}{\partial Z} \end{pmatrix}. \tag{4.28}$$

We find that[2]

$$\nabla\mathbf{u}^{(n,\omega)} = \begin{pmatrix} \frac{\partial W_{n,\omega}}{\partial R}\cos n\Theta\cos\omega Z & -R^{-1}\left(nW_{n,\omega} + V_{n,\omega}\right)\sin n\Theta\cos\omega Z & -\omega W_{n,\omega}\cos n\Theta\sin\omega Z \\ \frac{\partial V_{n,\omega}}{\partial R}\sin n\Theta\cos\omega Z & R^{-1}\left(nV_{n,\omega} + W_{n,\omega}\right)\cos n\Theta\cos\omega Z & -\omega V_{n,\omega}\sin n\Theta\sin\omega Z \\ \frac{\partial Z_{n,\omega}}{\partial R}\cos n\Theta\sin\omega Z & -nR^{-1}Z_{n,\omega}\sin n\Theta\sin\omega Z & \omega Z_{n,\omega}\cos n\Theta\cos\omega Z \end{pmatrix}, \tag{4.29}$$

$$\nabla\bar{\mathbf{u}}^{(n,\omega)} = \begin{pmatrix} \frac{\partial \bar{W}_{n,\omega}}{\partial R}\sin n\Theta\cos\omega Z & -R^{-1}\left(n\bar{W}_{n,\omega} + \bar{V}_{n,\omega}\right)\cos n\Theta\cos\omega Z & -\omega\bar{W}_{n,\omega}\sin n\Theta\sin\omega Z \\ \frac{\partial \bar{V}_{n,\omega}}{\partial R}\cos n\Theta\cos\omega Z & R^{-1}\left(n\bar{V}_{n,\omega} + \bar{W}_{n,\omega}\right)\sin n\Theta\cos\omega Z & -\omega\bar{V}_{n,\omega}\cos n\Theta\sin\omega Z \\ \frac{\partial \bar{Z}_{n,\omega}}{\partial R}\sin n\Theta\sin\omega Z & -nR^{-1}\bar{Z}_{n,\omega}\cos n\Theta\sin\omega Z & \omega\bar{Z}_{n,\omega}\sin n\Theta\cos\omega Z \end{pmatrix}. \tag{4.30}$$

The elastic operator (4.15) thus reduces to two ordinary differential equations of the following form

$$\mathbf{T}\cdot\mathbf{W}''_{(n,\omega)} + \sum_{0\le\alpha,\beta\le 2} n^\alpha\omega^\beta\mathbf{T}_{\alpha\beta}\cdot\mathbf{W}_{(n,\omega)} + n\mathbf{T}^{(n)}_\alpha\cdot\mathbf{W}'_{(n,\omega)} + \omega\mathbf{T}^\omega_\beta\cdot\mathbf{W}'_{(n,\omega)} + \mathbf{T}_0\cdot\mathbf{W}'_{(n,\omega)} = \mathbf{0}, \tag{4.31}$$

[2]The justification of 4.14 lies in (4.29) and (4.30), and the structure of $\frac{\partial\mathbf{P}}{\partial\mathbf{F}} : \nabla\mathbf{u}$ as outlined in (C.5) in the Appendix. The reason is that $\left(\frac{\partial\mathbf{P}}{\partial\mathbf{F}} : \nabla\mathbf{u}\right)_{RZ}$ is a multiple of $\nabla\mathbf{u}_{RZ}$ and $\nabla\mathbf{u}_{ZR}$, and both these terms are identically zero at $Z = 0$ and $Z = Z_0$. The same result holds for $\left(\frac{\partial\mathbf{P}}{\partial\mathbf{F}} : \nabla\mathbf{u}\right)_{\Theta Z}$.

and

$$\bar{\mathbf{T}}\cdot\bar{\mathbf{W}}''_{(n,\omega)}+\sum_{0\leq\alpha,\beta\leq 2} n^{\alpha}\omega^{\beta}\bar{\mathbf{T}}_{\alpha\beta}\cdot\bar{\mathbf{W}}_{(n,\omega)}+n\bar{\mathbf{T}}^{(n)}_{\alpha}\cdot\bar{\mathbf{W}}'_{(n,\omega)}+\omega\bar{\mathbf{T}}^{\omega}_{\beta}\cdot\bar{\mathbf{W}}'_{(n,\omega)}+\bar{\mathbf{T}}_0\cdot\bar{\mathbf{W}}'_{(n,\omega)}=\mathbf{0}. \quad (4.32)$$

The coefficient matrices may be obtained by substituting (4.29) and (4.30) into the expression for $\frac{\partial\mathbf{P}}{\partial\mathbf{F}} : \nabla\mathbf{u}$ given in Appendix C.0.13. The resulting expressions are complicated, so we do this using MAPLE and do not reproduce the coefficient matrices here.

The boundary condition at $R = R_1$ entails

$$\mathbf{P}_{(n,\omega)}\cdot\mathbf{n}=\bar{\mathbf{P}}_{(n,\omega)}\cdot\mathbf{n}=\mathbf{0}, \quad (4.33)$$

where $\mathbf{P}_{(n,\omega)}$ (respectively $\bar{\mathbf{P}}_{(n,\omega)}$) is the stress induced by $\mathbf{W}_{(n,\omega)}$ (respectively $\bar{\mathbf{W}}_{(n,\omega)}$). The boundary condition for large R depends on the model variant (these are outlined in Table 4.1). For the infinite geometry models, we require

$$\mathbf{W}_{(n,\omega)},\bar{\mathbf{W}}_{(n,\omega)}\to\mathbf{0}\text{ as }R\to\infty. \quad (4.34)$$

The null-displacement boundary condition (4.3) at $R = R_2$ is

$$\mathbf{W}_{(n,\omega)}=\bar{\mathbf{W}}_{(n,\omega)}=\mathbf{0}. \quad (4.35)$$

We are thus left with two separate boundary value problems: one in $\mathbf{W}_{(n,\omega)}$ and one in $\bar{\mathbf{W}}_{(n,\omega)}$.

We say that the fundamental state has gone unstable to a deformation of mode (n,ω) if there exists a solution $\mathbf{W}_{(n,\omega)}$ to the first boundary value problem (i.e. (4.31) with appropriate boundary conditions), or a solution $\bar{\mathbf{W}}_{(n,\omega)}$ to the second boundary value problem (i.e. (4.32) with appropriate boundary conditions). In fact it can be shown that $\mathbf{W}_{(n,\omega)} = (W_{(n,\omega)}, V_{(n,\omega)}, Z_{(n,\omega)})^T$ is a solution to the first boundary value problem if and only if $\bar{\mathbf{W}}_{(n,\omega)} = (W_{(n,\omega)}, -V_{(n,\omega)}, Z_{(n,\omega)})^T$ is a solution to the second boundary value problem. In other words $U^{(1)}_{n,\omega}$ and $U^{(2)}_{n,\omega}$ go unstable simultaneously. We determine when the fundamental state goes unstable to mode (n,ω) by integrating with respect to time until such solutions exist. In fact, if such solutions exist then through an appropriate orientation Θ we may assume $\bar{\mathbf{W}}_{(n,\omega)} = \mathbf{0}$. To demonstrate this we write $\mathbf{W}_{(n,\omega)}$ in the form

$(W_{(n,\omega)}, V_{(n,\omega)}, Z_{(n,\omega)})^T$ and $\bar{\mathbf{W}}_{(n,\omega)}$ in the form $s(W_{(n,\omega)}, -V_{(n,\omega)}, Z_{(n,\omega)})^T$, for constant s. The displacements corresponding to these vectors are

$$\begin{aligned}
u_r &= W_{n,\omega}(\cos(n\Theta) + s\sin(n\Theta))\cos(\omega Z) = W_{(n,\omega)}\sqrt{1+s^2}\cos(n\Theta + \Theta_0)\cos(\omega Z),\\
u_\theta &= V_{(n,\omega)}(\sin(n\Theta) - s\cos(n\Theta))\cos(\omega Z) = V_{(n,\omega)}\sqrt{1+s^2}\sin(n\Theta + \Theta_0)\cos(\omega Z),\\
u_z &= Z_{(n,\omega)}\sqrt{1+s^2}\cos(n\Theta + \Theta_0)\sin(\omega Z),
\end{aligned} \tag{4.36}$$

where $\tan(\Theta_0) = -s$. It can be seen the buckled shape is reflectively symmetric about the line $\theta = \Theta_0$. Without loss of generality we may assume $\Theta_0 = 0$, which means $s = 0$ and $\bar{\mathbf{W}}_{(n,\omega)} = 0$.

4.2 Post-Buckling Analysis

We investigate the existence and stability of buckled equilibrium states (which we label State II) which bifurcate from the fundamental solution branch. The system is assumed to have evolved to the mode (n,ω) critical time $t^*_{n,\omega}$, at which point there exists a solution in $U_{n,\omega}$ to the incremental equations of equilibrium as outlined in the previous section. At this point we look for a weakly nonlinear solution to the equations of equilibrium for a small perturbation δt in the time. We employ the Liapunov-Schmidt reduction to determine the leading order of the magnitude of the buckle. Finally in Section 4.2.4 we investigate the stability of the buckled equilibrium states according to the energy criterion of Lagrange: whereby a state is (mechanically) stable if the strain energy function has a local minimum.

We let $\epsilon \ll 1$ be a small parameter. We stipulate ϵ to indicate the order of magnitude of the buckle (i.e. the leading order of the perturbed displacement is $O(\epsilon)$). The small perturbation in time is set to be $\frac{1}{2}\epsilon^2\delta t + O(\epsilon^3)$: it will be seen that this is necessary for the leading order of the equation of mechanical equilibrium to be well-matched. We will find conditions for the existence of stable buckled equilibrium states which bifurcate from State I. We are interested in the existence of buckled equilibrium states of mode (n,ω) even if (n,ω) is not the first mode to go unstable. In this case, mode (n,ω) buckled equilibrium states exist, but (in the limit as $\epsilon \to 0$), they will be unstable to mode (j,γ) variations,

if mode (j,γ) has an earlier critical time. These states are still of importance because in reality the system will possess small inhomogeneities which will make it more disposed to buckling in one mode than another. Thus perhaps the system will be less disposed to mode (j,γ) variations, in which case the mode (n,ω) buckled equilibrium state could be stable.

Our condition for buckling does not account for any perturbation in the nutrient or growth. The reason for this, as we explained earlier in this chapter, is that the elastic response timescale is much faster than the diffusive or growth timescales, so that the system deforms before the nutrient distribution or growth can respond. However if the buckled equilibrium state is stable, then the system may spend a nontrivial amount of time in the buckled configuration and we cannot ignore the response of the nutrient distribution and the growth to the small increment in the displacement.

Therefore, the perturbation expansion is of the following form

$$\begin{aligned}
\mathbf{u} =& \mathbf{u}_0 + \epsilon \mathbf{u}_1 + \frac{\epsilon^2}{2}\mathbf{u}_2 + \dots, \\
c =& c_0 + \epsilon c_1 + \frac{\epsilon^2}{2} c_2 + \dots, \\
\bar{r}_\alpha =& r_{\alpha,0} + \epsilon r_{\alpha,1} + \frac{\epsilon^2}{2} r_{\alpha,2} + \dots, \\
G_\alpha =& G_{\alpha,0} + \epsilon G_{\alpha,1} + \dots, \\
\zeta_\alpha =& \zeta_{\alpha,0} + \epsilon \zeta_{\alpha,1} + \frac{\epsilon^2}{2}\zeta_{\alpha,2} + \dots, \\
t =& t_{n,\omega} + \frac{\epsilon^2}{2}\delta t + \frac{\epsilon^3}{6} t_3 + \dots,
\end{aligned} \tag{4.37}$$

for $\epsilon \ll 1$. We determine explicit expressions for these variables in the course of this Chapter.

4.2.1 The Liapunov-Schmidt Reduction

The Liapunov-Schmidt reduction provides a means of obtaining a weakly nonlinear solution to the mechanical equation of equilibrium close to a bifurcation point (i.e. at the time of buckling). The essence of the method is to reduce the equation of equilibrium - which is defined on an infinite-dimensional Banach Space - to the finite-dimensioned subspace spanned by the eigenmodes $\{\mathbf{u}^{(n,\omega)}, \bar{\mathbf{u}}^{(n,\omega)}\}$. This is done by splitting $\mathbf{u}$ according to $\mathbf{u} =$

$a\mathbf{u}^{(n,\omega)} + \mathbf{u}^{\perp}$, where $\mathbf{u}^{\perp}$ is perpendicular to $\mathbf{u}^{(n,\omega)}$, and obtaining $\mathbf{u}^{\perp}$ as a function of $\mathbf{u}^{(n,\omega)}$ using the implicit function theorem. A detailed overview of the method is presented in Golubitsky *et al* [63].

The Liapunov-Schmidt reduction centres around the application of the Fredholm Alternative to the linearisation of the equations of equilibrium. To do this, we must first perform a perturbation expansion of the equation of equilibrium and define the *incremental elastic operator*. We now consider $\mathbf{u}$ to give the total displacement from the reference configuration to State II (in the previous section $\mathbf{u}$ was the incremental displacement from State I to State II), i.e.

$$\mathbf{u} = \mathbf{u}_0 + \epsilon\mathbf{u}_1 + \frac{\epsilon^2}{2}\mathbf{u}_2 + \dots \tag{4.38}$$

The perturbation expansion of the deformation gradient and first Piola-Kirchhoff stress is given by,

$$\begin{aligned} \mathbf{F} &= \mathbf{F}_0 + \epsilon\nabla\mathbf{u}_1 + \frac{\epsilon^2}{2}\nabla\mathbf{u}_2 + \dots, \\ \mathbf{P} &= \mathbf{P}_0 + \epsilon\mathbf{P}_1 + \frac{\epsilon^2}{2}\mathbf{P}_2 + \dots, \end{aligned} \tag{4.39}$$

where the components are always with respect to the orthonormal cylindrical basis of the reference state (which is the same as the orthonormal cylindrical basis of State I). We stipulate the leading order of the displacement to be a multiple of the eigenmode, i.e. $\mathbf{u} = a\mathbf{u}^{(n,\omega)}$, where a is a constant we solve for later. We note that $(\nabla\mathbf{u})_j = \nabla(\mathbf{u}_j)$.

As stipulated earlier, State II is in mechanical equilibrium, which means

$$\nabla \cdot \mathbf{P}_j = \mathbf{0}, \tag{4.40}$$

$$\mathbf{P}_j \cdot \mathbf{n} = \mathbf{0} \text{ at } R = R_1 \text{ and,} \tag{4.41}$$

$$\mathbf{u}_j = \mathbf{0} \text{ at } R = R_2, \text{ for model A, or} \tag{4.42}$$

$$\mathbf{u}_j|_- = \mathbf{u}_j|_+ \text{ and } \mathbf{P}_j \cdot \mathbf{n}|_- = \mathbf{P}_j \cdot \mathbf{n}|_+ \text{ at } R = R_2, \text{ for model C,} \tag{4.43}$$

$$\mathbf{u}_j \to \mathbf{0} \text{ as } R \to \infty \text{ for models C,F and G.} \tag{4.44}$$

The axial component of $\mathbf{u}_j$ is zero at $Z = 0$ and $Z = Z_0$. Refer to Table 4.1 for an explanation of the boundary conditions. Now the $O(\epsilon)$ and $O(\epsilon^2)$ increments in the first

Piola Kirchhoff stress are given by

$$\begin{aligned}\mathbf{P}_1 =& \frac{\partial \mathbf{P}}{\partial \mathbf{F}} : \nabla \mathbf{u}_1, \\ \frac{1}{2}\mathbf{P}_2 =& \frac{1}{2}\frac{\partial^2 \mathbf{P}}{\partial \mathbf{F}^2} : \nabla \mathbf{u}_1 : \nabla \mathbf{u}_1 + \frac{1}{2}\frac{\partial \mathbf{P}}{\partial \mathbf{F}} : \nabla \mathbf{u}_2 + \frac{1}{2}\frac{\partial \mathbf{P}}{\partial \zeta_\alpha}\zeta_{\alpha,2},\end{aligned} \tag{4.45}$$

where we sum over α. All of the derivatives with respect to $\mathbf{F}$ and ζ_α throughout this chapter are evaluated at State I. Observe that we may write

$$\mathbf{P}_j = \mathbf{P}_j^* + \frac{\partial \mathbf{P}}{\partial \mathbf{F}} : \nabla \mathbf{u}_j, \tag{4.46}$$

where $\mathbf{P}_j^*$ is determined by $\{\mathbf{u}_k, \zeta_{\alpha,k}, \zeta_{\alpha,j}\}$ for $k < j$. Thus for each j, we may obtain $\mathbf{u}_j$ by solving the linear system,

$$\nabla \cdot \left(\frac{\partial \mathbf{P}}{\partial \mathbf{F}} : \nabla \mathbf{u}_j \right) = -\nabla \cdot \mathbf{P}_j^*, \tag{4.47}$$

$$\left(\frac{\partial \mathbf{P}}{\partial \mathbf{F}} : \nabla \mathbf{u}_j \right) \cdot \mathbf{n} = -\mathbf{P}_j^* \cdot \mathbf{n} \text{ at } R = R_1, \tag{4.48}$$

$$\mathbf{u}_j = \mathbf{0} \text{ at } R = R_2, \text{ for model A or} \tag{4.49}$$

$$\mathbf{u}_j|_- = \mathbf{u}_j|_+ \text{ and } \left(\frac{\partial \mathbf{P}}{\partial \mathbf{F}} : \nabla \mathbf{u}_j + \mathbf{P}_j^* \right)|_- \cdot \mathbf{n} = \frac{\partial \mathbf{P}}{\partial \mathbf{F}} : \nabla \mathbf{u}_j|_+ \cdot \mathbf{n} \text{ at } R = R_2 \text{ for model C}$$

$$\mathbf{u}_j \to 0 \text{ as } R \to \infty \text{ if the geometry is infinite (models C, F and G).} \tag{4.50}$$

Note that in model C, $\mathbf{P}_j^* = \mathbf{0}$ over the linear elastic domain (which is given by $R > R_2$). This is a direct consequence of the assumption of linearity.

By assumption, the homogeneous equation, i.e. (4.47)-(4.50) with $\mathbf{P}_j^* = \mathbf{0}$, has nontrivial solutions $\mathbf{u}^{(n,\omega)}$ and $\bar{\mathbf{u}}^{(n,\omega)}$ over mode (n, ω) (the eigenmodes). The essence of the Liapunov-Schmidt method is to locally reduce each order of the equation of equilibrium to the subspace spanned by these two eigenmodes. This allows us to apply the Fredholm Alternative, giving us a constraint on (4.47)-(4.50) necessary for there to be a solution.

We now determine the Fredholm Alternative condition for there to exist a solution to (4.47)-(4.50). We define the *incremental elastic operator* $\mathbf{L}$ over V_m in the following way,

$$\mathbf{L}\mathbf{u} = \nabla \cdot \left(\frac{\partial \mathbf{P}}{\partial \mathbf{F}} : \nabla \mathbf{u} \right). \tag{4.51}$$

We let the domain of $\mathbf{L}$ be ${}^{a}\mathbb{U}$. It can be seen that $\mathbf{L}$ is essentially the incremental elastic operator of Section 4.1.2, and the kernel of $\mathbf{L}$ is spanned by $\mathbf{u}^{(n,\omega)}$ and $\bar{\mathbf{u}}^{(n,\omega)}$. In fact $\mathbf{L}$ is self-adjoint, which can be observed from the following expansion of the energy

$$\iiint_{V_m} \frac{\partial \mathbf{P}}{\partial \mathbf{F}} : \nabla \mathbf{u} : \nabla \mathbf{v} dV = -\iiint_{V_m} \mathbf{v} \cdot \left(\nabla \cdot \frac{\partial \mathbf{P}}{\partial \mathbf{F}} : \nabla \mathbf{u} \right) + \nabla \cdot \left(\left(\frac{\partial \mathbf{P}}{\partial \mathbf{F}} : \nabla \mathbf{u} \right)^T \cdot \mathbf{v} \right) dV \tag{4.52}$$

$$= -\iiint_{V_m} \mathbf{v} \cdot \left(\nabla \cdot \frac{\partial \mathbf{P}}{\partial \mathbf{F}} : \nabla \mathbf{u} \right) dV + \iint_{\partial V_m} \mathbf{v} \cdot \frac{\partial \mathbf{P}}{\partial \mathbf{F}} : \nabla \mathbf{u} \cdot \mathbf{n} dV. \tag{4.53}$$

In the first line we applied the product rule, and in the second line we applied the divergence theorem. Due to the symmetry of $\frac{\partial \mathbf{P}}{\partial \mathbf{F}} = \frac{\partial^2 \psi}{\partial \mathbf{F}^2}$, (4.53) is equal to

$$-\iiint_{V_m} \mathbf{u} \cdot \left(\nabla \cdot \frac{\partial \mathbf{P}}{\partial \mathbf{F}} : \nabla \mathbf{v} \right) dV + \iint_{\partial V_m} \mathbf{u} \cdot \frac{\partial \mathbf{P}}{\partial \mathbf{F}} : \nabla \mathbf{v} \cdot \mathbf{n} dV. \tag{4.54}$$

It can be seen that $\mathbf{L}$ is formally self-adjoint, as the first terms in (4.53) and (4.54) are respectively $\langle \mathbf{v}, \mathbf{L}\mathbf{u} \rangle$ and $\langle \mathbf{u}, \mathbf{L}\mathbf{v} \rangle$. To find the domain of $\mathbf{L}^*$ (the adjoint of $\mathbf{L}$), we stipulate that $\mathbf{u} \in {}^{a}\mathbb{U}$ and look for the constraints on $\mathbf{v}$ necessary for the boundary integrals in (4.53) and (4.54) to be zero. For each of the model variants, the boundary condition is either null-displacement or null-stress (or a mix of both). It can be seen that if $\mathbf{u} = \mathbf{0}$ at a boundary then it is necessary that $\mathbf{v} = \mathbf{0}$ at the same boundary, and similarly if $\frac{\partial \mathbf{P}}{\partial \mathbf{F}} : \nabla \mathbf{u} \cdot \mathbf{n} = \mathbf{0}$ at a boundary then it is necessary that $\frac{\partial \mathbf{P}}{\partial \mathbf{F}} : \nabla \mathbf{v} \cdot \mathbf{n} = \mathbf{0}$ there too. At the boundaries $Z = 0$ and $Z = Z_0$, we have $u_Z = 0$ and $\left(\frac{\partial \mathbf{P}}{\partial \mathbf{F}} : \nabla \mathbf{u}\right)_{\gamma Z} = 0$ if $\gamma = R$ or $\gamma = \Theta$. We require $\mathbf{v}$ to have the same properties at these boundaries. Thus at all of the boundaries we see that the domain of $\mathbf{L}^*$ is the same as the domain of $\mathbf{L}$ (i.e. ${}^{a}\mathbb{U}$).

We investigate the solvability of the boundary value problem (4.47)-(4.50) by substituting $\mathbf{u} = \mathbf{u}_j$ into (4.52)-(4.54). We also stipulate that $\mathbf{v}$ is an eigenmode in these expressions. In doing this we are applying the Fredholm Alternative (refer to Marsden [98] for a more detailed discussion of the Fredholm Alternative). The fact that $\mathbf{v}$ is an eigenmode means that (4.54) is zero, and by implication (4.52) and (4.53) are also zero. We then substitute

(4.47)-(4.50) into (4.53), and find

$$-\iiint_{V_m} \mathbf{v} \cdot \left(\nabla \cdot \mathbf{P}_j^*\right) dV + \iint_{\partial V_m} \mathbf{v} \cdot \mathbf{P}_j^* \cdot \mathbf{n} dV = 0. \tag{4.55}$$

After an application of the divergence theorem and product rule to (4.55), we find

$$\iiint_{V_m} \mathbf{P}_j^* : \nabla \mathbf{v} dV = 0. \tag{4.56}$$

Since the kernel is spanned by $\mathbf{u}^{(n,\omega)}$ and $\bar{\mathbf{u}}^{(n,\omega)}$, the fact that (4.56) is zero is equivalent to the requirement that

$$\iiint_{V_m} \mathbf{P}_j^* : \nabla \mathbf{u}^{(n,\omega)} dV = 0 \ , \ \iiint_{V_m} \mathbf{P}_j^* : \nabla \bar{\mathbf{u}}^{(n,\omega)} dV = 0. \tag{4.57}$$

The equations (4.57) imposes a necessary condition on $\mathbf{P}_j^*$ for there to exist a solution $\mathbf{u}_j^*$. However on first appearances a solution is not guaranteed. If the Fredholm Condition is satisfied, a solution in $\mathbb{U}$ is guaranteed if the partial differential equation $\mathbf{Lu} = \mathbf{0}$ is *strongly elliptic* at all points in V_m, i.e.

$$\frac{\partial \mathbf{P}}{\partial \mathbf{F}} : (\mathbf{p} \otimes \mathbf{q}) : (\mathbf{p} \otimes \mathbf{q}) \geq K \|p\|^2 \|q\|^2, \tag{4.58}$$

for some $K > 0$ and all $\mathbf{p}, \mathbf{q} \in \mathbb{R}^3$. Refer to the discussion in Marsden [98] for more details. However we cannot assume that the elastic system is strongly elliptic because $\frac{\partial \mathbf{P}}{\partial \mathbf{F}}$ is dependent on the growth and displacement in the fundamental solution (although in practice we usually find that it is strongly elliptic at the time of buckling).

However we may remedy this problem through recalling that, due to the regularity of our annular geometry, we can easily decompose the partial differential equation (4.47) into its Fourier modes over Θ and Z. Upon doing this, for each $m \in \mathbb{Z}_+$, $\gamma \in \mathbb{R}$ the mode (m, γ) component of $\mathbf{Lu} = \mathbf{P}_j^*$ reduces to four separate second order linear ordinary differential equations in R; with each equation in one of $\{U_{m,\gamma}^{(1)}, U_{m,\gamma}^{(2)}, U_{m,\gamma}^{(3)}, U_{m,\gamma}^{(4)}\}$. We only need to worry about the case $m = n$ and $\gamma = \omega$, because by hypothesis this is the only mode for which the homogeneous equation has a nontrivial solution. The solvability of this system is thus governed by the Fredholm Alternative for integral equations. We may write the

projection of (4.47) onto $U^{(1)}_{n,\omega}$ as

$$(\mathbf{I}-\mathbf{K})\,\mathbf{z}_j = \tilde{P}^*_j|_{n,\omega}, \tag{4.59}$$

where $\mathbf{z}_j = (W^{(j)}_{n,\omega}, V^{(j)}_{n,\omega}, Z^{(j)}_{n,\omega}, W^{(j)'}_{n,\omega}, V^{(j)'}_{n,\omega}, Z^{(j)'}_{n,\omega})^T$, the projection of $\mathbf{u}_j$ onto ${}^a\mathbb{U}^{(1)}$ is $(W^{(j)}_{n,\omega}\cos(n\Theta)\cos(\omega Z), V^{(j)}_{n,\omega}\sin(n\Theta)\cos(\omega Z), Z^{(j)}_{n,\omega}\cos(n\Theta)\sin(\omega Z))^T$ and $\mathbf{K}$ is a suitably defined integral operator. Here $\tilde{P}^*_j|_{n,\omega}$ is the projection of $-\nabla\cdot\mathbf{P}^*_j$ onto ${}^a\mathbb{U}^{(1)}_{n,\omega}$ (with the trigonometric terms factored out). The operator $\mathbf{K}$ is compact as long as the coefficients of the double derivatives in (4.47) are each bounded below by a positive real number. The coefficients are the constants P_{RRRR}, $P_{\Theta R\Theta R}$ and P_{ZRZR} corresponding to a Blatz-Ko material given in Appendix C.0.13. It can be seen that they are both strictly greater than zero as long as $q<-1$ and the components of the deformation gradient of the fundamental solution are strictly greater than zero. Hence the conditions in (4.57) are both necessary and sufficient for a solution $\mathbf{u}_j$ to exist.

To conclude, we have found a necessary and sufficient condition (4.57) for the existence of a solution $\mathbf{u}_j$ to the j^{th} mechanical equation of equilibrium (4.47)-(4.50). In Section 4.2.3 we apply (4.57) to determine the leading order of the magnitude of the buckle. However before we do this we must determine expressions for the perturbation of the other variables in our model.

4.2.2 Perturbation Expansion in Nutrient and Growth

In this section we determine expressions for the leading order perturbations in the nutrient, growth and treatment. However we must firstly briefly review the equations governing the nutrient distribution and growth. The nutrient distribution is governed by

$$\nabla\cdot\left(J\mathbf{F}^{-1}\mathbf{F}^{-T}\nabla_0 c\right) = \frac{J\alpha c}{k_n+c}, \tag{4.60}$$

where $c=1$ at $R=R_1$ and $\frac{\partial c}{\partial R}=0$ at $R=R_2$. The growth dilation is given by

$$\zeta_\alpha = e^{\bar{r}_\alpha}, \tag{4.61}$$

where the total mass growth in the direction of $\mathbf{e}_\alpha$ is

$$\bar{r}_\alpha = \int_0^t G_\alpha \left(\frac{c}{k_c + c} - \mu \right) d\tau. \tag{4.62}$$

When the tumour is being treated with a chemotherapeutic drug, the drug distribution is governed by

$$\nabla \cdot \left(J\mathbf{F}^{-1}\mathbf{F}^{-T}\nabla_0 d \right) = k_{met} J d + \frac{J\alpha_d d}{k_d + d}, \tag{4.63}$$

where $d = d_i(t)$ at $R = R_1$ and $\frac{\partial d}{\partial R} = 0$ at $R = R_2$. In this case, the cell kill rate is given by one of the following

$$\mu = \mu^i d + \mu^{ii} \frac{d}{k_d + d} \tag{4.64}$$

$$\mu = \left(\mu^i d + \mu^{ii} \frac{d}{k_d + d} \right) \frac{K0}{K0 + c}, \tag{4.65}$$

according to the drug being administered. If radiotherapy is being administered, the cell kill rate is

$$\mu = (\triangle\ T)^{-1} \left(\alpha_h OER.D + \beta_h (OER.D)^2 \right), \tag{4.66}$$

where

$$OER_\alpha = \frac{cm_\alpha + K_m}{c + K_m} \tag{4.67}$$

$$OER_\beta = \frac{cm_\beta + K_m}{c + K_m}, \tag{4.68}$$

D is the dosage and $\triangle\ T$ is the time period of the dosage.

Perturbation in Growth

We find the components of the expansion of $\bar{r}_\alpha$ by substituting the perturbation expansions into (4.62), i.e.

$$\bar{r}_\alpha = \int_0^{t + \frac{1}{2}\epsilon^2 \delta t + \ldots} (G_{\alpha,0} + \epsilon G_{\alpha,1}) \left(\frac{c_0 + \epsilon c_1 + \ldots}{k_c + c_0 + \epsilon c_1 + \ldots} - \mu \right) d\tau. \tag{4.69}$$

We now Taylor expand the above integral with respect to the increment in time, and find

$$\begin{aligned} r_{\alpha,1} =& 0, \\ r_{\alpha,2} =& \delta t G_{\alpha,0} \left(\frac{c_0}{k_c + c_0} - \mu_0 \right). \end{aligned} \tag{4.70}$$

It can be seen that the leading order increments in the mass growth and dilation only depend on the increment in the fundamental solution caused by the increment in the time. They do not depend on the buckle in the displacement or the perturbation in the nutrient distribution. To find $r_{\alpha,3}$ we must integrate the following

$$\begin{aligned} \epsilon^3 \frac{1}{6} r_{\alpha,3} = \int_{t^*}^{t^* + 0.5\epsilon^2 \delta t} & \epsilon G_{\alpha,0} \left(\frac{c_1}{k_c} \left(1 + \frac{c_0}{k_c} \right)^{-2} - \mu_1 \right) + \epsilon G_{\alpha,1} \left(\frac{c_0}{k_c + c_0} - \mu_0 \right) dt \\ & + \frac{1}{6} \epsilon^3 t_3 G_{\alpha,0} \left(\frac{c_0}{k_c + c_0} - \mu_0 \right). \end{aligned} \tag{4.71}$$

This integral depends on the magnitude of the buckle and the time the system spends in the buckled state. Our quasi-static assumption does not allow us to determine this *a priori*, so we must defer our search for a specific expression for (4.71) until the following section.

We find, in turn, that the perturbation in the growth is given by

$$\begin{aligned} \zeta_{\alpha,1} =& 0, \\ \zeta_{\alpha,2} =& \zeta_{\alpha,0} r_{\alpha,2}, \\ \zeta_{\alpha,3} =& \zeta_{\alpha,0} r_{\alpha,3}. \end{aligned} \tag{4.72}$$

We defined the rate of change of the growth $G_\alpha r_g$ to be coaxial with the principal stresses. For the fundamental solution, these axes are in the direction of the cylindrical basis vectors. The multipliers are given by

$$G_{jj} = \exp\left(A K_t^{-1} \mathbf{T}_{jj} \right) G_\Sigma^{-1}, \tag{4.73}$$

$$G_\Sigma = \exp\left(A K_t^{-1} \mathbf{T}_{RR} \right) + \exp\left(A K_t^{-1} \mathbf{T}_{\Theta\Theta} \right) + \exp\left(A K_t^{-1} \mathbf{T}_{ZZ} \right). \tag{4.74}$$

Imposing the displacement $\epsilon \mathbf{u}$ on top of the fundamental solution induces a small perturba-

tion in both the magnitudes and axes of the principal stresses. However it may be readily verified that the perturbation in the axes is $O(\epsilon^2)$, so that to $O(\epsilon)$ accuracy we may assume that the principal stresses of the perturbed solution are coaxial with the principal stresses of the fundamental solution. We denote the increments in the principal stresses by $\{T_{1,RR}, T_{1,\Theta\Theta}, T_{1,ZZ}\}$. We may calculate the increments in the Cauchy Stress tensor $\mathbf{T}$ from its definition $\mathbf{T} = J^{-1}\mathbf{P}\mathbf{F}^T$. We find

$$\mathbf{T}_1 = J_0^{-1}\left(\frac{\partial \mathbf{P}}{\partial \mathbf{F}} : \nabla \mathbf{u}_1\right)\mathbf{F}_0^T + J_0^{-1}\mathbf{P}_0\left(\nabla \mathbf{u}_1^T - \left(\mathbf{F}_0^{-T} : \nabla \mathbf{u}_1\right)\mathbf{F}_0^T\right). \tag{4.75}$$

The increment $G_{\alpha,1}$ is

$$G_{\alpha,1} = \frac{A}{K_t}T_{\alpha\alpha,1}\exp\left(\frac{A}{K_t}T_{\alpha\alpha}\right)G_\Sigma^{-1} - \exp\left(\frac{A}{K_t}T_{\alpha\alpha}\right)G_\Sigma^{-2}G_{\Sigma,1}, \tag{4.76}$$

$$G_{\Sigma,1} = \frac{A}{K_t}T_{\beta\beta,1}\exp\left(\frac{A}{K_t}T_{\beta\beta}\right), \tag{4.77}$$

where $T_{\alpha\alpha,1}$ is the increment in the Cauchy Stress and we sum over β (but not α).

Perturbation in Nutrient Distribution

We obtain an ordinary differential equation governing c_1 by taking the first order increment of the equation governing the nutrient distribution (4.60), i.e.

$$\begin{aligned}\nabla \cdot \Big(&J_0(\mathbf{F}_0^{-T} : \nabla \mathbf{u}_1)\mathbf{F}_0^{-1}\mathbf{F}_0^{-T}\nabla c_0 - J_0\mathbf{F}_0^{-1}\nabla \mathbf{u}_1\mathbf{F}_0^{-1}\mathbf{F}_0^{-T}\nabla c_0 \\ &-J_0\mathbf{F}_0^{-1}\mathbf{F}_0^{-T}\nabla \mathbf{u}_1^T\mathbf{F}_0^{-T}\nabla c_0 + J_0\mathbf{F}_0^{-1}\mathbf{F}_0^{-T}\nabla c_1\Big) \\ &= \frac{J_0 c_1 \alpha}{k_n}\left(1 + \frac{c_0}{k_n}\right)^{-2} + \frac{J_0\alpha c_0\mathbf{F}_0^{-T} : \nabla \mathbf{u}_1}{k_n + c_0}.\end{aligned}$$

The boundary conditions are

$$c_1 = 0 \text{ at } R = R_1, \tag{4.78}$$

$$\frac{\partial c_1}{\partial R} = 0 \text{ at } R = R_2, \text{ if there is a finite geometry,} \tag{4.79}$$

$$c_1 \to 0 \text{ as } R \to \infty, \text{ if the geometry is infinite.} \tag{4.80}$$

In Section 4.2.3 we prove $\mathbf{u}_1$ is a multiple of the homogeneous solution, i.e. $\mathbf{u}_1 = a\mathbf{u}^{(n,\omega)}$. It follows that we may expand c_1 as $c_1 = aN_{n,\omega}\cos(n\Theta)\cos(\omega Z)$. We obtain the following equation governing $N_{n,\omega}$

$$\begin{aligned}
&\left(1+\frac{u_0}{R}\right)\left(1+\frac{du_0}{dR}\right)^{-1}\frac{d^2N_{n,\omega}}{dR^2}+R^{-1}\frac{dN_{n,\omega}}{dR}\left(1-(R+u_0)\left(1+\frac{du_0}{dR}\right)^{-2}\frac{d^2u_0}{dR^2}\right)\\
&-n^2R^{-2}\left(1+\frac{du_0}{dR}\right)\left(1+\frac{u_0}{R}\right)^{-1}N_{n,\omega}-J_0\frac{\alpha}{k_n}\left(1+\frac{c_0}{k_n}\right)^{-2}N_{n,\omega}-J_0\left(\mathbf{F}_0^{-T}:\nabla\mathbf{u}\right)\frac{\alpha c_0}{k_n+c_0}\\
&-\omega^2J_0N_{n,\omega}+\nabla\cdot\Big(J(\mathbf{F}_0^{-T}:\nabla\mathbf{u}^{(n,\omega)})\mathbf{F}_0^{-1}\mathbf{F}_0^{-T}\nabla c_0\\
&-H_0J_0\mathbf{F}_0^{-1}\nabla\mathbf{u}^{(n,\omega)}\mathbf{F}_0^{-1}\mathbf{F}_0^{-T}\nabla c_0-H_0J_0\mathbf{F}_0^{-1}\mathbf{F}_0^{-T}\nabla(\mathbf{u}^{(n,\omega)})^T\mathbf{F}_0^{-T}\nabla c_0\Big)=0.
\end{aligned}$$

Perturbation in Chemotherapy and Radiotherapy

We obtain expressions for the perturbations in the chemotherapy and radiotherapy in response to the displacement. For the drugs which have an uptake independent of the oxygen concentration, such as cisplatin, the uptake is

$$\mu_0 = \left(\mu^i d_0 + \mu^{ii}\frac{d_0}{k_d+d_0}\right), \tag{4.81}$$

$$\mu_1 = d_1\left(\mu^i + \frac{\mu^{ii}}{k_d}\left(1+\frac{d_0}{k_d}\right)^{-2}\right). \tag{4.82}$$

For drugs (such as Tirapazamine) with distributions dependent on the oxygen concentration, we have

$$\mu_0 = \left(\mu^i d_0 + \mu^{ii}\frac{d_0}{k_d+d_0}\right)\frac{K0}{K0+c_0}, \tag{4.83}$$

$$\mu_1 = d_1\left(\mu^i + \frac{\mu^{ii}}{k_d}\left(1+\frac{c_0}{k_d}\right)^{-2}\right)\frac{K0}{K0+c_0} - \left(\mu^i d_0 + \mu^{ii}\frac{d_0}{k_d+d_0}\right)\frac{K0}{(K0+c_0)^2}c_1. \tag{4.84}$$

For the radiotherapy we have

$$\mu_0 = (\lambda_c \triangle T)^{-1} \left(\alpha_h OER_\alpha . D + \beta_h (OER_\beta . D)^2\right), \tag{4.85}$$

$$OER_\alpha = \frac{c_0 m_\alpha + K_m}{c_0 + K_m}, \tag{4.86}$$

$$OER_\beta = \frac{c_0 m_\beta + K_m}{c_0 + K_m}, \tag{4.87}$$

$$\mu_1 = \frac{k_m}{\lambda_c \triangle T}(c_0 + k_m)^{-2} c_1 \left((m_\alpha - 1)\alpha_h D + 2\beta_h OER_\beta D^2 (m_\beta - 1)\right). \tag{4.88}$$

The ordinary differential equation governing d_1 has a similar form to that governing the nutrient increment c_1, except $\alpha \to \alpha_d$, $k_n \to k_d$ and the boundary condition at R_1 is $d_1 = d_{i,1}(t)$ (the increment in the concentration of the drug in the blood). The left hand side of the final equation has the additional terms

$$-\left(J_0 k_{met} d_1 + J_0 k_{met} c_0 \mathbf{F}_0^{-T} : \nabla \mathbf{u}_1\right). \tag{4.89}$$

The first order increment in the value at the boundary R_1 (c_i) is zero because the first order increment in time is zero.

We thus have expressions for the leading order perturbations of the nutrient, growth and treatment. We may now apply the Liapunov-Schmidt Reduction to determine the magnitude of the buckle.

4.2.3 Application of the Liapunov-Schmidt Reduction to our System

We are now in a position to apply the Liapunov-Schmidt reduction to our system. We give a brief overview of the reduction: for more details refer to Golubitsky *et al* [63]. Our discussion of the Fredholm Alternative in Section 4.2.1 indicates that ${}^a\mathbb{U}$ may be decomposed into a direct sum of the range of $\mathbf{L}$ and its kernel. Thus, at each order j, we may uniquely write the perturbation in the displacement $\mathbf{u}_j$ as $\mathbf{z}_j + \mathbf{y}_j$, where $\mathbf{z}_j$ is in the kernel of $\mathbf{L}$. We use the mechanical equations of equilibrium to implicitly solve for $\mathbf{y}_j$ as a function of $\{\mathbf{z}_k\}_{k<j}$ and δt in a neighbourhood of the fundamental solution at the critical time.[3] This solution may then be substituted back into the Fredholm solvability condition (4.57), so that the

[3]This solution exists as a consequence of the implicit function theorem.

solvability condition is now a function of $\{\mathbf{z}_k\}$ and δt only. The kernel of $\mathbf{L}$ is spanned by $\mathbf{u}^{(n,\omega)}$ and $\bar{\mathbf{u}}^{(n,\omega)}$, so we work relative to this basis and write $\mathbf{z}_j = a_j\mathbf{u}^{(n,\omega)} + \bar{a}_j\bar{\mathbf{u}}^{(n,\omega)}$.

The symmetry of our annular geometry allow us to eliminate $\bar{\mathbf{u}}^{(n,\omega)}$ through a reorientation of the zero of Θ (as we did in (4.36)). Thus we may assume without loss of generality that for all j,

$$\bar{a}_j = 0. \tag{4.90}$$

At the moment ϵ is an artificial small parameter indicating the distance from the buckling point. We could define ϵ by setting $t = t_{n,\omega} + \frac{1}{2}\epsilon^2\delta t$ in (4.37). However, as is common in buckling analyses, we choose to define ϵ to be the magnitude of the buckle in the direction of the eigenvector, so that $z_j = 0$ for $j > 1$, or equivalently $a_j = 0$ for $j > 1$ [10]. After these simplifications, the first Fredholm solvability condition

$$\iint_{V_m} \mathbf{P}_j^* : \nabla\mathbf{u}^{(n,\omega)} dV = 0 \tag{4.91}$$

translates to an equation of the form

$$g_j(a, \delta t, t_3, \ldots, t_j, \mathbf{u}^{(n,\omega)}, \mathbf{u}_2, \ldots, \mathbf{u}_{j-1}, \zeta_{\alpha,0}, \ldots, \zeta_{\alpha,j-1}) = 0, \tag{4.92}$$

for some function g_j. It can be shown that the second Fredholm solvability condition

$$\iint_{V_m} \mathbf{P}_j^* : \nabla\bar{\mathbf{u}}^{(n,\omega)} dV = 0 \tag{4.93}$$

is identically zero as a consequence of $\bar{a}_j = 0$. This can be proved by exploiting the symmetry of our annular geometry.

Leading Order Magnitude of the Buckle

We are now ready to determine the leading order of the magnitude of the buckle (i.e. a). Let $T_{n,\omega}$ be the set of all tensors of the form

$$\begin{pmatrix} X_{RR}\cos n\Theta\cos\omega Z & X_{R\Theta}\sin n\Theta\cos\omega Z & X_{RZ}\cos n\Theta\sin\omega Z \\ X_{\Theta R}\sin n\Theta\cos\omega Z & X_{\Theta\Theta}\cos n\Theta\cos\omega Z & X_{\Theta Z}\sin n\Theta\sin\omega Z \\ X_{ZR}\cos n\Theta\sin\omega Z & X_{Z\Theta}\sin n\Theta\sin\omega Z & X_{ZZ}\cos n\Theta\cos\omega Z \end{pmatrix}, \tag{4.94}$$

where $X_{\gamma\delta} \in L^2$. It can be seen that $\nabla \mathbf{u}^{(n,\omega)} \in T_{n,\omega}$.

The direct implication of the Trefftz condition (as explained in Section 4.1.1) is that

$$\iiint_{V_m} \frac{\partial \mathbf{P}}{\partial \mathbf{F}} : \nabla \mathbf{u}^{(n,\omega)} : \nabla \mathbf{w} dV = 0, \tag{4.95}$$

for any admissible $\mathbf{w} \in {}^a\mathbb{U}$, which means g_1 is identically zero. On substitution of $\mathbf{u}_1 = a\mathbf{u}^{(n,\omega)}$ into our definition of $\mathbf{P}_2^*$, we find that the mode (n,ω) component of $\mathbf{P}_2^*$ is $\mathbf{0}$, so that g_2 is also identically zero as a consequence of the symmetry of V_m. Incidentally, this is why we required the perturbation in t to be one order higher than the perturbation in $\mathbf{u}$. If they were of the same order, then g_2 would be of the form

$$g_2 = a \times \text{ constant } = 0, \tag{4.96}$$

since the projection of $\mathbf{P}_2^*$ onto $T_{n,\omega}$ is proportional to a. This is only satisfied (for nonzero a) in very particular circumstances (when the constant is zero), a case we do not worry about.

We thus need to consider g_3 to find a nontrivial governing condition for a. The $O(\epsilon^3)$ component of $\mathbf{P}$ is

$$\frac{1}{6}\mathbf{P}_3^* = \frac{1}{6}\frac{\partial^3 \mathbf{P}}{\partial \mathbf{F}^3} : \nabla \mathbf{u}_1 : \nabla \mathbf{u}_1 : \nabla \mathbf{u}_1 + \frac{1}{2}\frac{\partial^2 \mathbf{P}}{\partial \mathbf{F}^2} : \nabla \mathbf{u}_1 : \nabla \mathbf{u}_2 + \frac{1}{2}\frac{\partial^2 \mathbf{P}}{\partial \mathbf{F} \partial \zeta_\alpha} : \nabla \mathbf{u}_1 \zeta_{\alpha,2} + \frac{1}{6}\frac{\partial \mathbf{P}}{\partial \zeta_\alpha}\zeta_{\alpha,3}, \tag{4.97}$$

where we sum over α. We already have expressions for $\mathbf{u}_1$ (which is a multiple of the eigenmode) and $\zeta_{\alpha,2}$. We must still find expressions for $\mathbf{u}_2$ and $\zeta_{\alpha,3}$.

We use the Liapunov-Schmidt reduction to determine $\mathbf{u}_2$ as a function of a, δt, $\mathbf{u}^{(n,\omega)}$ and $\zeta_{\alpha,2}$. On solving $\nabla \cdot \mathbf{P}_2 = \mathbf{0}$, we find $\mathbf{u}_2 = a^2\mathbf{u}_2^a + \delta t \mathbf{u}_2^p$, where $\mathbf{u}_2^p$ and $\mathbf{u}_2^a$ are defined as follows

$$\begin{aligned}
\nabla \cdot \left(\frac{\partial \mathbf{P}}{\partial \mathbf{F}} : \nabla \mathbf{u}_2^a \right) &= -\nabla \cdot \left(\frac{\partial^2 \mathbf{P}}{\partial \mathbf{F}^2} : \nabla \mathbf{u}^{(n,\omega)} : \nabla \mathbf{u}^{(n,\omega)} \right), \\
\left(\frac{\partial \mathbf{P}}{\partial \mathbf{F}} : \nabla \mathbf{u}_2^a + \frac{\partial^2 \mathbf{P}}{\partial \mathbf{F}^2} : \nabla \mathbf{u}^{(n,\omega)} : \nabla \mathbf{u}^{(n,\omega)} \right) \cdot \mathbf{n} &= \mathbf{0} \text{ at } R = R_1, \\
\nabla \cdot \left(\frac{\partial \mathbf{P}}{\partial \mathbf{F}} : \nabla \mathbf{u}_2^p \right) &= -\nabla \cdot \frac{\partial \mathbf{P}}{\partial \zeta_\alpha}\zeta_{\alpha,2}^*, \\
\left(\frac{\partial \mathbf{P}}{\partial \mathbf{F}} : \nabla \mathbf{u}_2^p + \frac{\partial \mathbf{P}}{\partial \zeta}\zeta_{\alpha,2}^* \right) \cdot \mathbf{n} &= \mathbf{0} \text{ at } R = R_1,
\end{aligned} \tag{4.98}$$

where we sum over α and $\zeta_{\alpha,2} = \zeta^*_{\alpha,2}\delta t$. If the geometry is finite, the null-displacement outer boundary condition at R_2 is

$$\mathbf{u}_2^p = \mathbf{0}, \tag{4.99}$$

$$\mathbf{u}_2^a = \mathbf{0}. \tag{4.100}$$

For both types of infinite medium model we require $\mathbf{u}_2^a$ and its derivative with respect to R to converge to zero as $R \to \infty$. For model F (with decaying nutrient), we require $\mathbf{u}_2^p$ and its derivative to decay to zero as $R \to \infty$. For model G (a 'growing' annulus), we require the incremental stress to decay to zero, i.e.

$$\left(\frac{\partial \mathbf{P}}{\partial \mathbf{F}} : \nabla \mathbf{u}_2^p + \frac{\partial \mathbf{P}}{\partial \zeta_\alpha}\zeta^*_{\alpha,2}\right) \to 0.$$

The final variable we must determine is $\zeta_{\alpha,3}$. We recall from (4.71) that $\zeta_{\alpha,3} = \zeta_{\alpha,0}r_{\alpha,3}$ and

$$\epsilon^3\frac{1}{6}r_{\alpha,3} = \int_{t^*}^{t^*+0.5\epsilon^2\delta t} \epsilon G_{\alpha,0}\left(\frac{c_1}{k_c}\left(1+\frac{c_0}{k_c}\right)^{-2} - \mu_1\right) + \epsilon G_{\alpha,1}\left(\frac{c_0}{k_c+c_0} - \mu_0\right) dt \\ + \epsilon^3\frac{1}{6}G_{\alpha,0}\left(\frac{c_0}{k_c+c_0} - \mu_0\right) t_3. \tag{4.101}$$

The coefficient of t_3 is radially symmetric and therefore it contributes nothing to g_3 (which can be seen from an inspection of (4.91)).

The integral in (4.101) depends on the path taken by the solution in evolving from t^* to $t^* + \frac{1}{2}\epsilon^2\delta t$. The quasi-static assumption does not allow us to determine *a priori* the path that the sytem will take: for example it is theoretically possible that the system will always remain in the fundamental state, in which case the above integral is zero. This problem illustrates the dependence of our energy functional on the *deformation history*. The great majority of classical buckling problems, such as the Euler Strut, have an energy functional which is path independent.[4]

However we can determine an analytic expression for (4.101) if we assume that once the system adopts the buckled state, it remains in the buckled state. The justification of

[4]Interestingly, the leading order of the buckle in the Euler Strut is governed by the fourth order of the strain energy function just like our problem, as demonstrated by Antman in his perturbation expansion [10]. If one were to model a 'growing' Euler Strut, then one would arrive at the same problem as ours.

this assumption depends on the stability of the buckled state: a question we address in the following section. Thus we suppose that the system remains in the fundamental state up to $t + \frac{\epsilon^2}{2}\upsilon\delta t$, for some constant $0 \leq \upsilon \leq 1$, before it instantly adopts the buckled state. Our equations do not allow us to directly determine υ, so we consider it an unknown parameter to be stipulated. This assumption allows us to determine $\zeta_{\alpha,3}$, as follows. Since $\mathbf{u}_1 = a\mathbf{u}^{(n,\omega)}$, we may write the first order perturbations in the nutrient and growth anisotropy multipliers as

$$c_1 = a\mathbf{c}^{(n,\omega)},$$
$$G_{\alpha,1} = aG_{\alpha,1}^{(n,\omega)}.$$

The variables $\{c^{(n,\omega)}, G_{\alpha,1}^{(n,\omega)}\}$ may be obtained by substituting the eigenmode $\mathbf{u}^{(n,\omega)}$ into the definitions in (4.74) and (4.78). We consider a to be a function of δt, so that after switching the integrating variable from t to δt we may write (4.101) as

$$r_{\alpha,3} = 3\left(G_{\alpha,0}\left(\frac{c^{(n,\omega)}}{k_c}\left(1+\frac{c_0}{k_c}\right)^{-2} - \mu^{(n,\omega)}\right) + G_{\alpha,1}^{(n,\omega)}\left(\frac{c_0}{k_c+c_0} - \mu_0\right)\right) \times \int_{\upsilon\delta t}^{\delta t} a d(\delta t'). \tag{4.102}$$

After drawing all of the expressions in this section together, we obtain the following governing equation for a,

$$g_3\left(a(\delta t), \delta t\right) = C_1 a^3 + (\delta t)C_2 a + C_3 \int_{\upsilon\delta t}^{\delta t} a d(\delta t') = 0, \tag{4.103}$$

where

$$\begin{aligned}
C_1 &= \iiint_{V_m}\left(\frac{1}{6}\frac{\partial^3\mathbf{P}}{\partial\mathbf{F}^3} : \nabla\mathbf{u}^{(n,\omega)} : \nabla\mathbf{u}^{(n,\omega)} : \nabla\mathbf{u}^{(n,\omega)} + \frac{1}{2}\frac{\partial^2\mathbf{P}}{\partial\mathbf{F}^2} : \nabla\mathbf{u}^{(n,\omega)} : \nabla\mathbf{u}_2^a\right) : \nabla\mathbf{u}^{(n,\omega)} dV, \\
C_2 &= \iiint_{V_m}\left(\frac{1}{2}\frac{\partial^2\mathbf{P}}{\partial\mathbf{F}^2} : \nabla\mathbf{u}_2^p : \nabla\mathbf{u}^{(n,\omega)} + \frac{1}{2}\frac{\partial^2\mathbf{P}}{\partial\mathbf{F}\partial\zeta_\alpha} : \nabla\mathbf{u}^{(n,\omega)}\zeta_{\alpha,2}^*\right) : \nabla\mathbf{u}^{(n,\omega)} dV, \\
C_3 &= \frac{1}{2}\iiint_{V_m}\frac{\partial\mathbf{P}}{\partial\zeta_\alpha} : \nabla\mathbf{u}^{(n,\omega)}\zeta_{\alpha,0} \times \\
&\quad \left(G_{\alpha,0}\left(\frac{c^{(n,\omega)}}{k_c}\left(1+\frac{c_0}{k_c}\right)^{-2} - \mu^{(n,\omega)}\right) + G_{\alpha,1}^{(n,\omega)}\left(\frac{c_0}{k_c+c_0} - \mu_0\right)\right) dV,
\end{aligned} \tag{4.104}$$

and we sum over α. The roots of this cubic dictate the magnitude of the local equilibrium states. One of the roots is $a := 0$, corresponding to the unbuckled solution. Two other solutions of (4.103), are

$$a = \pm\sqrt{-\delta t\left(\frac{C_2}{C_1} + (1 - \upsilon^{\frac{3}{2}})\frac{2C_3}{3C_1}\right)}. \tag{4.105}$$

We have insisted that $a = 0$ when $\delta t = 0$. These roots are in fact identical: one buckled profile may be obtained by rotating the other buckled profile by an angle of $\frac{\pi}{n}$. The existence of local buckled equilibrium states requires the existence of a real solution for a. We defer discussion of this until after the next section, because we still need to formulate criteria governing the stability of the buckled equilibrium state.

We provide some commentary on the terms C_2 and C_3. It can be observed from the definition that C_2 is

$$C_2 = \frac{1}{2}\frac{\partial}{\partial t}\iiint_{V_m} \frac{\partial^2 \psi}{\partial \mathbf{F}^2} : \nabla \mathbf{u}^{(n,\omega)} : \nabla \mathbf{u}^{(n,\omega)} dV. \tag{4.106}$$

Since by definition

$$\iiint_{V_m} \frac{\partial^2 \psi}{\partial \mathbf{F}^2} : \nabla \mathbf{u}^{(n,\omega)} : \nabla \mathbf{u}^{(n,\omega)} dV > 0, \tag{4.107}$$

for all times less than the critical time, and the integral is equal to zero at the critical time, it follows that

$$C_2 \leq 0. \tag{4.108}$$

In almost every case we expect $C_2 < 0$. If $C_2 < 0$, then

$$\iiint_{V_m} \frac{\partial^2 \psi}{\partial \mathbf{F}^2} : \nabla \mathbf{u}^{(n,\omega)} : \nabla \mathbf{u}^{(n,\omega)} dV < 0 \tag{4.109}$$

for small increments of time beyond the critical time of buckling, which means that the fundamental solution is unstable to mode (n, ω) buckles for small increments of time beyond the critical time. The term C_3 is usually negative and represents a feedback effect. Cells near an 'inward' part of the buckle receive more of the nutrient and are therefore more likely to proliferate and accentuate the buckle. See Figure 4.1 for a diagram explaining this effect. If we are including anisotropic growth effects in our model, then the term also incorporates changes in the direction of growth due to the buckle. We discuss this effect in Sections 9.7

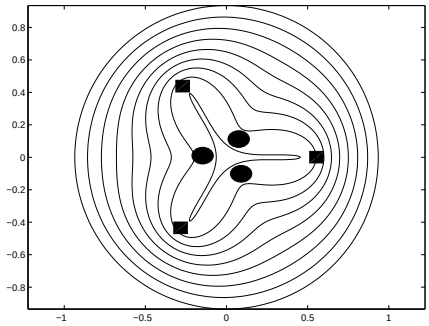

Figure 4.1: The feedback effects of buckling on growth, as represented by the term C_3 in (4.104). The lines represent contours of constant R (in Lagrangian coordinates). The cells positioned near the ellipses will receive more nutrient due to the buckle, and are therefore more likely to proliferate. The increased proliferation of these cells leads to more compressive pressure that accentuates the buckle. Cells positioned near the squares receive less nutrient due to the buckle, and are therefore less likely to proliferate. Similarly, if we are incorporating anisotropic growth in our model, the buckle relaxes the compressive stress tangential to the surface at the ellipses, which encourages more proliferation in this direction and accentuates the buckle.

and 9.8 of our results.

4.2.4 Stability of the Buckled State

Before we discuss the stability of buckled equilibrium states, we must assume that such states exist. That is, we assume the perturbation expansion of the previous section is valid and there exists a solution $a \in \mathbb{R}$ to (4.105). However this state could be unstable to further small perturbations in the displacement. In this section we derive an explicit expression governing the mechanical stability of the buckled equilibrium state. We have adapted the method of Koiter [86].

Mechanical Stability of the Buckled State

We investigate the *mechanical* stability of the buckled equilibrium state. To do this we consider the variation in the strain energy for a small admissible variation $\mathbf{v} \in {}^{a}\mathbb{U}$ of the displacement about the state of incremental mechanical equilibrium (State II). That is, we superpose the variation $\mathbf{v}$ on the displacement field $(\mathbf{u}_0 + \mathbf{u})$. We consider the other parameters $\{t, c, \zeta_\alpha\}$ to be fixed. Our fundamental reason for this, as we argued in Section 4.1.1, is that the elastic response timescale is faster than the diffusive and growth timescales.

We need to consider the sign of the change in energy

$$\triangle W = W\left(\mathbf{u}_0 + \mathbf{w}\right) - W\left(\mathbf{u}_0 + \mathbf{u}\right), \tag{4.110}$$

where $\mathbf{w} = \mathbf{u} + \mathbf{v}$. We search for the variation $\mathbf{v}$ which minimises (4.110). If there is a minimising variation which makes the variation of the strain energy $\triangle\psi(\mathbf{v})$ negative, the system is mechanically unstable. Otherwise the system is mechanically stable. We decompose $\mathbf{v}$ and $\mathbf{w}$ into perturbation expansions

$$\mathbf{v} = \epsilon\mathbf{v}_1 + \frac{1}{2}\epsilon^2\mathbf{v}_2 + \ldots, \tag{4.111}$$

so that $\mathbf{w}_j = \mathbf{v}_j + \mathbf{u}_j$. Because the buckled state is in equilibrium, the contribution of the first order terms (in ϵ) to the total energy is zero. We find that the $O(\epsilon^2)$ and $\mathrm{O}(\epsilon^3)$ components of the energy are respectively

$$\mathrm{O}(\epsilon^2):\ W_2^{(n,\omega)} = \iiint_{V_m} \frac{1}{2}\frac{\partial^2\psi}{\partial\mathbf{F}^2} : \nabla\mathbf{v}_1 : \nabla\mathbf{v}_1 dV \text{ and} \tag{4.112}$$

$$\begin{aligned}\mathrm{O}(\epsilon^3):\ W_3^{(n,\omega)} &= \iiint_{V_m} \frac{1}{2}\frac{\partial^2\psi}{\partial\mathbf{F}^2} : \nabla\mathbf{w}_1 : \nabla\mathbf{w}_2 - \frac{1}{2}\frac{\partial^2\psi}{\partial\mathbf{F}^2} : \nabla\mathbf{u}_1 : \nabla\mathbf{u}_2 dV \\ &+ \iiint_{V_m} \frac{1}{6}\frac{\partial^3\psi}{\partial\mathbf{F}^3} : \nabla\mathbf{w}_1 : \nabla\mathbf{w}_1 : \nabla\mathbf{w}_1 - \frac{1}{6}\frac{\partial^3\psi}{\partial\mathbf{F}^3} : \nabla\mathbf{u}_1 : \nabla\mathbf{u}_1 : \nabla\mathbf{u}_1 dV \\ &+ \iiint_{V_m} \frac{1}{2}\frac{\partial^2\psi}{\partial\mathbf{F}\partial\zeta_\alpha} : \nabla w_1\zeta_{\alpha,2} - \frac{1}{2}\frac{\partial^2\psi}{\partial\mathbf{F}\partial\zeta_\alpha} : \nabla u_1\zeta_{\alpha,2} dV,\end{aligned} \tag{4.113}$$

where we sum over α, and the derivatives in $\mathbf{F}$ and ζ_α are evaluated at the fundamental state and at the critical time. We have simplified the $O(\epsilon^2)$ equations using the fact $\mathbf{u}_1 = a\mathbf{u}^{(n,\omega)}$ and the identity

$$\iiint_{V_m} \frac{\partial^2\psi}{\partial\mathbf{F}^2} : \nabla\mathbf{u}^{(n,\omega)} : \nabla\mathbf{x} dV = 0, \tag{4.114}$$

for all admissible variations $\mathbf{x}$, which is a direct consequence of the Trefftz Condition (4.11).

If (n,ω) is the *first* mode to go unstable, then it follows from the Trefftz Condition that

$$\iiint_{V_m} \frac{1}{2}\frac{\partial^2\psi}{\partial\mathbf{F}^2} : \nabla\mathbf{v}_1 : \nabla\mathbf{v}_1 dV > 0, \tag{4.115}$$

as long as $\mathbf{v}_1$ is not an eigenmode. If $\mathbf{v}_1$ is an eigenmode then the above integral is zero. Since we are searching for the $\mathbf{v}_1$ which minimises the energy, we must set $\mathbf{v}_1 = \delta a\mathbf{u}^{(n,\omega)}$,

with δa thus far undetermined.

On the other hand, if (n, ω) is not the first mode to go unstable then (4.112) is less than zero for unstable modes. In this case, (4.112) reveals that the buckled equilibrium state is unstable for ϵ sufficiently small. Despite this fact, we argue that the system might still adopt this equilibrium state, for the following reasons. Our fundamental reason is that there may be small inhomogeneities which dispose the system more towards mode (n, ω) perturbations than other modes. Since the critical times of the different modes are highly clustered (a fact which may be seen from the results in Chapter 8), the small inhomogeneities may be sufficiently large that the system preferences mode (n, ω) over the other modes. In fact the critical times asymptote to a finite limit: we determine this asymptotic limit using a boundary layer analysis in Chapter 6. Moreover it can be shown using a perturbation expansion that the energetic differences of the modes are similarly clustered, so that if mode (n_2, ω_2) goes unstable at time t_{n_2,ω_2} with eigenmode $\mathbf{u}^{(n_2,\omega_2)}$, then at time t

$$\iiint_{V_m} \frac{\partial^2 \psi}{\partial \mathbf{F}^2} : \nabla \mathbf{u}^{(n_2,\omega_2)} : \nabla \mathbf{u}^{(n_2,\omega_2)} dV \simeq O\left(t - t_{n_2,\omega_2}\right). \tag{4.116}$$

The other major reason we are interested in buckled modes which are not the first to go unstable is that usually the modes which go unstable first have a very fine wavelength. We argue in Section 8.1 that our continuum approximation is invalid for these wavelengths, since we expect fine oscillations to be dissipated by the cellular phase.

To be consistent with our assumption that small inhomogeneities dictate that the sytem prefers buckles in $U_{n,\omega}$, we must restrict $\mathbf{v}_1$ to be in $U_{n,\omega}$ when testing the stability of the buckle. However since v_1 is defined to be a stationary point, it follows that $v_1 = \delta a \mathbf{u}^{(n,\omega)}$. It follows that (4.112) is identically zero and we must consider the higher order terms in the energy to assess the stability of the buckled equilibrium state.

The $\mathrm{O}(\epsilon^3)$ component of the variation in the strain energy (4.113) is zero for the following reasons. The first two terms are zero because of (4.114). The last two terms are zero because of the annular symmetry of V_m. We thus need to consider the $\mathrm{O}(\epsilon^4)$ component of $\triangle W$ to

investigate the stability of the buckled equilibrium state, i.e.

$$W_4^{(n,\omega)} = \iiint_{V_m} \frac{1}{4}\frac{\partial^3\psi}{\partial\mathbf{F}^3} : (\nabla\mathbf{w}_1) : (\nabla\mathbf{w}_1) : (\nabla\mathbf{w}_2) + \frac{1}{8}\frac{\partial^2\psi}{\partial\mathbf{F}^2} : (\nabla\mathbf{w}_2) : (\nabla\mathbf{w}_2)$$
$$+ \frac{1}{4}\frac{\partial^2\psi}{\partial\mathbf{F}\partial\zeta_\alpha} : (\nabla\mathbf{w}_2)\,\zeta_{\alpha,2} + \frac{1}{4}\frac{\partial^2\psi}{\partial\mathbf{F}\partial\zeta_\alpha} : (\nabla\mathbf{w}_1) : (\nabla\mathbf{w}_1)\,\zeta_{\alpha,2}$$
$$+\frac{1}{24}\frac{\partial^4\psi}{\partial\mathbf{F}^4} : (\nabla\mathbf{w}_1) : (\nabla\mathbf{w}_1) : (\nabla\mathbf{w}_1) : (\nabla\mathbf{w}_1)+\frac{1}{6}\frac{\partial^2\psi}{\partial\mathbf{F}^2} : \nabla\mathbf{w}_3 : \nabla\mathbf{w}_1+\frac{1}{6}\frac{\partial^2\psi}{\partial\mathbf{F}\partial\zeta_\alpha} : \nabla\mathbf{w}_1\zeta_{\alpha,3}dV, \tag{4.117}$$

where we sum over α.

The term with $\mathbf{w}_3$ integrates to zero as it is in the form of (4.114). To minimise (4.117) we use the following technique of Koiter [86]. We fix $\mathbf{w}_1$ and set $\mathbf{w}_2$ to extremise (4.117). The Euler-Lagrange equations we obtain upon doing this are of the same form as the equations defining $\mathbf{u}_2$ obtained using the Liapunov-Schmidt reduction, except the coefficient of $\mathbf{u}_1$ is now $(a + \delta a)$. If (n, ω) is the first mode to buckle then this extremum will be a global minimum because the quadratic is positive semi-definite. However this extremum will not be a minimum, but rather a saddle point, if (n, ω) is not the first mode to buckle. However, as we have already argued above, we are assuming that local inhomogeneities dictate that the system will not buckle in the direction of an unstable mode, and we saw in (4.116) that the energetic incentive encouraging this type of buckling is relatively weak.

We thus find

$$\mathbf{w}_2 = (a + \delta a)^2\mathbf{u}_2^a + \mathbf{u}_2^p, \tag{4.118}$$

where $\mathbf{u}_2^a$ and $\mathbf{u}_2^p$ are defined in (4.98). We make use of the following Lemma from Koiter [86]. Consider the functional $F_2[\mathbf{w}] + F_1[\mathbf{w}]$, where F_2 is quadratic and positive semi-definite and F_1 is linear. The value of the functional at its minimum $\mathbf{w}^*$ (obtained through solution of the Euler-Lagrange equations) is $-F_2[\mathbf{w}^*]$. Accordingly the value of (4.117) at its minimum

(with respect to $\mathbf{w}_2$) is

$$\bar{W}_4^{(n,\omega)} = \iiint_{V_m} -\frac{1}{8}\frac{\partial^2\psi}{\partial\mathbf{F}^2} : \left((a+\delta a)^2\nabla\mathbf{u}_2^a + \nabla\mathbf{u}_2^p\right) : \left((a+\delta a)^2\nabla\mathbf{u}_2^a + \nabla\mathbf{u}_2^p\right) + \frac{(a+\delta a)^4}{24}\frac{\partial^4\psi}{\partial\mathbf{F}^4} : \nabla\mathbf{u}^{(n,\omega)} : \nabla\mathbf{u}^{(n,\omega)} : \nabla\mathbf{u}^{(n,\omega)} : \nabla\mathbf{u}^{(n,\omega)} + \frac{(a+\delta a)^2}{4}\frac{\partial^3\psi}{\partial\mathbf{F}^2\partial\zeta_\alpha} : \nabla\mathbf{u}^{(n,\omega)} : \nabla\mathbf{u}^{(n,\omega)}\zeta_{\alpha,2} + \frac{(a+\delta a)}{6}\frac{\partial^2\psi}{\partial\mathbf{F}\partial\zeta_\alpha} : \nabla\mathbf{u}^{(n,\omega)}\zeta_{\alpha,3}dV. \quad (4.119)$$

However the magnitude of $\mathbf{w}_1$, which is governed by the parameter δa is undetermined. To find the minimum, we differentiate the above with respect to δa and set the resulting expression to zero. Before we differentiate, it is important to note that $\zeta_{\alpha,3}$ is independent of δa.[5] It depends on the history of the deformation between $t^* + \frac{\epsilon^2}{2}\delta t^*$ and $t^* + \frac{1}{2}\epsilon^2\delta t$, but not on the instantaneous perturbation δa.

After setting the derivative of (4.119) with respect to δa to 0, we find that $\delta a = 0$ at the extremum, which is in agreement with the condition for the existence of an equilibrium we derived in the previous section (4.103). The equivalence of the expressions derives from the following identities (which directly follow from the definitions of $\mathbf{u}_2^a$ and $\mathbf{u}_2^p$),

$$\iiint_{V_m} \frac{\partial^2\psi}{\partial\mathbf{F}^2} : \nabla\mathbf{u}_2^a : \nabla\mathbf{u}_2^a + \frac{\partial^3\psi}{\partial\mathbf{F}^3} : \nabla\mathbf{u}^{(n,\omega)} : \nabla\mathbf{u}^{(n,\omega)} : \nabla\mathbf{u}_2^a dV = - \iiint_{V_m} \mathbf{u}_2^a . \left(\nabla\cdot\left(\frac{\partial^2\psi}{\partial\mathbf{F}^2} : \nabla\mathbf{u}_2^a + \frac{\partial^3\psi}{\partial\mathbf{F}^3} : \nabla\mathbf{u}^{(n,\omega)} : \nabla\mathbf{u}^{(n,\omega)}\right)\right) + \iint_{\partial V_m} \mathbf{u}_2^a . \left(\left(\frac{\partial^2\psi}{\partial\mathbf{F}^2} : \nabla\mathbf{u}_2^a + \frac{\partial^3\psi}{\partial\mathbf{F}^3} : \nabla\mathbf{u}^{(n,\omega)} : \nabla\mathbf{u}^{(n,\omega)}\right)\cdot\mathbf{n}\right) dA = 0.$$

and

$$\iiint_{V_m} \frac{\partial^2\psi}{\partial\mathbf{F}^2} : \nabla\mathbf{u}_2^p : \nabla\mathbf{u}_2^a + \frac{\partial^3\psi}{\partial\mathbf{F}^3} : \nabla\mathbf{u}^{(n,\omega)} : \nabla\mathbf{u}^{(n,\omega)} : \nabla\mathbf{u}_2^p dV = 0. \quad (4.120)$$

This equilibrium is a local minimum, and hence is stable, with respect to variations of $\mathbf{w}_2$ which are perpendicular to the unstable modes (recall that, as explained above, we are not considering the unstable modes). We only need to investigate the stability of the local minimum with respect to variations in the direction of the eigenmode. Thus we differentiate

[5] Refer to Section 4.2.3 where we discuss this.

again with respect to δa and evaluate at $\delta a = 0$, obtaining the expression

$$\frac{\partial^2 \bar{W}_4^{(n,\omega)}}{\partial \delta a^2} = \iiint_{V_m} a^2 \left(\frac{1}{2} \frac{\partial^3 \mathbf{P}}{\partial \mathbf{F}^3} : \nabla \mathbf{u}^{(n,\omega)} : \nabla \mathbf{u}^{(n,\omega)} : \nabla \mathbf{u}^{(n,\omega)} + \frac{3}{2} \frac{\partial^2 \mathbf{P}}{\partial \mathbf{F}^2} : \nabla \mathbf{u}^{(n,\omega)} : \nabla \mathbf{u}_2^a \right) : \nabla \mathbf{u}^{(n,\omega)} + \left(\frac{1}{2} \frac{\partial^2 \mathbf{P}}{\partial \mathbf{F}^2} : \nabla \mathbf{u}_2^p : \nabla \mathbf{u}^{(n,\omega)} + \frac{1}{2} \frac{\partial^2 \mathbf{P}}{\partial \mathbf{F} \partial \zeta_\alpha} : \nabla \mathbf{u}^{(n,\omega)} \zeta_{\alpha,2} \right) : \nabla \mathbf{u}^{(n,\omega)} dV = 3C_1 a^2 + (\delta t) C_2, \tag{4.121}$$

where C_1 and C_2 are defined in (4.104) and we sum over α.

We have obtained our desired expression (4.121) governing the stability of the buckle: if $\frac{\partial^2 \bar{W}_4^{(n,\omega)}}{\partial \delta a^2}$ is greater than zero then the buckled equilibrium state is stable, and if it is less than zero the buckled state is unstable.

4.2.5 Criteria for the Existence and Stability of Buckled Equilibrium State

We are now in a position to formulate an explicit method for evaluating whether a stable mode (n, ω) buckled equilibrium state exists. We are only interested in the existence of such a state for a positive increment in time $\delta t > 0$ - a situation known as a *supercritical* bifurcation. We firstly recap our results thus far. We have seen that if a stable buckled equilibrium state exists, then the magnitude of the buckle is

$$a = \pm \sqrt{-\delta t \frac{C_2}{C_1} - (\delta t - \delta t^*) \frac{2C_3}{3C_1}}, \tag{4.122}$$

where the system first adopts the buckled equilibrium state at time $t + \frac{1}{2}\epsilon^2 \delta t^*$ (that is, we have defined $\delta t^* = \upsilon^{\frac{3}{2}} \delta t$). We cannot determine δt^* *a priori* from the equation of equilibrium. In (4.121) we see that the stability of the buckled equilibrium state is given by the sign of

$$\frac{\partial^2 \bar{W}_2^{(n,\omega)}}{\partial \delta a^2} = 3C_1 a^2 + \delta t C_2. \tag{4.123}$$

In (4.108) we saw that

$$C_2 \leq 0. \tag{4.124}$$

From (4.123) and (4.124) we infer that it is necessary that $C_1 \geq 0$ for a supercritical buckled equilibrium state to be stable. If $C_1 < 0$ we expect the system to move outside the regime of accuracy of our perturbation expansion at the critical time. If $C_1 = 0$ we need to consider higher order terms in the perturbation expansion; a case we do not worry about. Otherwise if $C_1 > 0$ (which we assume for the rest of this discussion), we infer that we can solve (4.122) for $a \in \mathbb{R}$ if $\delta t^* = \delta t$. Furthermore on substituting this expression for a back into (4.123) we see that (4.123) is equal to

$$-2(\delta t C_2 + (\delta t - \delta t^*)C_3), \tag{4.125}$$

which is greater than zero when $\delta t = \delta t^*$. This means that if the system remains in the fundamental state up until time $t + \frac{\epsilon^2}{2}\delta t$ before instantly jumping to the buckled state, then the buckled state is stable at that instant.

We now consider when $\delta t^* < \delta t$. We have seen that initially the buckled state is stable when $\delta t = \delta t^*$. We must consider the effect of the feedback term C_3 on the buckled state. If

$$\frac{2C_3}{3} > -C_2, \tag{4.126}$$

then as δt increases the feedback term forces the buckle to smoothly shrink back to the unbuckled state. Note that if the difference between the terms in (4.126) is not great then the system could leave the regime of accuracy of the perturbation expansion before this occurs. If $\frac{2C_3}{3} = -C_2$ we need to consider higher order terms - a situation we do not worry about. If

$$-C_2 > \frac{2C_3}{3} > 0, \tag{4.127}$$

then the feedback term reduces the magnitude of the buckle, but the buckle continues to grow in size. If

$$C_3 < 0, \tag{4.128}$$

the feedback term accentuates the magnitude of the buckle. We have already noted that we almost always (4.128) to occur in our results, i.e. in general we expect the feedback terms to accentuate the magnitude of the buckle. If $C_2 + C_3 > 0$ then eventually the buckle destabilises because (4.125) becomes negative. However as long as $C_3 < 0$ we do not worry about this occurring as $C_2 < 0$ too.

To anticipate our results in coming chapters, we generally find $|C_3| \ll |C_2|$, so that the path dependent effects are reasonably negligible. As stated earlier, we cannot determine δt^* *a priori*. However if $C_1 < 0$ and either (4.127) or (4.128) hold, then unless there are good reasons to think otherwise, we assume the system immediately adopts the buckled configuration (i.e. $\delta t^* = \upsilon = 0$).

4.3 Summary of Key Results

In this chapter we analysed the onset of buckling in the system without a differentiated capillary wall structure. We applied the Trefftz Condition to find a condition governing the onset of buckling for each wavenumber. For each set of wavenumbers (n, ω), at the time of buckling we performed a perturbation expansion to investigate the evolution of the buckled state. In particular, we employed the Liapunov-Schmidt reduction to obtain the leading order terms in the buckled displacement. We obtained specific criteria governing the stability of the buckled state through an investigation of its potential energy.

Chapter 5

Onset of Buckling in Model with Distinct Capillary Wall Structure

In this chapter we investigate the stability of the composite system. We include the growing tumour and also a distinct capillary wall structure. The mathematics of this chapter is thus very similar to the mathematics of Chapter 4, and we do not provide too many details. The equations governing the stability and postbuckling behaviour have the same form as Chapter 4. The major difference is that the domain of definition of the variables is extended to include the capillary wall.

The reference configuration of the tumour body is denoted by V_m and the reference configuration of the capillary wall is V_c. We let R_0 be the inner radius of the capillary, R_1 the outer radius of the capillary, and in the case of a finite geometry, we let R_2 be

Key	Geometry	Description
A	Finite	Null Displacement and zero nutrient flux at $R = R_2$.
C	Infinite	$[R_2, \infty)$ is linearly elastic, zero nutrient flux at $R = R_2$.
F	Infinite	Nutrient Distribution and Displacement decay to 0 as $R \to \infty$.
G	Infinite	$\frac{\partial c}{\partial R} = 0$ at $R = R_2$ and $c(R) = c(R_2)$ for $R > R_2$. $\mathbf{P} \to \mathbf{0}$ as $R \to \infty$.

Table 5.1: The various boundary conditions and geometries. The inner radius of the capillary wall is R_0 and the outer radius of the capillary wall is R_1. If the geometry is finite, the outer radius of the tumour annulus is R_2. The axial displacement u_z is zero at $Z = 0$ and $Z = Z_0$. At $R = R_1$, we equate the traction and displacement, i.e. $\mathbf{u}|_- = \mathbf{u}|_+$ and $\mathbf{P}|_- \cdot \mathbf{n} = \mathbf{P}|_+ \cdot \mathbf{n}$. The (scaled) nutrient concentration at R_1 is $n = 1$. There is no traction at R_0, i.e. $\mathbf{P} \cdot \mathbf{n} = \mathbf{0}$.

the outer radius of the tumour. As previously, we work in cylindrical coordinates, and naturally extend the domain of definition of variables defined over V_m in Chapter 4 to V_c. As previously, we assume the system is initially radially symmetric. This state is denoted State I. We will use the Trefftz criterion to determine when State I becomes unstable.

We briefly review our model of the mechanical structure of the capillary. Recall that the capillary is modelled as an incompressible Neo-Hookean material, with strain energy per reference configuration volume and first Piola-Kirchhoff stress given by

$$\psi = \frac{G_c}{2}\left(\mathbf{F}:\mathbf{F}-3\right) - p(J-1), \tag{5.1}$$

$$\mathbf{P} = G_c\mathbf{F} - pJ\mathbf{F}^{-T}. \tag{5.2}$$

Here p is the Lagrange Multiplier corresponding to the incompressibility constraint $J = 1$. The boundary conditions at R_1 and R_0 are

$$\begin{aligned} \mathbf{P}|_{R_1}^{-} \cdot \mathbf{n} =& \mathbf{P}|_{R_1}^{+} \cdot \mathbf{n}, \\ u|_{R_1}^{-} =& u|_{R_1}^{+}, \\ \mathbf{P}|_{R_0} \cdot \mathbf{n} =& \mathbf{0}, \end{aligned} \tag{5.3}$$

where $\mathbf{n} = -\mathbf{e}_R$ is the unit normal at both R_1 and R_0. The boundary conditions at R_1 are necessary for continuity of the stress and traction at the interface of the capillary wall and tumour.

We assume the solution in State I is purely radial. Over V_m and V_c the displacement is hence given by $u_0(R)\mathbf{e}_R$. The Lagrange multiplier in State I is $p_0(R)$. To find the solution in State I we solve the force balance equation and incompressibility constraint simultaneously with the force balance equation over the tumour matrix, i.e.

$$\begin{aligned} \nabla \cdot \mathbf{P}_0 =& \mathbf{0}, \\ J_0 =& \left(1 + \frac{u_0}{R}\right)\left(1 + \frac{\partial u_0}{\partial R}\right) = 1, \end{aligned} \tag{5.4}$$

with boundary conditions given in (5.3).

5.1 Implementation of Trefftz Condition

The implementation of the Trefftz Condition for the composite system is essentially the same as for the homogeneous system of the previous chapter. We consider the total displacement to be of the form $\mathbf{u}_0 + \mathbf{u}$ and the Lagrange Multiplier to be of the form $p_0 + \delta p$, where $\mathbf{u}$ and δp are small.

We require $(\mathbf{u}, \delta p)$ to be *admissible*, meaning that it satisfies the following criteria. The variation $\mathbf{u}$ must be a member of the Sobolev space $W^{1,1}(V_c \cup V_m)$ and the increment in the Lagrange Multiplier δp must be in $L^2(V_c)$. The following boundary conditions must also be satisfied (for an explanation of the boundary conditions refer to Section 2.2). The increment in the null-stress boundary condition at the inner boundary $R = R_0$ is

$$\left(\frac{\partial \mathbf{P}}{\partial \mathbf{F}} : \nabla \mathbf{u} + \frac{\partial \mathbf{P}}{\partial p}\delta p\right) \cdot \mathbf{n} = \mathbf{0}, \tag{5.5}$$

where $\mathbf{n} = -\mathbf{e}_R$ is the unit normal. At the interface of V_c and V_m at $R = R_1$,

$$\mathbf{u}|_- = \mathbf{u}|_+ \text{ and} \tag{5.6}$$

$$\left(\frac{\partial \mathbf{P}}{\partial \mathbf{F}} : \nabla \mathbf{u} + \frac{\partial \mathbf{P}}{\partial p}\delta p\right)|_- \cdot \mathbf{n} = \left(\frac{\partial \mathbf{P}}{\partial \mathbf{F}} : \nabla \mathbf{u}\right)|_+ \cdot \mathbf{n}. \tag{5.7}$$

The displacement u must satisfy the first order increment in the incompressibility condition over V_c,

$$\frac{\partial J}{\partial \mathbf{F}} : \nabla \mathbf{u} = J_0 \mathbf{F}_0^{-T} : \nabla \mathbf{u} = 0. \tag{5.8}$$

and

$$u_z = 0 \text{ at the axial boundaries of the annulus at } Z = 0 \text{ and } Z = Z_0. \tag{5.9}$$

For the models with an infinite geometry, we require $\mathbf{u}, \delta p \to \mathbf{0}$ as $R \to \infty$ (refer to Table 5.1 for an explanation of the model variants). For model A, we require at $R = R_2$,

$$\mathbf{u} = \mathbf{0}. \tag{5.10}$$

For model C, the increment in the traction and displacement must be equal either side of

R_2, i.e.

$$\left(\frac{\partial \mathbf{P}}{\partial \mathbf{F}} : \nabla \mathbf{u}|_+\right) \cdot \mathbf{n} = \left(\frac{\partial \mathbf{P}}{\partial \mathbf{F}} : \nabla \mathbf{u}|_-\right) \cdot \mathbf{n}, \tag{5.11}$$

$$\mathbf{u}|_+ = \mathbf{u}|_-. \tag{5.12}$$

We denote the set of all admissible $(\mathbf{u}, \delta p)$ by ${}^a\mathbb{U}$.

We begin our implementation of the Trefftz condition by Taylor expanding the strain energy density of the capillary about State I to obtain the energy of State II, i.e.

$$\psi[\mathbf{F}] - \psi[\mathbf{F}_0] = (\nabla \mathbf{u}) : {}^{(I)}\mathbf{P} + \frac{\partial \psi}{\partial p}\delta p + \frac{1}{2}\nabla \mathbf{u} : \left(\frac{\partial \mathbf{P}}{\partial \mathbf{F}} : \nabla \mathbf{u}\right) + \frac{\partial^2 \psi}{\partial \mathbf{F} \partial p} : \nabla \mathbf{u} \delta p, \tag{5.13}$$

where we have neglected higher order terms. Note that $\frac{\partial^2 \psi}{\partial p^2} = 0$. We find the quadratic component of the change in energy from State I to State II to be

$$\begin{aligned} W_2 = \iiint_{V_m} -\mathbf{u}.\left(\frac{1}{2}\left(\nabla \cdot \frac{\partial \mathbf{P}}{\partial \mathbf{F}} : \nabla \mathbf{u}\right)\right) dV \\ \iiint_{V_c} -\mathbf{u}.\left(\nabla \cdot \left(\frac{1}{2}\frac{\partial \mathbf{P}}{\partial \mathbf{F}} : \nabla \mathbf{u} + \frac{\partial \mathbf{P}}{\partial p}\delta p\right)\right) dV \\ + \iint_{\partial V_m} \left(\left(\frac{1}{2}\left(\frac{\partial \mathbf{P}}{\partial \mathbf{F}} : \nabla \mathbf{u}\right)\right) \cdot \mathbf{n}\right) \cdot \mathbf{u} dA \\ + \iint_{\partial V_c} \left(\left(\frac{1}{2}\left(\frac{\partial \mathbf{P}}{\partial \mathbf{F}} : \nabla \mathbf{u} + \frac{\partial \mathbf{P}}{\partial p}\delta p\right)\right) \cdot \mathbf{n}\right) \cdot \mathbf{u} dA, \end{aligned} \tag{5.14}$$

where we have applied the product rule and divergence theorem. To implement the Trefftz condition (which was outlined in Section 4.1.1), we take the first variation of (5.14) in the direction $(\tilde{\mathbf{u}}, \delta\tilde{p}) \in {}^a\mathbb{U}$. If the geometry of the tumour is finite, with outer radius R_2, we find

$$\begin{aligned} \frac{\partial W_2}{\partial \mathbf{u}} \cdot \tilde{\mathbf{u}} + \frac{\partial W_2}{\partial p}\delta\tilde{p} = -\iiint_{V_m} \tilde{\mathbf{u}}.\left(\nabla \cdot \left(\frac{\partial \mathbf{P}}{\partial \mathbf{F}} : \nabla \mathbf{u}\right)\right) dV \\ - \iiint_{V_c} \tilde{\mathbf{u}}.\left(\nabla \cdot \left(\frac{\partial \mathbf{P}}{\partial \mathbf{F}} : \nabla \mathbf{u} + \frac{\partial \mathbf{P}}{\partial p}\delta p\right)\right) + \delta\tilde{p}\frac{\partial^2 \psi}{\partial \mathbf{F} \partial p} : \nabla \mathbf{u} dV \\ + \iint_{\partial V_m} \tilde{\mathbf{u}}.\left(\left(\frac{\partial \mathbf{P}}{\partial \mathbf{F}} : \nabla \mathbf{u}\right) \cdot \mathbf{n}\right) dA + \iint_{\partial V_c} \tilde{\mathbf{u}}.\left(\left(\frac{\partial \mathbf{P}}{\partial \mathbf{F}} : \nabla \mathbf{u} + \frac{\partial \mathbf{P}}{\partial p}\delta p_u\right) \cdot \mathbf{n}\right) dA \end{aligned} \tag{5.15}$$

where $\mathbf{n}$ is the unit normal. We have made use of the fact that $\frac{\partial \mathbf{P}}{\partial \mathbf{F}} : \nabla \mathbf{u} : \nabla \tilde{\mathbf{u}} = \frac{\partial \mathbf{P}}{\partial \mathbf{F}} : \nabla \tilde{\mathbf{u}} : \nabla \mathbf{u}$, which derives from the fact $\mathbf{P}$ is the derivative of a potential ψ. The boundary integral is zero as a consequence of $(\tilde{\mathbf{u}}, \delta\tilde{p}), (\mathbf{u}, \delta p) \in {}^a\mathbb{U}$. The coefficient of $\delta\tilde{p}$ is the incompressibility condition (5.8) and hence is identically zero. It follows that in order that (5.15) is zero for all admissible $(\tilde{\mathbf{u}}, \delta\tilde{p})$, the incremental displacement $\mathbf{u}$ must satisfy

$$\nabla \cdot \left(\frac{\partial \mathbf{P}}{\partial \mathbf{F}} : \nabla \mathbf{u} \right) = \mathbf{0} \text{ in } V_m, \tag{5.16}$$

$$\nabla \cdot \left(\frac{\partial \mathbf{P}}{\partial \mathbf{F}} : \nabla \mathbf{u} + \frac{\partial \mathbf{P}}{\partial p} \delta p \right) = \mathbf{0} \text{ in } V_c, \tag{5.17}$$

$$\frac{\partial^2 \psi}{\partial \mathbf{F} \partial p} : \nabla \mathbf{u} = \mathbf{F}_0^{-T} : \nabla \mathbf{u} = 0 \text{ in } V_c. \tag{5.18}$$

The field equations (5.16)-(5.18) together with the admissibility boundary conditions constitute a linear boundary value problem governing the stability of the system: the existence of a solution indicates the onset of buckling.

5.1.1 Fourier Decomposition

As in Section 4.1.2, we stipulate $\mathbf{u}$ and p to be of a particular Fourier mode (n, ω). Let $p = X_{n,\omega} \cos(n\Theta) \cos(\omega Z)$ and $\mathbf{u} = \mathbf{u}^{(n,\omega)}$, where

$$u_r^{(n,\omega)} = W_{n,\omega}(R) \cos(n\Theta) \cos(\omega Z), \tag{5.19}$$

$$u_\theta^{(n,\omega)} = V_{n,\omega}(R) \sin(n\Theta) \cos(\omega Z), \tag{5.20}$$

$$u_z^{(n,\omega)} = Z_{n,\omega}(R) \cos(n\Theta) \sin(\omega Z). \tag{5.21}$$

Over V_m we write the components of $\mathbf{u}$ as $\mathbf{W}_{n,\omega} = (W_{n,\omega}, V_{n,\omega}, Z_{n,\omega})^T$, and over V_c we write $\mathbf{W}_{n,\omega} = (W_{n,\omega}, V_{n,\omega}, Z_{n,\omega}, X_{n,\omega})^T$.

We already have an expression for the incremental equations over V_m in (4.31). Over V_c, (5.16)-(5.18) results in an ordinary differential equation of the following form

$$\mathbf{T} \cdot \mathbf{W}''_{n,\omega} + \sum_{0 \le \alpha, \beta \le 2} n^\alpha \omega^\beta \mathbf{T}_{\alpha\beta} \cdot \mathbf{W}_{n,\omega} + n\mathbf{T}_\alpha^{(n)} \cdot \mathbf{W}'_{n,\omega} + \omega \mathbf{T}_\beta^\omega \cdot \mathbf{W}'_{n,\omega} + \mathbf{T}_0 \cdot \mathbf{W}'_{n,\omega} = \mathbf{0}. \tag{5.22}$$

The structure of the coefficient matrices is outlined in Chapter 7, where we outline our

method of numerical solution. Let the stress induced by $\mathbf{W}_{n,\omega}$ be $\mathbf{P}_{n,\omega}$. The inner boundary condition at R_0 is

$$\mathbf{P}_{n,\omega} \cdot \mathbf{n} = \mathbf{0}, \tag{5.23}$$

where $\mathbf{n} = -\mathbf{e}_R$ is the unit normal. We match the displacements and stress at R_1, i.e.

$$W_{n,\omega}|_- = W_{n,\omega}|_+, \tag{5.24}$$

$$V_{n,\omega}|_- = V_{n,\omega}|_+, \tag{5.25}$$

$$Z_{n,\omega}|_- = Z_{n,\omega}|_+, \tag{5.26}$$

$$\mathbf{P}_{n,\omega}|_- \cdot \mathbf{n} = \mathbf{P}_{n,\omega}|_+ \cdot \mathbf{n}. \tag{5.27}$$

The other boundary conditions (for large R) are outlined in Section 4.1.2.

5.2 Post-Buckling Analysis

In this section, we determine the existence and stability of buckled equilibrium states (labelled State II) bifurcating from the fundamental solution branch (State I). The method is essentially the same as that in Section 4.2, so we do not provide many details. We assume the system has evolved to the point where there exists a nonzero solution to the boundary value problem of the previous section (with field equation (5.22)) for some (n, ω). We denote the time $t^*_{n,\omega}$ at which such a solution exists the mode (n, ω) critical time. As previously, we perform a perturbation expansion in the neighbourhood of this point. The increments in the nutrient and treatment distributions, mass growth and dilation are outlined in Section 4.2.2. The postbucklng analysis has two major parts: in the first part we determine the leading order of the magnitude of the buckle using the Liapunov-Schmidt reduction, and in the second part we investigate the stability of the buckled state.

5.2.1 Liapunov-Schmidt Reduction

The Liapunov-Schmidt reduction is used to find the leading order of the displacement and Lagrange Multiplier similarly to Chapter 4. However the application of the Liapunov-Schmidt reduction is slightly different due to extra complications arising from V_c being

incompressible. Our method is to firstly define the *incremental elastic operator* for the composite system, before applying the Fredholm Alternative to determine the leading order of the magnitude of the buckle. We begin our analysis by performing the following perturbation expansion in the displacement, Lagrange Multiplier and growth, i.e.

$$\begin{aligned}
\mathbf{u} =& \mathbf{u}_0 + \epsilon \mathbf{u} + \frac{\epsilon^2}{2}\mathbf{u}_2 + \dots \\
p =& p_0 + \epsilon p_1 + \frac{\epsilon^2}{2} p_2 + \dots \\
\zeta =& \zeta_0 + \epsilon \zeta_1 + \frac{\epsilon^2}{2}\zeta_2 + \dots \\
t =& t^*_{n,\omega} + \frac{\epsilon^2}{2}\delta t.
\end{aligned} \tag{5.28}$$

for $\epsilon \ll 1$. Here $\mathbf{u}$ and $\mathbf{u}_j$ are defined over $V_m \cup V_c$. The increments in the Lagrange Multiplier p_j are only defined over V_c. The increments in the other variables (the nutrient distribution and treatment) are outlined in Section 4.2.

The perturbations in the deformation gradient, first Piola-Kirchhoff stress and determinant of the deformation gradient assume the following form

$$\begin{aligned}
\mathbf{F} =& \mathbf{F}_0 + \epsilon \nabla \mathbf{u}_1 + \frac{\epsilon^2}{2}\nabla \mathbf{u}_2 + \dots, \\
\mathbf{P} =& \mathbf{P}_0 + \epsilon \mathbf{P}_1 + \frac{\epsilon^2}{2}\mathbf{P}_2 + \dots, \\
J =& J_0 + \epsilon J_1 + \frac{\epsilon^2}{2} J_2 + \dots
\end{aligned} \tag{5.29}$$

The incremental components of the equation of mechanical equilibrium over $V_m \cup V_c$ and

the incompressibility condition amount to the following system

$$J_j = 0 \text{ for } j > 0, \text{ and } J_0 = 1 \text{ over } V_c, \tag{5.30}$$

$$\nabla \cdot \mathbf{P}_j = \mathbf{0} \text{ over } V_c \cup V_m, \tag{5.31}$$

$$(\mathbf{P}_j|_+)\,.\mathbf{n} = (\mathbf{P}_j|_-) \cdot \mathbf{n} \text{ at } R = R_1,$$

$$\mathbf{u}_j|_+ = \mathbf{u}_j|_- \text{ at } R = R_1,$$

$$\mathbf{P}_j \cdot \mathbf{n} = \mathbf{0} \text{ at } R = R_0 \text{ and} \tag{5.32}$$

$$\mathbf{u}_j = \mathbf{0} \text{ for a null-displacement boundary condition at } R = R_2 \text{ or} \tag{5.33}$$

$$\mathbf{u}_j \to \mathbf{0} \text{ as } R \to \infty \text{ if the geometry is infinite.} \tag{5.34}$$

Now the $O(\epsilon)$ and $O(\epsilon^2)$ increments in the first Piola Kirchhoff stress are given by

$$\begin{aligned}
\mathbf{P}_1 &= \frac{\partial \mathbf{P}}{\partial \mathbf{F}} : \nabla \mathbf{u}_1 + \frac{\partial \mathbf{P}}{\partial p} p_1 \\
\frac{1}{2}\mathbf{P}_2 &= \frac{1}{2}\frac{\partial^2 \mathbf{P}}{\partial \mathbf{F}^2} : \nabla \mathbf{u}_1 : \nabla \mathbf{u}_1 + \frac{1}{2}\frac{\partial \mathbf{P}}{\partial \mathbf{F}} : \nabla \mathbf{u}_2 + \frac{1}{2}\frac{\partial \mathbf{P}}{\partial \zeta}\zeta_2 \\
&\quad + \frac{1}{2}\frac{\partial^2 \mathbf{P}}{\partial p^2} p_1^2 + \frac{1}{2}\frac{\partial \mathbf{P}}{\partial p} p_2 + \frac{\partial^2 \mathbf{P}}{\partial \mathbf{F} \partial p} : \nabla \mathbf{u}_1 p_1,
\end{aligned} \tag{5.35}$$

where the terms containing ζ, or a differential with respect to ζ, are zero over V_c and the terms containing p are only nonzero over V_c. The double derivative of $\mathbf{P}$ with respect to p is identically zero. We obtain the zeroth, first and second order components of the incompressibility condition by differentiating J with respect to the deformation gradient, i.e.

$$\begin{aligned}
J_0 &= 1, \\
J_1 &= J_0 \mathbf{F}_0^{-T} : \nabla \mathbf{u}_1, \\
J_2 &= \frac{\partial^2 J}{\partial \mathbf{F}^2} : \nabla \mathbf{u}_1 : \nabla \mathbf{u}_1 + \frac{\partial J}{\partial \mathbf{F}} : \nabla \mathbf{u}_2, \\
&= \mathbf{F}_0^{-T} : \nabla \mathbf{u}_2 - \left(\mathbf{F}_0^{-T} \nabla \mathbf{u}_1^T \mathbf{F}_0^{-T} \right) : \nabla \mathbf{u}_1 \\
\frac{1}{6} J_3 &= \frac{1}{6}\frac{\partial J}{\partial \mathbf{F}} : \mathbf{u}_3 + \frac{1}{6}\frac{\partial^3 J}{\partial \mathbf{F}^3} : \nabla \mathbf{u}_1 : \nabla \mathbf{u}_1 : \nabla \mathbf{u}_1 + \frac{1}{2}\frac{\partial^2 J}{\partial \mathbf{F}^2} : \nabla \mathbf{u}_1 : \nabla \mathbf{u}_2, \\
&= \frac{1}{6} \nabla \mathbf{u}_3 : \mathbf{F}_0^{-T} + \frac{1}{3} \left(\mathbf{F}_0^{-T} \nabla \mathbf{u}_1^T \mathbf{F}_0^{-T} \nabla \mathbf{u}_1^T \mathbf{F}_0^{-T} \right) : \nabla \mathbf{u}_1 - \frac{1}{2} \left(\mathbf{F}_0^{-T} \nabla \mathbf{u}_1^T \mathbf{F}_0^{-T} \right) : \nabla \mathbf{u}_2.
\end{aligned}$$

We write $\mathbf{P}_j = \mathbf{P}_j^* + \frac{\partial \mathbf{P}}{\partial \mathbf{F}} : \nabla \mathbf{u}_j + \frac{\partial \mathbf{P}}{\partial p} p_j$ and $J_j = \frac{\partial J}{\partial \mathbf{F}} : \nabla \mathbf{u}_j + J_j^*$ in the the capillary, for some $\mathbf{P}_j^*$ and J_j^* which only depend on variables of lower order than j. We similarly write $\mathbf{P}_j = \mathbf{P}_j^* + \frac{\partial \mathbf{P}}{\partial \mathbf{F}} : \nabla \mathbf{u}_j$ in the tumour matrix. Observe that we may obtain $\mathbf{u}_j$ and p_j in the capillary by solving the linear system,

$$\begin{aligned}
\nabla \cdot \left(\frac{\partial \mathbf{P}}{\partial \mathbf{F}} : \nabla \mathbf{u}_j + \frac{\partial \mathbf{P}}{\partial p} p_j \right) &= -\nabla \cdot \mathbf{P}_j^* \text{ over } V_c, && (5.36)\\
\mathbf{F}_0^{-T} : \nabla \mathbf{u}_j &= -J_j^* \text{ over } V_c, && (5.37)\\
\left(\frac{\partial \mathbf{P}}{\partial \mathbf{F}} : \nabla \mathbf{u}_j + \frac{\partial \mathbf{P}}{\partial p} p_j \right) |_- \cdot \mathbf{n} &= \left(\mathbf{P}_j |_+ - \mathbf{P}_j^* |_- \right) \cdot \mathbf{n} \text{ at } R = R_1, && (5.38)\\
\left(\frac{\partial \mathbf{P}}{\partial \mathbf{F}} : \nabla \mathbf{u}_j + \frac{\partial \mathbf{P}}{\partial p} p_j \right) \cdot \mathbf{n} &= -\mathbf{P}_j^* \cdot \mathbf{n} \text{ at } R = R_0. && (5.39)
\end{aligned}$$

The equations governing the displacement over V_m are similar and are given in the previous chapter. By assumption, the homogeneous equation, with $\mathbf{P}_j^* = \mathbf{0}$ and $J_j^* = 0$, has nontrivial solutions $\{\mathbf{u}^{(n,\omega)}, p^{(n,\omega)}\} \in U_{n,\omega}^{(1)}$ (note that there is another nontrivial solution in an orthogonal subspace we need not worry about). This is the eigenmode of Section 5.1.

We now derive the Fredholm condition for the existence of a solution to (5.36)-(5.39). The derivation is similar to that of Section 4.2, except that we now need to consider two domains: V_m and V_c. We expand the second variation of the energy in terms of $(\mathbf{u}, \delta p_u)$

and $(\mathbf{v}, \delta p_v)$ as follows,

$$\iiint_{V_c} \frac{\partial^2 \psi}{\partial \mathbf{F}^2} : \nabla \mathbf{u} : \nabla \mathbf{v} + \frac{\partial^2 \psi}{\partial \mathbf{F} \partial p} : \nabla \mathbf{u} \delta p_v + \frac{\partial^2 \psi}{\partial \mathbf{F} \partial p} : \nabla \mathbf{v} \delta p_u dV + \iiint_{V_m} \frac{\partial^2 \psi}{\partial \mathbf{F}^2} : \nabla \mathbf{u} : \nabla \mathbf{v} dV \tag{5.40}$$

$$\begin{aligned}
&= \iiint_{V_c} -\mathbf{v} \cdot \left(\nabla \cdot \left(\frac{\partial^2 \psi}{\partial \mathbf{F}^2} : \nabla \mathbf{u} + \frac{\partial^2 \psi}{\partial \mathbf{F} \partial p} \delta p_u \right) \right) + \nabla \cdot \left(\left(\frac{\partial^2 \psi}{\partial \mathbf{F}^2} : \nabla \mathbf{u} + \frac{\partial^2 \psi}{\partial \mathbf{F} \partial p} \delta p_u \right)^T \cdot \mathbf{v} \right) dV \\
&- \iiint_{V_c} \delta p_v \mathbf{F}_0^{-T} : \nabla \mathbf{u} dV \\
&+ \iiint_{V_m} -\mathbf{v} \cdot \left(\nabla \cdot \left(\frac{\partial^2 \psi}{\partial \mathbf{F}^2} : \nabla \mathbf{u} \right) \right) + \nabla \cdot \left(\left(\frac{\partial^2 \psi}{\partial \mathbf{F}^2} : \nabla \mathbf{u} \right)^T \cdot \mathbf{v} \right) dV \\
&= \iiint_{V_c} -\mathbf{v} \cdot \left(\nabla \cdot \left(\frac{\partial^2 \psi}{\partial \mathbf{F}^2} : \nabla \mathbf{u} + \frac{\partial^2 \psi}{\partial \mathbf{F} \partial p} \delta p_u \right) \right) - \delta p_v \mathbf{F}_0^{-T} : \nabla \mathbf{u} dV \\
&+ \iiint_{V_m} -\mathbf{v} \cdot \left(\nabla \cdot \left(\frac{\partial^2 \psi}{\partial \mathbf{F}^2} : \nabla \mathbf{u} \right) \right) dV \\
&+ \iint_{\partial (V_c \cup V_m)} \mathbf{v}^T \cdot \left(\left(\frac{\partial^2 \psi}{\partial \mathbf{F}^2} : \nabla \mathbf{u} \right) \cdot \mathbf{n} \right) dA + \iint_{R=R_0} \mathbf{v}^T \cdot \left(\left(\frac{\partial^2 \psi}{\partial \mathbf{F} \partial p} \delta p_u \right) \cdot \mathbf{n} \right) \\
&+ \iint_{R=R_1} \mathbf{v}^T \cdot \left(\left(\frac{\partial^2 \psi}{\partial \mathbf{F}^2} : \nabla \mathbf{u}|_- + \frac{\partial^2 \psi}{\partial \mathbf{F} \partial p} \delta p_u|_- - \frac{\partial^2 \psi}{\partial \mathbf{F}^2} : \nabla \mathbf{u}|_+ \right) \cdot \mathbf{e}_R \right) dA.
\end{aligned} \tag{5.41}$$

We obtain the Fredholm solvability condition by substituting the equations in (5.36)-(5.39) into (5.41). We also stipulate that $(\mathbf{v}, \delta p_v)$ is an eigenmode, which means that (5.41) is zero, because it is symmetric in $(\mathbf{u}, \delta p_u)$ and $(\mathbf{v}, \delta p_v)$. We thus obtain the following necessary condition for the existence of a solution to (5.36)-(5.39), i.e.

$$\iint_{V_c \cup V_m} \mathbf{P}_j^* : \nabla \mathbf{v} dV - \iint_{V_c} J_j^* \delta p_v dV = 0, \tag{5.42}$$

where $\{\mathbf{v}, \delta p_v\}$ is an eigenmode. The proof of this is very similar to the proof in Section 4.2.3. We use (5.42) to determine the leading order of the magnitude of the buckle.

As we explained in Section 4.2.3, we may stipulate that $\mathbf{u}_1 = a\mathbf{u}^{(n,\omega)}$ and $p_1 = ap^{(n,\omega)}$ for some a. We insist that $(\mathbf{u}_j, p_j)$ is orthogonal to the eigenmode $(\mathbf{u}^{(n,\omega)}, p^{(n,\omega)})$ for $j \geq 2$. We write (5.42) as

$$g_j = \iint_{V_c \cup V_m} \mathbf{P}_j^* : \nabla \mathbf{u}^{(n,\omega)} dV - \iint_{V_c} J_j^* \delta p^{(n,\omega)} dV = 0, \tag{5.43}$$

for some function g_j. We use g_3 to obtain the magnitude a of the first order displacement, as g_1 is identically zero as a consequence of the Trefftz Condition and g_2 is identically zero as a consequence of the radial symmetry. An expression for $\mathbf{P}_3$ over V_m is given in (4.97). The $O(\epsilon^3)$ component of $\mathbf{P}$ over V_c is

$$\frac{1}{6}\mathbf{P}_3^* = \frac{1}{6}\frac{\partial^3 \mathbf{P}}{\partial \mathbf{F}^3} : \nabla \mathbf{u}_1 : \nabla \mathbf{u}_1 : \nabla \mathbf{u}_1 + \frac{1}{2}\frac{\partial^2 \mathbf{P}}{\partial \mathbf{F}^2} : \nabla \mathbf{u}_1 : \nabla \mathbf{u}_2 + \frac{1}{2}\frac{\partial^3 \mathbf{P}}{\partial \mathbf{F}^2 \partial p} : \nabla \mathbf{u}_1 : \nabla \mathbf{u}_1 p_1 + \frac{1}{2}\frac{\partial^2 \mathbf{P}}{\partial \mathbf{F} \partial p} : \nabla \mathbf{u}_2 p_1 + \frac{1}{2}\frac{\partial^2 \mathbf{P}}{\partial \mathbf{F} \partial p} : \nabla \mathbf{u}_1 p_2. \quad (5.44)$$

The structure of the derivatives is outlined in Appendix C.0.14.

We obtain $\mathbf{u}_2$ by solving the $O(\epsilon^2)$ component of (5.39). We find that the solution to the second order equations can be written as $\mathbf{u}_2 = a^2 \mathbf{u}_2^a + \mathbf{u}_2^p$ and $p_2 = a^2 p_2^a + p_2^p$, where

$$\begin{aligned}
&\nabla \cdot \left(\frac{\partial \mathbf{P}}{\partial \mathbf{F}} : \nabla \mathbf{u}_2^a + \frac{\partial \mathbf{P}}{\partial p} p_2^a \right) = -\nabla \cdot \left(\frac{\partial^2 \mathbf{P}}{\partial \mathbf{F}^2} : \nabla \mathbf{u}^{(n,\omega)} : \nabla \mathbf{u}^{(n,\omega)} + 2\frac{\partial^2 \mathbf{P}}{\partial \mathbf{F} \partial p} : \nabla \mathbf{u}^{(n,\omega)} p^{(n,\omega)} \right) \text{ over } V_c, \\
&\left(\frac{\partial \mathbf{P}}{\partial \mathbf{F}} : \nabla \mathbf{u}_2^a + \frac{\partial \mathbf{P}}{\partial p} p_2^a + \mathbf{P}_2^*|_- \right) \cdot \mathbf{n} = (\mathbf{P}_2|_+) \cdot \mathbf{n} \text{ at } R = R_1, \\
&\left(\frac{\partial \mathbf{P}}{\partial \mathbf{F}} : \nabla \mathbf{u}_2^a + \frac{\partial \mathbf{P}}{\partial p} p_2^a + \mathbf{P}_2^* \right) \cdot \mathbf{n} = \mathbf{0} \text{ at } R = R_0, \\
&\left(\frac{\partial \mathbf{P}}{\partial \mathbf{F}} : \nabla \mathbf{u}_2^p|_- + \frac{\partial \mathbf{P}}{\partial p} p_2^p \right) \cdot \mathbf{n} = \left(\frac{\partial \mathbf{P}}{\partial \mathbf{F}} : \nabla \mathbf{u}_2^p|_+ \frac{\partial \mathbf{P}}{\partial \zeta_\alpha} \zeta_{2,\alpha} \right) \cdot \mathbf{n} \text{ at } R = R_1, \quad (5.45) \\
&\nabla \cdot \left(\frac{\partial \mathbf{P}}{\partial \mathbf{F}} : \nabla \mathbf{u}_2^p + \frac{\partial \mathbf{P}}{\partial p} p_2^p \right) = \mathbf{0} \text{ over } V_c, \\
&\left(\frac{\partial \mathbf{P}}{\partial \mathbf{F}} : \nabla \mathbf{u}_2^p + \frac{\partial \mathbf{P}}{\partial p} p_2^p \right) \cdot \mathbf{n} = \mathbf{0} \text{ at } R = R_0. \quad (5.46)
\end{aligned}$$

The equations governing $\mathbf{u}_2$ over V_m are outlined in Section 4.2.3. We assume, as in the previous section, that the system first enters the buckled state at time $t_* + \epsilon \upsilon \delta t$ for some $0 \leq \upsilon \leq 1$. Upon solution of $g_3 = 0$ we find that

$$a = \pm \sqrt{-\delta t \frac{C_2}{C_1} - (\delta t - \delta t^*) \frac{2C_3}{3C_1}}, \quad (5.47)$$

where $\delta t^* = \upsilon^{\frac{3}{2}} \delta t$ and

$$C_1 = C_1^{cap} + C_1^{tum}$$

$$C_1^{cap} = \iiint_{V_c} \left(\frac{1}{6}\frac{\partial^3 \mathbf{P}}{\partial \mathbf{F}^3} : \nabla \mathbf{u}^{(n,\omega)} : \nabla \mathbf{u}^{(n,\omega)} : \nabla \mathbf{u}^{(n,\omega)} + \frac{1}{2}\frac{\partial^2 \mathbf{P}}{\partial \mathbf{F}^2} : \nabla \mathbf{u}^{(n,\omega)} : \nabla \mathbf{u}_2^a \right.$$
$$+ \frac{1}{2}\frac{\partial^3 \mathbf{P}}{\partial \mathbf{F}^2 \partial p} : \nabla \mathbf{u}^{(n,\omega)} : \nabla \mathbf{u}^{(n,\omega)} p^{(n,\omega)}$$
$$\left. + \frac{1}{2}\frac{\partial^2 \mathbf{P}}{\partial \mathbf{F} \partial p} : \nabla \mathbf{u}_2^a p^{(n,\omega)} + \frac{1}{2}\frac{\partial^2 \mathbf{P}}{\partial \mathbf{F} \partial p} : \nabla \mathbf{u}^{(n,\omega)} p_2^a \right) : \nabla \mathbf{u}^{(n,\omega)} dV$$
$$- \iiint_{V_c} \left(\frac{1}{6}\frac{\partial^3 J}{\partial \mathbf{F}^3} : \nabla \mathbf{u}^{(n,\omega)} : \nabla \mathbf{u}^{(n,\omega)} : \nabla \mathbf{u}^{(n,\omega)} + \frac{1}{2}\frac{\partial^2 J}{\partial \mathbf{F}^2} : \nabla \mathbf{u}^{(n,\omega)} : \nabla \mathbf{u}_2^a \right) p^{(n,\omega)} dV$$

$$C_1^{tum} = \iiint_{V_m} \left(\frac{1}{6}\frac{\partial^3 \mathbf{P}}{\partial \mathbf{F}^3} : \nabla \mathbf{u}^{(n,\omega)} : \nabla \mathbf{u}^{(n,\omega)} : \nabla \mathbf{u}^{(n,\omega)} + \frac{1}{2}\frac{\partial^2 \mathbf{P}}{\partial \mathbf{F}^2} : \nabla \mathbf{u}^{(n,\omega)} : \nabla \mathbf{u}_2^a \right) : \nabla \mathbf{u}^{(n,\omega)} dV$$

$$C_2 = C_2^{cap} + C_2^{tum}$$

$$C_2^{cap} = \iiint_{V_c} \left(\frac{1}{2}\frac{\partial^2 \mathbf{P}}{\partial \mathbf{F}^2} : \nabla \mathbf{u}_2^p : \nabla \mathbf{u}^{(n,\omega)} + \frac{1}{2}\frac{\partial^2 \mathbf{P}}{\partial \mathbf{F} \partial p} : \nabla \mathbf{u}_2^p p^{(n,\omega)} + \frac{1}{2}\frac{\partial^2 \mathbf{P}}{\partial \mathbf{F} \partial p} : \nabla \mathbf{u}^{(n,\omega)} p_2^p \right) : \nabla \mathbf{u}^{(n,\omega)}$$
$$- \iiint_{V_c} \frac{1}{2}\frac{\partial^2 J}{\partial \mathbf{F}^2} : \nabla \mathbf{u}^{(n,\omega)} : \nabla \mathbf{u}_2^p p^{(n,\omega)} dV$$

$$C_2^{tum} = + \iiint_{V_m} \left(\frac{1}{2}\frac{\partial^2 \mathbf{P}}{\partial \mathbf{F}^2} : \nabla \mathbf{u}_2^p : \nabla \mathbf{u}^{(n,\omega)} + \frac{1}{2}\frac{\partial^2 \mathbf{P}}{\partial \mathbf{F} \partial \zeta} : \nabla \mathbf{u}^{(n,\omega)} \zeta_2^* \right) : \nabla \mathbf{u}^{(n,\omega)} dV, \tag{5.48}$$

$$C_3 = \frac{1}{2} \iiint_{V_m} \frac{\partial \mathbf{P}}{\partial \zeta_\alpha} : \nabla \mathbf{u}^{(n,\omega)} \zeta_{\alpha,0} \times$$
$$\left(G_{\alpha,0} \left(\frac{c^{(n,\omega)}}{k_c} \left(1 + \frac{c_0}{k_c} \right)^{-2} - \mu^{(n,\omega)} \right) + G_{\alpha,1}^{(n,\omega)} \left(\frac{c_0}{k_c + c_0} - \mu_0 \right) \right) dV. \tag{5.49}$$

We sum over α and $\zeta_{\alpha,2} = \zeta_{\alpha,2}^* \delta t$. We have insisted that $a = 0$ when $\delta t = 0$. The variable δt^* is the time increment at which the system first enters the buckled state; it is discussed in more depth in Section 4.2.3.

5.2.2 Stability of Buckled States

The analysis governing the stability of the buckled state is the same as Section 4.2.4. The stability of the buckled equilibrium state is governed by the sign of

$$3C_1 a^2 + (\delta t) C_2. \tag{5.50}$$

If this is positive, the buckled equilibrium state (if it exists) is stable; if it is negative, the buckled equilibrium state is unstable. Refer to Section 4.2.5 for a discussion of the effect of the variables $\{a, \delta t, \delta t^*, C_1, C_2, C_3\}$ on the existence and stability of buckled equilibrium

states.

5.2.3 Postbuckled Treatment of Tumour

We model the treatment of a tumour in a postbuckled equilibrium state. We are interested in determining the effect of the treatment on the buckle. Suppose there exists a mode (n, ω) buckled state for small increments of time beyond $t_{n,\omega}$. That is, the perturbation expansion is given by

$$\mathbf{u} = \mathbf{u}_0 + \epsilon a \mathbf{u}_1^{(n,\omega)} + \frac{\epsilon^2}{2} a^2 \mathbf{u}_2^a + \frac{\epsilon^2 \delta t}{2} \mathbf{u}_2^p + \dots \tag{5.51}$$

$$c = c_0 + \epsilon a c^{(n,\omega)} + \dots \tag{5.52}$$

$$\bar{r}_a = r_0 + \frac{\epsilon^2}{2} r_{\alpha,2} + a\delta t \frac{\epsilon^3}{6} r^*_{\alpha,3} + \dots \tag{5.53}$$

$$\zeta_\alpha = \zeta_{\alpha,0} + \frac{\epsilon^2 \delta t}{2} \zeta^*_{\alpha,2} + a\delta t \frac{\epsilon^3}{6} \zeta^*_3 + \dots \tag{5.54}$$

$$t = t_{n,\omega} + \frac{\epsilon^2}{2} \delta t \tag{5.55}$$

$$G_\alpha = G_{\alpha,0} + \epsilon G_{\alpha,1} + \dots \tag{5.56}$$

We initiate treatment at time $t^*_{n,\omega} + \frac{\epsilon^2 \delta t_c}{2}$, where $\delta t - \delta t_c \geq 0$ is small.

The leading order terms of the growth are now

$$\begin{aligned}\zeta_\alpha = \zeta_{\alpha,0} + \frac{\delta t}{2}\epsilon^2 \zeta_{\alpha,2} + \frac{\epsilon^2(\delta t - \delta t_c)}{2} \zeta^c_{\alpha,2} + \\ \frac{\epsilon^3}{2}\left(G_{\alpha,0}\left(\frac{c^{(n,\omega)}}{k_c}\left(1 + \frac{c_0}{k^*_c}\right)^{-2}\right) + G^{(n,\omega)}_{\alpha,1}\left(\frac{c_0}{k_c + c_0}\right)\right) \int_0^{\delta t} a d(\delta t) \\ - \left(G_{\alpha,0}\mu^{(n,\omega)} + G^{(n,\omega)}_{\alpha,1}\mu_0 \right) \frac{\epsilon^3}{2} \int_{\delta t_c}^{\delta t} a d(\delta t) + \dots .\end{aligned}$$

where

$$\zeta^c_{\alpha,2} = -G_{\alpha,0}\zeta_{\alpha,0}\mu_0 \tag{5.57}$$

The perturbation expansion in $\mathbf{u}$ becomes

$$\mathbf{u} = \mathbf{u}_0 + \epsilon a \mathbf{u}^{(n,\omega)} + \frac{\epsilon^2}{2} a^2 \mathbf{u}_2^a + \frac{\epsilon^2 \delta t}{2} \mathbf{u}_2^p + \frac{\epsilon^2 (\delta t - \delta t_c)}{2} \mathbf{u}_2^c + \ldots, \tag{5.58}$$

where $\mathbf{u}_2^c$ is defined analogously to $\mathbf{u}_2^p$, i.e.

$$\begin{aligned}
\nabla \cdot \left(\frac{\partial \mathbf{P}}{\partial \mathbf{F}} : \nabla \mathbf{u}_2^c \right) &= - \nabla \cdot \frac{\partial \mathbf{P}}{\partial \zeta} \zeta_{\alpha,2}^c \text{ over } V_m, \\
\left(\frac{\partial \mathbf{P}}{\partial \mathbf{F}} : \nabla \mathbf{u}_2^c|_+ + \frac{\partial \mathbf{P}}{\partial \zeta} \zeta_{\alpha,2}^c \right) \cdot \mathbf{n} &= \left(\frac{\partial \mathbf{P}}{\partial \mathbf{F}} : \nabla \mathbf{u}_2^c|_- + \frac{\partial \mathbf{P}}{\partial p} \delta p^c \right) \cdot \mathbf{n} \text{ at } R = R_1, \\
\left(\frac{\partial \mathbf{P}}{\partial \mathbf{F}} : \nabla \mathbf{u}_2^c + \frac{\partial \mathbf{P}}{\partial p} \delta p^c \right) \cdot \mathbf{n} &= \mathbf{0} \text{ at } R = R_0,
\end{aligned} \tag{5.59}$$

$$\mathbf{u}^c = \mathbf{0} \text{ for models A,} \tag{5.60}$$

$$\mathbf{u}^c \to \mathbf{0} \text{ as } R \to \infty \text{ for the infinite geometry models.} \tag{5.61}$$

The derivatives are evaluated at $t_{n,\omega}^*$ instead of $t_{n,\omega}^* + 0.5\delta t \epsilon^2$. The difference between evaluating them at these points is only $\mathrm{O}(\epsilon^2(\delta t - \delta t_c))$, so to leading order this approximation is valid.

In determining $\mathbf{u}_2^c$ we make use of the following identities. The derivative of the increment in the growth is

$$\zeta_{\alpha,2}^{c\,\prime} = -\delta t \mu_0 \left(\zeta_{\alpha,0} G'_{\alpha,0} + \zeta'_{\alpha,0} G_{\alpha,0} \right) - \delta t \mu'_0 \zeta_{\alpha,0} G_{\alpha,0}. \tag{5.62}$$

For the radiotherapy,

$$\mu'_0 = \left(\alpha_h OER'_\alpha D + 2\beta_h OER_\beta OER'_\beta D^2 \right), \tag{5.63}$$

with

$$OER_\alpha = \frac{c_0 m_\alpha + k_m}{c_0 + k_m} \quad , \quad OER_\beta = \frac{c_0 m_\beta + k_m}{c_0 + k_m}, \tag{5.64}$$

$$OER'_\alpha = k_m (m_\alpha - 1)(c_0 + k_m)^{-2} \frac{\partial c_0}{\partial R}, \tag{5.65}$$

$$OER'_\beta = k_m (m_\beta - 1)(c_0 + k_m)^{-2} \frac{\partial c_0}{\partial R}. \tag{5.66}$$

For the chemotherapy,

$$\mu_0' = \left(\mu^i d_0' + k_d \mu^{ii} \left(k_d + d_0\right)^{-2} \frac{\partial d_0}{\partial R}\right) \frac{K0}{K0 + c_0} - \left(\mu^i d_0 + \mu^{ii} \frac{d_0}{k_d + d_0}\right) K0 \left(K0 + c_0\right)^{-2} \frac{\partial c_0}{\partial R}. \tag{5.67}$$

The leading order of g_3 is now

$$g_3 = C_1 a^3 + C_2 \delta t a + C_2^c (\delta t - \delta t_c) a + C_3 \int_{\delta t^*}^{\delta t} a d(\delta t) + C_3^c \int_{\delta t_c}^{\delta t} a d(\delta t) = 0 \tag{5.68}$$

where

$$\begin{aligned}
C_2^c = & \frac{1}{2} \iiint_{V_m} \left(\frac{\partial^2 \mathbf{P}}{\partial \mathbf{F}^2} : \nabla \mathbf{u}_2^c : \nabla \mathbf{u}^{(n,\omega)} + \frac{\partial^2 \mathbf{P}}{\partial \mathbf{F} \partial \zeta} : \nabla \mathbf{u}^{(n,\omega)} \zeta_{\alpha,2}^c \right) : \nabla \mathbf{u}^{(n,\omega)} dV, \\
& \iiint_{V_c} \left(\frac{1}{2} \frac{\partial^2 \mathbf{P}}{\partial \mathbf{F}^2} : \nabla \mathbf{u}_2^c : \nabla \mathbf{u}^{(n,\omega)} + \frac{1}{2} \frac{\partial^2 \mathbf{P}}{\partial \mathbf{F} \partial p} : \nabla \mathbf{u}_2^c p^{(n,\omega)} + \frac{1}{2} \frac{\partial^2 \mathbf{P}}{\partial \mathbf{F} \partial p} : \nabla \mathbf{u}^{(n,\omega)} p_2^c \right) : \nabla \mathbf{u}^{(n,\omega)} dV, \\
& - \iiint_{V_c} \frac{1}{2} \frac{\partial^2 J}{\partial \mathbf{F}^2} : \nabla \mathbf{u}^{(n,\omega)} : \nabla \mathbf{u}_2^c p^{(n,\omega)} dV \\
C_3^c = & -\frac{1}{2} \iiint_{V_m} \frac{\partial \mathbf{P}}{\partial \zeta_\alpha} : \nabla \mathbf{u}^{(n,\omega)} \zeta_{\alpha,0} \times \left(G_{\alpha,0} \mu^{(n,\omega)} + G_{\alpha,1}^{(n,\omega)} \mu_0 \right) dV.
\end{aligned} \tag{5.69}$$

We assume that δt^*, which we recall gives the increment in time when the system first adopts the buckled state, is zero. The solution for a is thus

$$a^2 = -\delta t \left(\frac{C_2}{C_1} + \frac{2C_3}{3C_1} \right) - (\delta t - \delta t_c) \left(\frac{C_2^c}{C_1} + \frac{2C_3^c}{3C_1} \right). \tag{5.70}$$

Our assumption at the start of this analysis was that buckled equilibrium states exist, which means the right hand side must be positive when $\delta t_c = \delta t$. As we decrease δt_c towards zero, the equilibrium state will merge with the fundamental solution if the only solution of $g_3 = 0$ is $a = 0$. For this argument to hold we also require $(\delta t - \delta t_c)$ and ϵ to remain within the domain of accuracy of our perturbation expansion. The stability of the equilibrium state is given by the sign of

$$3C_1 a^2 + \delta t C_2 + (\delta t - \delta t_c) C_2^c, \tag{5.71}$$

where a^2 satisfies (5.70). If the sign is positive then the equilibrium state is stable. If it is negative, then the equilibrium state is unstable.

There are three outcomes of the treatment we consider. The first possibility is that the

system remains buckled after treatment (Case A). The second is that the system remains buckled initially, but the magnitude of the buckle smoothly decreases back to zero (Case B). The third possibility is that the buckled state becomes unstable (Case C). We use our perturbation expansion to find criteria governing the occurrence of each of these possibilities. It is of course possible that the system moves outside the regime of accuracy of our perturbation expansion before any of these criteria are realised.

Since by assumption there exists a buckled state at time $t + \frac{\epsilon^2}{2}\delta t_c$ (i.e. $\delta t = \delta t_c$), there must initially exist a real solution for a of (5.70), and (5.71) must initially be positive. We firstly find criteria for the treatment destabilising the buckle (Case C). This is governed by (5.71) transitioning from positive to negative. We do not worry about there no longer being a real solution of (5.70), as for this to happen a^2 must pass through zero, and this is covered by Case B. At the point of transition, (5.71) is zero, which requires

$$\delta t_c = \delta t \left(1 + \frac{C_2 + C_3}{C_2^c + C_3^c}\right). \tag{5.72}$$

This solution must lie in the acceptable range

$$0 \leq \delta t_c \leq \delta t. \tag{5.73}$$

Case B occurs when $a^2 = 0$. This requires

$$\delta t_c = \delta t \left(1 + \frac{3C_2 + 2C_3}{3C_2^c + 2C_3^c}\right). \tag{5.74}$$

There must exist a solution in the acceptable range (5.73). The order of occurrence of (5.72) and (5.74) dictates whichever of Case C or Case B occurs first. If neither of these are satisfied, then the system remains buckled.

Chapter 6

Boundary Layer Analysis

The results to be outlined in following chapters indicate there is a boundary layer in the displacement at R_1 for large azimuthal wavenumber n or axial wavenumber ω. The deformation is greatest at R_1 and in the large wavenumber asymptotic limit, the deformation decays exponentially as R increases (with the exponent being proportional to the wavenumber). This behaviour is analogous to the development of Rayleigh Surface Wave instabilities in a compressed infinite elastic half-space [117, 22, 109]. In that case, if there is a homogeneous uniaxial compression in an infinite elastic half-space, then all the wavelengths (for transverse buckles) become unstable simultaneously because there is no natural length scale and therefore the wavelengths are indistinguishable. Ben Amar and Ciarletta similarly observed a vanishing of the wavelength in the swelling of gels attached to a stationary substrate [3]. We obtain a similar result for our annular problem. The key difference is that the wavenumbers n and ω are present in our incremental equations of equilibrium, whereas in the half-space problem mentioned above the solution of the incremental equations of equilibrium is independent of the wavenumber. Thus even if the growth in our annular problem was completely homogeneous, and the outer radius was infinite, so that there was no natural lengthscale (from the point of view of the equations of mechanical equilibrium), the wavenumbers would not be indistinguishable because the wavenumber is present in the (cylindrical-coordinates) equations of equilibrium. That is, in our annular problem, the wavelengths go unstable at different times. The solution of the leading order (in the asymptotic limit of the small parameters n^{-1} and ω^{-1}) of the incremental equations of equilibrium allows us to determine

the asymptotic limit t_∞ of the critical times $\{t^*_{n,\omega}\}$. Solution of the lower order equations gives us a refined approximation for the critical times of large wavenumbers.

6.0.4 Asymptotic Behaviour of the Eigenmode

We perform a boundary layer analysis as the mode numbers n and ω asymptote to infinity. That is, we fix $n = \beta_1\varsigma$ and $\omega = \beta_2\varsigma$ for fixed (β_1, β_2) and consider the behaviour of the system as $\varsigma \to \infty$. In this section we only consider the system without a differentiated capillary wall structure.

We scale the length variable R near R_1 as

$$R = R_1 + \frac{\rho}{\varsigma}, \tag{6.1}$$

so that $\frac{d}{dR} = \varsigma\frac{d}{d\rho}$. Let $(W_{n,\omega}, V_{n,\omega}, Z_{n,\omega})^T$ be the components of the homogeneous solution $\mathbf{u}^{(n,\omega)}$ relative to U_n. We write $\mathbf{W} = (W_{n,\omega}, V_{n,\omega}, Z_{n,\omega}, W_{n,\omega,\rho}, V_{n,\omega,\rho}, Z_{n,\omega,\rho})^T$, where the subscript ρ denotes differentiation with respect to ρ. We obtain from (4.31) a governing equation in the boundary layer of the form

$$\varsigma^2\mathbf{W}_\rho = \varsigma^2\mathbf{S}_1 \cdot \mathbf{W} + \varsigma\mathbf{S}_2 \cdot \mathbf{W} + \mathbf{S}_3 \cdot \mathbf{W}. \tag{6.2}$$

The matrices $\mathbf{S}_j$ are functions of R and β and can be obtained from the matrices in Section 7. The components of the deformation gradient (relative to $T_{n,\omega}$ - we omit the trigonometric coefficients here, and throughout the chapter) are

$$\nabla\mathbf{W} = \varsigma\begin{pmatrix} W_4 & -\beta_1 R^{-1}W_1 & -\beta_2 W_1 \\ W_5 & \beta_1 R^{-1}W_2 & -\beta_2 W_2 \\ W_6 & -\beta_1 R^{-1}W_3 & \beta_2 W_3 \end{pmatrix} + \begin{pmatrix} 0 & -R^{-1}W_2 & 0 \\ 0 & R^{-1}W_1 & 0 \\ 0 & 0 & 0 \end{pmatrix}. \tag{6.3}$$

The boundary condition at R_1 is

$$\mathbf{P}^{(0)} \cdot \nabla\mathbf{W} := \begin{pmatrix} P_{RRRR}\nabla\mathbf{W}_{RR} + P_{RR\Theta\Theta}\nabla\mathbf{W}_{\Theta\Theta} + P_{RRZZ}\nabla\mathbf{W}_{ZZ} \\ P_{\Theta R\Theta R}\nabla\mathbf{W}_{\Theta R} + P_{\Theta RR\Theta}\nabla\mathbf{W}_{R\Theta} \\ P_{ZRZR}\nabla\mathbf{W}_{ZR} + P_{ZRRZ}\nabla\mathbf{W}_{RZ} \end{pmatrix} = \mathbf{0}. \tag{6.4}$$

To leading order, the matrices $\{\mathbf{S}_1, \mathbf{S}_2, \mathbf{S}_3\}$ are constant over the boundary layer and equal

to their values at R_1. The same holds for their eigenvalues and eigenvectors. This suggests that diagonalising the leading order equations of (6.2) might simplify their solution, i.e.

$$\mathbf{S}_1 = \mathbf{E} \cdot \mathbf{D} \cdot \mathbf{E}^{-1}, \tag{6.5}$$

where $\mathbf{D}$ is diagonal and its first three eigenvalues $\{\lambda_1, \lambda_2, \lambda_3\}$ have negative real part. It can be shown the other three eigenvalues are $\{-\lambda_1, -\lambda_2, -\lambda_3\}$. We are careful to normalise $\mathbf{E}$ so that it is continuous and differentiable with respect to R. We let $\mathbf{V} = \mathbf{E}^{-1} \cdot \mathbf{W}$ be the solution vector corresponding to this diagonalisation. We expand the eigenvalues, eigenvectors and matrices with respect to ς^{-1} as follows

$$\begin{aligned} \mathbf{E} &= \mathbf{E}_0 + \varsigma^{-1} (\rho \mathbf{E}_R + t_1 \mathbf{E}_t) + \ldots, \\ \mathbf{D} &= \mathbf{D}_0 + \varsigma^{-1} (\rho \mathbf{D}_R + t_1 \mathbf{D}_t) + \ldots, \\ \lambda_j &= \lambda_j|_0 + \frac{\rho}{\varsigma} \frac{d\lambda_j}{dR} + \varsigma^{-1} t_1 \frac{d\lambda}{dt} + \ldots, \end{aligned} \tag{6.6}$$

where the derivatives are evaluated at R_1 and the asymptotic value of the critical time t^*. Further below we explain how to obtain t^* (the asymptotic limit of the critical time $t^*_{n,\omega}$ as $\varsigma \to \infty$).

We thus find

$$\varsigma^2 \mathbf{E}^{-1} \cdot \mathbf{W}' = \varsigma^2 \mathbf{D} \cdot \mathbf{E}^{-1} \cdot \mathbf{W} + \varsigma \mathbf{E}^{-1} \cdot \mathbf{S}_2 \cdot \mathbf{W} + \mathbf{E}^{-1} \cdot \mathbf{S}_3 \cdot \mathbf{W}, \tag{6.7}$$

and therefore

$$\varsigma^2 \mathbf{V}' = \varsigma^2 \mathbf{D} \cdot \mathbf{V} + \varsigma \left(\mathbf{E}^{-1} \cdot \mathbf{S}_2 \cdot \mathbf{E} + \frac{d}{dR} \left(\mathbf{E}^{-1} \right) \cdot \mathbf{E} \right) \cdot \mathbf{V} + \left(\mathbf{E}^{-1} \cdot \mathbf{S}_3 \cdot \mathbf{E} \right) \cdot \mathbf{V}, \tag{6.8}$$

where we have used the fact $\frac{d}{d\rho} = \varsigma^{-1} \frac{d}{dR}$. The leading order solution must satisfy

$$\mathbf{V}_0' = \mathbf{D}_0 \mathbf{V}_0. \tag{6.9}$$

In our solution of (6.9) we only keep the components of $\mathbf{V}_0$ corresponding to the eigenvalues

with negative real part, i.e.

$$V_{0,j} = V_j^0 \exp(\varsigma \lambda_j), \text{ if } j \in \{1,2,3\}, \text{ and} \tag{6.10}$$

$$V_{0,j} = 0 \text{ otherwise,} \tag{6.11}$$

where $\{V_j^0\}_{j=1}^3$ are constants. The reason for this is that we require the solution to be exponentially decaying as $\rho \to \infty$ in order that the boundary layer solution matches the outer solution. To see this we consider an expansion $\mathbf{W} = \mathbf{W}_0 + \varsigma^{-1}\mathbf{W}_1 + \ldots$ in the rest of the domain (the 'outer' solution). The $O(\varsigma^2)$ equation is

$$\mathbf{T}_1 \cdot \mathbf{W}_0 = \mathbf{0}, \tag{6.12}$$

necessitating that $\mathbf{W}_0 = \mathbf{0}$ to leading order. We subsequently find that $\mathbf{W}_j = \mathbf{0}$ for all other j. Asymptotic matching thus requires that $\{V_4, V_5, V_6\}$ are identically zero at leading order because their corresponding eigenvalues are positive (and thus the solution would diverge to ∞ as $\rho \to \infty$ if the coefficients were not zero). Substitution of (6.10) into the leading order of the boundary condition (6.4) yields an equation of the form

$$\mathbf{A} \cdot \begin{pmatrix} V_1^0 \\ V_2^0 \\ V_3^0 \end{pmatrix} = \mathbf{0}, \tag{6.13}$$

where $\mathbf{A}$ is determined by the incremental elastic moduli, β_1,β_2, $\mathbf{E}$ and the eigenvalues $\{\lambda_1, \lambda_2, \lambda_3\}$. The condition we use to solve for the asymptotic limit of the critical times t^* is that there is a nontrivial solution to (6.13), i.e.

$$|\mathbf{A}| = 0. \tag{6.14}$$

At the critical time, we assume the kernel of $\mathbf{A}$ is one-dimensional and spanned by the eigenvector $\mathbf{V}^0$.

6.0.5 Asymptotic Behaviour of Critical Time

In this section we obtain the next order of $\mathbf{V}$ and $\mathbf{W}$. We use this to determine t_1, which governs the asymptotic behaviour of the critical time as $\varsigma \to \infty$ (as explained further below). This expression for t_1 is needed in order that the leading order of the postbuckled equations in the following section may be solved.

The next order of $\mathbf{V}$ (i.e. $\mathbf{V}_1$) is a solution of the following equation

$$\mathbf{V}_1' = \mathbf{D}_0 \cdot \mathbf{V}_1 + \mathbf{D}_1 \cdot \mathbf{V}_0 + \left(\mathbf{E}_0^{-1} \cdot \mathbf{S}_2 \cdot \mathbf{E}_0 + \frac{d}{dR}\left(\mathbf{E}^{-1}\right) \cdot \mathbf{E}_0 \right) \cdot \mathbf{V}_0, \tag{6.15}$$

where we take the leading orders of $\mathbf{S}_2$ and $\frac{d}{dR}\mathbf{E}^{-1}$ (i.e. they are constant and equal to their values at R_1). Writing $\mathbf{B} = \mathbf{E}^{-1} \cdot \mathbf{S}_2 \cdot \mathbf{E} + \frac{d}{dR}\left(\mathbf{E}^{-1}\right) \cdot \mathbf{E}$ the j^{th} equation is

$$V_{1,j}' = \lambda_j V_{1,j} + B_{jk} V_k^0 \exp\left(\rho\lambda_k\right) + \left(t_1 \frac{d\lambda_j}{dt} + \rho \frac{d\lambda_j}{dR} \right) V_j^0 \exp\left(\rho\lambda_j\right), \tag{6.16}$$

where we sum over $k \in \{1,2,3\}$ and $1 \leq j \leq 6$. We find a particular solution to be

$$\begin{aligned} V_{1,j} &= V_k^0 B_{jk} \left(\lambda_k - \lambda_j\right)^{-1} \exp\left(\rho\lambda_k\right) + V_j^0 \left(B_{jj} + t_1 \frac{d\lambda_j}{dt} + \frac{\rho}{2} \frac{d\lambda_j}{dR} \right) \rho \exp\left(\rho\lambda_j\right) + V_j^{00} \exp\left(\rho\lambda_j\right), \\ &= V_k^0 B_{jk} \left(\lambda_k - \lambda_j\right)^{-1} + V_j^{00} \text{ at } \rho = 0, \end{aligned} \tag{6.17}$$

where we sum over all $k \in \{1,2,3\}$ and $k \neq j$, $\{V_1^{00}, V_2^{00}, V_3^{00}\}$ are undetermined constants and $V_4^{00} = V_5^{00} = V_6^{00} = 0$.

We thus find the $O(1)$ component of $\nabla\mathbf{W}$ at $R = R_1$ is

$$(\nabla\mathbf{W})_1 = t_1 X_1 + X_2, \tag{6.18}$$

where

$$X_1 = \sum_{j=1}^{3} V_j^0 \begin{pmatrix} E_{t,4j} & -\beta_1 R_1^{-1} E_{t,1j} & -\beta_2 E_{t,1j} \\ E_{t,5j} & \beta_1 R_1^{-1} E_{t,2j} & -\beta_2 E_{t,2j} \\ E_{t,6j} & -\beta_1 R_1^{-1} E_{t,3j} & \beta_2 E_{t,3j} \end{pmatrix},$$

$$X_2 = \sum_{j=1..6, k=1..3, k\neq j} B_{jk}(\lambda_k - \lambda_j)^{-1} V_k^0 \begin{pmatrix} E_{4j} & -\beta_1 R_1^{-1} E_{1j} & -\beta_2 E_{1j} \\ E_{5j} & \beta_1 R_1^{-1} E_{2j} & -\beta_2 E_{2j} \\ E_{6j} & -\beta_1 R_1^{-1} E_{3j} & \beta_2 E_{3j} \end{pmatrix} +$$

$$\sum_{j=1..3} V_j^0 \begin{pmatrix} 0 & -R_1^{-1} E_{2j} & 0 \\ 0 & R_1^{-1} E_{1j} & 0 \\ 0 & 0 & 0 \end{pmatrix} + \sum_{j=1}^{3} V_j^{00} \begin{pmatrix} E_{4j} & -\beta_1 R_1^{-1} E_{1j} & -\beta_2 E_{1j} \\ E_{5j} & \beta_1 R_1^{-1} E_{2j} & -\beta_2 E_{2j} \\ E_{6j} & -\beta_1 R_1^{-1} E_{3j} & \beta_2 E_{3j} \end{pmatrix}, \quad (6.19)$$

where $\{V_j^{00}\}$ are undetermined constants. We note that this is not the displacement gradient of $\mathbf{W}_1$. On substitution of this into the boundary condition we obtain an equation of the form

$$\kappa \mathbf{A}_1 + \mathbf{P}^{(0)} \cdot X_2 + t_1 \left(\frac{\partial \mathbf{P}^{(0)}}{\partial t} \cdot \nabla \mathbf{W}_0 + \mathbf{P}^{(0)} \cdot X_1 \right) = \mathbf{0}, \quad (6.20)$$

where $\mathbf{A}_1$ is in the span of $\mathbf{A}$ and κ is an undetermined constant. We dot multiply (6.20) with a vector perpendicular to the span of $\mathbf{A}$ to obtain t_1.

6.0.6 Boundary Layer Analysis in Model With Distinct Capillary Structure

In this case we may similarly apply a boundary layer analysis for large wavenumbers just as we did in the model without a distinct capillary wall structure. The only difference is that the boundary layer occurs in small neighbourhoods of R_0 (i.e. in V_c). Convergence requires the width of the boundary layer to be less than the width of the capillary. Since h/R_1 is of the order of 0.01, this means our boundary layer analysis only converges for n and ω) of the order of 100. Such high wavenumbers are beyond the accuracy of our model. In particular, they are highly incongruent with our approximation of the cells as a continuum. If we wanted to accurately model such fine oscillations we would require a highly sophisticated composite mechanical model of the cell. In practice it is much more likely that small inhomogeneities would dispose the system to buckles of smaller wavenumber.

6.0.7 Asymptotic Behaviour of PostBuckled Solution

We investigate the asymptotic behaviour of the second order displacement $\mathbf{u}_2^a$ as $\varsigma \to \infty$ and $n = \beta_1\varsigma$, $\omega = \beta_2\varsigma$. Recall that the field equation and boundary condition at R_1 for $\mathbf{u}_2^a$ is

$$\nabla \cdot \left(\frac{\partial \mathbf{P}}{\partial \mathbf{F}} : \nabla \mathbf{u}_2^a \right) = -\nabla \cdot \left(\frac{\partial^2 \mathbf{P}}{\partial \mathbf{F}^2} : \nabla \mathbf{u}^{(n,\omega)} : \nabla \mathbf{u}^{(n,\omega)} \right) \text{ over } V_m, \tag{6.21}$$

$$\left(\frac{\partial \mathbf{P}}{\partial \mathbf{F}} : \nabla \mathbf{u}_2^a + \frac{\partial^2 \mathbf{P}}{\partial \mathbf{F}^2} : \nabla \mathbf{u}^{(n,\omega)} : \nabla \mathbf{u}^{(n,\omega)} \right) \cdot \mathbf{n} = \mathbf{0}. \tag{6.22}$$

We are solving for $\mathbf{u}_2^a$ in the neighbourhood of the asymptotic limit t^* of the critical times (which we determine using the method outlined in the previous section). We stipulate the magnitude of the leading order of the asymptotic expansion of the homogeneous solution $\mathbf{u}^{(n,\omega)}$ to be ς^{-1} (the magnitude is undetermined). Note that $\mathbf{u}_2^a$ has nontrivial components in the subspaces $\{U_{0,0}, U_{2n,0}, U_{0,2\omega}, U_{2n,2\omega}\}$. Note that if $n = 0$ or $\omega = 0$ then there are only two distinct subspaces in the previous list.

In fact $\mathbf{u}_2|_{2n,2\omega}$ dominates[1] the other components of $\mathbf{u}_2$ as $\varsigma \to \infty$. This is because in the asymptotic limit, (n, ω) is indistinguishable from $(2n, 2\omega)$, which means that the leading order of the asymptotic equations equations governing $\mathbf{u}|_{2n,2\omega}$ are singular. More precisely, there is a nontrivial solution to the following system over the boundary layer,

$$\nabla \cdot \left(\frac{\partial \mathbf{P}}{\partial \mathbf{F}} : \nabla \mathbf{u}_2^a|_{2n,2\omega} \right) = \mathbf{0} \text{ over } V_m, \tag{6.23}$$

$$\left(\frac{\partial \mathbf{P}}{\partial \mathbf{F}} : \nabla \mathbf{u}_2^a|_{2n,2\omega} \right) \cdot \mathbf{n} = \mathbf{0}. \tag{6.24}$$

This follows from the fact that the leading order of (6.23) is the same as the leading order of (6.2), and the leading order of (6.24) is the same as the leading order of (6.4). This means that we require $\mathbf{u}_2^a|_{2,2n,2\omega}$ to have leading asymptotic order of 1 for (6.21) and (6.22) to be well-matched. The other components - $\mathbf{u}_2^a|_{0,0}$, $\mathbf{u}_2^a|_{2n,0}$ and $\mathbf{u}_2^a|_{0,2\omega}$ - all have leading asymptotic order ς^{-1} and can be neglected in the asymptotic limit.

We now obtain an explicit expression for the leading order of $\mathbf{u}_2^a|_{2n,2\omega}$. We adopt the

[1] Recall that $\mathbf{v}|_{\beta_1,\beta_2}$ denotes the projection of $\mathbf{v}$ onto U_{β_1,β_2}.

scaling

$$R = R_1 + \frac{\gamma}{2\varsigma}, \tag{6.25}$$

so that $\frac{d}{dR} = 2\varsigma\frac{d}{d\gamma}$. For convenience we use similar notation to the previous section, so that $\mathbf{W} = (W_{2n,2\omega}, V_{2n,2\omega}, Z_{2n,2\omega}, W_{2n,2\omega,\gamma}, V_{2n,2\omega,\gamma}, Z_{2n,2\omega,\gamma})^T$ where $(W_{2n,2\omega}, V_{2n,2\omega}, Z_{2n,2\omega})^T$ are the components of $\mathbf{u}_2^a|_{2n,2\omega}$. The differentiation is with respect to γ. The $\mathrm{O}((2\varsigma)^2)$ and $\mathrm{O}(2\varsigma)$ terms in the field equation governing $\mathbf{W}$ are of the form

$$(2\varsigma)^2\mathbf{W}_\gamma = (2\varsigma)^2\mathbf{S}_1\cdot\mathbf{W} + 2\varsigma\mathbf{S}_2\cdot\mathbf{W} + \mathbf{S}_3\cdot\mathbf{W} + 2\varsigma\mathbf{E}\sum_{1\le l,m\le 3}\mathbf{F}_{lm}\exp\left(\frac{\gamma}{2}(\lambda_l+\lambda_m)\right). \tag{6.26}$$

We obtain an explicit expression for $\mathbf{F}_{lm}$ by taking the leading order of the divergence in cylindrical coordinates (see (A.72)). Let

$$\mathbf{P}_{lm} = \frac{\partial^2\mathbf{P}}{\partial\mathbf{F}^2} : \nabla\mathbf{u}_l^i : \nabla\mathbf{u}_m^i, \tag{6.27}$$

where

$$\nabla\mathbf{u}_m^i = V_m^0\begin{pmatrix} E_{4m} & -\beta_1 R^{-1}E_{1m} & -\beta_2 E_{1m} \\ E_{5m} & \beta_1 R^{-1}E_{2m} & -\beta_2 E_{2m} \\ E_{6m} & -\beta_1 R^{-1}E_{3m} & \beta_2 E_{3m}\end{pmatrix}. \tag{6.28}$$

We consequently find

$$\mathbf{F}_{lm} = -\mathbf{E}^{-1}\cdot\begin{pmatrix} 0 \\ 0 \\ 0 \\ \frac{1}{2}(\lambda_l+\lambda_m)P_{lm,RR} + \frac{\beta_1}{R_1}P_{lm,R\Theta} + \beta_2 P_{lm,RZ} \\ \frac{1}{2}(\lambda_l+\lambda_m)P_{lm,\Theta R} - \frac{\beta_1}{R_1}P_{lm,\Theta\Theta} + \beta_2 P_{lm,\Theta Z} \\ \frac{1}{2}(\lambda_l+\lambda_m)P_{lm,ZR} + \frac{\beta_1}{R_1}P_{lm,Z\Theta} - \beta_2 P_{lm,ZZ}\end{pmatrix}. \tag{6.29}$$

The boundary condition at R_1 is

$$\mathbf{P}^{(0)}\cdot\nabla\mathbf{W} = -\left(\frac{\partial^2\mathbf{P}}{\partial\mathbf{F}^2} : \nabla\mathbf{u}^{(n,\omega)} : \nabla\mathbf{u}^{(n,\omega)}\right)\cdot\mathbf{n}|_{2n,2\omega}. \tag{6.30}$$

As previously, we let $\mathbf{V} = \mathbf{E}^{-1}\mathbf{W}$, and expand

$$W = W_0 + \varsigma^{-1} W_1 + \dots \tag{6.31}$$

$$V = V_0 + \varsigma^{-1} V_1 + \dots, \tag{6.32}$$

taking care not to confuse these variables with their counterparts in the previous section. The leading order component of $\mathbf{V}$ must be a solution of (6.23) and (6.24), so that it is a multiple of (6.10), i.e.

$$V_{0,j} = x_0 V_j^0 \exp(\lambda_j \gamma) \text{ for } 1 \le j \le 3, \tag{6.33}$$

for some constant x_0. The first three elements of $\mathbf{V}^0$ are the eigenvector of $\mathbf{A}$ in (6.13) and $V_4^0 = V_5^0 = V_6^0 = 0$. We determine the constant x_0 by considering the next order of the equations as follows.

We recall that the asymptotic expansion of the buckling time is

$$\begin{aligned} t =& t^* + \varsigma^{-1} t_1 + \dots \\ =& t^* + (2\varsigma)^{-1} (2t_1). \end{aligned} \tag{6.34}$$

The factor of 2 arises because the critical time of buckling is that corresponding to the buckle in $U_{n,\omega}$, but the equations governing $\mathbf{u}_{2,2n}$ are over $U_{2n,2\omega}$. We thus find the next order of the field equations is

$$\begin{aligned} V_{1,j}' = & \lambda_j V_{1,j} + x_0 B_{jk} V_k^0 \exp(\gamma \lambda_k) \\ & + x_0 \left(2t_1 \frac{d\lambda_j}{dt} + \gamma \frac{d\lambda_j}{dR} \right) V_j^0 \exp(\gamma \lambda_j) + \sum_{1 \le l \le m \le 3} F_{lm} \exp\left(\frac{\gamma}{2} (\lambda_l + \lambda_m) \right) \end{aligned} \tag{6.35}$$

where B_{jk} is defined in the previous section. Upon integration we find

$$\begin{aligned} V_{1,j} = & x_0 B_{jk} V_k^0 (\lambda_k - \lambda_j)^{-1} e^{\gamma \lambda_k} + x_0 V_j^0 \left(B_{jj} + 2t_1 \frac{d\lambda_j}{dt} + \frac{\gamma}{2} \frac{d\lambda_j}{dR} \right) \gamma e^{\gamma \lambda_j} + V_j^{00} e^{\gamma \lambda_j} \\ & + \sum_{1 \le l,m \le 3} \left(\frac{1}{2} (\lambda_l + \lambda_m) - \lambda_j \right)^{-1} F_{lm,j} \exp\left(\frac{\gamma}{2} (\lambda_l + \lambda_m) \right) \end{aligned} \tag{6.36}$$

$$= x_0 B_{jk} V_k^0 (\lambda_k - \lambda_j)^{-1} + \sum_{1 \le l,m \le 3} \left(\frac{1}{2} (\lambda_l + \lambda_m) - \lambda_j \right)^{-1} F_{lm,j} + V_j^{00} \text{ at } \gamma = 0, \tag{6.37}$$

where we sum over all $l, m \in \{1, 2, 3\}$ except when $l + m \neq 2j$. Here V_j^{00} are undetermined coefficients corresponding to the homogeneous solution of the previous section. We thus find the $O(1)$ component of $\nabla \mathbf{W}$ is

$$(\nabla \mathbf{W})_1 = x_0 Y_1 + Y_2, \tag{6.38}$$

at $R = R_1$, where

$$\begin{aligned}
Y_1 = {} & 2t_1 \sum_{j=1}^{3} V_j^0 \begin{pmatrix} E_{t,4j} & -\beta_1 R_1^{-1} E_{t,1j} & -\beta_2 E_{t,1j} \\ E_{t,5j} & \beta_1 R_1^{-1} E_{t,2j} & -\beta_2 E_{t,2j} \\ E_{t,6j} & -\beta_1 R_1^{-1} E_{t,3j} & \beta_2 E_{t,3j} \end{pmatrix} + \sum_{j=1}^{3} V_j^0 \begin{pmatrix} 0 & -R_1^{-1} E_{2j} & 0 \\ 0 & R_1^{-1} E_{1j} & 0 \\ 0 & 0 & 0 \end{pmatrix}, \\
& + \sum_{j=1\ldots6, k=1\ldots3, k\neq j} B_{jk} \left(\lambda_k - \lambda_j\right)^{-1} V_k^0 \begin{pmatrix} E_{4j} & -\beta_1 R_1^{-1} E_{1j} & -\beta_2 E_{1j} \\ E_{5j} & \beta_1 R_1^{-1} E_{2j} & -\beta_2 E_{2j} \\ E_{6j} & -\beta_1 R_1^{-1} E_{3j} & \beta_2 E_{3j} \end{pmatrix} \\
Y_2 = {} & \sum_{j=1..6, 1\leq l,m\leq 3} F_{lm,j} \left(\frac{1}{2}\left(\lambda_l + \lambda_m\right) - \lambda_j\right)^{-1} \begin{pmatrix} E_{4j} & -\beta_1 R_1^{-1} E_{1j} & -\beta_2 E_{1j} \\ E_{5j} & \beta_1 R_1^{-1} E_{2j} & -\beta_2 E_{2j} \\ E_{6j} & -\beta_1 R_1^{-1} E_{3j} & \beta_2 E_{3j} \end{pmatrix}, + \\
& + \sum_{j=1}^{3} V_j^{00} \begin{pmatrix} E_{4j} & -\beta_1 R_1^{-1} E_{1j} & -\beta_2 E_{1j} \\ E_{5j} & \beta_1 R_1^{-1} E_{2j} & -\beta_2 E_{2j} \\ E_{6j} & -\beta_1 R_1^{-1} E_{3j} & \beta_2 E_{3j} \end{pmatrix},
\end{aligned} \tag{6.39}$$

where $\{V_j^{00}\}$ are undetermined constants and in the penultimate summation $l + m \neq 2j$. We note that this is not the displacement gradient of $\mathbf{W}_1$. On substitution of this into the boundary condition we obtain an equation of the form

$$\kappa_2 \mathbf{A}_1 + x_0 \left(\mathbf{P}^{(0)} \cdot Y_1 + 2t_1 \frac{\partial \mathbf{P}^{(0)}}{\partial t} \cdot \nabla \mathbf{W}_0\right) + \mathbf{P}^{(0)} \cdot Y_2 + \left(\frac{\partial^2 \mathbf{P}}{\partial \mathbf{F}^2} : \nabla \mathbf{u}^{(n,\omega)} : \nabla \mathbf{u}^{(n,\omega)}\right) \cdot \mathbf{n}|_{2n,2\omega} = \mathbf{0}, \tag{6.40}$$

where $\mathbf{A}_1$ is in the span of $\mathbf{A}$ and κ_2 is an undetermined constant. We dot (6.40) with a nonzero vector perpendicular to the span of $\mathbf{A}$ to obtain x_0.

6.0.8 Asymptotic Behaviour of the Integrals Governing the Postbuckled Solution

We have seen in Section 4.2 that the postbuckling behaviour is governed by the following body integrals

$$
\begin{aligned}
C_1 &= \iiint_{V_m} \left(\frac{1}{6} \frac{\partial^3 \mathbf{P}}{\partial \mathbf{F}^3} : \nabla \mathbf{u}^{(n,\omega)} : \nabla \mathbf{u}^{(n,\omega)} : \nabla \mathbf{u}^{(n,\omega)} + \frac{1}{2} \frac{\partial^2 \mathbf{P}}{\partial \mathbf{F}^2} : \nabla \mathbf{u}^{(n,\omega)} : \nabla \mathbf{u}_2^a \right) : \nabla \mathbf{u}^{(n,\omega)} dV, \\
C_2 &= \iiint_{V_m} \left(\frac{1}{2} \frac{\partial^2 \mathbf{P}}{\partial \mathbf{F}^2} : \nabla \mathbf{u}_2^p : \nabla \mathbf{u}^{(n,\omega)} + \frac{1}{2} \frac{\partial^2 \mathbf{P}}{\partial \mathbf{F} \partial \zeta_\alpha} : \nabla \mathbf{u}^{(n,\omega)} \zeta_{\alpha,2}^* \right) : \nabla \mathbf{u}^{(n,\omega)} dV, \\
C_3 &= \frac{1}{2} \iiint_{V_m} \frac{\partial \mathbf{P}}{\partial \zeta_\alpha} : \nabla \mathbf{u}^{(n,\omega)} \zeta_{\alpha,0} \left(G_{\alpha,0} \left(\frac{c^{(n,\omega)}}{k_c} \left(1 + \frac{c_0}{k_c} \right)^{-2} \right) + G_{\alpha,1}^{(n,\omega)} \left(\frac{c_0}{k_c + c_0} \right) \right) dV.
\end{aligned}
\tag{6.41}
$$

Since $\mathbf{u}^{(n,\omega)}$ and $\mathbf{u}_2$ are both zero (in the asymptotic limit) outside the boundary layer, the asymptotic limit of these integrals converges to their integral over the boundary layer. The integral over the boundary layer may be written in the form

$$
\varsigma^{-1} \sum_{i=1}^{3} \int_0^\infty f e^{\rho \lambda_i} d\rho, \tag{6.42}
$$

for some function f. The ς^{-1} is there because we are integrating with respect to ρ instead of R. As originally defined, this function is a function of R, which means that to leading order f is constant, i.e.

$$
f = f(R_1) + \frac{\rho}{\varsigma} f'(R_1) + \dots \tag{6.43}
$$

Thus the leading order of (6.42) is

$$
-\varsigma^{-1} \sum_{i=1}^{3} f(R_1) \lambda_i^{-1}. \tag{6.44}
$$

The leading asymptotic orders of $\nabla \mathbf{u}^{(n,\omega)}$ and $\nabla \mathbf{u}_2^a|_{2n,2\omega}$ are

$$
\begin{aligned}
\nabla \mathbf{u}^{(n,\omega)} &= \sum_j \nabla \mathbf{u}_j^i, \\
\nabla \left(\mathbf{u}_2|_{2n,2\omega} \right) &= 2 x_0 \varsigma \sum_j \nabla \mathbf{u}_j^i,
\end{aligned}
\tag{6.45}
$$

where

$$\nabla \mathbf{u}_j^i = V_j^0 \begin{pmatrix} E_{4j} & -\beta_1 R_1^{-1} E_{1j} & -\beta_2 E_{1j} \\ E_{5j} & \beta_1 R_1^{-1} E_{2j} & -\beta_2 E_{2j} \\ E_{6j} & -\beta_1 R_1^{-1} E_{3j} & \beta_2 E_{3j} \end{pmatrix}. \tag{6.46}$$

The expressions in (6.45) give the components of the deformation gradient with respect to $T_{n,\omega}$ (for $\nabla \mathbf{u}^{(n,\omega)}$) and $T_{2n,2\omega}$ (for $\nabla \mathbf{u}_2|_{2n,2\omega}$). In the asymptotic limit, C_2 is dominated by

$$\iiint_{V_m} \frac{\partial^3 \psi}{\partial \mathbf{F}^3} : \nabla \mathbf{u}^{(n,\omega)} : \nabla \mathbf{u}^{(n,\omega)} : \nabla \mathbf{u}_2^a dV. \tag{6.47}$$

The leading asymptotic order of (6.47) is

$$-4\pi x_0 R_1 Z_0 \left(\sum_{j,k,l=1}^{3} \frac{1}{s(j,k,l)} \frac{\partial^3 \psi}{\partial \mathbf{F}^3} : \nabla \mathbf{u}_j^i : \nabla \mathbf{u}_k^i : \nabla \mathbf{u}_l^i \right), \tag{6.48}$$

where $s(j,k,l) = 2\lambda_j + \lambda_k + \lambda_l$. Similarly the leading order of

$$\iiint_{V_m} \frac{\partial^3 \psi}{\partial \mathbf{F}^3} : \nabla \mathbf{u}^{(n,\omega)} : \nabla \mathbf{u}^{(n,\omega)} : \nabla \mathbf{u}_2^p dV \tag{6.49}$$

is

$$-2\pi R_1 Z_0 \varsigma^{-1} \sum_{j,k=1}^{3} \frac{1}{\lambda_j + \lambda_k} \frac{\partial^3 \psi}{\partial \mathbf{F}^3} : \nabla \mathbf{u}_j^i : \nabla \mathbf{u}_k^i : \nabla \mathbf{u}_2^p. \tag{6.50}$$

The leading order of

$$\iiint_{V_m} \frac{\partial^3 \psi}{\partial \mathbf{F}^2 \partial \zeta} : \nabla \mathbf{u}^{(n,\omega)} : \nabla \mathbf{u}^{(n,\omega)} \delta\zeta dV \tag{6.51}$$

is

$$-2\pi R_1 Z_0 \delta\zeta \varsigma^{-1} \sum_{j,k=1}^{3} \frac{1}{\lambda_j + \lambda_k} \frac{\partial^3 \psi}{\partial \mathbf{F}^2 \partial \zeta} : \nabla \mathbf{u}_j^i : \nabla \mathbf{u}_k^i. \tag{6.52}$$

Writing

$$G_{\alpha,1}|_{n,\omega} \simeq \sum_{i=1}^{3} H_{\alpha,i}^* e^{\rho \lambda_i} \cos(n\Theta) \cos(\omega Z), \tag{6.53}$$

we find

$$C_3 \simeq -\pi R_1 \left(\frac{n_0}{k_c + n_0} \right) \zeta_{\alpha,0} \sum_{i,j=1}^{3} \frac{H_{\alpha,i}^*}{\lambda_i + \lambda_j} \frac{\partial \mathbf{P}}{\partial \zeta_\alpha} : \nabla \mathbf{u}_j^i. \tag{6.54}$$

Asymptotic Behaviour of the Incremental Nutrient Solution

It can be shown that the leading order of the increment in the nutrient distribution c_1 is $O(\varsigma^{-1})$. This means the contribution of c_1 to C_3 is negligble in the asymptotic limit.

Chapter 7

Numerical Solution of Incremental Equations

In this chapter we outline the numerical method used to solve the incremental (buckled) equations outlined in Chapters 4 and 5. We note that we have already outlined our numerical method for the fundamental solution in Chapter 3.

7.1 Numerical Solution of Incremental Equations

We begin by summarising the system to be solved. We may write the system of ordinary differential equations governing the perturbation in the displacement over the tumour body (V_m) in the form (4.31)

$$\tilde{\mathbf{u}}' = \mathbf{L}^{n,\omega} \cdot \tilde{\mathbf{u}}, \tag{7.1}$$

Key	Geometry	Description
A	Finite	Null Displacement and zero nutrient flux at $R = R_2$.
C	Infinite	$[R_2, \infty)$ is linearly elastic, zero nutrient flux at $R = R_2$.
F	Infinite	Nutrient Distribution and Displacement decay to 0 as $R \to \infty$.
G	Infinite	$\frac{\partial c}{\partial R} = 0$ at $R = R_2$ and $c(R) = c(R_2)$ for $R > R_2$. $\mathbf{P} \to \mathbf{0}$ as $R \to \infty$.

Table 7.1: The various boundary conditions and geometries. The radius of the cavity (which represents the capillary) is R_1. If the geometry is finite, the outer radius of the tumour annulus is R_2. At $R = R_1$, we equate the traction and displacement, i.e. $\mathbf{u}|_- = \mathbf{u}|_+$ and $\mathbf{P}|_- \cdot \mathbf{n} = \mathbf{P}|_+ \cdot \mathbf{n}$. The (scaled) nutrient concentration at R_1 is $n = 1$. There is no traction $\mathbf{P} \cdot \mathbf{n} = \mathbf{0}$ at R_0.

where $\mathbf{L}^{n,\omega}$ depends on R, the fundamental solution (u_0, p_0) and the growth ζ_α. Here $\tilde{\mathbf{u}} = (W_{n,\omega}, W'_{n,\omega}, V_{n,\omega}, V'_{n,\omega}, Z_{n,\omega}, Z'_{n,\omega})^T$, where $\{W_{n,\omega}, V_{n,\omega}, Z_{n,\omega}\}$ are respectively the radial, azimuthal and axial components of an incremental solution with azimuthal mode n and axial mode ω. We determine $\mathbf{L}^{n,\omega}$ using MAPLE. Over the capillary wall V_c, the governing equations are of the form

$$\tilde{\mathbf{u}}' = \mathbf{L}_c^{n,\omega} \cdot \tilde{\mathbf{u}}, \tag{7.2}$$

where $\tilde{\mathbf{u}} = (W_{n,\omega}, X_{n,\omega}, V_{n,\omega}, V'_{n,\omega}, Z_{n,\omega}, Z'_{n,\omega})^T$. Here $X_{n,\omega}$ is the component of the Lagrange Multiplier. Note that $\tilde{\mathbf{u}}$ is defined differently over the capillary compared to the tumour. We determine $\mathbf{L}^{n,\omega}$ using MAPLE and outline the components of $\mathbf{L}_c^{n,\omega}$ in (D.1) in Appendix D.1. There are a variety of boundary conditions we consider, depending on the model variant.

Over the capillary, the derivative of $W_{n,\omega}$ is obtained using the incompressibility condition (5.8), i.e.

$$\frac{\partial W_{n,\omega}}{\partial R} = -R^{-1}\left(1 + \frac{\partial u_0}{\partial R}\right)^2 (nV_{n,\omega} + W_{n,\omega}) - \omega\left(1 + \frac{\partial u_0}{\partial R}\right) Z_{n,\omega}. \tag{7.3}$$

The derivatives of the variables $\{V'_{n,\omega}, Z'_{n,\omega}, X_{n,\omega}\}$ are obtained using (respectively) the azimuthal, axial and radial components of the force balance (4.31) over V_c. The expression for the derivative of $X_{n,\omega}$ involves a double derivative of $W_{n,\omega}$. We obtain this by analytically differentiating the above expression for $W'_{n,\omega}$, i.e.

$$\begin{aligned}\frac{\partial^2 W_{n,\omega}}{\partial R^2} = &-R^{-1}\left(1 + \frac{\partial u_0}{\partial R}\right)^2 \left(n\frac{\partial V_{n,\omega}}{\partial R} + \frac{\partial W_{n,\omega}}{\partial R}\right) \\ &+ (nV_{n,\omega} + W_{n,\omega})\left(R^{-2}\left(1 + \frac{\partial u_0}{\partial R}\right)^2 - 2R^{-1}\left(1 + \frac{\partial u_0}{\partial R}\right)\frac{\partial^2 u_0}{\partial R^2}\right) \\ &- \omega\left(\frac{\partial^2 u_0}{\partial R^2} Z_{n,\omega} + \left(1 + \frac{\partial u_0}{\partial R}\right) Z'_{n,\omega}\right).\end{aligned} \tag{7.4}$$

After substituting the identity for $\frac{\partial W_{n,\omega}}{\partial R}$, we find

$$\frac{\partial^2 W_{n,\omega}}{\partial R^2} = -n\frac{\partial V_{n,\omega}}{\partial R}R^{-1}\left(1+\frac{\partial u_0}{\partial R}\right)^2 + (W_{n,\omega}+nV_{n,\omega})\left(R^{-2}\left(1+\frac{\partial u_0}{\partial R}\right)^2 - 2R^{-1}\left(1+\frac{\partial u_0}{\partial R}\right)\frac{\partial^2 u_0}{\partial R^2} + R^{-2}\left(1+\frac{\partial u_0}{\partial R}\right)^4\right) + \omega R^{-1}\left(1+\frac{\partial u_0}{\partial R}\right)^3 Z_{n,\omega} - \omega\left(\frac{\partial^2 u_0}{\partial R^2}Z_{n,\omega} + \left(1+\frac{\partial u_0}{\partial R}\right)Z'_{n,\omega}\right). \quad (7.5)$$

At R_1, we equate the displacements and stresses in the capillary and tumour. We write this as

$$\mathbf{P}_{inc}^{n,\omega,-}\cdot\tilde{\mathbf{u}}^- = \mathbf{P}_{inc}^{n,\omega,+}\cdot\tilde{\mathbf{u}}^+. \quad (7.6)$$

Here $\tilde{\mathbf{u}}^-$ is in the capillary wall and $\tilde{\mathbf{u}}^+$ is in the tumour. We outline the structure of $\mathbf{P}_{inc}^{n,\omega,-}$ and $\mathbf{P}_{inc}^{n,\omega,+}$ (which are 6×6 matrices) in (D.4) in Appendix D.1. The null stress boundary condition at R_0 may be written as

$$\mathbf{P}_0^{n,\omega}\cdot\tilde{\mathbf{u}} = \mathbf{0}, \quad (7.7)$$

where $\mathbf{P}_0^{n,\omega}$ is also defined in Appendix D.1.

7.1.1 Method of Numerical Solution for Finite Geometry

We consider the solution of the incremental equations over the finite annulus first. In this case, the solution space of vectors satisfying the boundary condition at $R = R_2$ is of three dimensions. Our method of solution is as follows. We find three different solutions by stipulating three linearly independent starting values for $\mathbf{u}$ at R_2 and integrating to R_1. Each of these solutions satisfies the boundary condition at R_2. Since the system is linear, any linear combination of these three solutions is also a solution. We define $\mathbf{U}(R)$ to be the solution matrix, with each column one of these solutions. A buckled solution exists if a linear combination of these three solutions satisfies the boundary condition at R_1. That is, there is a nontrivial solution to the incremental equations if there exists a vector $\mathbf{m}$ such that $\tilde{\mathbf{u}} = \mathbf{U}\cdot\mathbf{m}$, and

$$\left(\frac{\partial \mathbf{P}}{\partial \mathbf{F}} : \nabla\mathbf{u}\right)\cdot\mathbf{n} = \mathbf{P}_{inc}^{n}\cdot\mathbf{U}\cdot\mathbf{m} = \mathbf{0} \text{ at } R = R_1. \quad (7.8)$$

One possible numerical method is to integrate (7.1) from R_2 to R_1. The existence of a solution could be determined according to whether the determinant of $\mathbf{P}_{inc}^{n} \cdot \mathbf{U}$ is zero. This method is known as the *determinant* method [71, 72]. However there are severe numerical instabilities with this method, which become particularly acute for large n or ω (see for example Davey [46]). The boundary layer analysis in Chapter 6 sheds light on this fact. Over the boundary layer, the leading asymptotic order of the solution is a sum of terms of order $\exp(\varsigma\lambda_i)$, where $i = 1, 2, 3$, with $Re(\lambda_1) < Re(\lambda_2) < Re(\lambda_3) < 0$ and ς gives the order of magnitude of (n, ω). We could in fact have performed this asymptotic expansion throughout the entire R domain, an analysis known as a WKB expansion. We must resolve both terms to implement the buckling condition. Let us suppose we require the relative error in each term to be δ. Since we are integrating in the negative direction, the $\exp(\omega\lambda_1)$ term grows much more rapidly than the $\exp(\omega\lambda_2)$ term. Resolution of the subdominant $\exp(\omega\lambda_2)$ term to a relative accuracy of δ thus requires resolution of the sum of the two terms to an accuracy of order $\delta \exp(\omega(\lambda_1 - \lambda_2))$. Thus the required accuracy grows rapidly as n increases.

A similar argument shows why we must integrate from R_2 to R_1 rather than from R_1 to R_2. Over the boundary layer we saw that the system has three positive $\{\varsigma\lambda_4, \varsigma\lambda_5, \varsigma\lambda_6\}$ and three negative eigenvalues $\{\varsigma\lambda_1, \varsigma\lambda_2, \varsigma\lambda_3\}$ (where ς is of the order of the maximum of $\{n, \omega\}$). We are required to resolve the three negative eigenvalues. However if we were to integrate in the positive direction, then the positive eigenvalues would dominate the negative ones, and errors would grow exponentially. However when we integrate in the negative direction, the three negative eigenvalues dominate, and the undesired positive eigenvalues decay exponentially.

The method of compound matrices provides us with a means to circumvent the difficulties associated with the determinant method. Refer to Ng and Reid [107] for a more full discussion of this method. Instead of integrating the individual solution directly, we

integrate the *minors* of the matrix $\mathbf{U}$. We ennumerate the twenty 3×3 minors of U as

$$y_{ijk} = \begin{vmatrix} U_i \\ U_j \\ U_k \end{vmatrix}, \tag{7.9}$$

where U_i is the i^{th} row of $\mathbf{U}$. The minors $\{y_{c,ijk}\}$ over the capillary wall V_c are defined similarly. We find the values of $\{y_{ijk}\}$ at R_2 by stipulating that the columns of $\mathbf{U}$ must initially be independent of each other, and each column must satisfy the boundary condition at R_2. The evolution of the minors is governed by

$$\mathbf{y}' = \mathbf{B} \cdot \mathbf{y}, \tag{7.10}$$

$$\mathbf{y}_c' = \mathbf{B}_c \cdot \mathbf{y}_c, \tag{7.11}$$

where $\mathbf{B}$ and $\mathbf{B}_c$ are 20×20 matrices which depend linearly on $\mathbf{L}$ and $\mathbf{L}_c$ respectively. The structure of these matrices is outlined in Reid and Ng [107]. We integrate $\mathbf{y}$ from R_2 to R_1 using (7.10). We rearrange the boundary condition at R_1 to be of the form

$$\tilde{\mathbf{u}}^- = \mathbf{Q}_{inc}^{n,\omega} \cdot \tilde{\mathbf{u}}^+, \tag{7.12}$$

where $\mathbf{Q}_{inc}^{n,\omega} = \left(\mathbf{P}_{inc}^{n,\omega,-}\right)^{-1} \cdot \mathbf{P}_{inc}^{n,\omega,+}$. We use (7.12) to obtain an expression for the minors $\{y_{c,ijk}\}_{i<j<k}$ of $\tilde{\mathbf{u}}^-$ in terms of the minors $\{y_{ijk}\}_{i<j<k}$ of $\tilde{\mathbf{u}}^+$ at R_1. Let $\mathbf{Q}_{ijk,lmn}$ be the 3×3 matrix with first row the i^{th} row of $\mathbf{Q}_{inc}^{n,\omega}$, second row the j^{th} row of $\mathbf{Q}_{inc}^{n,\omega}$ and third row the k^{th} row of $\mathbf{Q}_{inc}^{n,\omega}$, and similarly first column the l^{th} column, second column the m^{th} column and third column the n^{th} column of $\mathbf{Q}_{inc}^{n,\omega}$. Let $Q_{ijk,lmn}$ be the determinant of this matrix. Making use of the determinant theorem of Laplace, we thus have

$$y_{c,ijk} = \sum_{0 \le l < m < n \le 6} Q_{ijk,lmn} y_{lmn}. \tag{7.13}$$

Using (7.13) as a starting value, we may then integrate the minors $y_{c,ijk}$ from R_1 to R_0.

Through an application of the determinant theorem of Laplace, it follows from (7.7) that

$$\sum_{1\leq i<j<k\leq 6} P_{ijk} y_{c,ijk} = 0, \tag{7.14}$$

where $\{P_{ijk}\}$ are the minors of $\mathbf{P}_{0,n,\omega}$ (which is given in (7.7)).

This method is much more accurate than the determinant method because we do not need to resolve a subdominant solution. It can be shown that the eigenvalues of $\mathbf{B}$ in (7.10) are the pairwise sums $\{\gamma_i + \gamma_j\}$ $(i \neq j)$ of the eigenvalues $\{\gamma_i\}$ of $\mathbf{L}^{n,\omega}$ in the original differential equation (in (7.1)) [46]. We thus expect the leading order of the minors $\mathbf{y}$ to be[1] $\exp(\varsigma(\lambda_1 + \lambda_2))$. However it can be seen from our asymptotic analysis in Section 6.0.4 that the determinant of $\mathbf{P}^n_{inc} \cdot \mathbf{U}$ at R_1 is also of this order. Thus we are not required to resolve a subdominant solution and therefore the method of compound matrices is much better conditioned than the determinant method.

We obtain $\tilde{\mathbf{u}}$ from our solution of the minors $\{y_{c,ijk}\}$ by integrating back from R_0 to R_2. To obtain the starting values of $\mathbf{u}$ at R_0, we note that three of the equations are given by

$$\mathbf{P}_{0,n,\omega} \cdot \tilde{\mathbf{u}} = \mathbf{0}, \tag{7.15}$$

and three other equations are given by the identities (which are proven in [107])

$$y_{c,234}u_1 - y_{c,134}u_2 + y_{124}u_3 - y_{123}u_4 = 0, \tag{7.16}$$

$$y_{c,345}u_2 - y_{c,245}u_3 + y_{c,235}u_4 - y_{c,234}u_5 = 0, \tag{7.17}$$

$$y_{c,456}u_3 - y_{c,356}u_4 + y_{c,346}u_5 - y_{c,345}u_6 = 0. \tag{7.18}$$

On first appearances it might seem that we may simply use the governing equations stipulated earlier when we integrate to find $\tilde{\mathbf{u}}$. However we noted previously that this system has three large positive eigenvalues. Thus when we integrate in the positive direction over a large R domain, errors grow exponentially, whereas our desired solution typically decays exponentially. We thus use the minors to find an alternative expression for the governing

[1]This can also be seen from the fact the $\exp(\varsigma\lambda_1)$ component of $\mathbf{u}$ must be a multiple of the $\exp(n\lambda_1)$ component of $\mathbf{v}$, and therefore the $\exp(2\varsigma\lambda_1)$ component of $\mathbf{y}$ must be zero through the additive property of determinants.

ordinary differential equation. This method is outlined at the end of Appendix D.2 and the ordinary differential equations are given in (D.42).

7.1.2 Method of Solution for Infinite Medium

We essentially have two infinite medium models: one in which the nutrient is constant for $r > R_2$ (model G), and one in which the nutrient decays to zero as $R \to \infty$ (model F). The third infinite medium model (C) may be solved in a very similar manner to model F: we do not consider this here but detail it further below. In all of the infinite medium models, the deformation gradient and growth (corresponding to the fundamental solution) asymptote to constants, which means that the incremental elastic moduli $\{P_{\alpha\beta\gamma\delta}\}$ also asymptote to constants.[2] In model F the incremental elastic moduli $\frac{\partial \mathbf{P}}{\partial \mathbf{F}}$ asymptote to the constants of linear elasticity, i.e.

$$P_{\alpha\alpha\alpha\alpha} \to 2G_t + \lambda_t, \tag{7.19}$$

$$P_{\alpha\alpha\beta\beta} \to \lambda_t, \tag{7.20}$$

$$P_{\alpha\beta\alpha\beta} \to G_t, \tag{7.21}$$

$$P_{\alpha\beta\beta\alpha} \to G_t, \tag{7.22}$$

where $\alpha \neq \beta$, G_t is the shear modulus and λ_t is the Lame Constant.

Our method of solution is to divide the annulus into two regions: $[R_1, R_u]$ and $[R_u, \infty)$. In the outer region $[R_u, \infty)$ we require the incremental elastic moduli $\frac{\partial \mathbf{P}}{\partial \mathbf{F}}$ to be within ϵ_{inc} (the error tolerance) of their asymptotic limits. We obtain an approximate analytic solution in this outer region by assuming the elastic moduli are constant, so that the difference between the actual solution and the approximate analytic solution is $\mathrm{O}(\epsilon_{inc})$. This general analytic solution can then be used to find a starting value for the minors $\mathbf{y}$, and then the minors may be integrated from R_u to R_1 as outlined in the previous section.

The equation of equilibrium over the outer region is

$$\nabla \cdot \left(\mathbf{P}^{(l)}_{inc} : \nabla \mathbf{u} \right) = \mathbf{0}, \tag{7.23}$$

[2] Recall $P_{\alpha\beta\gamma\delta} = \frac{\partial P_{\alpha\beta}}{\partial F_{\gamma\delta}}$.

where $\mathbf{P}^{(l)}_{inc}$ is equal to the asymptotic limit of $\frac{\partial \mathbf{P}}{\partial \mathbf{F}}$ as $R \to \infty$. We equate the traction and displacement at either side of R_u, i.e.

$$\frac{\partial \mathbf{P}}{\partial \mathbf{F}} : \nabla \mathbf{u} \cdot \mathbf{n} = \mathbf{P}^{(l)}_{inc} : \nabla \mathbf{u} \cdot \mathbf{n}, \tag{7.24}$$

$$\mathbf{u}|_- = \mathbf{u}|_+. \tag{7.25}$$

We could have equated the displacement derivatives $\mathbf{u}'$ either side of R_u and obtained very similar results, because by definition the linear solution is a very close approximation to the nonlinear solution. However we choose to follow the convention in elasticity of equating the traction and displacement at the interface of two materials.

We expect the space of solutions of (7.23) which decay to $\mathbf{0}$ as $R \to \infty$ to be of dimension three. We let $\mathbf{Q}_4(R)$ be the solution matrix, so that the general solution may be written as

$$\mathbf{u} = \mathbf{Q}_4 \cdot \mathbf{C}, \tag{7.26}$$

for some constant vector $\mathbf{C}$. The stress at R_u may therefore be written in the form

$$\mathbf{P}^{(l)}_{inc} : \nabla \mathbf{u} \cdot \mathbf{n} = \mathbf{Q}_3 \cdot \mathbf{C}, \tag{7.27}$$

for some matrix $\mathbf{Q}_3$. We obtain explicit expressions for $\mathbf{Q}_4$ and $\mathbf{Q}_3$ in the sections below. However when we equate the traction at either side of R_u we find

$$\begin{aligned} \mathbf{P}^{(l)}_{inc} : \nabla \mathbf{u}|_+ \cdot \mathbf{n} &= \frac{\partial \mathbf{P}}{\partial \mathbf{F}} : \nabla \mathbf{u}|_- \cdot \mathbf{n} \\ &:= \mathbf{Q}_1 \cdot \mathbf{u}|_- + \mathbf{Q}_2 \cdot \mathbf{u}'|_-. \end{aligned} \tag{7.28}$$

The structure of $\mathbf{Q}_1$ and $\mathbf{Q}_2$ may be inferred from (C.5) in the Appendix. We infer from (7.26), (7.27) and (7.28) that

$$\mathbf{u}' = \mathbf{Q}_2^{-1} \cdot (\mathbf{Q}_3 - \mathbf{Q}_1 \cdot \mathbf{Q}_4) \cdot \mathbf{C}. \tag{7.29}$$

The equations (7.26) and (7.29) are sufficient for us to obtain an expression for $\mathbf{U}$ at R_u, and we may then perform the integration as outlined in Section 7.1.1.

It remains for us to determine the radius R_u at which we may accurately transition from

the linear to the nonlinear regime. In Section 3.2 we proved that as $R \to \infty$, the leading order of the strain of the fundamental solution is $C_u R^{-2}$, where C_u is a constant defined in (3.16). We saw that the growth decays exponentially, and so for large R the effect of the growth on the incremental equations is negligible compared to the effect of the strain (resulting from the fundamental displacement). We thus define R_u such that

$$R_u = O\left(\sqrt{\frac{C_u}{\epsilon_{inc}}}\right), \tag{7.30}$$

where ϵ_{inc} is the desired tolerance of the incremental equations. In the case of model C, we use the expressions for $\mathbf{Q}_3$ and $\mathbf{Q}_4$ corresponding to model F, but stipulate that $R_u = R_2$.

We now outline the derivation of $\mathbf{Q}_3$ and $\mathbf{Q}_4$ for each of the models with an infinite geometry. To determine these matrices we require an analytic solution of the linear elastic equations over $[R_u, \infty)$.

Linear Elastic Solution Over a Three Dimensional Annulus For Model F

We obtain a general solution to the equation of equilibrium (7.23) when the incremental stress tensor $\frac{\partial \mathbf{P}}{\partial \mathbf{F}}$ is that of linear elasticity (i.e. its components are equal to the asymptotic limits in (7.22)-(7.22)). We solve this using the Galerkin Vector method.[3] Galerkin's method states that if $\mathcal{G}$ is such that

$$\nabla^2 \nabla^2 \mathcal{G} = \mathbf{0}, \tag{7.31}$$

then

$$\mathbf{u} = \frac{1}{2G}\left(2(1-\nu)\nabla^2 \mathcal{G} - \nabla\left(\nabla \cdot \mathcal{G}\right)\right) \tag{7.32}$$

is a solution of the equation of equilibrium (7.23). Note that the Galerkin vector is not necessarily unique: different Galerkin vectors may produce the same displacement. We desire the displacement to be in $U_{n,\omega}$, i.e.

$$u_r = W\cos(n\Theta)\cos\left(\omega Z\right), \tag{7.33}$$

$$u_\theta = V\sin(n\Theta)\cos\left(\omega Z\right), \tag{7.34}$$

$$u_z = Z\cos(n\Theta)\sin\left(\omega Z\right), \tag{7.35}$$

[3] Refer to Fung [57] for a fuller explanation.

and we ensure this by stipulating the Galerkin Vector to also be in $U_{n,\omega}$. That is,

$$\mathcal{G} = \begin{pmatrix} \mathcal{G}_r \cos(n\Theta)\cos(\omega Z) \\ \mathcal{G}_\theta \sin(n\Theta)\cos(\omega Z) \\ \mathcal{G}_z \cos(n\Theta)\sin(\omega Z) \end{pmatrix}. \tag{7.36}$$

The three components of $\nabla^2\mathcal{G}$ are thus

$$\left(\frac{\partial^2\mathcal{G}_r}{\partial R^2} + \frac{1}{R}\frac{\partial\mathcal{G}_r}{\partial R} - \frac{n^2}{R^2}\mathcal{G}_r - \frac{2n}{R^2}\mathcal{G}_\theta - \frac{\mathcal{G}_r}{R^2} - \omega^2\mathcal{G}_r\right)\cos(n\Theta)\cos(\omega Z)\,\mathbf{e}_R, \tag{7.37}$$

$$\left(\frac{\partial^2\mathcal{G}_\Theta}{\partial R^2} + \frac{1}{R}\frac{\partial\mathcal{G}_\Theta}{\partial R} - \frac{n^2}{R^2}\mathcal{G}_\Theta - \frac{2n}{R^2}\mathcal{G}_R - \frac{\mathcal{G}_\Theta}{R^2} - \omega^2\mathcal{G}_\Theta\right)\sin(n\Theta)\cos(\omega z)\,\mathbf{e}_\Theta, \tag{7.38}$$

$$\left(\frac{\partial^2\mathcal{G}_z}{\partial R^2} + \frac{1}{R}\frac{\partial\mathcal{G}_z}{\partial R} - \frac{n^2}{R^2}\mathcal{G}_z - \omega^2\mathcal{G}_z\right)\cos(n\Theta)\sin(\omega z)\mathbf{e}_z. \tag{7.39}$$

The form of (7.37)-(7.39) suggests that we may find solutions of (7.31) in terms of Modified Bessel Functions. We only choose Modified Bessel Functions of the Second Kind because we require the solutions to decay to 0 as $R \to \infty$. Furthermore we do not require the general solution of (7.31): we only need to find enough solutions such that the dimension of the space of all valid displacements induced by the Galerkin Vector is 3. The reason we expect the dimension to be 3 is that we require the solution to be uniquely determined if either the displacement or the traction is specified at $R = R_u$.[4] Specifying the displacement or traction amounts to applying three constraints on the general solution (so in general we require there to be three unknowns). In the case that $\omega \neq 0$ (corresponding to axial buckling), we found four linearly independent solutions of (7.31), such that the Galerkin Vector may be written as

$$\mathcal{G} = \begin{pmatrix} AK_{n+1}(\omega R) + BRK_{n+2}(\omega R) \\ AK_{n+1}(\omega R) + BRK_{n+2}(\omega R) \\ CK_n(\omega R) + DRK_{n+1}(\omega R) \end{pmatrix}, \tag{7.40}$$

where A,B, C and D are undetermined constants. We treat the case $\omega = 0$ in Section 7.1.2. The terms with coefficients A and C satisfy $\nabla^2\mathcal{G} = \mathbf{0}$. We may now determine the

[4] It is a classic result of linear elasticity that the solution to such a problem is unique in the absence of a body force.

displacement corresponding to this vector using (7.32). We begin by noting

$$\nabla \cdot \mathcal{G} = -\omega \left(AK_n(\omega R) + BRK_{n+1}(\omega R) - CK_n(\omega R) - DRK_{n+1}(\omega R) \right). \tag{7.41}$$

Observe that the coefficient of A is the negative of the coefficient of C in (7.41). Since the coefficients of A and C satisfy $\nabla^2 \mathcal{G} = \mathbf{0}$, from an inspection of (7.31) we may without loss of generality assume $C = 0$. We thus obtain the following expressions for the displacements and stresses

$$\begin{aligned}
u_r =& \frac{\omega}{2RG} \left(-4BRK_{n+1}(\omega R) + 4B\nu RK_{n+1}(\omega R) - AR\omega K_{n+1}(\omega R) + AnK_n(\omega R) \right. \\
& \left. -B\omega R^2 K_n(\omega R) - BnRK_{n+1}(\omega R) + D\omega R^2 K_n(\omega R) + DnRK_{n+1}(\omega R) \right) \qquad (7.42) \\
u_\theta =& -\frac{\omega}{2GR} \left(4BRK_{n+1}(\omega R) - 4\nu BRK_{n+1}(\omega R) + AnK_n(\omega R) + BnRK_{n+1}(\omega R) \right. \\
& \left. -DnRK_{n+1}(\omega R) \right) \\
u_z =& -\frac{\omega}{2G} \left(4DK_n(\omega R) - 4D\nu K_n(\omega R) + \omega AK_n(\omega R) + \omega BRK_{n+1}(\omega R) - D\omega RK_{n+1}(\omega R) \right) \\
P_{RR} =& \frac{\omega}{R^2} \left[K_n(\omega R) \left(R^2 \left(-2B\nu\omega - 2D\nu\omega + D\omega + 3B\omega + A\omega^2 \right) - An + An^2 \right) \right. \\
& \left. +K_{n+1}(\omega R) \left(R^3 \left(-D\omega^2 + B\omega^2 \right) + R(-4nB\nu + Bn^2 - 4B\nu + 4B + 5Bn + A\omega - Dn^2 - Dn) \right) \right] \\
P_{\Theta R} =& -\frac{\omega}{R^2} K_n(\omega R) \left(R^2 \left(-nB\omega + nD\omega + 2B\nu\omega - 2B\omega \right) - An + An^2 \right) \\
& -\frac{\omega}{R} K_{n+1}(\omega R) \left(-Bn^2 - 4B + 4nB\nu - nA\omega + 4B\nu - 5Bn + Dn + Dn^2 \right) \\
P_{ZR} =& -\frac{\omega}{R} K_n(\omega R) \left(An\omega - BR^2\omega^2 + 2Dn + DR^2\omega^2 - 2D\nu n \right) \\
& -\omega K_{n+1}(\omega R) \left(-2B\omega + 2B\omega\nu - A\omega^2 + D\omega n - 2D\omega - B\omega n + 2D\nu\omega \right). \qquad (7.43)
\end{aligned}$$

We use (7.42)-(7.43) to infer the structure of $\mathbf{Q}_3$ and $\mathbf{Q}_4$ in Section 7.1.2.

Scaling of Axial Incremental Equations

The asymptotic form of the Bessel functions for large R is

$$K_n(\omega R) \sim K_{n+1}(\omega R) \sim \sqrt{\frac{\pi}{2\omega R}} \exp(-\omega R). \tag{7.44}$$

Thus for large ω the incremental equations decay extremely rapidly. With this in mind, we

adopt the scaling

$$W = bW_1, \quad V = bW_3, \quad X = bW_5 \tag{7.45}$$

$$\frac{\partial W}{\partial R} = cW_2, \quad \frac{\partial V}{\partial R} = cW_4, \quad \frac{\partial X}{\partial R} = cW_6, \tag{7.46}$$

where

$$b = \sqrt{R}\exp(-\omega R), \quad b' = \exp(-\omega R)\left(-\omega\sqrt{R} + \frac{1}{2}R^{-\frac{1}{2}}\right), \tag{7.47}$$

$$c = \omega b, \quad c' = \omega b'. \tag{7.48}$$

We find that

$$\frac{\partial W_1}{\partial R} = \frac{c}{b}W_2 - \frac{b'}{b}W_1, \quad \frac{\partial W_2}{\partial R} = \frac{1}{c}\frac{\partial^2 W}{\partial R^2} - \frac{c'}{c}W_2, \tag{7.49}$$

$$\frac{\partial W_3}{\partial R} = \frac{c}{b}W_4 - \frac{b'}{b}W_3, \quad \frac{\partial W_4}{\partial R} = \frac{1}{c}\frac{\partial^2 V}{\partial R^2} - \frac{c'}{c}W_4, \tag{7.50}$$

$$\frac{\partial W_5}{\partial R} = \frac{c}{b}W_6 - \frac{b'}{b}W_5, \quad \frac{\partial W_6}{\partial R} = \frac{1}{c}\frac{\partial^2 X}{\partial R^2} - \frac{c'}{c}W_6. \tag{7.51}$$

We transform the minors accordingly, so that the numerical integration is more stable.

General Solution over Infinite Medium for Planar Buckling

The solution of the previous section is of no use if $\omega = 0$ (in the case of planar buckling). We must therefore use another method to determine an analytic solution of the incremental equations over the outer region. The asymptotic limit $\mathbf{P}^{(l)}_{inc}$ of the incremental elastic tensor $\frac{\partial \mathbf{P}}{\partial \mathbf{F}}$ assumes the following form

$$P^{(l)}_{inc,RRRR} = P^{(l)}_{inc,\Theta\Theta\Theta\Theta} = a, \tag{7.52}$$

$$P^{(l)}_{inc,RR\Theta\Theta} = P^{(l)}_{inc,\Theta\Theta RR} = b, \tag{7.53}$$

$$P^{(l)}_{inc,R\Theta R\Theta} = P^{(l)}_{inc,\Theta R\Theta R} = c, \tag{7.54}$$

$$P^{(l)}_{inc,R\Theta\Theta R} = P^{(l)}_{inc,\Theta RR\Theta} = d, \tag{7.55}$$

$$a = b + c + d. \tag{7.56}$$

These identities may be inferred from (C.5) in Appendix C.0.13. Refer to the beginning of this section, and (7.23) in particular, for a discussion of $\mathbf{P}^{(l)}_{inc}$. We do not worry about finding an expression for $P^{(l)}_{inc,\alpha_1\alpha_2\alpha_3\alpha_4}$ if one of $\{\alpha_j\}$ is Z because this does not affect planar buckling. We assume that $\mathbf{u}$ is of Fourier mode n, i.e. $\mathbf{u} = W(R)cos(n\Theta)\mathbf{e}_R + V(R)sin(n\Theta)\mathbf{e}_\Theta$. Upon substitution of $\mathbf{u}$ into the equations of equilibrium, we find

$$a\frac{\partial^2 W}{\partial R^2} + \frac{W}{R^2}\left(-a - cn^2\right) + \frac{a}{R}\frac{\partial W}{\partial R} + \frac{n}{R}\frac{\partial V}{\partial R}(b+d) + \frac{V}{R^2}(-an - cn) = 0 \tag{7.57}$$

$$c\frac{\partial^2 V}{\partial R^2} + \frac{c}{R}\frac{\partial V}{\partial R} + \frac{V}{R^2}(-an^2 - c) + \frac{n}{R}(-b-d)\frac{\partial W}{\partial R} + \frac{W}{R^2}(-an - cn) = 0. \tag{7.58}$$

We substitute $\{W = wR^k,\, V = vR^k\}$ into (7.57)-(7.58), obtaining the matrix equation

$$\begin{pmatrix} ak^2 - a - cn^2 & n(k(b+d) - a - c) \\ -n(k(b+d) + a + c) & ck^2 - an^2 - c \end{pmatrix} \cdot \begin{pmatrix} w \\ v \end{pmatrix} = \mathbf{0}. \tag{7.59}$$

In order that there are nontrivial solutions, we require the determinant of the above matrix to be zero. This leaves us with the quartic

$$ack^4 + k^2\left(-a(an^2 + c) - c(a + cn^2) + n^2(b+d)^2\right) + ac\left(n^2 - 1\right)^2 = 0. \tag{7.60}$$

After substituting (7.56) into (7.60), it simplifies to

$$k^4 + 2k^2(-1 - n^2) + (n^2 - 1)^2 = 0, \tag{7.61}$$

with roots $\pm(n \pm 1)$. We require the solution to decay to 0 as $R \to \infty$, so we only take the roots $k_1 = -n - 1$ and $k_2 = -n + 1$. It is interesting to notice that k_1 and k_2 are independent of the elastic moduli. The general solution is

$$\begin{pmatrix} W(R) \\ V(R) \end{pmatrix} = a_n R^{-n-1}\begin{pmatrix} 1 \\ 1 \end{pmatrix} + b_n R^{1-n}\begin{pmatrix} n\left(1 - \frac{c}{a}\right) + 2\frac{c}{a} \\ n\left(1 - \frac{c}{a}\right) - 2 \end{pmatrix}, \tag{7.62}$$

where a_n and b_n are constants. The derivative is

$$\begin{pmatrix} W'(R) \\ V'(R) \end{pmatrix} = a_n(-n-1)R^{-n-2}\begin{pmatrix} 1 \\ 1 \end{pmatrix} + b_n(1-n)R^{-n}\begin{pmatrix} n\left(1 - \frac{c}{a}\right) + 2\frac{c}{a} \\ n\left(1 - \frac{c}{a}\right) - 2 \end{pmatrix}. \tag{7.63}$$

From this we calculate the stress

$$\begin{pmatrix} P_{RR} \\ P_{\Theta R} \end{pmatrix} = \mathbf{Q}_3 \cdot \begin{pmatrix} a_n \\ b_n \end{pmatrix}, \text{ where} \tag{7.64}$$

$$\begin{aligned}
Q_{3,11} &= R^{-n-2}(b-a)(n+1), \\
Q_{3,12} &= R^{-n}\left((1-n)(n(a-c)+2c) + b\left(n^2\left(1-\frac{c}{a}\right) - n + \frac{c}{a}(2-n)\right)\right), \\
Q_{3,21} &= R^{-n-2}(n+1)(-c-d), \\
Q_{3,22} &= R^{-n}\left(c(1-n)\left(n\left(1-\frac{c}{a}\right)-2\right) - d\left((n^2+n)\left(1-\frac{c}{a}\right) + 2n\frac{c}{a} - 2\right)\right).
\end{aligned}$$

We use (7.62) and (7.64) to infer the structure of $\mathbf{Q}_3$ and $\mathbf{Q}_4$, which are defined in Section 7.1.2.

7.2 Solution of Second Order Equations

We outline our method of solution of the second order equations in Appendix D.2.

Chapter 8

Buckling Results for Model without Distinct Tumour and Capillary Wall

In this chapter we investigate the sensitivity of buckling (both planar and axial) to growth anisotropy and the intercapillary distance. Our investigation proceeds from the radially symmetric results of Chapter 3. In this chapter we argued that model F (with an infinite annular geometry), together with anisotropic growth, seems the most plausible combination of our model variants. However there is still some uncertainty over the outer boundary condition (for large R - these are outlined in Table 8.1) and the growth anisotropy. Hence in this chapter we investigate their effect on buckling. We apply the buckling analysis of Chapter 4. Typical parameter values are outlined in Table 8.2. In our modelling of the

Key	Tumour Geometry	Description
A	Finite	Null Displacement and zero nutrient flux at $R = R_2$.
C	Infinite	$[R_2, \infty)$ is linearly elastic, zero nutrient flux at $R = R_2$.
F	Infinite	Nutrient Distribution and Displacement decay to 0 as $R \to \infty$.
G	Infinite	$\frac{\partial c}{\partial R} = 0$ at $R = R_2$ and $c(R) = c(R_2)$ (for $R > R_2$). $\mathbf{P} \to \mathbf{0}$ as $R \to \infty$.

Table 8.1: The various boundary conditions and geometries we consider in this chapter. The radius of the cavity (which represents the capillary) is R_1. If the geometry is finite, the outer radius of the tumour annulus is R_2. At $R = R_1$, the boundary condition is always that of null stress $\mathbf{P} \cdot \mathbf{n} = \mathbf{0}$ and fixed nutrient concentration $n = 1$.

Dimensional Parameter	Value	Description
R_2	$10^{-4}m$	Outer Radius of Annulus (for finite geometries).
R_1	1.5×10^{-5}	Inner Radius of Annulus.
q	-7.9	Tumour Elastic Parameter.
f	0.2	Tumour Elastic Parameter.
λ_n	$0.01mMs^{-1}$	Rate of Uptake of Oxygen.
k_n	$4.6 \times 10^{-3}mM$	Michaelis Constant for Oxygen Uptake.
k_c	$8.3 \times 10^{-3}mM$	Michaelis Constant for Cell Growth.
D	$1.5 \times 10^{-9}m^2s^{-1}$	Diffusion Coefficient of Oxygen in Tumour.
c_0	$0.1mM$	Oxygen Concentration at R_1.
Nondimensional Parameter	Value	Description
α	0.015	$\lambda_n R_1^2/D$
k_n^*	0.046	k_n/n_0
k_c^*	0.083	k_c/n_0
R_2^*	6.6667	R_2/R_1.

Table 8.2: The default parameter values we use in our results, unless otherwise indicated. In our nondimensionalisation the lengthscale is R_1, the nutrient scale is the concentration at R_1 and the timescale is the average time it takes for a tumour cell to proliferate. We do not provide a value for the characteristic proliferation rate because it does not effect our results. The tumoural elastic modulii (E_t, f and q) are for glioblastoma. Refer to Appendix B for an explanation of these parameters and the papers from which they are sourced.

growth anisotropy, we employ the 'stress' anisotropic growth multipliers given in (3.39). We drop the asterixes from our scaled variables for convenience.

With the planar buckling results, we produce the critical time for azimuthal modes $\{2, 3, 4, 5, 10, 20\}$, as well as the asymptotic limit as $n \to \infty$. For the axial buckling results, we consider azimuthal modes $\{1, 2, 3, 4, 5\}$ and a variety of values for ω, as well as the asymptotic limit as $(n, \omega) \to \infty$. In the postbuckled stability plots, we plot an '$\times$' if there exists a stable buckled equilibrium state, and an 'o' otherwise. The stability of the buckled state is evaluated using the criteria in Section 4.2.5. Recall that in our perturbation expansion the current time is $t_{n,\omega} + \frac{\epsilon^2}{2}\delta t + O(\epsilon^4)$ and the time when the system jumps to the buckled state is $t_{n,\omega} + \frac{\epsilon^2}{2}\delta t^*$, where $0 \leq \delta t^* \leq \delta t$. The magnitude of the buckle (if it exists) is given by

$$a = \pm\sqrt{-\delta t \frac{C_2}{C_1} - (\delta t - \delta t^*)\frac{2C_3}{3C_1}}, \tag{8.1}$$

where C_1, C_2 and C_3 are defined in (4.104). When such a buckled state exists, in plotting our results we assume that the system enters the buckled state immediately, so that the

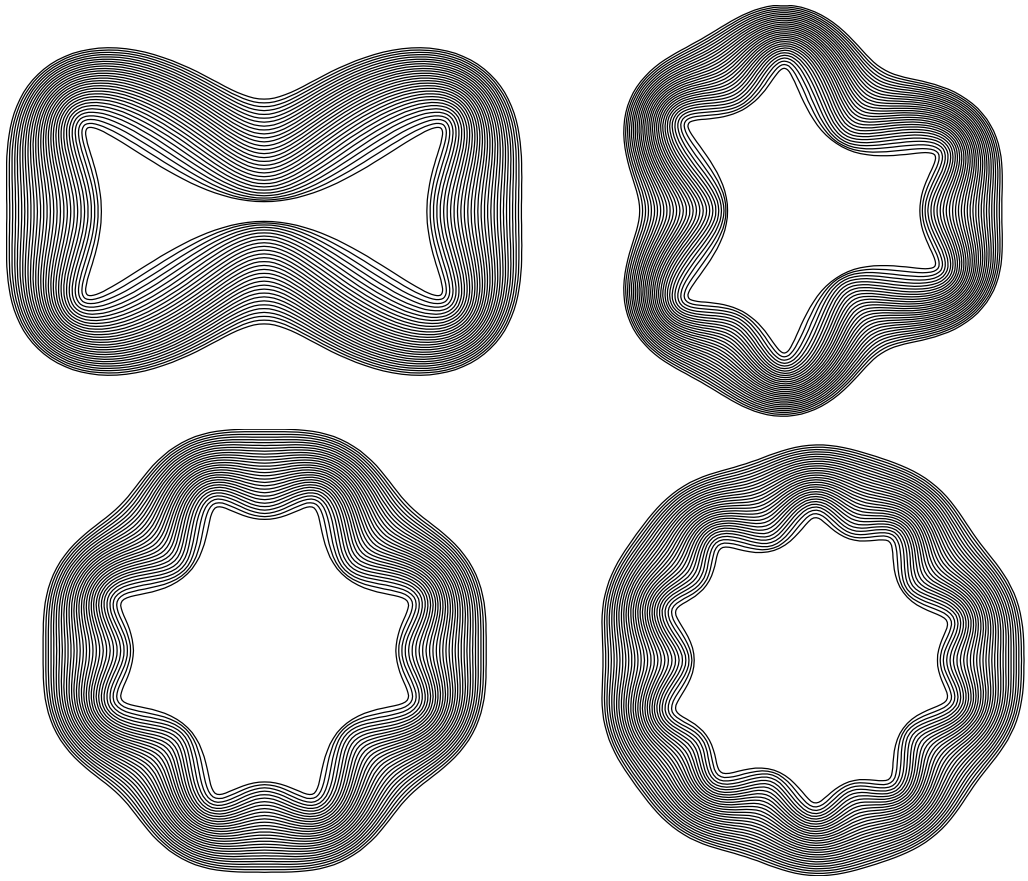

Figure 8.1: The planar buckled profiles. We plot the displacement up to quadratic accuracy, i.e. $\mathbf{u} = \mathbf{u}_0 + \epsilon a \mathbf{u}^{(n,\omega)} + \frac{1}{2}\epsilon^2 a^2 \mathbf{u}_2^a + \delta t \frac{1}{2}\epsilon^2 \mathbf{u}_2^p$ and $t = t^* + \frac{1}{2}\epsilon^2 \delta t + \ldots$. We implemented model F, with anisotropic growth and $A = 10$ (the data derives from the $A = 10$ results in Figure 8.5). Each plot is such that $\frac{1}{2}\epsilon^2 \delta t = 0.5$. The lines represent contours of constant radius (in the reference coordinates) spaced evenly from R_1 to $1.05 \times R_1$. The eigenmode (i.e. $\mathbf{u}^{(n,\omega)}$) of the top figure is $(n, \omega) = (2, 0)$, and the others (in a clockwise direction) are respectively modes $(3, 0), (5, 0)$ and $(4, 0)$. The other dimensional parameters are given in Table 8.2.

time of entry (δt^*) is zero. It follows from (4.105)

$$\frac{a^2}{\delta t} = -\frac{C_2}{C_1} - \frac{2C_3}{3C_1}. \tag{8.2}$$

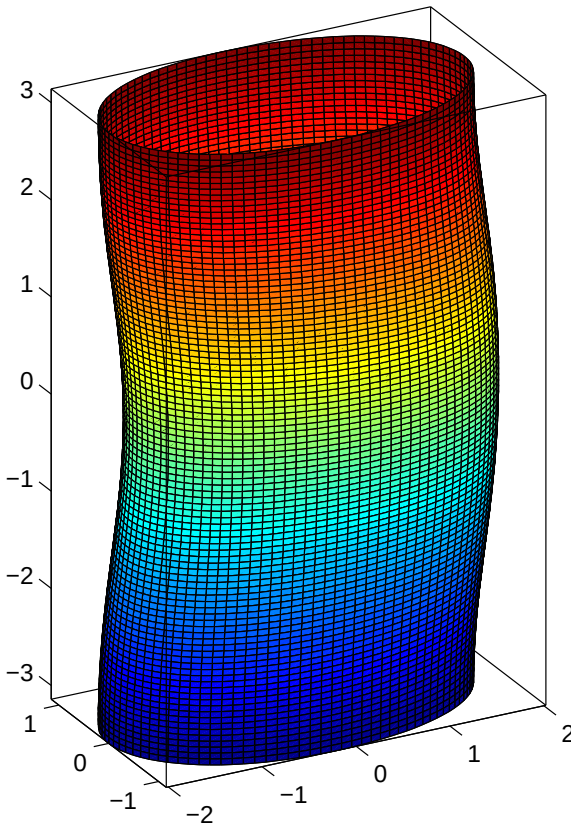

Figure 8.2: The buckled equilibrium state, with $n = 1$ and $\omega = 1$. We used model F, with isotropic growth. The plot is for a time increment $\frac{1}{2}\epsilon^2\delta t = 1$ past the critical time. The dimensional parameters are given in Table 8.2

8.1 Buckled Profiles

We produce figures of the buckled shape for a typical selection of parameters (given in Table 8.2). The shapes of the planar buckles of modes $2, 3, 4, 5$ are plotted in Figure 8.1. Note that we only need to stipulate $\epsilon^2\delta t$, and not these variables individually, since the magnitude a of the buckle is proportional to this. Observe that as the mode number increases, the amplitude of the buckle gets smaller (in the boundary layer analysis of Chapter 6 we proved that the asymptotic behaviour of the amplitude is of order $n^{-\frac{3}{2}}\sqrt{\delta t}$ for large n and small δt). It can also be observed that the decay as $R \to \infty$ of the buckle is much slower for low n than high n, which is also predicted by our boundary layer analysis. Some diagrams of the profiles of axial buckles are plotted in Figures 8.2, 8.3 and 8.4.

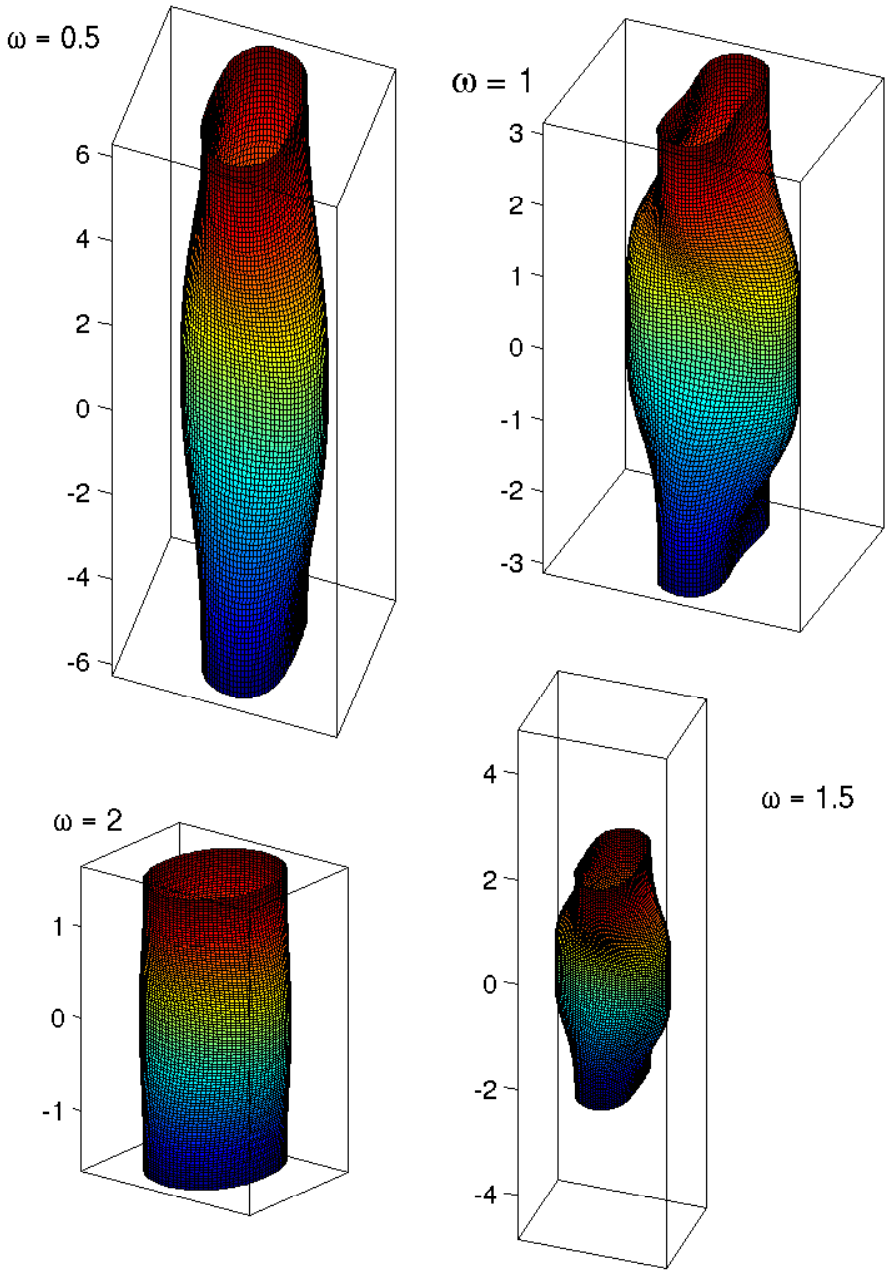

Figure 8.3: The buckled equilibrium states, with $n = 2$ and $\omega = \{0.5, 1, 1.5, 2\}$. We used model F, with anisotropic growth ($A = 10$). The plot is for a time increment $\frac{1}{2}\epsilon^2\delta t = 0.05$ past the critical time. The axes are scaled equally. The dimensional parameters are given in Table 8.2.

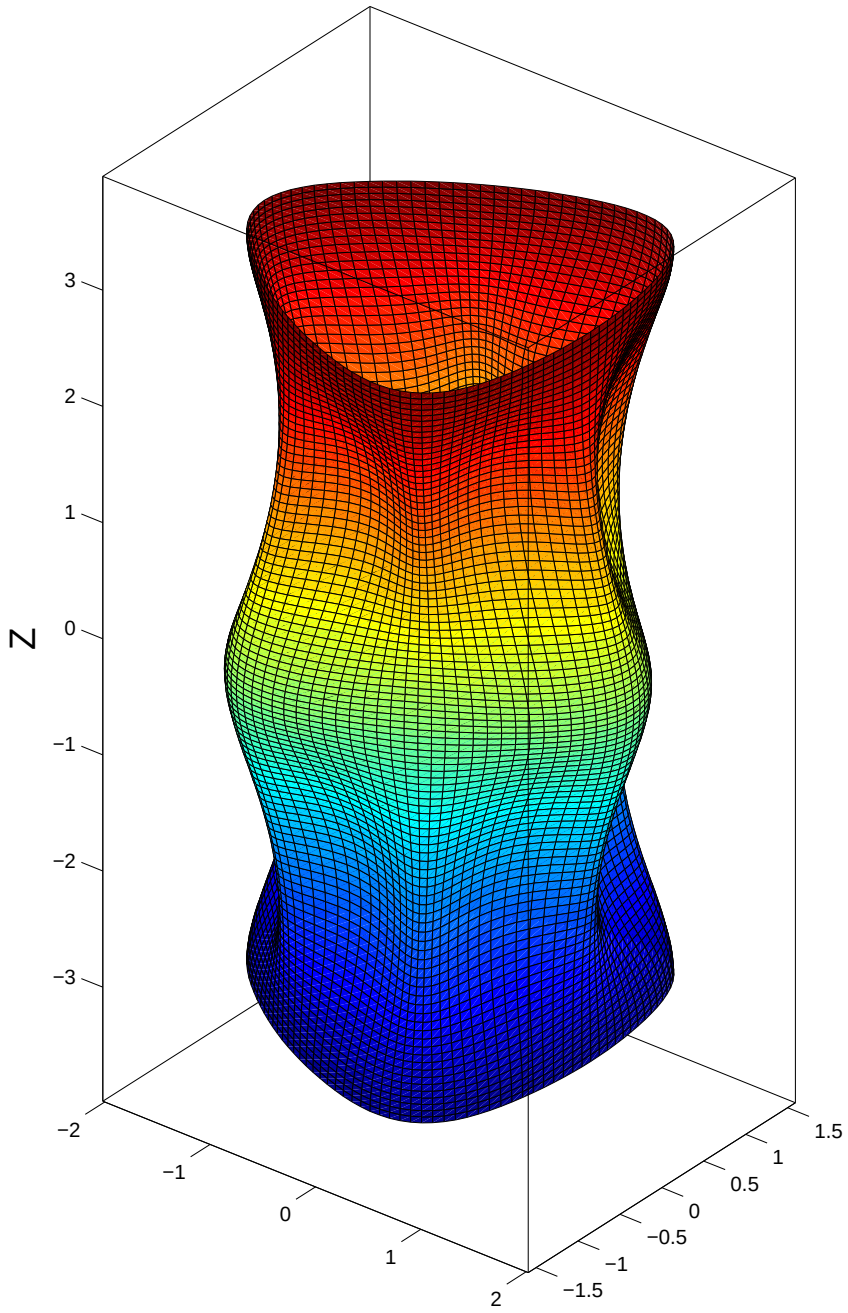

Figure 8.4: The buckled equilibrium state, with $n = 3$ and $\omega = 1$. We used model F, with isotropic growth. The plot is for a time increment $\frac{1}{2}\epsilon^2\delta t = 1$ past the critical time. In the bottom four figures the variables are evaluated at R_2. The other dimensional parameters are given in Table 8.2.

8.2 Altering the Growth Anisotropy Coefficient

In Figures 8.5 and 8.6 we plot the effect of varying the growth mutliplier constant A from 0 to 50 on the onset of planar buckling. Recall that the growth anisotropy is determined by the level of stress through the following constitutive relation

$$G_{jj} = \exp\left(AK_t^{-1}T_{jj}\right) G_{\Sigma}^{-1} \tag{8.3}$$

$$G_{\Sigma} = \exp\left(AK_t^{-1}T_{RR}\right) + \exp\left(AK_t^{-1}T_{\Theta\Theta}\right) + \exp\left(AK_t^{-1}T_{ZZ}\right), \tag{8.4}$$

where K_t is the bulk modulus. When $A = 0$ the growth is isotropic, and increasing A increases the responsiveness of the growth to the prevailing stress field.

A priori, we might have expected the critical time of buckling to increase monotonically as the growth anisotropy coefficient increases. The reason is that as A increases, the growth becomes more responsive to the prevailing stress field and one might think that this would have a stabilising effect since it lessens the disparity between the three principal stresses $\{T_{RR}, T_{\Theta\Theta}, T_{ZZ}\}$. Indeed for values of A greater than approximately 35 the critical times for all of the modes (including the asymptotic limit) gradually increase as A increases. However as A ranges from $5 - 10$ the critical times of most of the modes *decrease*. The reason for this appears to be as follows. The inwards displacement at R_1 is greatly increased as A increases, probably mostly due to the fact that the radial growth in the vicinity of R_1 increases due to the increased responsiveness of the growth to the low radial stress T_{RR}. This greatly decreases the azimuthal strain $F_{e,\Theta\Theta}$, which in turn makes the azimuthal stress at R_1 more compressive. This effect appears to be much greater than the countereffect caused by the azimuthal growth being lessened because of the increased responsiveness of the growth to the high azimuthal stress. The increased azimuthal stress is probably a major reason behind the sooner onset of buckling.

It can be observed in Figure 8.5(A) that the critical time of buckling asymptotes to a finite limit as the wavenumber n asymptotes to infinity. It can be observed from Figure 8.5(F) that the asymptotic limit of the critical times is their *infimum* for larger values of A (since t_1 is negative), but this is not the case for smaller values of A. We plot this

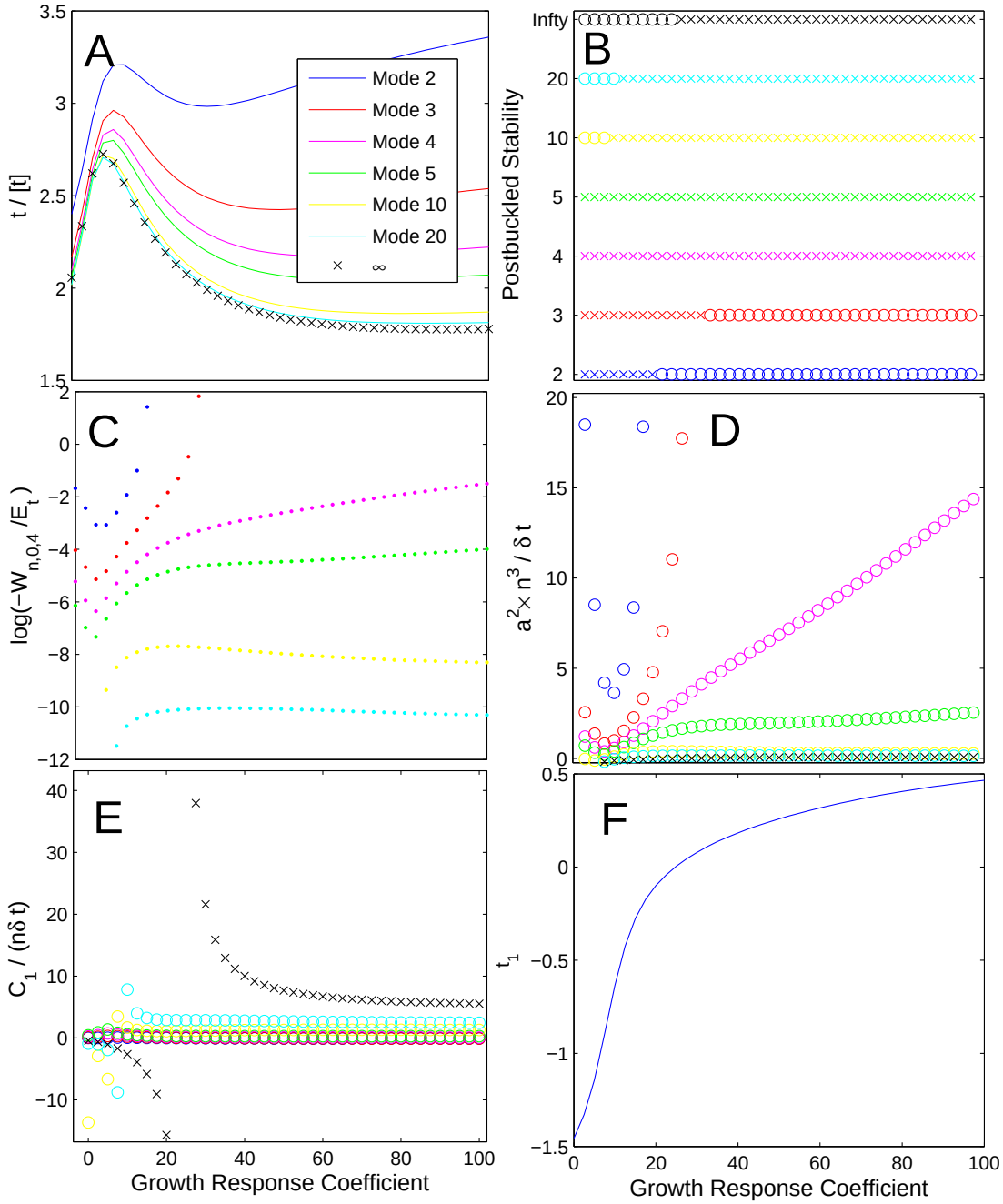

Figure 8.5: The effect of altering the growth isotropy coefficient A on the buckling of modes $\{2, 3, 4, 5, 10, 20\}$. Increasing A increases the sensitivity of the growth to the prevailing stress field. We implement model variant F. Unless otherwise indicated, the variables which depend on R are evaluated at $R = R_1$. In the postbuckled stability plot, we plot an 'x' if there exists a stable buckled state, and an 'o' otherwise. The plot labelled t_1 gives the asymptotic behaviour of the critical time t as $n \to \infty$: i.e. $t_{n,0} = t^* + n^{-1}t_1 + \ldots$. The parameters are listed in Table 8.2. The plots are continued in Figure 8.6.

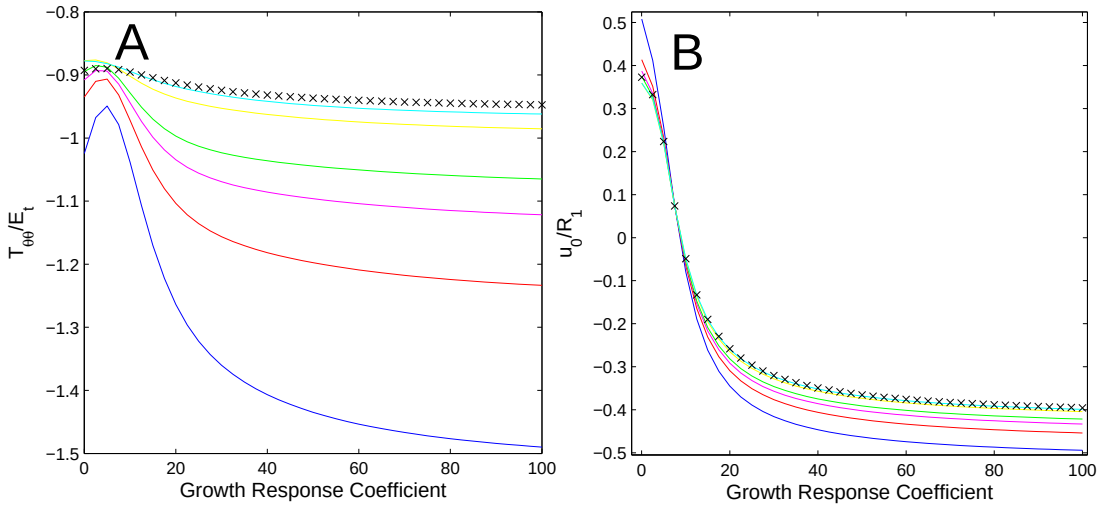

Figure 8.6: The effect of altering the growth anisotropy coefficient A, continued from Figure 8.5. The hoop stress and radial displacement at R_1 at the critical time of buckling.

asymptotic limit largely out of mathematical interest: in practice we expect buckles of very fine wavelength to be outside of the scope of accuracy of our continuum approximation. In other words, one would need to consider the particular local arrangement of the individual cells, extracellular matrix and interstitial fluid to effectively model oscillations of such fine wavelength. This can be seen from the fact that the cellular diameter is of the order of $5 - 10\mu$m [67], which is approximately half the radius of the capillary. We expect the accuracy of our continuum model to rapidly diminish once the wavelength is of the order of the cellular diameter, because it seems likely that the cellular phase might dissipate the highly localised oscillation in the stress. In other words, we do not expect the system to actually be able to realise buckles with such a fine wavelength. This means our model could be inaccurate for planar wavenumbers of approximately 10 or greater. Nevertheless it is of mathematical interest to investigate the asymptotic convergence of the buckling. Indeed, the above discussion does not entirely rule out the occurrence of such fine wavelength buckles, but only suggests that we cannot fully trust our model in such situations.

8.2.1 Change in the Asymptotic Limit (as $n \to \infty$) of the Stability as Growth Anisotropy Increases

Observe (in Figure 8.5(B)) that as the growth multiplier constant A increases, the stability of the buckle in the asymptotic limit $n \to \infty$ changes from unstable to stable. It is important we explore this phenomenon because it explains why the asymptotic convergence of C_1 (which is a key determinant of the stability of the buckled equilibrium state) in Figure 8.5(E) is very slow for values of A near the threshold. Recall that the perturbed displacement is of the form

$$\mathbf{u} = u_0\mathbf{e}_R + \epsilon a\mathbf{u}^{(n,\omega)} + \epsilon^2 a^2\mathbf{u}_2^a + \epsilon^2\delta t\mathbf{u}_2^p + \dots \tag{8.5}$$

where we decompose $\mathbf{u}_2^a$ into its mode $2n$ and mode 0 components as follows, $\mathbf{u}_2^a = \mathbf{u}_{2,2n}^a + \mathbf{u}_{2,0}^a$.

The change in stability occurs precisely when $t_1 = 0$, where we recall the asymptotic behaviour of the critical time is given by $t^* + n^{-1}t_1$. The reason for this can be seen from the equation (6.40) governing x_0. We recall that x_0 is the scalar governing the magnitude of the asymptotic limit of $\mathbf{u}_{2,2n}^a$. In other words, if the components of $\mathbf{u}_1$ asymptote to $(W^*, V^*)^T$, then the components of $\mathbf{u}_{2,2n}^a$ asymptote to $x_0(W^*, V^*)^T$. When $t_1 = 0$, after an inspection of (6.40), it can be seen that the coefficient of x_0 in (6.20) is zero (once the dot product is taken), so that we cannot solve for x_0. Since we are approaching a division by zero as $t_1 \to 0$, this explains why x_0 asymptotes to $-\infty$ for $t_1 \to 0^-$ and x_0 asymptotes to $+\infty$ for $t_1 \to 0^+$. The change in sign of x_0 from positive to negative entails a change in the sign of the asymptotic limit of the constant c_1, which in turn entails a change in the asymptotic limit of the buckle from unstable to stable.

When we consider the physical meaning of x_0, there is nothing surprising about the fact that a change in its sign leads to a change in stability. When $x_0 > 0$, the inward cusps of $\mathbf{u}_1$ coincide with the inward cusps of $\mathbf{u}_{2,2n}$. In other words the $O(\epsilon^2)$ correction 'exacerbates' the buckle; a situation which from an intuitive point of view seems unstable. Conversely when $x_0 < 0$, the inward cusps of $\mathbf{u}_1$ coincide with outward cusps of $\mathbf{u}_{2,2n}^a$, so that the $O(\epsilon^2)$ correction 'mollifies' the buckle.

In general, when we are near the region where $t_1 = 0$, for large n, C_1 is small and the size

of $\mathbf{u}^a_{2,2n}$ (which is inversely proportional to C_1) can be very large. Indeed the results in Figure 8.5 suggest that the higher modes behave similarly to the asymptotic limit: as the growth multiplier increases, C_1 transitions from $-\infty$ to ∞, and there is a concomitant change in the buckle from unstable to stable. In the neighbourhood of $t_1 = 0$, the asymptotic convergence of $\mathbf{u}^a_{2,2n}$ can be very slow. This is illustrated in Figure 8.7. It is not until approximately mode 50 that the asymptotic convergence of the critical time reaches the $O(n^{-1})$ domain: for smaller modes than this, the critical time *decreases* as the mode increases, despite t_1 being negative. Since the asymptotic behaviour of $\mathbf{u}^a_{2,2n}$ is determined by matching in the $O(n^{-1})$ domain, it is not surprising that the asymptotic convergence of $\mathbf{u}^a_{2,2n}$ cannot be observed until approximately mode 50. A conclusion we draw from this analysis is that we need not worry that the initial asymptotic behaviour of $\mathbf{u}^a_{2,2n}$ seems contrary to the predictions of our boundary layer analysis: we instead conclude that the convergence is extremely slow. Indeed in Figure 8.8 we choose a value of the growth multiplier constant A well away from the value for which $t_1 = 0$, and we see that $\mathbf{u}^a_{2,2n}$ converges quickly to its asymptotic limit.

8.2.2 Wavelength Doubling

It has been observed by some experimentalists that the wavelength of a buckled pattern in an elastic substance doubles in length as compressive forces increase [92, 93, 27]. We explain how this might occur in our system as follows. We have seen in Figure 8.5(A) that buckles with very small wavelength go unstable first. However in Figure 8.5(C) we see that buckles with large wavelengths, which go unstable afterwards, tend to be energetically more favourable. Thus it seems plausible to think that the system might first adopt a buckled pattern with low wavelength, but over time small inhomogeneities might be sufficient for the system to jump to a solution branch with higher wavelength, given that this is energetically more favourable. To demonstrate the possibility of period doubling, we have plotted the evolution of the mode 4 and mode 8 buckles in Figure 8.9. Mode 8 goes unstable first. A short time later mode 4 goes unstable, and the mode 4 equilibrium state grows to have a lower potential energy than the mode 8 equilibrium state.

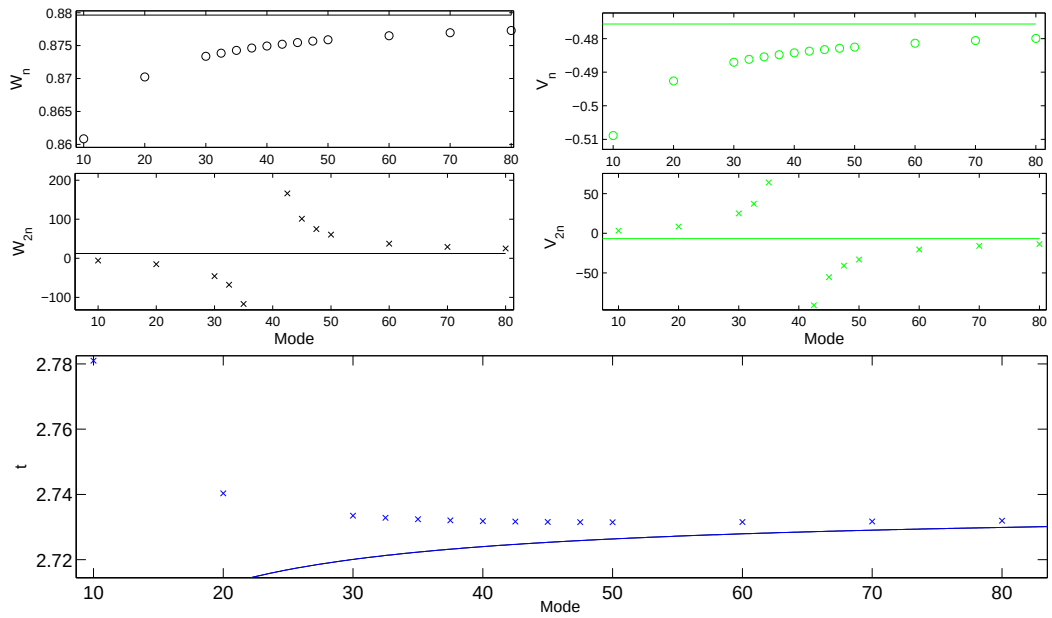

Figure 8.7: The asymptotic behaviour of the incremental solutions $\mathbf{u}_1 = (W_n \cos(n\Theta), V_n \sin(n\Theta))$ and $\mathbf{u}^a_{2,2n} = (W_{2n} \cos(2n\Theta), V_{2n} \sin(2n\Theta))$. We implement model variant C. The ratio R_1/R_2 is 0.4. We employed the growth multipliers given in (8.4), with the constant A equal to 5. In the top figures we plot the asymptotic limit in a straight line. In the bottom figure we plot the critical time of buckling. The $O(n^{-1})$ asymptote is plotted in the solid line. The asymptotic convergence is very slow: it is not until the mode is past 50 that it starts increasing (the increase cannot be easily discerned in the plot).

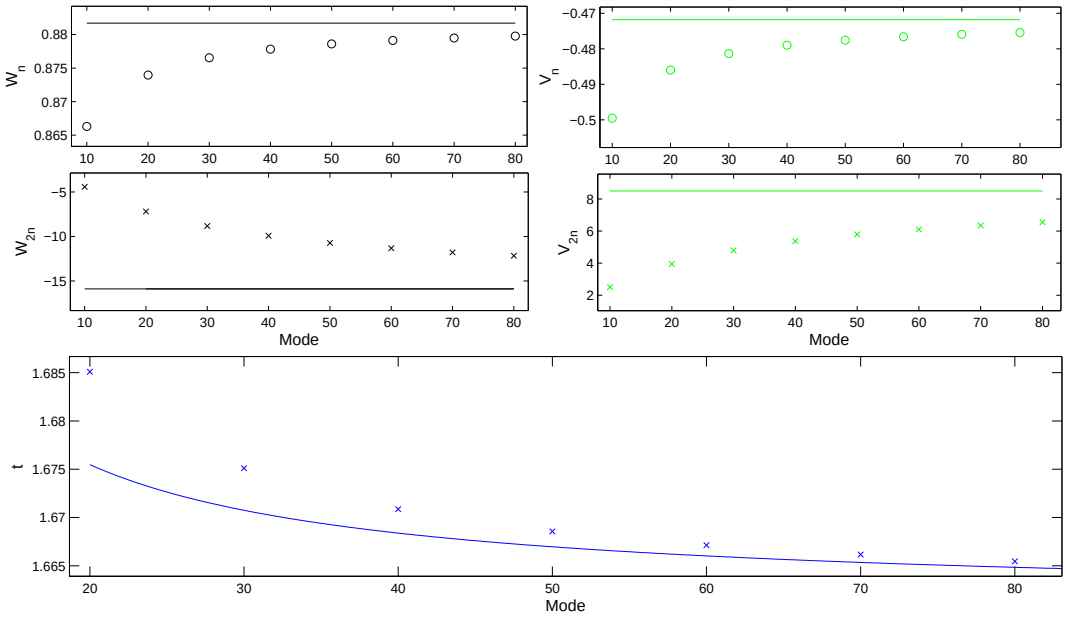

Figure 8.8: The asymptotic behaviour of the incremental solutions $\mathbf{u}_1 = (W_n \cos(n\Theta), V_n \sin(n\Theta))$ and $\mathbf{u}^a_{2,2n} = (W_{2n} \cos(2n\Theta), V_{2n} \sin(2n\Theta))$. We implement model variant C. The ratio R_1/R_2 is 0.4. We employed the growth multipliers given in (8.4), with the constant A equal to 20. In the top figures we plot the asymptotic limit in a straight line. In the bottom figure we plot the critical time of buckling.

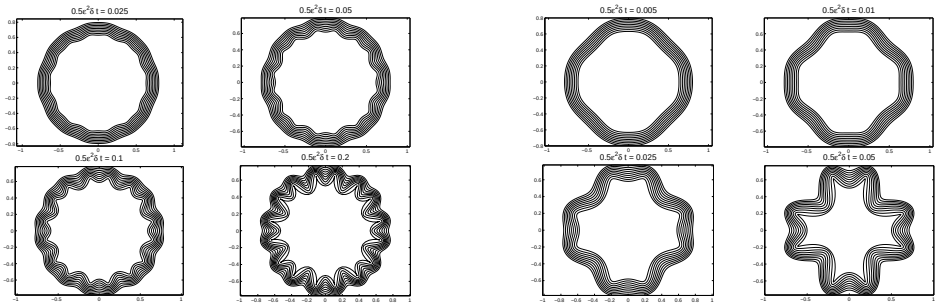

Figure 8.9: The mode 8 (the four figures on the left) and mode 4 (the four figures on the right) buckled profiles at times $t_{n,0} + \frac{1}{2}\epsilon^2\delta t$. We implemented a null-displacement outer boundary condition (model A) to obtain these profiles; an infinite medium yields profiles which are qualitatively very similar (in the immediate vicinity of the capillary wall).

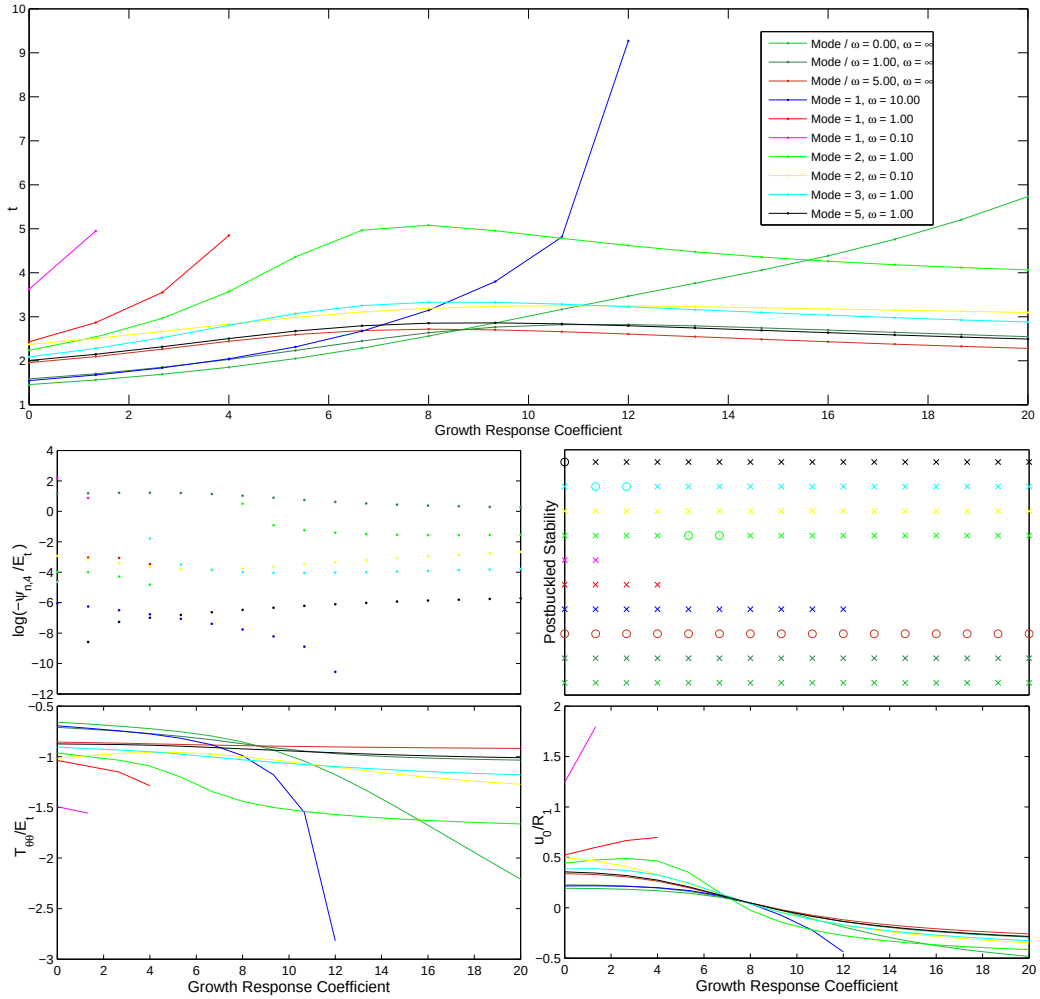

Figure 8.10: The response of axial buckling to the growth anisotropy coefficient A. We used model F. In the bottom two figures the variables are evaluated at R_2. The other dimensional parameters are given in Table 8.2. We terminated our search for a solution at $t^* = 10$.

8.2.3 Axial Buckling

The response of the axial buckling to variations in the growth anisotropy is plotted in Figure 8.10. We firstly determine the range of possible values we expect the axial wavenumber ω to take. Recall that ω is of the order of $m\pi/Z_0$, where Z_0 is the interbranch distance[1] and m is a positive integer. Our data in Appendix B demonstrates a huge variance in the interbranch distance within tumours, with Z_0 ranging from 5.7 to 920.8 micrometers, with a mean of 131 micrometers in the tumour centre. We take the mean value to be the

[1]Note that the lengthscales have been nondimensionalised such that $R_1 = 1$.

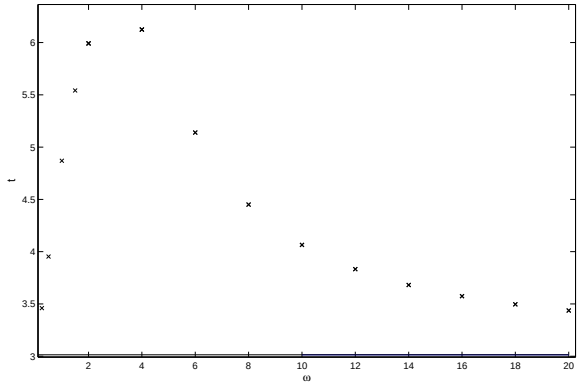

Figure 8.11: The response of the critical time of buckling to ω. We used model F and fixed $n = 2$. The line indicates the asymptotic limit as $\omega \to \infty$. The other dimensional parameters are given in Table 8.2.

representative value of the interbranch distance, and $m = 1$, so that a representative value of ω is 1. However we consider values of ω both higher and lower than this too. We term a buckle with eigenmode in $U_{n,\omega}$ an (n, ω) buckle. We make some brief observations,

- As with the planar buckling, we typically (but not always) find $U_{n,\omega}$ goes unstable after $U_{m,\omega}$ if $n < m$, however the magnitude of the (n, ω) buckle is greater and it is energetically more favourable.

- For small A (i.e. approximately less than 10), then $U_{n,\omega}$ typically goes unstable *before* $U_{n,\gamma}$ if $\omega > \gamma$. In other words, the more axial wrinkling a buckle has, the sooner it becomes unstable. The planar buckle often goes unstable *last* (which is evident from a careful comparison of Figure 8.10 to Figure 8.6). This is not surprising because the system can relieve stress more easily in the planar direction by expanding outwards, but in the axial direction the displacement is fixed.

- For large A of approximately 10 or greater, typically $U_{n,\omega}$ goes unstable *after* $U_{n,\gamma}$ if $\omega > \gamma$. In other words, the more responsive the growth is to the stress, the more the system favours planar buckles over axial buckles. This is evident in Figure 8.11, although observe that the asymptotic limit as $\omega \to \infty$ of the critical times appears to be their infimum. However we expect that these very large values of ω lie outside the range of validity of our model.

8.3 Compatibility of the Model Variants with the Rest of the Tumour

One of the fundamental aims of this thesis is to explain the buckling of a capillary in terms of its immediate microenvironment only. It is crucial that the predictions of our model, with a geometry localised around a capillary, can be compatibly integrated into the broader tumour environment. We have already discussed this for the radially symmetric case in Section 3.4.4. We now continue this discussion in the light of our buckled solutions. We do not need to worry about the buckle in one capillary interacting nonlinearly with its neighbour, as the nonlinear interaction between the fundamental solutions will almost always be more substantial. This is because the increment in the deformation due to a buckle of mode n decays more rapidly than the fundamental deformation,[2] since they have asymptotic order

$$\nabla \mathbf{u}_1 \simeq O(R^{-n}). \tag{8.6}$$

For the models with a finite outer radius R_2, we investigate the effect of varying this radius on the model behaviour. The radius represents half the mean intercapillary distance. We note that in the papers of Konerding *et al*, the mean intercapillary distance varied from approximately 20 to 2000 micrometers [87], with a mean of approximately 170 micrometers in the tumour centre. We plot results from model A in Figure 8.12; results from model C in Figure 8.13; and results from model G in Figure 8.14. It can be seen that the approach of model A to model F is much slower than the approach of models C and G. This is not surprising, because in model A the displacement is only matched to the asymptotic limit of the displacement in model F (which is $\mathbf{u}_0 = \mathbf{0}$). However in models C and G the displacement at R_2 matches the displacement in model F at R_2 to *linear* order. We plot the $O(R^{-1})$ asymptotic convergence of the growth strain $F_{e,\alpha\alpha} - 1 \simeq \nabla \mathbf{u}_{\alpha\alpha} + (1 - \zeta_\alpha)$ and stress at $R = R_2$ for model G in Figure 8.14. We consider models C and G to probably be more accurate than most circumstances because they allow the distance between existing

[2] Occasionally mode 2 buckles are relevant in the asymptotic limit as $R \to \infty$, as they decay as $\mathrm{O}(R^{-2})$ in the radius like the fundamental displacement.

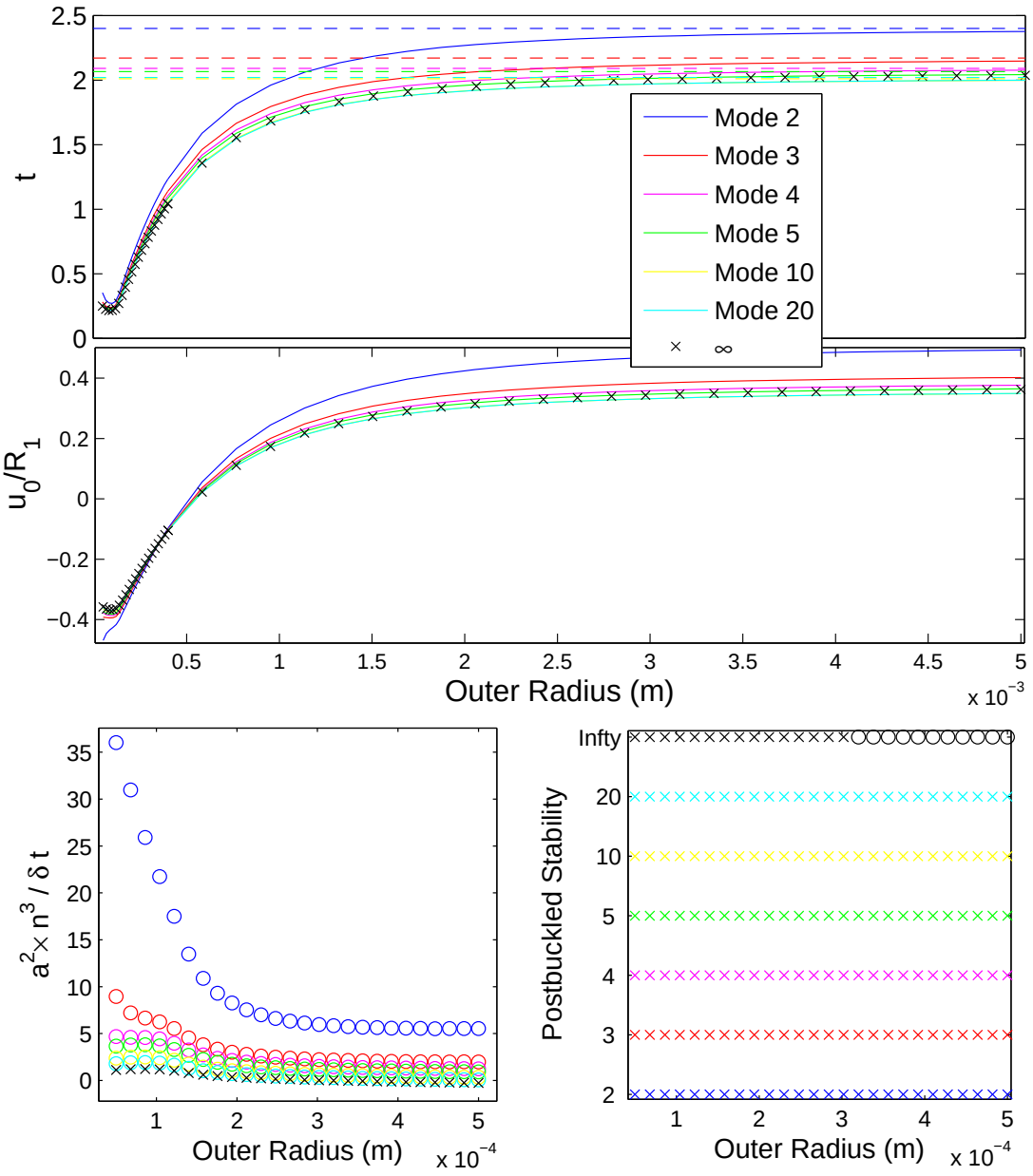

Figure 8.12: The effect of varying the outer radius from 50 micrometers to 5 millimeters on buckling. We implemented model A and the growth is isotropic. The asymptotic limit corresponds to $A = 0$ in the plot in Figure 8.5. The displacement is evaluated at $R = R_1$. In the stability plot, we plot an 'x' if stable buckled equilibrium states exist, and an 'o' otherwise. The dimensional parameter values are given in Table 8.2

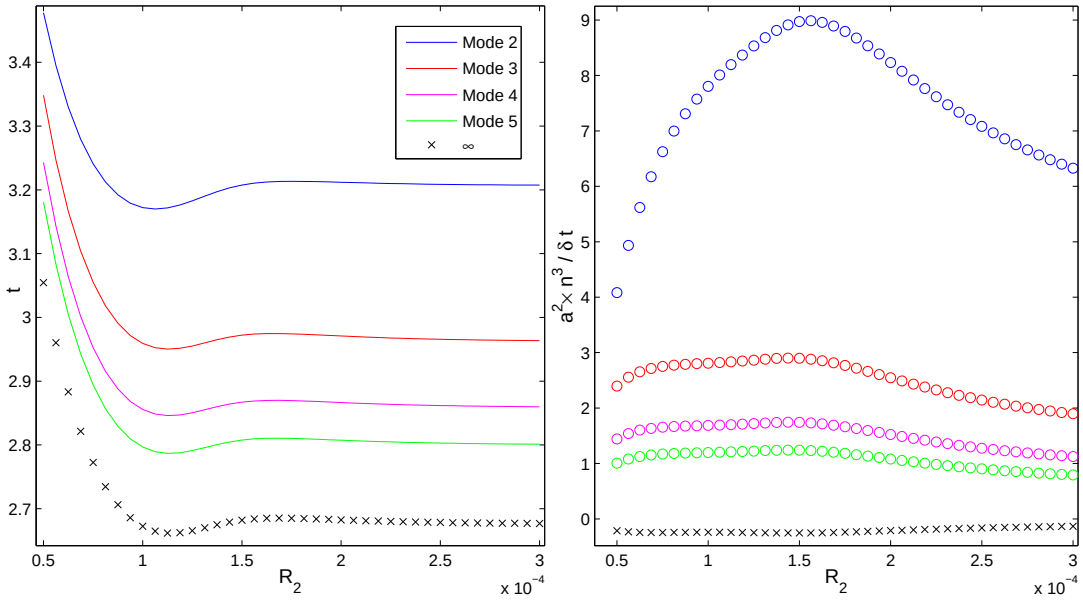

Figure 8.13: The effect of varying the outer radius from 50 micrometers to 5 millimeters on buckling. We implement model C. The growth was anisotropic with $A = 10$. There exist stable buckled equilibrium states for all of the plotted modes, although such states to not exist in the asymptotic limit as $n \to \infty$. The other dimensional parameters are outlined in Table 8.2.

capillaries to naturally increase as the tumour swells. Indeed the results for the onset of buckling in the unconstrained models (C and G) are very close to their asymptotic limit (model F) for

$$R_2 \simeq 2 \times 10^{-4} m \tag{8.7}$$

or greater. This increases our confidence that for values of R_2 greater than or equal to this benchmark, the nonlinear interaction of neighbouring capillaries is minimal and the argument of Section 3.4.4 holds.

A difficulty is that the mean value of R_2 in Konerding *et al* [87] is approximately 10^{-4} m, which is approximately half the value of R_2 in (8.7) for which the unconstrained model variants converge. The models differ markedly at this value of R_2. This means that for tumours with capillaries spaced close to this mean intervessel distance we cannot be confident about the onset of capillary buckling. We expect neighbouring capillaries to interact nonlinearly and the onset of buckling to be heavily affected by macroscopic geometric constraints on the growing tumour. For example in model G, which represents a situation where the growing tumour is highly unconstrained and there is plenty of nutrient, the critical time

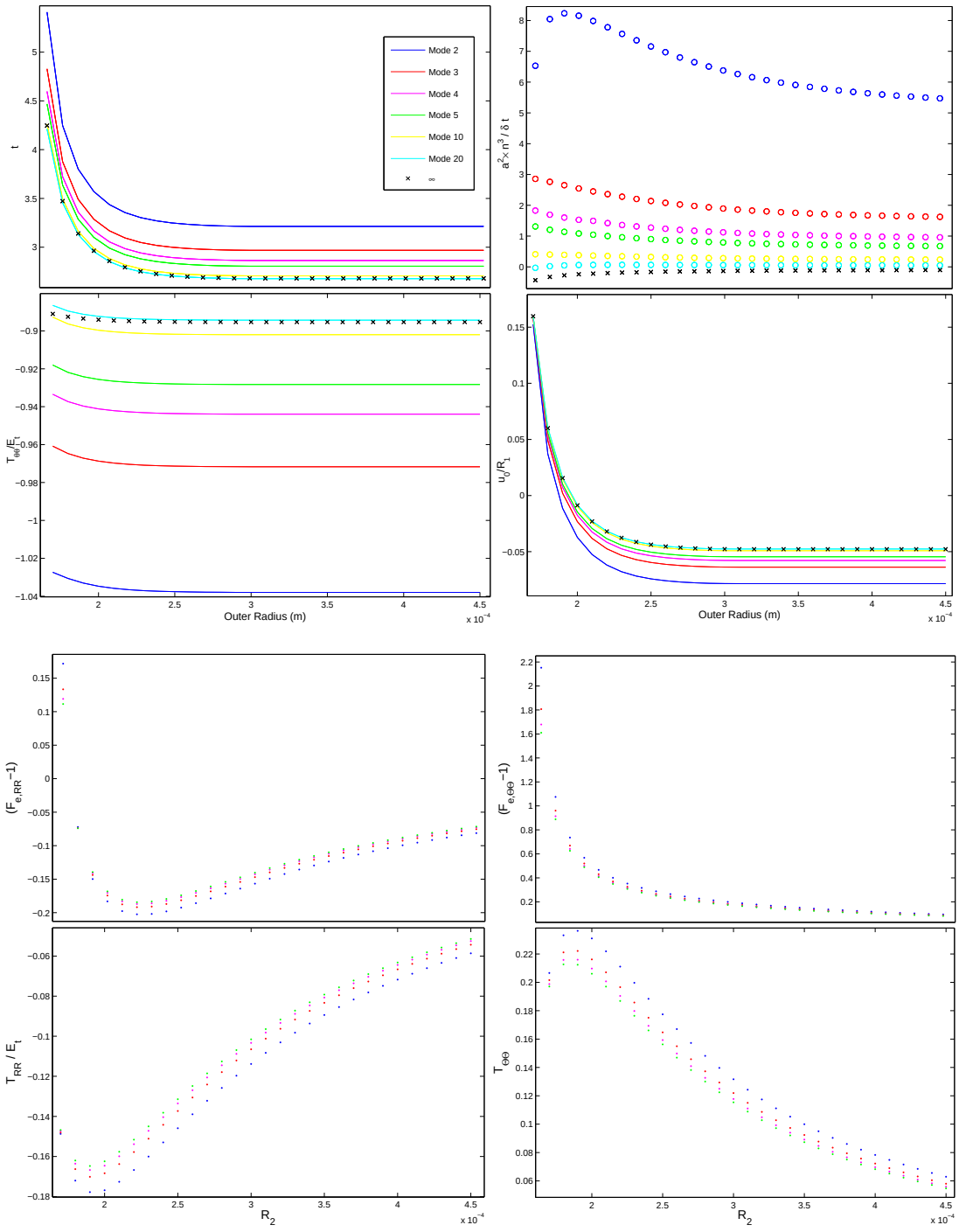

Figure 8.14: The effect of varying the outer radius from 50 micrometers to 5 millimeters on buckling. We implement model G. The growth was anisotropic with $A = 10$. In the bottom four figures the variables are evaluated at R_2. The other dimensional parameters are given in Table 8.2.

rapidly *increases* as R_2 decreases. By contrast, in model A (where the tumour is highly constrained) the buckling time *decreases* as R_2 decreases, essentially because the average level of growth is higher due to the decreased intercapillary distance, but the growth is also constrained. Furthermore for small R_2 in particular, we expect the grown strain, stress and nutrient concentration in model A to each be in the nonlinear regime at $R = R_2$. As explained in Section 3.4.4, in these circumstances we expect the model accuracy to potentially be severely weakened by the restriction of the geometry to an annulus. However model A is still of value in these circumstances because it gives an *upper bound* on the onset of buckling, as inhomogeneities usually cause buckling to occur more readily [10]. An imperfection analysis might help us to quantify this further, however it is beyond the scope of this thesis.

8.4 Summary of Key Results

- The critical time $t^{(n,\omega)}$ asymptotes to a finite constant as $\varsigma \to \infty$, where $(n, \omega) = \varsigma(a_1, a_2)$.

- Most of the buckles are stable, except occasionally buckles with planar mode 2. Generally, if $n < m$, we expect $U_{n,\omega}$ to go unstable after $U_{m,\omega}$, but in time the equilibrium state of the latter becomes energetically more favourable. All of these phenomena taken together are suggestive of period doubling.

- Buckling is reasonably sensitive to the level of growth anisotropy. As the responsiveness of the growth to the prevailing stress field increases, the system switches from preferring axial buckles to planar buckles.

- As the outer radius $R_2 \to \infty$, the behaviour of all the model variants approaches model variant F. The unconstrained models (C and G) produce very similar predictions to model F about the onset of buckling for $R_2 \geq 2 \times 10^{-4}$m. Their convergence is much faster than the finite geometry models because they match model F in the linear limit as $R \to \infty$.

Chapter 9

Results for Buckling in Composite System

In this chapter we investigate buckling in the composite model. In this model, a growing tumour interstitium compresses a cylindrical capillary wall. As previously, unless otherwise stated we discard chemotherapeutic treatment, radiotherapeutic treatment and growth inhibition from our model. The onset of buckling is determined using the linear stability analysis outlined in Chapter 5. Our general methodology is to fix most of the parameters to the values outlined in Table 9, before varying one parameter and investigating how the onset of buckling is affected. We proceed from the results established for the radially symmetric solution in Chapter 3 and for buckling in the system without a distinct capillary wall in Chapter 8. In these results we found that model F, in which the outer radius of the annulus is infinite and the nutrient distribution and displacement decay to 0 as $R \to \infty$, is our most preferred model. However we are also interested in investigating model A, which has a finite geometry with outer radius R_2. In model A, at R_2 there is null-displacement and the nutrient flux $\frac{\partial c}{\partial R}$ is zero. Broadly speaking, model F applies to buckling in tumours which are free to expand, and model A applies to buckling in tumours which are constrained. In Chapter 3 we also motivated a value for the growth anisotropy coefficient A of 10. We refer to these chapters for a more detailed discussion of the strengths and weaknesses of each of these models.

Dim. Parameter	Value	Description
R_2	$10^{-4}m$	Outer Radius of Annulus (for finite geometries).
R_1	1.5×10^{-5}	Inner Radius of Annulus.
q	-7.9	Tumour Elastic Parameter.
f	0.2	Tumour Elastic Parameter.
E_t	7800 Pa	Young's Modulus of Tumour.
λ_n	$0.01mMs^{-1}$	Rate of Uptake of Oxygen.
k_n	$4.6 \times 10^{-3}mM$	Michaelis Constant for Oxygen Uptake.
k_c	$8.3 \times 10^{-3}mM$	Michaelis Constant for Cell Growth.
D	$1.5 \times 10^{-9}m^2s^{-1}$	Diffusion Coefficient of Oxygen in Tumour.
n_0	$0.1mM$	Oxygen Concentration at R_1.
E_c	2MPa	Young's Modulus of Basement Membrane.
h	50 nm	Thickness of Basement Membrane
Nond. Parameter	Value	Description
α	0.015	$\lambda_n R_1^2/D$
k_n^*	0.046	k_n/n_0
k_c^*	0.083	k_c/n_0
R_2^*	6.6667	R_2/R_1.

Table 9.1: The default parameter values we use in this chapter, unless otherwise indicated. In our nondimensionalisation the lengthscale is R_1, the nutrient scale is the concentration at R_1 and the timescale is the average time it takes for a tumour cell to proliferate. We do not provide a value for the characteristic proliferation rate because it only changes our timescale. The tumoural elastic modulii (E_t, f and q) are for glioblastoma. Refer to Appendix B for an explanation of these parameters and the papers from which they are sourced.

We generally investigate buckling in the following selection of planar modes $n = \{2, 3, 4, 5, 10, 20\}$, and axial modes $(n, \omega) = \{(1, 0.1), (1, 1), (1, 10), (2, 0.1), (2, 1), (3, 1), (4, 1), (5, 1)\}$. We terminated our search either at $t = 10$, or at $t = 5$ if the displacement at R_0 is positive (we argued in Chapter 3 that a positive displacement is physically unrealistic). In all of the results, the axial modes $(1, 0.1)$ and $(1, 1)$ did not go unstable before this limit, so they are not reflected in our results.

In this chapter we emphasise the medical and biological implications of our model. We are therefore particularly interested in determining the effect of *measurable* variables and parameters on the onset of buckling. In many respects the fundamental critical parameter - time - is one of the least measurable parameters in our model. We may loosely think of $t = 0$ as the time at which a new blood vessel forms, or the time at which the tumour starts to proliferate more rapidly (due to factors which we have not incorporated into our model). However this definition is necessarily imprecise, and therefore it is very difficult for the critical time to be measured. More generally, due to the difficulty of us determining, or even rigorously defining, the base state at $t = 0$, Lagrangian variables such as the first Piola-Kirchhoff Stress, the strain or the growth dilation ζ_α are similarly difficult to measure. It is important to remember that our model is a mathematical idealisation: tumoural growth and vascular buckling is a very complicated process, so we cannot expect our model to exactly correspond to reality.

In contrast, Eulerian variables seem to show much more promise than Lagrangian variables of being measurable. In particular, the Cauchy Stress, whether in the capillary wall or the tumour, is of great interest. We are also interested in plotting the radial displacement u_0 at R_0 at the time of buckling: perhaps this could be estimated by subtracting the mean capillary diameter from the diameter of a capillary at the time of buckling.

For convenience of expression we may write the hoop stress (in State I) of the capillary at R_0 as a direct function of the displacement as follows. The incompressibility condition and the null-stress boundary condition mean that $(1 + \frac{\partial u_0}{\partial R})(1 + \frac{u_0}{R}) = 1$ and $T_{RR} = 0$ at

R_0. After eliminating the Lagrange Multiplier and $\frac{\partial u_0}{\partial R}$ we find

$$T_{\Theta\Theta}/G_c = \left(1 + \frac{u_0}{R_0}\right)\left(1 + \frac{u_0}{R_0} - \left(1 + \frac{u_0}{R_0}\right)^{-3}\right). \tag{9.1}$$

For $u_0/R_0 \ll 1$, this is approximately

$$T_{\Theta\Theta}/G_c \simeq \frac{4u_0}{R_0}. \tag{9.2}$$

The magnitude a of the buckle is governed by

$$a/\sqrt{\delta t} = \pm\sqrt{-\frac{C_2}{C_1} - \frac{2C_3}{3C_1}} \tag{9.3}$$

where the constants $\{C_1, C_2, C_3\}$ are given in (5.47). We have assumed that the time increment when the system enters the buckled state δt^* is zero.[1]

Finally, we are also interested in understanding the distribution of the strain energy. Although this is difficult to measure, it helps us discern the key factors driving the onset of buckling. We saw that the leading order of the difference in energy of State II (the buckled state) and State I (the unbuckled state) is[2]

$$W_4^{(n,\omega)} = \epsilon^4 \delta t^2 \left(W_{c,4}^{(n,\omega)} + W_{t,4}^{(n,\omega)}\right) + o(\epsilon^4), \tag{9.4}$$

where

$$\begin{aligned} W_{c,4}^{(n,\omega)} &= \frac{1}{4}a^4 C_1^{cap} + \frac{1}{2}a^2 C_2^{cap}, \\ W_{t,4}^{(n,\omega)} &= \frac{1}{4}a^4 C_1^{tum} + \frac{1}{2}a^2 C_2^{tum} + \frac{1}{2}a^2 C_3 \end{aligned} \tag{9.5}$$

and $\{C_1^{cap}, C_1^{tum}, C_2^{cap}, C_2^{tum}, C_3\}$ are defined in (5.69). We may think of $W_{c,4}^{(n,\omega)}$ and $W_{t,4}^{(n,\omega)}$ as indicating the 'energetic contribution' of respectively the capillary wall and tumour to the buckled state. If $(W_{t,4}^{(n,\omega)} - W_{c,4}^{(n,\omega)}) < 0$, then the energetic relaxation in the tumour

[1] Refer to Section 4.2.5 for an explanation of this.

[2] It is important the reader does not confuse this with the radial component of the buckled displacement $W^{(n,\omega)}$

resulting from the buckle is greater than the energetc relaxation of the capillary wall. The converse holds if this variable is positive.

9.1 Variance of the Basement Membrane Stiffness and Thickness

In this section we discuss the effect of varying the basement membrane stiffness and thickness on the onset of buckling. We begin with our results for model F, which we recall is a capillary in an infinite tumour. We expect the basement membrane stiffness and thickness to vary considerably from tumour to tumour due to the poorly developed tumour vasculature. We plot the effect of varying the basement membrane Young's Modulus in Figure 9.1, and we plot the effect of varying the basement membrane thickness in Figures 9.2 and 9.3. We make the following observations,

- Generally the critical time of buckling increases as the thickness h or stiffness E_c of the capillary wall increases, although this does not always hold. This can be seen in Figures 9.1(A) and (C), and Figures 9.2(A) and (C).

- The asymptotic limit of the critical times as the mode number tends to ∞ is much greater than the critical times plotted in Figure 9.1(C). This is not surprising because the capillary wall is very thin ($h = R_1/125$), which means that the mode needs to be very great since the width of the boundary layer is of order n^{-1}. Since such fine wavelengths are outside of the scope of accuracy of our model, we do not again search for the asymptotic limit in subsequent results.

- Of the plotted modes, the buckles with a fine wavelength (or high wavenumber(s)) tend to go unstable first (although this rule of thumb does not hold in the asymptotic limit). However, despite these results, we generally expect the system to prefer the larger wavelengths (with planar modes (1,2,3,4)) for the following reasons. It can be seen in Figures 9.3(I) and (L) that these modes probably become energetically more favourable over time, as the leading order of the change in energy $W_4^{(n,\omega)}$ from the unbuckled to the buckled state is more negative. Furthermore, as we discussed

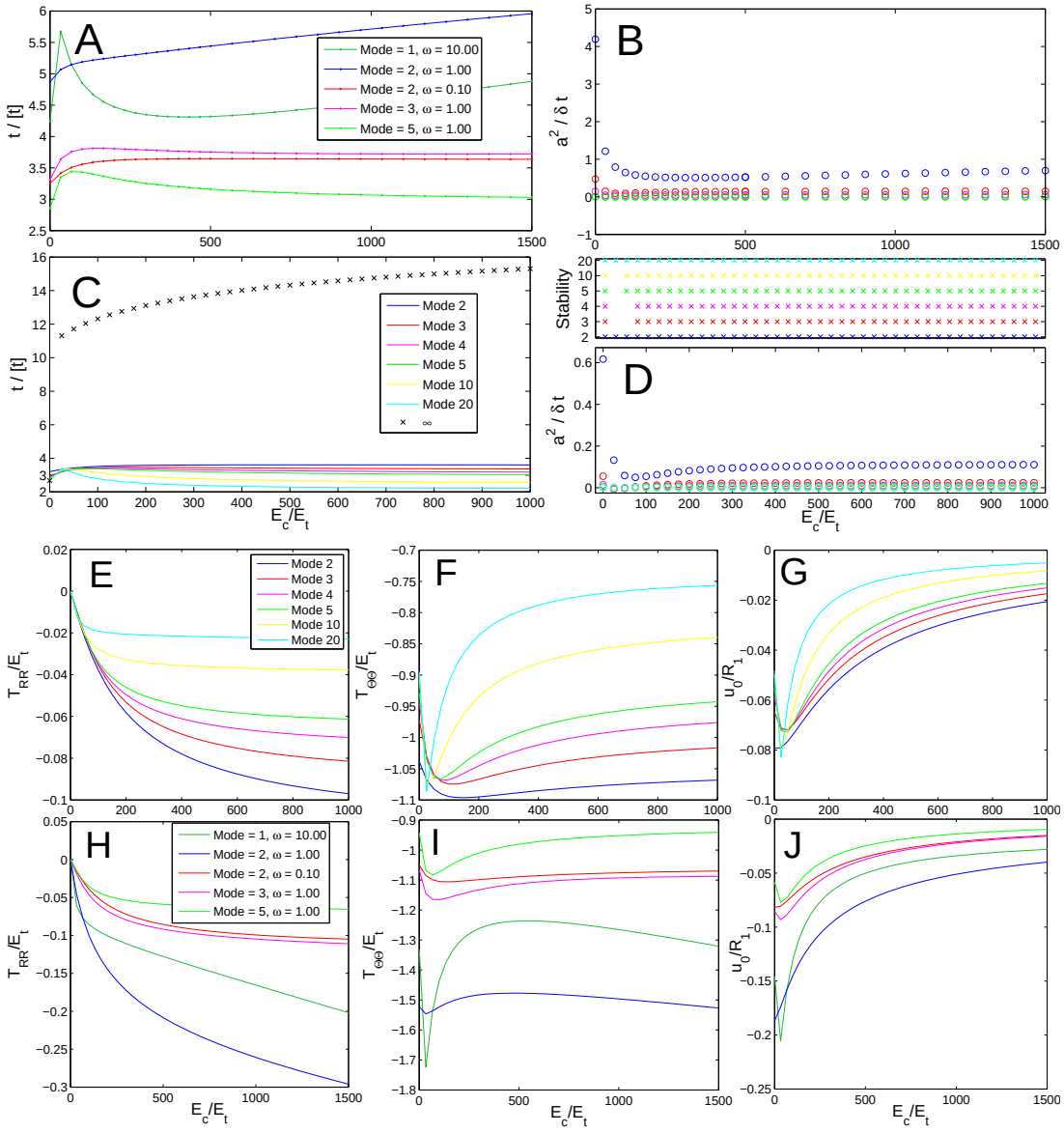

Figure 9.1: In the above simulations we varied the Youngs Modulus of the capillary wall over the stated values. We implement model F. In each set of figures, the top set represents planar buckles and the bottom set represents axial buckles. In the stability plot, we plot an 'x' if there exists a stable buckled equilibrium state, and an '.' otherwise. Over all of the plotted axial modes, the buckled state is stable. The stress plots are the tumoural stresses at R_1 at the time of buckling, and the displacement plot is the displacement u_0 at R_1 at the time of buckling.

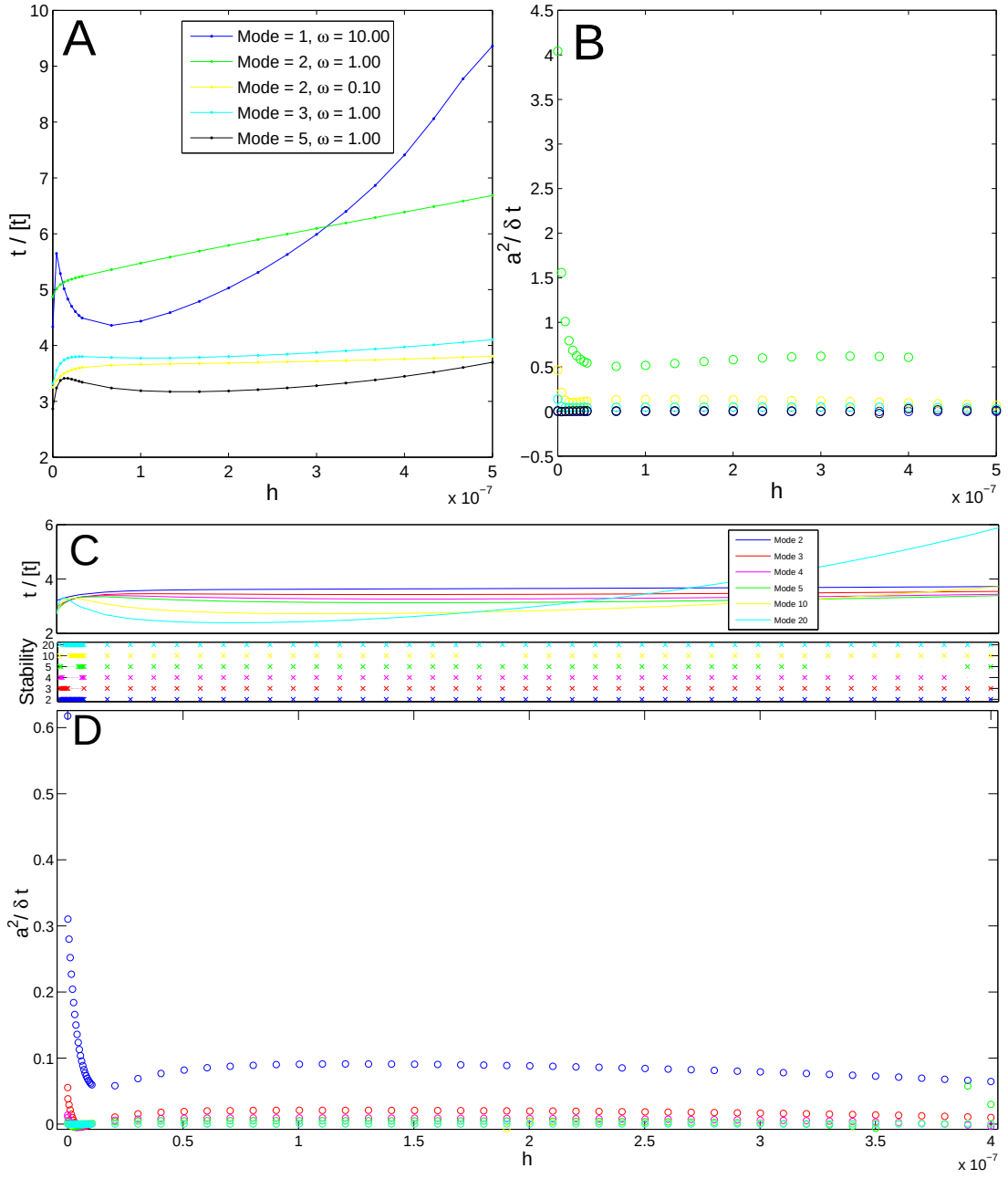

Figure 9.2: In the above simulations we varied the thickness of the basement membrane from 10^{-10}m to 10^{-6}m. We implement model F. In the top two figures we plot the critical time and magnitude a of axial buckles. In the bottom three figures we plot the critical time and magnitude of planar buckles. In the stability plot, we plot an 'x' if there exists a stable buckled equilibrium state, and an '.' otherwise. For all values of h and for all of the plotted axial modes, the buckled state is stable. Note that a is very sensitive to h when $h \ll 10^{-8}$m. The asymptotic limit as $h \to 0$ of a is equal to the result for $E_c = 0$ in Figure 9.1.

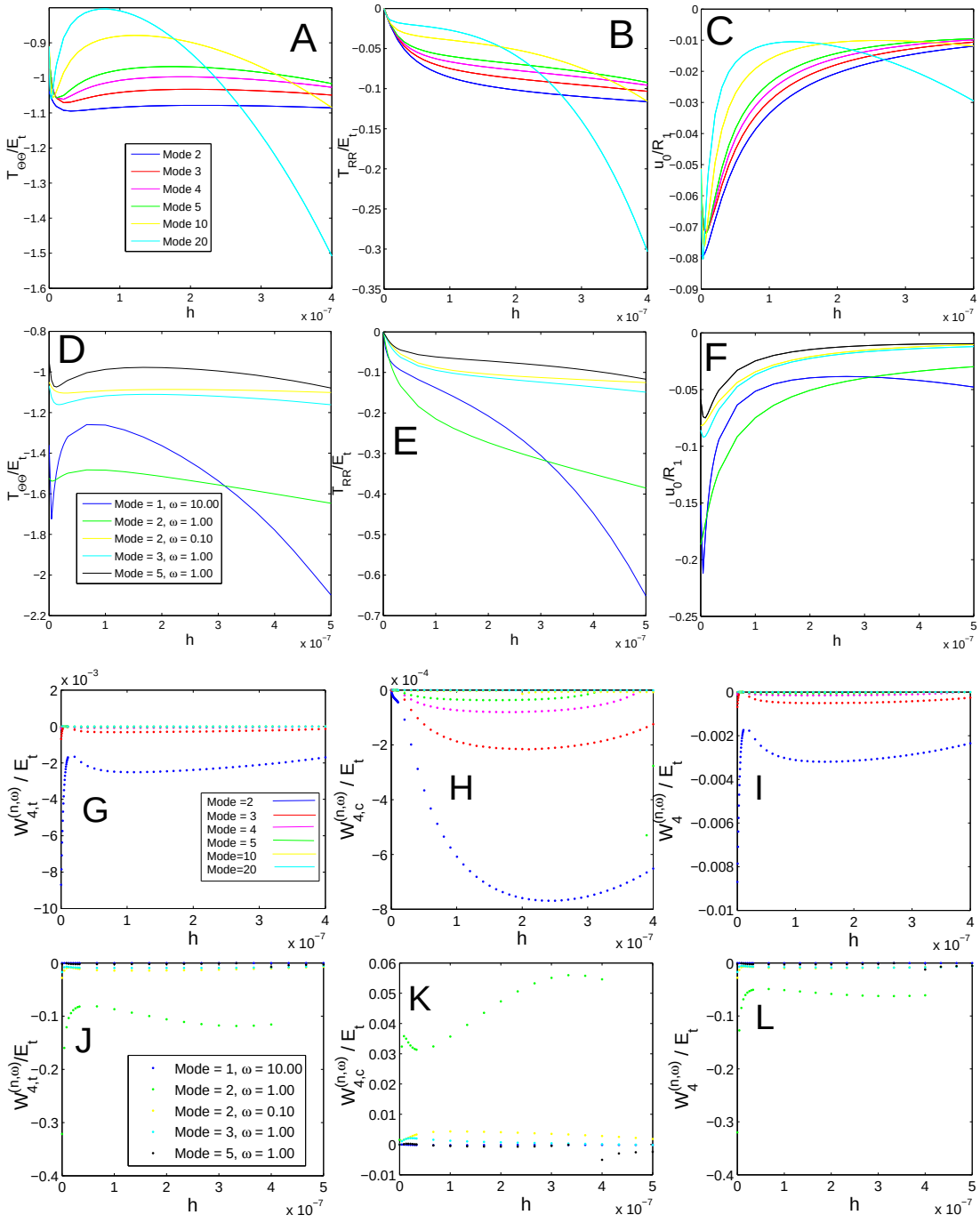

Figure 9.3: In the above simulations we varied the thickness of the basement membrane from 10^{-10}m to 10^{-6}m. The stress plots are the tumoural stresses at R_1 at the time of buckling.

in Section 8.1, we expect that our continuum approximation breaks down for fine wavelength buckles, and that fine wavelength buckles might be dissipated by the cellular phase. Finally, Stoll only observed planar buckles of wavenumber 2 and 3 in his experimental results [129]. It appears that he did not directly look for axial buckles (in any case it would possibly be very difficult to discern axial buckling).

- The bifurcation of the axial modes is stable, and the bifurcation of the planar modes is almost always stable (it can be seen in Figures 9.2(B) and (D) that there almost always exists a positive solution for a^2). The unstable planar modes are typically of low wavenumber (i.e. typically $n \in \{2, 3, 4, 5\}$) and only occur when the capillary wall is less strong than average. That is, the unstable bifurcations only occur when either the thickness of the capillary wall is less than its 'average' value of 10^{-7}m, or the Young's Modulus of the capillary wall is less than its 'average' value of $260E_t$ (where E_t is the Young's Modulus of the tumour).

- The magnitude of the buckle is greatest when the capillary wall is weak (i.e. when it is very thin, or when its Young's Modulus is very low). It can be seen in Figures 9.2(B) and (D) that the magnitude a of the buckle initially decreases rapidly as h or E_c is increased from 0. Once h and E_c are at mean values of $h = 10^{-7}m$ and $E_c = 260E_t$, the magnitude a of the buckle is approximately one quarter to one sixth the magnitude of the buckle in the system without a distinct capillary wall.

- The tumoural radial stress T_{RR} at R_1 increases as h increases (see Figure 9.3(B) and Figure 9.3(E)). However the tumoural hoop stress $T_{\Theta\Theta}$ always has greater magnitude than the radial stress over the entire parametric range (see Figure 9.3(A) and Figure 9.3(D)). A similar result holds for the hoop stress as E_c is increased: these results are plotted in Figure 9.1. The tumoural hoop stress $T_{\Theta\Theta}(R_1)$ at the time of buckling is reasonably *invariant* to variation of h or E_c. It is significantly more invariant than the tumoural radial stress $T_{RR}(R_1)$. It is also more invariant than the displacement $u_0(R_1)$, and it is more invariant than the capillary hoop stress $T_{\Theta\Theta}$ (as it can be inferred from (9.2) that the capillary hoop stress is approximately proportional to u_0). Thus of all the variables in our model, the tumoural hoop stress is perhaps the

most suitable indicator of the onset of buckling.

- The magnitude of the change in stored energy of the tumour (i.e. $W_{4,t}^{(n,\omega)}$) is almost always greater than the magnitude of the change in stored energy of the capillary wall (i.e. $W_{4,c}^{(n,\omega,4)}$). This can be seen in Figures 9.3 (G)-(L). This suggests that the instability is primarily driven by *residual stress in the tumour*, rather than residual stress in the capillary wall.

We plot the effect of varying the capillary wall thickness h on the onset of buckling in model A (with null-displacement outer boundary condition) in Figure 9.4. Model A contrasts model F because the critical time generally *decreases* as we strengthen the capillary wall by increasing h (see Figure 9.4(A)), but in model F the critical time increases. Furthermore the magnitude a of the buckle in Model A generally *increases* as we increase h (see Figure 9.4(B)), whereas in model F it decreases. It appears that the basic reason why model A buckles more readily when there is a capillary wall is that the capillary wall constrains the growth, so that compressive forces build up more rapidly and the system buckles sooner. It is interesting to notice that the relative energetic contribution of the capillary wall to the buckle is greater than in model F (i.e. the magnitude of $W_{4,c}^{(n,\omega)}/W_4^{(n,\omega)}$ is greater): indeed for large values of h the energetic contribution of the capillary wall $W_{4,c}^{(n,\omega)}$ is greater than the energetic contribution of the tumour $W_{4,t}^{(n,\omega)}$. These results can be observed in Figures 9.4(C) - (E).

9.2 Effect of Treatment on Buckling

We have outlined a model of cell death due to chemotherapy or radiotherapy in Section 2.4.4. We may investigate the stability of capillaries in tumours that are being treated by incorporating a nonzero cell death term into our fundamental solution (the method of numerical solution in Section 3.1 is the same). The stability analysis is the same as for when the growth is positive. However when we actually implemented the stability analysis, the system never buckled over any physically realistic parametric ranges. This is probably due to the fact that the microenvironment surrounding the capillary is dominated by tensile rather than compressive forces due to the cellular death.

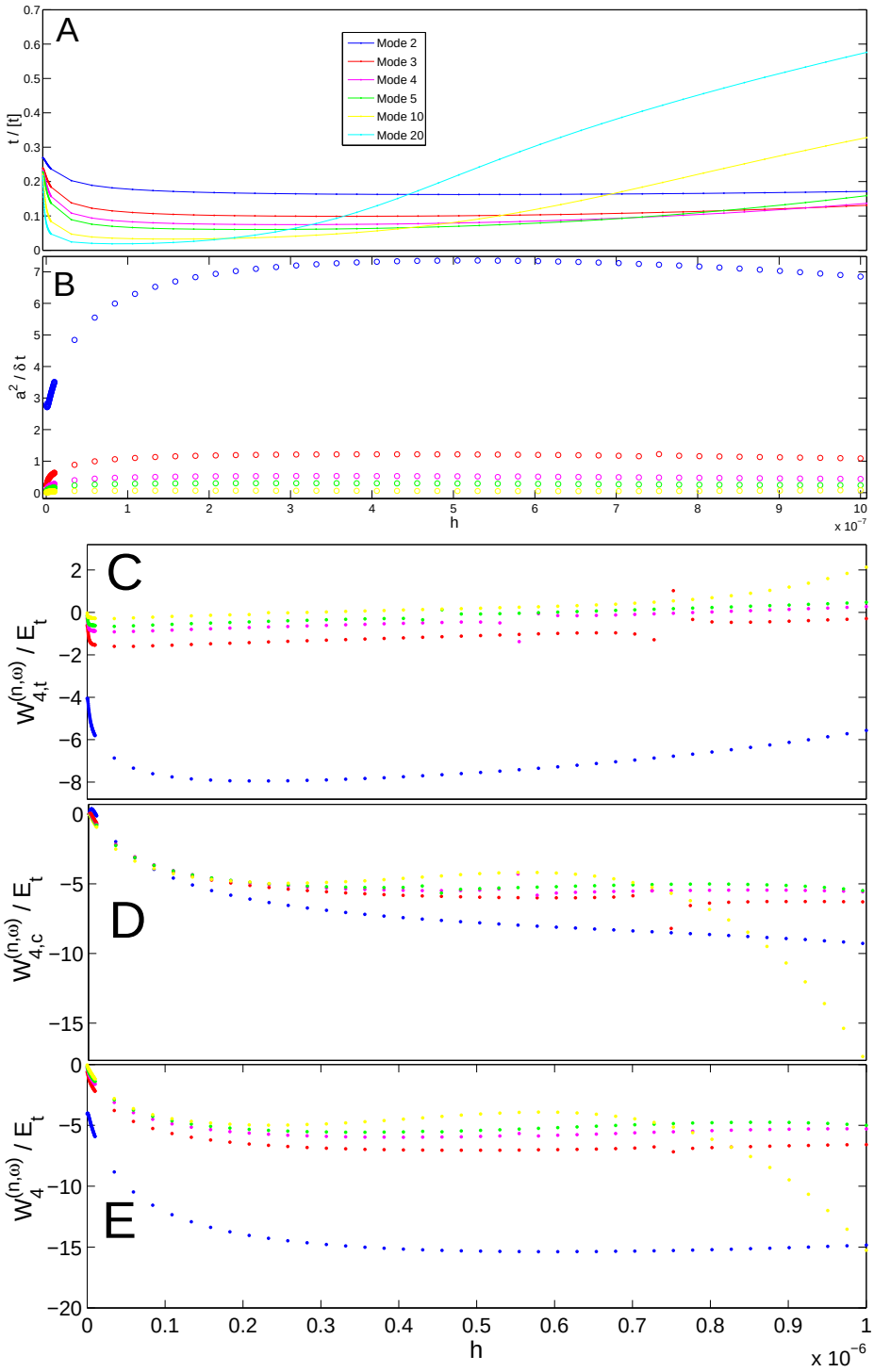

Figure 9.4: In the above simulations we varied h from 10^{-10} to 10^{-7}m. We implement model A, with isotropic growth. The stress plots are the tumoural stresses at R_1 at the time of buckling. All of the plotted equilibrium states are stable, except mode 20, which destabilises as h increases.

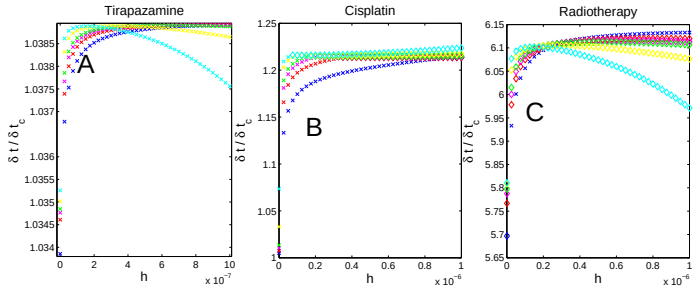

Figure 9.5: In the above simulations we varied h from 10^{-10} to 10^{-7}m. We implement model A, with isotropic growth. The results are continued from Figure 9.4. In this plot we initiate treatment after buckling has occurred and determine what happens to the buckle, as explained in Section 9.2. We plot a diamond if the buckle destabilises first (i.e. if the expression for δt_c in (9.6) is greater than the expression in (9.7)), or otherwise an 'x' if the buckle smoothly closes.

We may also model the experiments of Padera *et al* [111]. They injected a cytotoxin into a tumour with collapsed lumen and discovered that the lumen reopened. The authors hypothesised that the cellular death relieved the compressive forces which had closed the lumen. We modelled this phenomenon in Section 5.2.3 by considering the effect of introducing a nonzero cell death term into an already buckled system. More precisely, we assume that there is a mode (n, ω) buckle and that treatment began at time $t^*_{n,\omega} + \frac{\epsilon^2 \delta t_c}{2}$, where $\delta t_c < \delta t$. We consider how small $\delta t / \delta t_c$ must be for the buckle to close. We showed in Section 5.2.3 that the buckle destabilises[3] if

$$\delta t_c = \delta t \left(1 + \frac{C_2 + C_3}{C_2^c + C_3^c} \right), \tag{9.6}$$

where C_2^c and C_3^c are constants determined by the treatment. Similarly the buckle smoothly reopens if

$$\delta t_c = \delta t \left(1 + \frac{3C_2 + 2C_3}{3C_2^c + 2C_3^c} \right). \tag{9.7}$$

It can be seen in Figure 9.5 that all of the buckles reopen / destabilise very quickly when the chemotherapeutic drugs cisplatin and tirapazamine are administered. The buckle also reopens / destabilises when the tumour is treated with radiotherapy, however it takes considerably longer. These results are in broad agreement with Padera *et al* [111].

[3]If the buckled state becomes unstable, it will not necessarily move back to the unbuckled state.

9.3 Comparison of our Model to the Thin-Ring Model

We now compare our model to the model of the capillary wall as an inextensible flexural ring. The capillary wall has been modelled as an inextensible flexural ring by Stoll, Mollica and Moreno [129, 102, 103]. In this section we refer to our model as the 'composite' model and the other model as the 'flexural ring' model. Before we discuss the flexural ring model we must provide a brief overview of Koiter's shell theory, with which the model is formulated.[4] The fundamental assumptions of this theory, known as the Kirchhoff-Love assumptions, are

(a) points which lie on a particular normal to the undeformed middle-surface of the shell also lie on a particular normal to the deformed middle-surface, (9.8)

(b) the displacements in the normal direction are the same for all points on a normal. (9.9)

In Koiter's shell theory, the strain energy is equal to the sum of a quadratic form in the strains (i.e. the tangential stretch) and a quadratic form in the change of curvature tensor. In the flexural ring model, the deformation is assumed to be planar (so that the capillary wall is in effect a one-dimensional ring, and the only nonzero components of the strain and change in curvature tensors are the azimuthal components). The strain energy of the ring is then given by

$$V = \oint_{\text{Ring Mid-Surface}} \frac{E_c}{1-\nu_c^2}\left(\frac{h}{2}\gamma_{\Theta\Theta}^2 + \frac{1}{24}h^3\rho_{\Theta\Theta}^2\right) ds, \tag{9.10}$$

were E_c is the Young's Modulus, ν_c is the Poisson's ratio and $\hat{R}$ is the radius of the shell mid-surface. To linear accuracy in $\mathbf{u}$,

$$\gamma_{\Theta\Theta} = \frac{1}{\hat{R}}\left(u_r + \frac{\partial u_\theta}{\partial \Theta}\right). \tag{9.11}$$

$$\rho_{\Theta\Theta} \simeq \hat{R}^{-2}\left(\frac{\partial^2 u_\Theta}{\partial \Theta^2} - \frac{\partial u_\Theta}{\partial \Theta} - u_r\right), \tag{9.12}$$

[4] For a more in-depth discussion consult Niordson [108] or Ciarlet [44]).

where $\gamma_{\Theta\Theta}$ is the shell deformation gradient (the strain), and $\rho_{\Theta\Theta}$ is the change in curvature tensor.

In the models of Stoll, Mollica and Moreno [129, 102, 103], the capillary wall is modelled as an inextensible one-dimensional rod. The buckling of circular inextensible rods is a classic problem of nonlinear elasticity and has been extensively analysed: refer to Tadjbakhsh and Odeh [132], Antman [10] and Pozrikidis [114] for more details. The assumption of inextensibility means that the strain $\gamma_{\Theta\Theta}$ is negligible, so that the strain energy of the ring is given by

$$E = \oint \frac{1}{2}\kappa_{BM}\rho_{\Theta\Theta}^2 d\mathbf{s}, \tag{9.13}$$

The bending modulus κ_{BM} is $E_c h^3/(12(1-\nu_c^2)\hat{R}^3)$. An external hydrostatic pressure p_{ring} is applied normal to the wall of the ring. An energy potential for the hydrostatic pressure (which represents the compressive force of the tumour) is therefore equal to the pressure multiplied by the area enclosed by the capillary wall. The equation of equilibrium (i.e. the Euler-Lagrange equation resulting from (9.13)) may be simplified to a nonlinear second order ordinary differential equation in the curvature $\rho_{\Theta\Theta}$ which is solved numerically (note that the full nonlinear curvature is solved for, not the linearisation in (9.12)) [132, 114]. Tadjbakhsh and Odeh showed that the critical pressure at which a mode n buckle bifurcates from the radially symmetric solution is [132]

$$p_{ring} = \kappa_{BM}(n^2 - 1). \tag{9.14}$$

In Figure 9.6, we compare the onset of buckling in the flexural ring model to the onset of buckling in models A and F. It can be observed in the figures in the centre and on the right that the critical pressure of the flexural ring model is typically much less than the critical pressure T_{RR} at the capillary-tumour interface of models A and F. This is particularly when h is close to its typical value of 0.01 and when the buckling mode is small (i.e. less than or equal to four).

There are two major reasons for the massive difference in the critical pressure of the flexural ring model compared to the critical pressure of our models. The first reason, which we have already discussed in Section 9.1, is that in our models (F and A) the tumoural stored

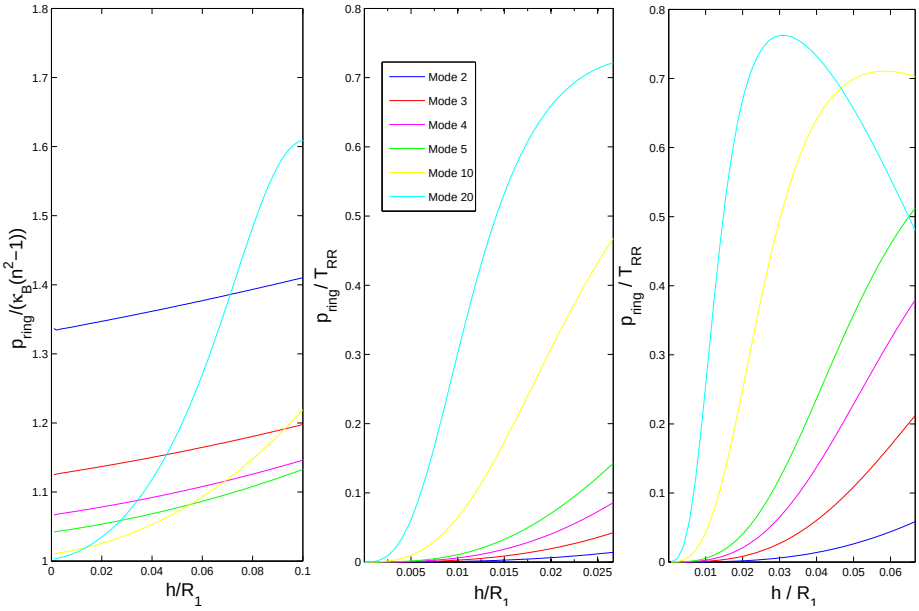

Figure 9.6: Here we compare the flexural ring model of Stoll [129] to our model. On the left we plot the critical pressure of buckling when the ring is modelled as a two-dimensional Neohookean annulus of thickness h and outer radius 1, subject to an external pressure p_{ring}. In the middle we plot the critical pressure of the flexural ring model p_{ring} (as given in (9.14)) divided by the critical pressure T_{RR} at the capillary-tumour interface predicted by model F (T_{RR} is separately plotted in Figure (9.3). The data in the figure on the right is the same as the data in the middle, except that the critical pressure T_{RR} derives from model A (which is separately plotted in Figure 9.4).

elastic energy dominates the capillary wall stored elastic energy. It is in the modelling of the tumour where our composite model differs the most from the thin-ring model: in the latter, the 'tumour' is a hydrostatic pressure. This result confirms one of the key goals of this thesis, namely, that consideration of the stored elastic energy in the microenvironment surrounding capillaries in elastic tumours is essential for us to understand capillary buckling.

The second reason is that at the time of buckling, the elastic behaviour of the capillary wall in our composite model is very different from the elastic behaviour of the capillary wall in the flexural ring model. To see this, we must explore in greater detail the underlying assumptions of the flexural ring model. The assumption of inextensibility is justified when the external pressure is of the order of $E_c h^3$ and the shell is free to deform in a manner which preserves its metric.[5] Thus our NeoHookean model of the capillary wall is consistent with the inextensible flexural ring approximation when the radial pressure at the outside of the capillary wall is of the order of the cube of h. However the two models become inconsistent once the pressure leaves this regime. We now demonstrate these two assertions.

We firstly demonstrate the consistency of our NeoHookean model with the flexural ring model for low levels of pressure. To do this, we demonstrate that if we consider the NeoHookean capillary wall in isolation, then its critical pressure of buckling is similar to the critical pressure predicted by the flexural ring model. Thus in this simple model we neglect the tumour and consider a thin annulus composed of an incompressible NeoHookean material with (nondimensionalised) outer radius 1 and thickness h. A constant hydrostatic pressure p_{ring} is exerted on the outer edge of the annulus, and the inner edge is unstressed. We gradually increase the pressure and investigate the stability of the annulus using the Trefftz Condition (using the method outlined in Section 4.1.2). The critical pressures at which the system becomes unstable to various modes is plotted in the figure on the left in Figure 9.6. Note that $h/R_1 \simeq 0.01$ is the approximate order of magnitude of the capillary wall thickness. It can be seen that the critical pressure is of the same order as the critical pressure predicted by the flexural ring approximation given in (9.14), so that in these initial stages the two models seem broadly consistent.[6]

[5] For an in depth discussion and analysis of this refer to Ciarlet [44].

[6] One of the reasons that the results do not agree in the asymptotic limit as $h \to 0$ appears to be that in the incompressible NeoHookean model $\frac{\partial V_n}{\partial R}$ asymptotes to a finite constant, where the buckle is of the form

However in the composite model, to which we now return, the system does not buckle in these initial stages as the tumour has a reinforcing effect on the capillary wall. This result confirms the 'tunnel-in-gel' hypothesis of Fung, namely, that the stability of capillaries derives more from the elastic support of the surrounding tissue than the rigidity of the basement membrane [56]. As a consequence of the capillary not buckling immediately, the decrease in the capillary radius becomes non-negligible as it contracts inwards, which is inconsistent with the assumption of inextensibility in the flexural ring model. Indeed if the metric of the capillary wall is to be preserved then it is necessary that either its radius remains constant, or it buckles. Furthermore in the composite model, in the fundamental state (recall this is radially symmetric) the hoop stress $T_{\Theta\Theta}$ grows to rapidly dominate the bending moment $\kappa_B \rho_{\Theta\Theta}$. This means that if the composite model was to be approximated with shell theory then the first term in (9.10) should no longer be neglected. However an even more fundamental problem with a shell theory approximation of the capillarty wall in the composite model is that the radial strain $\frac{\partial u_0}{\partial R}$ grows to be of the same order of magnitude as the azimuthal strain $\frac{u_0}{R}$. This violates the second Kirchhoff-Love assumption (9.8).

We may use these results to speculate about the buckling of capillaries in tumours which cannot sustain an elastic pressure gradient, such as the carcinomas outlined in Appendix B.0.12. We expect that such materials behave more like fluids than solids, so that the flexural ring model of Stoll is much more accurate than our nonlinearly elastic model. In light of the above discussion, we might expect the capillaries in such fluid-like materials to buckle much more readily than the capillaries in materials with an elastic pressure gradient, because they do not receive elastic support from the surrounding tissue (note that such behaviour is contradictory to the hypothesis of Fung outlined in the previous paragraph). However on the other hand, we expect that the buildup of pressure in fluid-like tissues would be much less quick than the buildup of pressure in elastic tissues, because the cells are free to migrate further away from the capillary. In turn we expect the cellular migration to be governed by the macroscopic geometric constraints on the tumour. Thus we expect that the buildup of pressure, and consequently the buckling, would be determined by the overall level

$\mathbf{u} = (W_n(R)\cos(n\Theta), V_n(R)\sin(n\Theta))^T$. This contradicts the first of the Kirchhoff-Love assumptions (9.8). However the results are still sufficiently close to be acceptable.

of geometric constraint of the tumour. We conclude that it is difficult to determine whether capillaries in fluid-like tumours buckle more or less readily than capillaries in elastic-like tumours.

We finish this section by comparing the wavenumber preference of the composite model to the flexural ring model. The flexural ring model is much more inclined to low wavenumber buckles (particularly buckles of wavenumber 2), because the critical pressure is proportional to the square of the wavenumber (as can be seen from (9.14)). Any inhomogeneities, whether in the elastic structure of the ring or the applied pressure, would have to be very substantial if the ring were to prefer another wavenumber to 2. Furthermore it has been demonstrated by Tajdbakhsh and Odeh that the buckled equilibrium state is stable, so that once the system adopts a particular branch in the bifurcation diagram we expect it to remain on that branch [132]. In contrast, in the composite model the low wavenumber buckles usually go unstable *last*.[7] The reason for the difference between the two models can be seen in their strain energy functions. In the flexural ring, buckling occurs when the increase in the shell bending energy resulting from the buckle matches the decrease in the hydrostatic potential energy (which is proportional to the area enclosed by the capillary wall) caused by the buckle. Low wavenumbers buckle first because the increase in the bending energy is not as great: this can be inferred from (9.12), where the curvature is of order n^2. In contrast, the energetic landscape of the composite model is dominated by the tumoural stored elastic energy (this was argued in Section 9.1). The composite model favours buckles of high wavenumber because of the enormous hoop stress $T_{\Theta\Theta}$ at R_1. There is an energetic imperative for the tumour to relieve the hoop stress by increasing the length of the boundary at R_1; a need which is best satisfied by high wavenumber buckles. This effect is compounded by the fact that the growth attenuates rapidly as R increases. This heightens the system's preference for buckles which are localised at R_1: a preference which is satisfied by high wavenumber buckles since these attenuate more rapidly as R increases (this can be seen from (7.62)). However once the wavenumber n is so large that the buckle is concentrated in the capillary wall (and not in the tumour), then we expect the critical time to increase as

[7]However, it is important for the reader to note that we nevertheless expect the system to prefer low wavenumber buckles. This point is argued in Section 9.1.

n increases as the buckled energy of the capillary wall dominates the buckled energy of the tumour. This is why the asymptotic limit of the critical times as $n \to \infty$ in Figure 9.1 is much greater than the plotted critical times. However we do not worry about this regime as we consider buckles of such fine wavenumber to be outside of the scope of accuracy of our model.[8]

9.4 Variation of the Tumour Compressibility Coefficient q

In Figure 9.7 we investigate the dependence of buckling on the compressibility coefficient q. This governs the compressibility of the tumour. Its valid range is $(-\infty, -1)$. The tumour becomes incompressible in the limit as $q \to -\infty$. We fitted q to confined compression tests of glioblastoma in Appendix B.0.12 and obtained a median value of -7.9. However there was some uncertainty in our fitting, with the 95 per cent confidence interval extending from -6.4 to -9.3. We also fit it to human soft tissue sarcoma, which has a 95 per cent confidence interval for q ranging from -8.5 to -13.3.

We see in Figure 9.7(A) that as q decreases, the critical time of buckling *increases*. In Figure 9.7(C) we see that the fundamental displacement u_0 becomes positive as q decreases. This is not surprising, because if the tumour is strongly resistant to compression then it must expand outwards to relieve the pressure. Once the displacements are positive we observe that the order of buckling of the modes *reverses*: so that the lower modes go unstable first. Furthermore in Figure 9.7(B) we see that the buckled state destabilises. We have previously seen (in Section 8.2) that a positive fundamental displacement is often accompanied by these two phenomena: a reversal in the order of buckling and a destabilisation of the buckled state.

9.5 Variance of the Rate of Uptake

In Figure 9.8 we vary the rate of uptake of oxygen λ_n from 0.06 to 0.5 mMs^{-1}. The only nondimensional parameter this changes is α, which essentially governs the sharpness of the decline in the nutrient distribution (which can be seen from (2.69)). Thus increasing

[8] We argued this in Section 8.1.

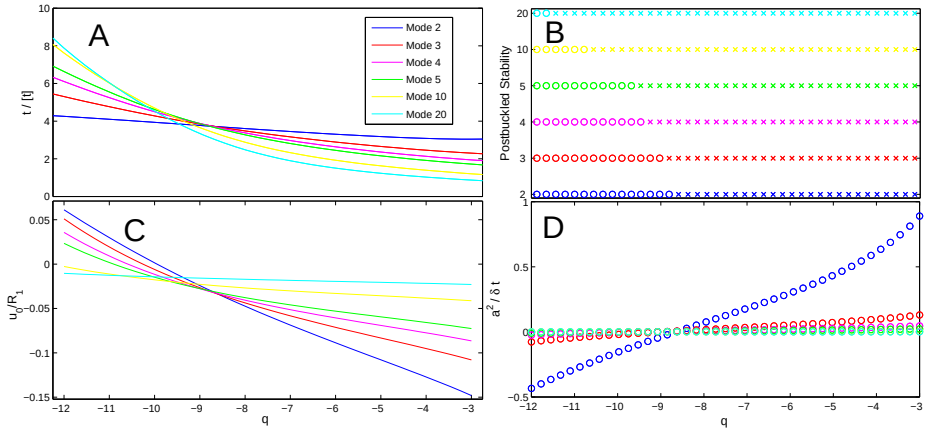

Figure 9.7: In the above simulations we varied q from -3 to -12.

λ_n makes the nutrient profile decrease more rapidly; the same effect could be achieved by decreasing the diffusion coefficient D. It is interesting to observe in Figures 9.8(A) and 9.8(F) that this has only a marginal effect on the time of buckling, and does not alter the existence and stability of the buckled states. The reason for this can be seen from the equation governing the growth, which we recall is (in nondimensionalised form)

$$\zeta_\alpha = \exp\left(\int_0^t G_\alpha \frac{c}{k_c^* + c} dt\right). \tag{9.15}$$

Since $k_c^* = 0.08 \ll c(R_1) = 1$, the growth ζ_α is initially very *insensitive* to the nutrient concentration in a neighbourhood of R_1. These results demonstrate that the growth in the immediate vicinity of the capillary is a key determinant of the buckling. We generally expect the cellular proliferation rate λ_c to correlate with the rate of uptake λ_n. Recall that λ_c defines the timescale $[t] = \lambda_c^{-1}$, but other than this does not affect the nondimensionalised results. Let us suppose that λ_c is directly proportional to λ_n in Figure 9.8. Since the (scaled) critical time changes little as λ_n varies, but $[t] = \lambda_c^{-1}$ decreases as λ_n increases, we find that the (uncscaled) critical time of buckling decreases as λ_n increases.

It is interesting to observe in Figures 9.8(E) and 9.8(J) that the radial growth dilation ζ_R at the time of buckling for planar buckles is typically much less than for axial buckles. This result generally holds for all parametric regimes. The essential reason is that the growth dilation depends exponentially on the rate of mass growth (which can be inferred from (9.15). Thus even if the critical times of the axial and planar buckles might seem close, the

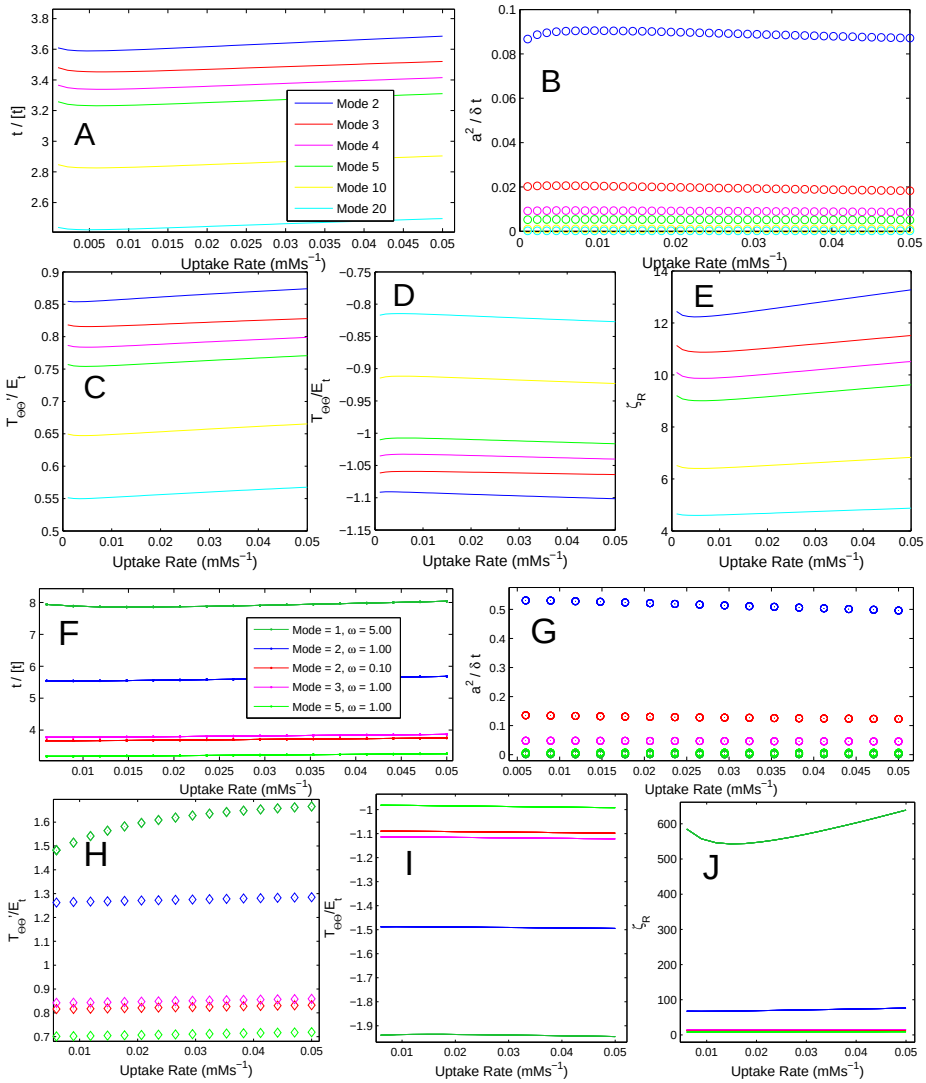

Figure 9.8: The effect of varying the rate of uptake of the oxygen λ_n from 0.06 to 0.5 mMs^{-1}. We implement model variant F. In the top set of figures we plot the results for planar buckling, and in the bottom set of figures we plot the results for axial buckling. The derivative $T'_{\Theta\Theta}$ is with respect to the spatial radial coordinate r, and the spatially-varying variables are evaluated at r_1. All of the buckled equilibrium states are stable.

exponential nature of the growth means that the growth dilation ζ_α at the time of buckling is considerably different. If we were to incorporate growth inhibition into our model, then we expect that the critical times of the axial and planar buckles would be further separated.

9.6 Variance of the Radius of the Capillary

We consider the effect of varying the radius of the capillary on the onset of buckling, by fixing the thickness of the capillary to be $h = R_1/125$ and vary R_1. However (in the case of model F) this is equivalent to fixing R_1 and h and varying the uptake parameter λ_n (which can be seen from an inspection of the nondimensionalised equations). We have already investigated the dependence of the buckling on λ_n in Section 9.5; and we saw that variance of λ_n had little effect on the onset of buckling. Thus varying R_1 in this manner would also have little effect on the onset of buckling.

9.7 Variance of the Growth Anisotropy Parameter

We plot the effect of varying the growth anisotropy coefficient A on the onset of buckling in Figures 9.9 and 9.10. The results are generally similar to the results for the model without a distinct capillary structure in Section 8.2. We make some observations:

- For low values of A, the growth is more isotropic, the displacement at R_1 is positive (which we argued in Section 3.4 is physically unrealistic) and the system tends to buckle later.

- Conversely, as A increases the growth is more responsive to the prevailing stress field, the displacement at R_1 decreases and the buckling time decreases. In addition, it can be seen that $|T_{\Theta\Theta} - T_{RR}|$ decreases as A increases, which is what we expect because as A increases, the growth is increasingly responsive to the stress, and therefore it 'homogenises' the stress field.

- For large A, the system with a distinct capillary wall structure buckles *more* readily than the system without this. This can be seen by comparing these results to Figure 8.5.

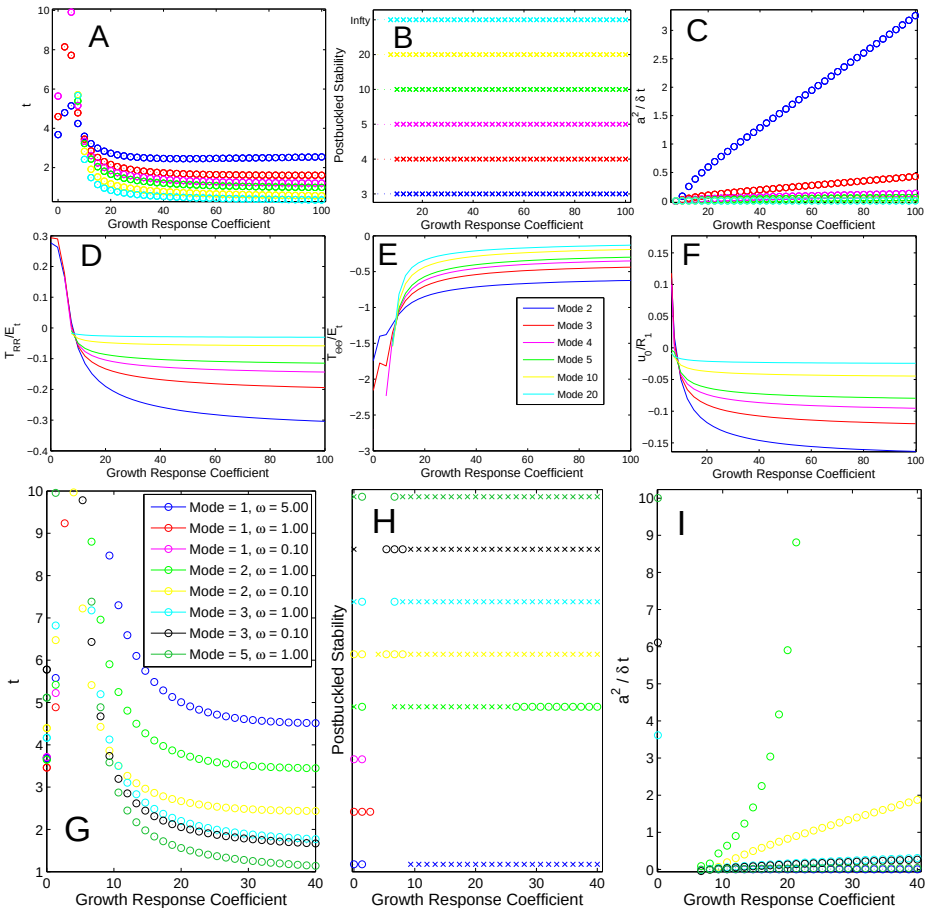

Figure 9.9: The effect of varying the growth anisotropy coefficient A. We implement model F. The simulation was terminated at $t = 10$. In the stability graph we plot an 'x' if there exists a buckled equilibrium state, an 'o' if the buckle is unstable. These results should be compared with the results for the model without a distinct capillary structure in Figures 8.5 and 8.6.

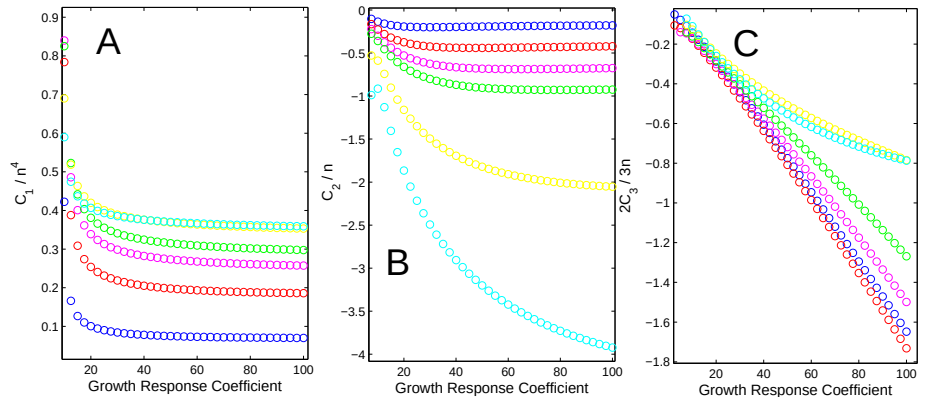

Figure 9.10: The effect of varying the growth anisotropy coefficient A, continued from Figure 9.9. We plot the variables C_1, C_2 and C_3, which are defined in (4.104). These plots correspond to the planar buckles in Figure 9.9.

The magnitude a of the buckle generally increases as A increases. This result seems counterintuitive because one might think that a more homogeneous stress field resulting from a large A would have a stabilising effect. However this result can be explained using the plots of $\{C_1, C_2, C_3\}$ in Figure 9.10. (Recall that the magnitude a of the buckle is determined by $a^2/\delta t = -(C_2 + \frac{2}{3}C_3)/C_1$.) As we explained in Section 4.2.3, C_3 represents a feedback effect of the buckle on itself. In brief, the buckle results in an increment $c^{(n,\omega)}$ in the nutrient distribution and the growth multipliers $G_\alpha^{(n,\omega)}$; however in turn these two variables affect the magnitude of the buckled state by affecting C_3, since

$$C_3 = \frac{1}{2}\iiint_{V_m} \frac{\partial \mathbf{P}}{\partial \zeta_\alpha} : \nabla \mathbf{u}^{(n,\omega)} \zeta_{\alpha,0} \times \left(G_{\alpha,0} \frac{c^{(n,\omega)}}{k_c} \left(1 + \frac{c_0}{k_c}\right)^{-2} + G_\alpha^{(n,\omega)} \frac{c_0}{k_c + c_0} \right) dV. \quad (9.16)$$

For low values of A, it can be seen in Figure 9.10 that C_3 is negligible compared to C_2, and therefore the feedback effect has a negligible effect on the magnitude of the buckle. However as A increases, $\{G_\alpha^{(n,\omega)}\}$ typically increases in magnitude because the stress relaxation resulting from the buckle has a bigger effect on the direction of the growth. This is what causes C_3 to increase as A increases, such that, for the low modes in particular, C_3 comes to dominate C_2 for large A. If we did not incorporate the feedback effect into our model (i.e. if we stipulated C_3 to be zero), then the magnitude a of the buckle would instead asymptote to a constant as A increases.

9.8 Variance of the Blood Oxygen Molarity

In this section we investigate the dependence of the capillary buckling on the blood oxygen concentration. Recall that we set the oxygen concentration at R_1 to be equal to the oxygen concentration in the blood. The blood oxygen concentration levels typically vary substantially throughout rapidly proliferating tumours. Varying the blood oxygen concentration level affects the nondimensional parameters $k_n^* = k_n/[c]$ (the scaled Michaelis constant for the oxygen distribution), $k_c^* = k_c/[c]$ (scaled Michaelis constant for growth) and α (which is inversely proportional to $[c]$). Generally speaking, decreasing the blood oxygen molarity decreases the level of oxygen, and thereby decreases the growth. Decreasing the blood oxygen

molarity also increases k_c^*, which moves the tumour growth closer to the quiescent regime (which is characterised by the oxygen concentration being of the same order of magnitude as the Michaelis constants, as can be seen from (9.15)), so that the growth decay at R_1 is sharper.

The results for model F are plotted in Figures 9.11 and 9.12, and the results for model A (with isotropic growth) are plotted in Figure 9.13. As we might expect, the critical time decreases as the blood oxygen concentration falls. This is not surprising because the rate of growth decreases when the blood oxygen concentration falls. With model F, it is interesting to observe (in Figure 9.12) that for a low blood oxygen concentration, the level of growth at the critical time is greater, but the growth decay $\frac{\partial \eta}{\partial r}$ (recall $\eta = \zeta_R \zeta_\Theta \zeta_Z$) is also greater.

We plot the terms C_2 and C_3 corresponding to model A in Figure 9.13. Recall that C_3, which is given in (9.16) and discussed in Section 4.2.3, represents the contribution of feedback effects to the magnitude a of the buckle, and that a is proportional to $(C_2 + \frac{2}{3}C_3)$. Since the growth is isotropic, C_3 is proportional to $c^{(n,\omega)}$. It can be seen that the relative magnitude of C_3 is almost always much less than C_2 (except perhaps for an extremely low blood oxygen concentration). This means that the feedback effect of the perturbation in the oxygen distribution on the growth is negligible for model A. A similar result holds for model F, and indeed for all 'reasonable' parameter values, although these results are not plotted. This contrasts the potentially very substantial feedback effect of the perturbation in the growth anisotropy multipliers on the magnitude of the buckle (which was discussed in Section 9.7).

9.9 Occlusion and Tortuosity of the Vessel

One of the major motivations for our study of capillary buckling is to understand the impedance of blood flow. There are two ways we approach this question: we consider how the buckled solution obtained using the perturbation expansion directly affects blood flow, and we consider how blood flow is impeded as the system evolves well beyond the point of bifurcation (and outside of the validity of our perturbed solution).

We begin with the first question. The radius of a blood cell is typically of the order of

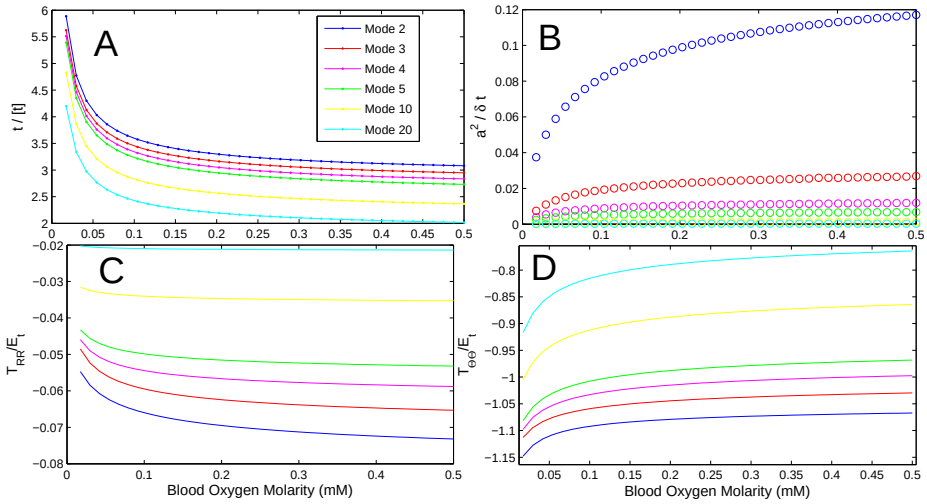

Figure 9.11: The effect of varying the oxygen concentration at the inner boundary (at $R = R_1$) from 0.01mM to 0.5 mM. We implement model F and investigate planar buckling. All of the buckled equilibrium states are stable. The radial growth ζ_R at R_1 is plotted in Figure 9.12.

5μm, i.e. about one third the radius of the capillary. Poiseuille's Law relates the flow of a fluid through a cylindrical vessel to the pressure difference driving the flow: it indicates that the flow is proportional to the square of the area of the cross section of the vessel [114]. Thus we expect that the flow of blood through a buckled vessel is at most of this order. In fact we expect the impedance to be even greater than this because the buckle effectively increases the ratio of the perimeter of a (planar) buckled cross section to its area, so that we expect there to be increased surface contact between the blood and the capillary wall as a result of the buckle.

We determine an expression for the change in area of the buckle. We may write the leading order of a buckled displacement in the form

$$\mathbf{u} = u_0\mathbf{e}_R + \epsilon a\left(W^{(n,\omega)}\cos(n\Theta)\cos(\omega Z)\mathbf{e}_R + V^{(n,\omega)}\sin(n\Theta)\cos(\omega Z)\mathbf{e}_\Theta + Z^{(n,\omega)}\cos(n\Theta)\sin(\omega Z)\right) + \ldots \tag{9.17}$$

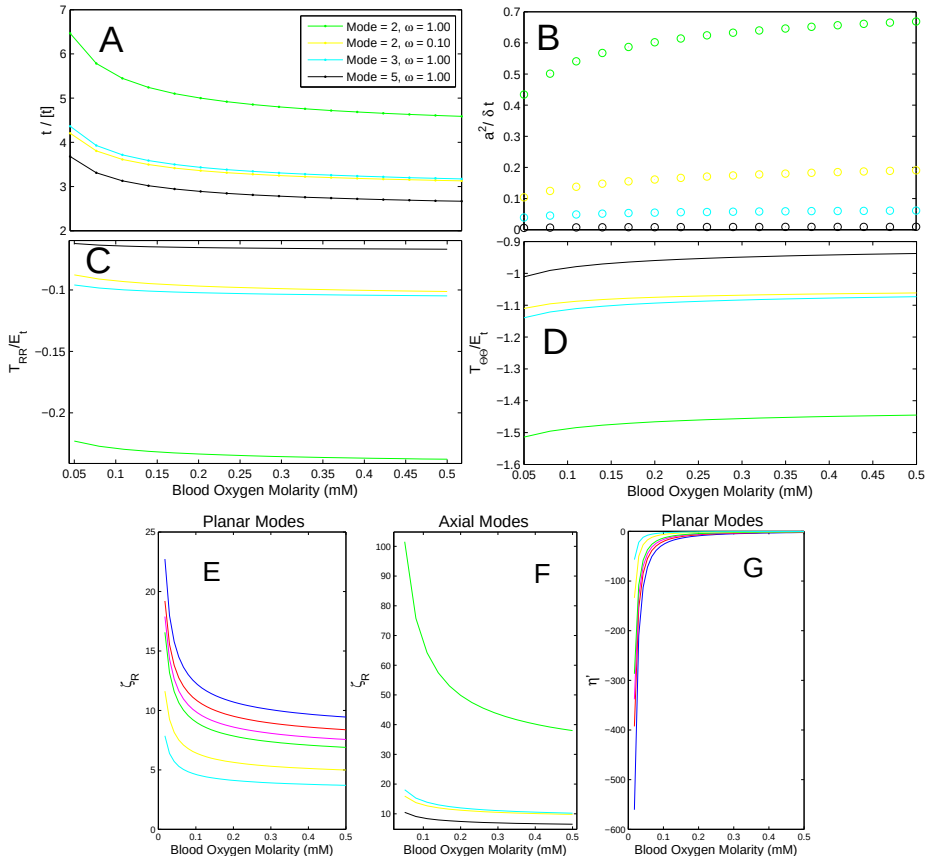

Figure 9.12: The effect of varying the oxygen concentration at the inner boundary from 0.01mM to 0.5 mM. We implement model F and investigate axial buckling. All of the buckled equilibrium states are stable. In plots E and F we plot the growth at R_1, and in plot G we plot the derivative of the total growth $\eta = \zeta_R\zeta_\Theta\zeta_Z$ with respect to the spatial coordinate r. Plots E and G derive from the results presented in Figure 9.11.

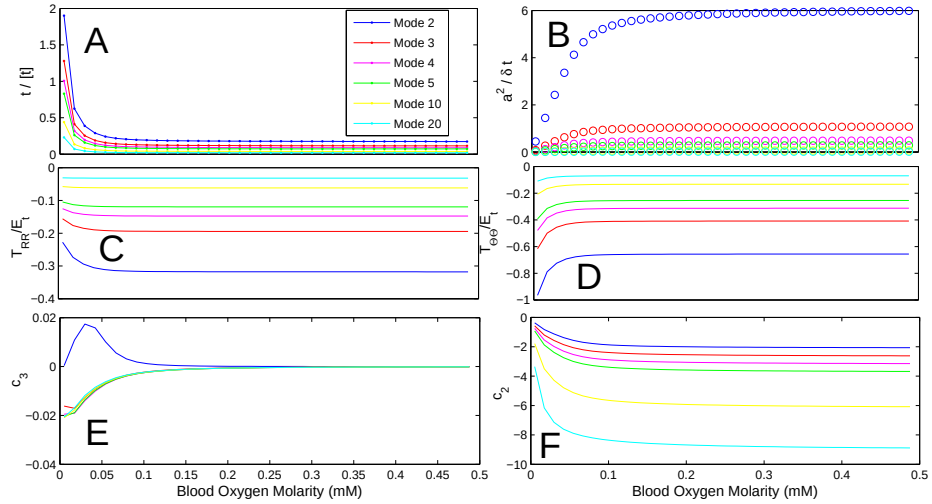

Figure 9.13: The effect of varying the oxygen concentration at the inner boundary from 0.01mM to 0.5 mM. We implement model A, with isotropic growth. In the bottom two figures we plot the variables C_2 and C_2, which are defined in (4.104).

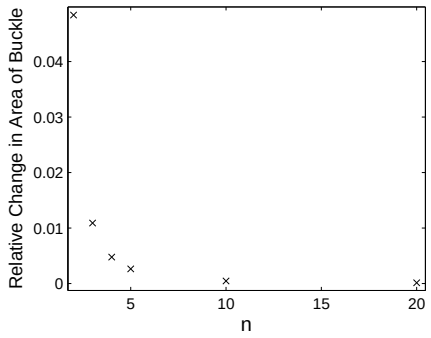

Figure 9.14: In the above simulations we vary the mode number n and plot the fractional rate of change of the area of the capillary (as given by $\mathcal{A}$ in (9.19)).

It can be seen from Appendix A.1.9 that the area enclosed by a planar buckle is

$$\pi\left((R+u_0)^2+\frac{1}{2}a^2\epsilon^2\left((W^{(n,\omega)})^2+(V^{(n,\omega)})^2\right)\right)+\ldots, \tag{9.18}$$

when $\omega = 0$. This expression (9.18) also gives the area enclosed by the planar slice of an axial buckle at $Z = 0$ or $Z = Z_0$. We thus define the rate of fractional change in the area of the capillary induced by a buckle as

$$\mathcal{A}=\frac{1}{2}a^2(R+u_0)^{-2}\left((W^{(n,\omega)})^2+(V^{(n,\omega)})^2\right)/\delta t. \tag{9.19}$$

Note that we have divided by δt because a^2 is proportional to δt. We investigate the rate of fractional change in the area of the capillary for planar buckles in Figure 9.14. It can be seen that, over the plotted modes, $\mathcal{A}$ monotonically decreases. This means that the capillary is most occluded by mode 2 buckles. We plot $\mathcal{A}$ for axial buckles with azimuthal wavenumber 2 in Figure 9.15. Of the plotted modes, $\mathcal{A}$ is highest when $\omega = 0.75$, but decays after this. Although this might seem to imply that axial buckles occlude the capillary more than planar buckles, it must be remembered that the axial buckle goes unstable *after* the planar buckle, so the compressive forces causing the axial buckle are greater.

The planar buckles of low wavenumber (particularly mode 2) may potentially be a precursor to intraluminal bridging. We recall that intraluminal bridging is the process by which endothelial cells extended cytoplasmic processes across the lumen, forming bridges which separate the blood flow into separate channels [105]. Since the magnitude a of the low wavenumber buckles is great, they seem to have the most potential of developing to the

extent that opposite ends touch.

Blood flow is also impeded through vessel tortuosity. Blood must travel further when the vasculature is tortuous, and there is increased resistance due to the twisting and turning. It seems very unlikely that a buckle would contribute to vessel tortuosity if its azimuthal mode is not 1. The reason for this, is that each planar 'slice' of such a buckle remains centred on the Z-axis. Refer to the axial buckled profiles in Figures 8.3 and 8.4 for a diagram of this. On the other hand, when the azimuthal mode is one, it can be shown that to leading order $\mathrm{O}(\epsilon)$, each planar cross-section is an ellipse, which is not centred on the Z-axis. The distance from the centre of the ellipse to the Z-axis is $\mathbf{u}_{1,R}$. This greatest value this distance can take is $aW^{(1,\omega)}$ (note that we can stipulate without loss of generality that $W^{(n,\omega)} > 0$). Since a is proportional to $\sqrt{\delta t}$, this motivates us to define the rate of axial strain induced by the buckle as

$$\mathcal{B} = a(\delta t)^{-0.5} W^{(n,\omega)}/Z_0. \tag{9.20}$$

This gives us an approximate measure of the relative azimuthal deviation of the buckle from the Z-axis. Recall that $\omega = \frac{m\pi}{Z_0}$, where m is the number of oscillations over the annulus. We assume that $m = 1$ (if $m > 1$ we can just rescale Z_0), so that $\mathcal{B}$ is

$$\mathcal{B} = a(\delta t)^{-0.5} W^{(n,\omega)} \frac{\omega}{\pi}. \tag{9.21}$$

We plot $\mathcal{B}$ in Figure 9.16 for a selection of axial wavenumbers. Observe that the rate of axial strain $\mathcal{B}$ decreases as ω increases. It can also be observed that the rate of axial strain is very small, in comparison to the relative change in area of the buckle $\mathcal{A}$ (as plotted in Figure 9.15(B)). This suggests that occlusion of the capillary is much more substantial than axial strain. We summarise the results of this chapter and discuss them further in the following chapter.

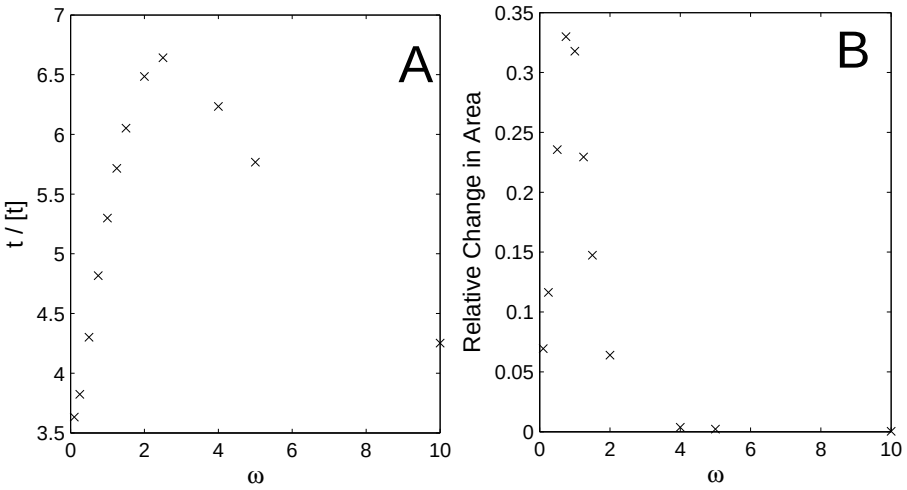

Figure 9.15: In the above simulations we vary ω, and fix the mode number n to be 2. In figure A we plot the critical time of buckling. In figure B we plot the relative change in area induced by the buckle (i.e. $\mathcal{A}$, as defined in (9.19)).

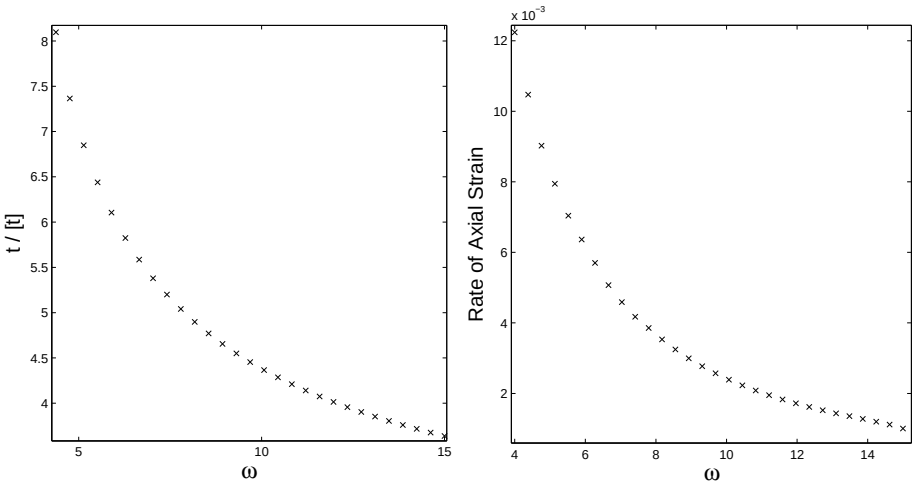

Figure 9.16: In the above simulations we vary ω, and fix the mode number n to be 1. We plot the critical time of buckling and $\mathcal{B}$, as defined in (9.21)).

Chapter 10

Conclusions and Further Work

We have achieved the principal aim of this thesis: to explain the onset of buckling in a tumoural capillary in terms of its immediate microenvironment. We found that for a cylindrical capillary embedded in a growing infinite tumour (model F), eventually the growth induced stress becomes great enough for the system to buckle, in the absence of any external load or constraint. Furthermore buckling occurred before the yield pressure was exceeded. We now summarise the argument of this thesis and draw conclusions.

10.1 Radially Symmetric Solution

In Chapter 2 we outlined a model for the growth and elastic deformation of a tumour in an annulus surrounding a single capillary. We outlined several variants of our model where there was uncertainty: thus we developed seven boundary conditions, three models of growth anisotropy and three models of growth inhibition. In Chapter 3 we evaluated these model variants in the case that there is not a distinct capillary wall structure and the growth and deformation is radially symmetric. We concluded that model F (which is a capillary in an infinite annulus), with anisotropic growth, is the most physically realistic. We neglected growth inhibition because it was difficult to parameterise and did not qualitatively affect our results. Model F has the following strengths:

- It is the most consistent in keeping with our aim of explaining buckling through reference to the microenvironment of a single capillary. If a model with a finite

geometry is substantially different from model F, then it is likely that the restriction to a finite annulus surrounding the capillary produces distorted results.

- It allows the intercapillary distance to naturally increase as the tumour grows.
- The stresses remain relatively low as the tumour grows. More precisely, for $t \leq 8$, the stress is of the order of the Young's Modulus.
- The radial displacement at the capillary-tumour interface is negative when we incorporate growth anisotropy, which is consistent with our expectation that the growing tumour exerts a compressive force on the capillary wall.

10.2 Buckling in Model without Distinct Capillary Wall Structure

In Chapter 8 we investigated the onset of buckling in the absence of a distinct capillary wall structure. We saw that the critical times of the various modes are highly clustered. We employed a boundary layer analysis to determine the asymptotic limit of the critical times as $\varsigma \to \infty$, where the azimuthal and axial wavenumbers are given by $(n, \omega) = \varsigma(n_1, \omega_1)$ (for some n_1, ω_1). We also determined the stability of the buckled state in the asymptotic limit as $\varsigma \to \infty$. Generally, modes with lower azimuthal wavenumber go unstable last.

Most of the buckles are stable, except occasionally buckles with planar mode 2. We discovered the following two phenomena which are suggestive of period doubling: generally modes with short wavelength go unstable before modes of long wavelength, however the modes of long wavelength appear to become energetically more favourable over time. As the outer radius $R_2 \to \infty$, the behaviour of all the model variants with a finite geometry approached model variant F. The unconstrained models (C and G) produce very similar predictions to model F about the onset of buckling for $R_2 \geq 2 \times 10^{-4}$m. Their convergence is much faster than the finite geometry models because they match model F in the linear limit as $R \to \infty$.

10.3 Buckling in Model with Distinct Capillary Wall Structure

In the following discussion, unless we acknowledge otherwise, it should be assumed that we are discussing model F. The tumoural potential energy dominates the capillary wall potential energy. This was the case even when the capillary wall was very thick or stiff. This means that adding the capillary wall to the model only marginally increased the critical time of buckling, and it confirms the hypothesis of Fung [56] that the stability of the capillary wall derives more from the substrate in which it is anchored than the basement membrane. From our analysis of the buckling of thin rings subject to a hydrostatic pressure we conclude that capillaries in fluid-like tumours probably buckle at a much lower radial pressure, however this is counterbalanced by the fact that such tumours probably also dissipate stress much more easily. The magnitude of the buckle in the system with a distinct capillary wall typically ranges from half to a third of the magnitude of the buckle in the sytem without a distinct capillary call.

10.3.1 The Preferred Buckling Modes of the System

The order in which the modes go unstable is highly invariant across the parametric regimes with which we investigated our model. Generally, buckles with a high azimuthal wavenumber go unstable before buckles with a low azimuthal wavenumber. Conversely with axial buckles, if $t^{(n,\omega)}$ is the critical time of a buckle with these wavenumbers, then $t^{(n,\omega)}$ initially increases as ω increases from zero, before starting to decrease once ω is approximately 1. There were only two phenomena in our results which altered this ordering of the modes. Firstly if the displacement at R_1 is *positive*, then typically the ordering is approximately reversed (which happens for very low values of the growth anisotropy coefficient A, or if the tumour is highly incompresssible). Secondly, if the strength of the capillary wall is increased (either through increasing its thickness or Young's Modulus), then the capillary wall comes to dominate the energy landscape. The capillary wall naturally seeks to minimise its bending energy, so it prefers lower modes.

Despite the fact that buckles with low azimuthal mode go unstable last, we have argued

that the system might well prefer these buckles to high wavenumber buckles. The experimental results seem to indicate this, as Stoll only observed azimuthal buckles of wavenumber 2 and 3 [129]. We stated three reasons for this: the low wavenumber buckles become energetically more favourable over time, buckles with a high wavelength might be dissipated by the cellular phase (and are thereby outside of the scope of accuracy of our model) and local inhomogeneities could bias the system to low wavenumber buckles (since the modes are highly clustered). We have seen that low wavenumber buckles almost always have greater magnitude, and occlude the capillary more.

One of the goals of this thesis was to investigate whether the high tortuosity of capillaries in tumours can be partly explained as a growth-induced instability. In some respects our model has met this goal, because it has demonstrated that growth-induced stress can lead to axial buckling. However on a closer inspection of our results, it seems more likely that our model is probably not the best explanation for the tortuosity of tumour capillaries. Our fundamental reason is that planar modes almost always go unstable before axial buckles with azimuthal wavenumber 1 (it is necessary that this is 1 in order that the buckle is not centred on the Z-axis). Although the difference between the critical times may only be a few units of time, it needs to be remembered that the growth is essentially exponential (as can be seen from (2.12)). The growth dilation needed for an axial buckle (particularly a buckle with $n = 1$) is of the order of a 100 times the growth dilation needed for a planar buckle (as can be seen from Figure 9.8). If we were to incorporate growth inhibition into the buckling analysis, then the difference in critical times would likely be much greater. We also saw in Section 9.9 that the rate of axial strain $\mathcal{B}$ tends to be dominated by the rate of occlusion of the capillary $\mathcal{A}$. Finally, there are other plausible explanations for tortuous capillaries, such as Nagy's hypothesis that this is due to excessive lengthening of a capillary tethered at both ends [105].

10.4 Parametric Sensitivity of Buckling

We summarise the effect of varying the parameters and boundary conditions of our model on the onset of buckling.

At the start of Chapter 9 we noted that we are particularly interested in any Eulerian variables which correlate with the onset of buckling. Such variables are of interest to experimentalists, especially in light of the fact that much our model is formulated in terms of Lagrangian variables which are difficult to measure. The Cauchy hoop stress $T_{\Theta\Theta}$ at R_1 seems the most suitable. It is almost always of the order of the Young's Modulus E_t at the time of buckling. Its value at the time of buckling is largely invariant to changes in the capillary wall properties, oxygen uptake rate and blood oxygen level. The fact that the tumoural hoop stress is much more invariant than the capillary hoop stress is essentially due to the fact that the tumour dominates the energy landscape.

The onset of buckling is extremely sensitive to the mechanical outer boundary condition. The results thus far have concerned model F, in which the capillary is embedded in a tumour of infinite radius. However the system buckles much more quickly if we implement model A, which has null-displacement and zero nutrient flux at a fixed outer radius R_2 (representing half the intercapillary distance). The magnitude of the buckle in model A is typically much greater than the magnitude of the buckle in model F. However we consider model A to have serious flaws. In particular, the restriction of the geometry to an annulus surrounding the capillary probably distorts the results.[1] We have seen that models which allow the displacement to be positive at R_2 (such as models C and F) approach model F much more rapidly than model A.

We finish by commenting on the impedance of the blood flow as the system evolves well beyond the point of bifurcation. Such a scenario is outside the scope of our perturbation expansion. However we have good reasons to expect the buckle to continue to grow in size. In particular, we have seen that feedback effects resulting from the growth anisotropy and the perturbation in the nutrient distribution seem to reinforce the buckle. Furthermore, we have seen that if the growth anisotropy coefficient A is very large, and the azimuthal wavenumber of buckling is small, then these feedback effects can be dominant. In this case the feedback effect causes the buckle to further grow in size. It is likely, however, that as the buckle continues to grow in size the blood flow and oxygen delivery will be impeded, and our assumption of a constant blood oxygen level would be weakened.

[1] As argued in Section 3.4.4.

10.5 Further Work

We outline some directions of future work.

We could use a linear stability analysis to investigate the hypothesis of Nagy that capillary tortuosity is primarily caused by excessive lengthening of a capillary which is anchored at both ends.

We could solve our full nonlinear model with finite element methods. This might be computationally very difficult, but it would allow us to determine the evolution of the buckle beyond our perturbation expansion. It would potentially also allow us to explore for instance the interactions of neighbouring capillaries.

We could develop a multiphase model of the tumoural mechanics and apply our stability analysis to this. A multiphase model could potentially better account for the complicated interaction of the different phases. In particular, we could account for stress relaxation through a viscoelastic relaxation of the phases. It would potentially be very difficult to apply a stability analysis to such a model because traditionally stability analyses are applied to systems in quasi-static equilibrium.

Finally, we could develop a more sophisticated model of the tumoural growth. For instance, we could incorporate growth inhibition (through growth inhibition or cell contact), or the influence of chemical factors on growth.

Appendix A

Mathematical Preliminaries

In this section we give an overview of the mathematics required to model elastic growth in the tumour.

A.1 Nonlinear Solid Mechanics

Nonlinear solid mechanics is formulated using differential geometry. We provide a brief introduction to this.

A.1.1 General Bases and Tensors

We begin with an overview of some fundamental concepts of differential geometry. In nonlinear elasticity there are two important configurations: the *reference configuration* and the *current* or *deformed* configuration (later on we will introduce a third configuration, but need not worry about this now). The reference configuration, which we will denote by $B_0 \subset \mathbb{R}^3$, is the body prior to elastic deformation. The current configuration, which we will denote by $B_2 \subset \mathbb{R}^3$ gives the deformed shape of the body. The elastic deformation is a map $\phi : B_0 \to B_2$ that describes where points in the reference configuration move to.

The *tangent space* at a point P gives us an understanding of the effect of the deformation on small vectors emanating from P. To construct the tangent space, to each point P in a configuration B_i we affix a copy of $\mathbb{R}^3$. This can be regarded as vectors emanating from P. The set of all such vectors at P is called the tangent space at P and denoted $T_P B_i$. A *one*

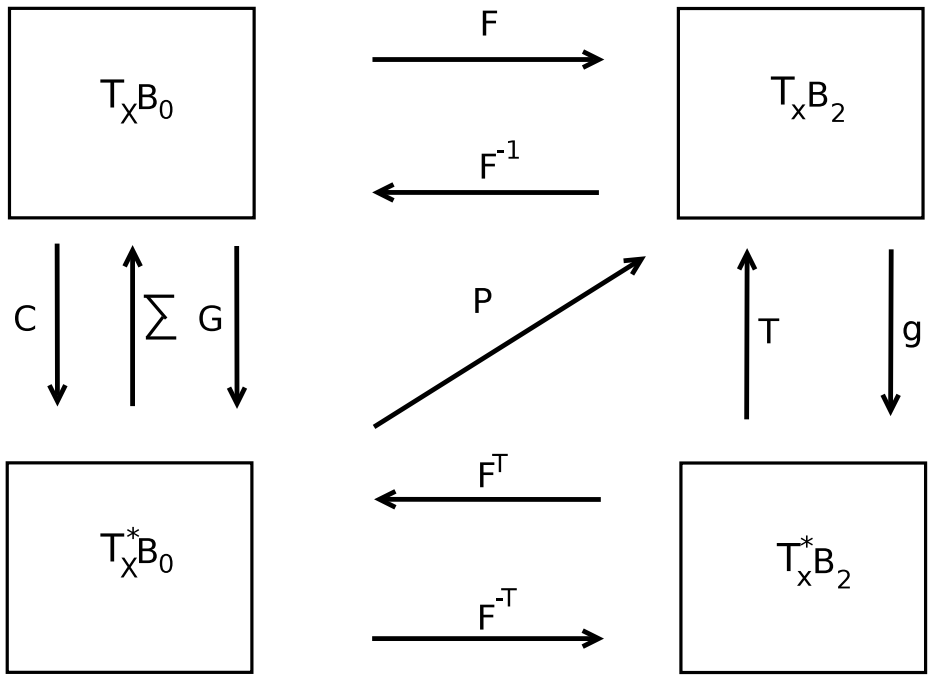

Figure A.1: The operation on the tangent and co-tangent spaces of the deformation gradient $\mathbf{F}$, metric tensors $\mathbf{G}$ and $\mathbf{g}$, strain tensor $\mathbf{C}$ and stress tensors $\mathbf{T}, \mathbf{P}$ and $\mathbf{S}$. Here B_0 is the reference configuration and B_2 is the current configuration.

form is a linear map $T_P B_i \to \mathbb{R}$. The *co-tangent space* is the set of all one forms over B_i and is denoted $T_P^* B_i$.

Suppose $\{\mathbf{e}_i\}$ is a basis for $T_P B_i$. We can define the corresponding *contravariant* basis for $T_P^* B_i$, $\{\mathbf{e}^i\}$ as follows

$$\mathbf{e}^i(\mathbf{e}_j) = \delta^i_j, \tag{A.1}$$

where δ^i_j is the Kronecker delta function. We now define curvilinear coordinates. Suppose $B_0 \subset \mathbb{R}^3$ and let $\gamma : B_0 \to \mathbb{R}^3$ be a continuous, one-to-one mapping. Suppose that γ and γ^{-1} have continuous derivatives up to any order. Let $\mathbf{X} \in B_0$ be a point. The *coordinates* of $\mathbf{X}$ are the three scalar fields $\gamma(\mathbf{X}) = \big(\gamma^1(\mathbf{X}), \gamma^2(\mathbf{X}), \gamma^3(\mathbf{X})\big)$. We can equivalently think of $\mathbf{X}$ as a vector function of the three variables $\big(\gamma^1, \gamma^2, \gamma^3\big)$. The *natural basis vectors* $\{\mathbf{g}_i\}$ can be obtained by differentiating $\mathbf{X}$ with respect to the coordinates, i.e.

$$\mathbf{g}_i = \frac{\partial \mathbf{X}}{\partial \gamma^i}. \tag{A.2}$$

We similarly define natural basis vectors for the cotangent space by stipulating

$$\mathbf{g}^i\left(\mathbf{g}_k\right) = \delta^i_j. \tag{A.3}$$

In this thesis we will be working with cylindrical coordinates. These are detailed in Appendix A.1.8. We are now read to define *tensors*. A tensor on B_0 of order (r, s) is a multilinear map (i.e. linear in each of its components) of the form

$$T : T^*_X B_0 \times \ldots \times T^*_X B_0 \times T_X B_0 \times \ldots \times T_X B_0 \to \mathbb{R}. \tag{A.4}$$

where there are r 'copies' of $T^*_X B_0$ and s copies of $T_X B_0$. Here r is the *contravariant* order of $\mathbf{T}$ and s is the covariant order of $\mathbf{T}$. We may form tensors by taking the *dyadic product* of vectors and one forms. Suppose $\{\mathbf{v}_1, \ldots, \mathbf{v}_r\}$ is a set of vectors in $T_P B_i$ and $\{\mathbf{w}^1, \ldots, \mathbf{w}^s\}$ is a set of one forms in $T^*_P B_i$. The dyadic product

$$\mathbf{T} = \mathbf{v}_1 \otimes \ldots \otimes \mathbf{v}_r \otimes \mathbf{w}^1 \otimes \ldots \otimes \mathbf{w}^s \tag{A.5}$$

is the tensor of order (r, s) defined such that

$$\mathbf{T}\left(\mathbf{a}^1, \ldots, \mathbf{a}^r, \mathbf{b}_1, \ldots, \mathbf{b}^s\right) = \mathbf{v}_i\left(\mathbf{a}^i\right)\mathbf{w}_j\left(\mathbf{b}^j\right). \tag{A.6}$$

We have made use of the summation convention. Unless otherwise stated, we sum over a repeated index on the top and bottom, so that the above equation is equal to

$$\sum_{i=1,j=1}^{3} \mathbf{v}_i\left(\mathbf{a}^i\right)\mathbf{w}_j\left(\mathbf{b}^j\right). \tag{A.7}$$

We obtain a basis for the set of all tensors of order (r, s) by taking dyadic products of the basis vectors. The *components* of a tensor $\mathbf{T}$ relative to a basis $\{\mathbf{g}_i\}$ may be obtained by evaluating $\mathbf{T}$ on the dyadic products of the basis vectors, i.e.

$$T^{i_1,\ldots,i_r}_{j_1,\ldots,j_s} = \mathbf{T}\left(\mathbf{g}_{i_1}, \ldots, \mathbf{g}_{i_r}, \mathbf{g}^{j_1}, \ldots, \mathbf{g}^{j_s}\right). \tag{A.8}$$

Suppose $\mathbf{S}$ is a tensor of order (l, k) and $\mathbf{T}$ is a tensor of order (m, n), then the *tensor product* $\mathbf{S} \otimes \mathbf{T}$ defines the tensor with components

$$(\mathbf{S} \otimes \mathbf{T})^{i_1\ldots i_l i_{l+1}\ldots i_{l+m}}_{j_1\ldots j_k j_{k+1}\ldots j_{k+n}} = \mathbf{S}^{i_1\ldots i_l}_{j_1\ldots j_k}\,\mathbf{T}^{i_{l+1}\ldots i_{l+m}}_{j_{k+1}\ldots j_{k+n}}. \tag{A.9}$$

In nonlinear elasticity we frequently work with second order tensors. It is often more natural in elasticity theory to understand a second order tensor as a linear map from the (co) tangent space to the (co) tangent space, as follows. If $\mathbf{T}$ is contravariant, the corresponding map is $T' : T^*_X B_0 \to T_X B_0$, where $T'(a_j \mathbf{e}^j) = T^{ij} a_j \mathbf{e}_i$. Similarly, if $\mathbf{T}$ is covariant, the corresponding map is $T' : T_X B_0 \to T^*_X B_0$, where $T'\left(a^j \mathbf{e}_j\right) = T_{ij} a^j \mathbf{e}^i$.

We now define the metric tensor. Let $\{\mathbf{G}_i\}$ be the natural basis vectors with respect to some coordinate system. The metric tensor $\mathbf{G} : T_X B_0 \to T^*_X B_0$ gives us a natural way of identifying contravariant vectors in the tangent space with covariant vectors in the cotangent space. It is defined in the following way

$$\left(\mathbf{G}(\mathbf{u})\right)(\mathbf{v}) = \mathbf{u} \cdot \mathbf{v}. \tag{A.10}$$

We see that its components are given by

$$\mathbf{G} = G_{ij} \mathbf{G}^i \otimes \mathbf{G}^j, \tag{A.11}$$

where $G_{ij} = \mathbf{G}_i \cdot \mathbf{G}_j$. It can be easily shown that its inverse has (contravariant) components $G^{ij} = \mathbf{G}^i \cdot \mathbf{G}^j$. In the special case that $\{\mathbf{G}_i\}$ is an orthogonal basis, we can define an orthonormal basis by $e^i = \sqrt{G_{ii}} \mathbf{G}^i$ (note that the summation convention does not apply). It follows that (A.11) simplifies to

$$\delta_{ij} e^i \otimes e^j. \tag{A.12}$$

We may *contract* a tensor $\mathbf{T}$ of order (m, n) to produce a tensor of order $(m-1, n-1)$. The (p, q) contraction of the tensor $T^{i_1 \ldots i_m}_{j_1 \ldots j_n}$ is the tensor

$$T^{i_1 \ldots i_m}_{j_1 \ldots j_{q-1} i_p j_{q+1} \ldots j_n} = T^{i_1 \ldots i_{p-1} j_q i_{p+1} \ldots i_m}_{j_1 \ldots j_n}. \tag{A.13}$$

A contraction of a $(1, 1)$ tensor is known as taking the *trace*. The product $\mathbf{ST}$ is obtained by taking the tensor product of $\mathbf{S}$ and $\mathbf{T}$ and contracting. For example if $\mathbf{S}$ is a $(2, 0)$ tensor and $\mathbf{T}$ is a $(0, 2)$ tensor then

$$(\mathbf{S} \cdot \mathbf{T})^i_j = S^{ik} T_{kj}. \tag{A.14}$$

The *double contraction* $S : T$ is obtained by taking the tensor product and contracting

twice. For example if $\mathbf{S}$ is a $(4,0)$ tensor and $\mathbf{T}$ is a $(0,2)$ tensor then

$$(\mathbf{S} : \mathbf{T})^{ij} = S^{ijkl} T_{kl}. \tag{A.15}$$

It can be seen that we may raise or lower an index in a tensor by multiplying by the metric tensor. In elasticity we often prefer to work with the *physical* components of a tensor. The physical components of a tensor are defined relative to an orthonormal basis. In order to obtain the physical components it is necessary that the basis is orthogonal. We may then multiply by the magnitude of the basis vectors to obtain the physical components.

We define the orthonormal basis vectors via $\mathbf{e}_\alpha = \sqrt{G^{\alpha\alpha}}\mathbf{g}_\alpha = \sqrt{G_{\alpha\alpha}}\mathbf{g}^\alpha$. We give some examples of the physical components of tensors. If $\mathbf{v} = v^\alpha \mathbf{g}_\alpha$ is a contravariant vector, then the physical components are $\hat{v}^\alpha = \sqrt{G_{\alpha\alpha}} v^\alpha$. If $\mathbf{P}$ is a contravariant 2nd order tensor, then the physical components are $\hat{P}^{\alpha\beta} = P^{\alpha\beta}\sqrt{G_{\alpha\alpha} G_{\beta\beta}}$.

Differentiation and Integration of Tensors

Let $T^{i_1 \ldots i_m}$ be a contravariant tensor. We denote by $T^{i_1 \ldots i_m}_{,h}$ the partial derivative with respect to the h'th coordinate. The covariant derivative of $\mathbf{T}$ comes from differentiating each component, taking into account the derivatives of the basis vectors. It is defined as follows

$$\mathbf{T}_{|h} = T^{i_1 \ldots i_m}_{|h} \mathbf{g}_{i_1} \otimes \ldots \otimes \mathbf{g}_{i_m}, \tag{A.16}$$

where the covariant derivative is

$$T^{i_1 \ldots i_m}_{|h} = \frac{\partial T^{i_1 \ldots i_m}}{\partial x^{(n,\omega)}} + \sum_{p=1}^{m} \Gamma^{i_p}_{hj} T^{i_1 \ldots j \ldots i_m}. \tag{A.17}$$

Here the *Christoffel Symbols* are

$$\Gamma^r_{ij} = -\mathbf{g}_i \cdot \mathbf{g}^r_{,j}. \tag{A.18}$$

The gradient of a tensor is obtained by taking the covariant derivative of each of the components, i.e.

$$(\nabla \otimes \mathbf{T})^{j_1 \ldots j_m}_{i_1 \ldots i_n i} = T^{j_1 \ldots j_m}_{i_1 \ldots i_n | i}. \tag{A.19}$$

We denote the *divergence* of a contravariant tensor $\mathbf{T}$ by $\nabla \cdot \mathbf{T}$. It is obtained by taking the

contraction of the covariant derivative, i.e. $\nabla \cdot \mathbf{T}$ has components

$$(\nabla \cdot \mathbf{T})^{i_1 \ldots i_m} = T^{i_1 \ldots i_m i}_{|i}. \tag{A.20}$$

There are m possible indices to contract over. By convention we contract over the last one, although some authors (such as Ogden [110]) contract over the first one. The *Divergence Theorem* for tensors is

$$\iint_{\partial B_0} \mathbf{T}\mathbf{n} dA = \iiint_{B_0} \nabla \cdot \mathbf{T} dV, \tag{A.21}$$

where $\mathbf{T}$ is a contravariant tensor. Also of use is the chain rule for differentiating tensor products, i.e. if $\mathbf{T}$ is a (2,0) contravariant tensor and $\mathbf{u}$ is a (0,1) covariant tensor then

$$\nabla \cdot \left(\mathbf{T}^T \mathbf{u}\right) = (\nabla \cdot \mathbf{T}) \cdot \mathbf{u} + \mathbf{T} : \nabla \mathbf{u}. \tag{A.22}$$

A.1.2 Deformation Gradient and Strain

We recall the deformation $\phi : B_0 \to B_2$ is a map describing the movement of points in the reference configuration to points in the deformed configuration. We assume the deformation is sufficiently smooth and differentiable. Since the deformation is a contravariant vector field, we may take its tensor gradient

$$\mathbf{F} = \nabla \otimes \phi. \tag{A.23}$$

We denote this the *deformation gradient*. This is a tensor which measures the local change of infinitesimal line elements under the deformation. Consider a line element $\mathbf{a}$ in the tangent space of the reference configuration $T_X B_0$. Under the deformation ϕ this line element is mapped to a line element $\mathbf{b}$ in the current configuration $T_x B_2$. The deformation gradient $\mathbf{F}$, is the map corresponding to this, i.e.

$$\mathbf{b} = \mathbf{F}_X \mathbf{a}. \tag{A.24}$$

We similarly define the *displacement* to be $\mathbf{u} = \phi(\mathbf{X}) - \mathbf{X}$. The displacement gradient is

$$\nabla \mathbf{u} = \nabla \otimes \mathbf{u} = \mathbf{F} - \mathbf{I}. \tag{A.25}$$

Technically $\mathbf{F}$ and $\nabla \mathbf{u}$ are *two point* tensors, mapping vectors in the tangent space of the reference configuration to the tangent space of the current configuration. We let J be the determinant of $\mathbf{F}$. It measures the local change in volume under the deformation. That is, if a small block of the material has volume dV in the reference configuration, and deforms to a small block of material with volume dv in the current configuration, then $dv = JdV$. We derive an expression for the deformation gradient in cylindrical coordinates in the Appendix.

In this thesis all tensors (except the ones in shell theory) are expressed in terms of their *physical* components. That is, we multiply them by factors of the metric tensor $\sqrt{G_{\alpha\alpha}}$ until they are relative to an orthonormal basis (as explained in the previous section). Under this understanding, the contravariant / covariant / mixed components of a tensor are all equivalent to the same physical tensor. Therefore we do not worry about the position of indices, but merely write $F_{\alpha\beta}$ to denote the physical components of $\mathbf{F}$. The reason we have introduced a distinction between the contravariant and covariant components of a tensor is that they transform differently under the operations of the pull-back and push-forward, which will be seen below. It is important to note that the physical components of tensors are not necessarily tensors, and therefore do not necessarily transform tensorially.

The *dual* $\mathbf{F}^T$ is the map from $T_x^* B_2 \to T_X^* B_0$ such that if $\mathbf{b} \in T_x^* B_2$ then the one form $\mathbf{F}^* b$ is defined as follows

$$\left(\mathbf{F}^T \mathbf{b}\right)(\mathbf{a}) = \mathbf{b}\left(\mathbf{F}\mathbf{a}\right), \tag{A.26}$$

where $\mathbf{a} \in T_X B_0$. The physical components of $\mathbf{F}^T$ are the transpose of the physical components of $\mathbf{F}$. We may similarly define the inverse deformation gradient $\mathbf{F}^{-1}$ and its dual $\mathbf{F}^{-T}$. The dual of the inverse is the inverse of the dual.

The *pullback* and *pushforward* are maps which transpose a tensor defined in one configuration to a tensor defined in another. If we understand the change of configuration to be a change in coordinates, then the pullback and pushforward correspond to the coordinate transformation rule for tensors. Refer to Figure A.1 for a diagram. Suppose $\mathbf{s} : T_x B_2 \to T_x^* B_2$ is a covariant second order tensor. Its pull-back to B_0 is the covariant

tensor $\mathbf{T} : T_X B_0 \to T_X^* B_0$,

$$\mathbf{F}^T \mathbf{s} \mathbf{F}. \tag{A.27}$$

Conversely if $\mathbf{S} : T_X B_0 \to T_X^* B_0$ is a covariant second order tensor on B_0, we define its pushforward to B_2 to be the tensor

$$\mathbf{F}^{-T} \mathbf{S} \mathbf{F}^{-1}. \tag{A.28}$$

Push-Forwards and pull-backs can also be defined on contravariant second order tensors. The pull back of such a tensor $\mathbf{T} : T_x^* B_2 \to T_x B_2$ to B_0 is

$$\mathbf{F}^{-1} \mathbf{T} \mathbf{F}^{-T}. \tag{A.29}$$

The pushforward to B_2 of a contravariant second order tensor $\mathbf{t} : T_X^* B_0 \to T_X B_0$ is

$$\mathbf{F} \mathbf{t} \mathbf{F}^T. \tag{A.30}$$

We can also define a transformation on $\mathbf{T}$ called the *Piola Transform*. Suppose $\mathbf{T}$ is a second order contravariant tensor on B_2: $\mathbf{T} : T_x^* B_2 \to T_x B_2$. The Piola Transform pulls the domain of $\mathbf{T}$ back to B_0 only, i.e.

$$J \mathbf{T} \mathbf{F}^{-T}, \tag{A.31}$$

where $J = detF$. Thus the Piola Transform of $\mathbf{T}$ is a *two-point tensor*, with its domain on $T_X^* B_0$ and its range in $T_x B_2$. The Piola Transform will be useful in subsequent sections because it gives us a way of relating area elements in B_0 to area elements in B_2. Suppose an area element of magnitude dA with unit outward normal $\mathbf{N}$ in B_0 is transformed by the deformation to the area element of magnitude da with unit outward normal $\mathbf{n}$ in B_2. Then

$$J \left| \mathbf{F}^{-T} \mathbf{N} \right| dA = da. \tag{A.32}$$

The Green deformation tensor is

$$\mathbf{C} = \mathbf{F}^T \mathbf{g} \mathbf{F}. \tag{A.33}$$

In this thesis the expressions for our tensors are always with respect to *physical* coordinates (i.e. with respect to an orthonormal basis). Since the metric tensor is merely the identity

(with respect

$$\mathbf{C} = \mathbf{F}^T\mathbf{F}. \tag{A.34}$$

The Green deformation tensor is defined on B_0 and measures the stretch of a line element under the deformation. It is the pullback of the metric tensor $\mathbf{g}$. That is, if $\mathbf{d}X$ is a small line element in the reference configuration and $\mathbf{d}x$ is a line element in the current configuration,

$$|\mathbf{d}x|^2 = \mathbf{d}X^T\mathbf{C}\mathbf{d}X. \tag{A.35}$$

The Green St-Venant strain tensor $\mathbf{E}$ is defined on B_0 and measures the difference in metrics under the deformation, i.e.

$$\mathbf{E} = \frac{1}{2}(\mathbf{C} - \mathbf{I}) \tag{A.36}$$

We use the polar decomposition theorem to write $\mathbf{F} = \mathbf{R}\mathbf{U}$, where $\mathbf{R}$ is orthonormal and $\mathbf{U}$ is symmetric and positive definite. In turn, we may decompose $\mathbf{U}$ spectrally as

$$\mathbf{U} = \lambda_i \mathbf{e}_i \otimes \mathbf{e}_i. \tag{A.37}$$

The scalars $\{\lambda_i\}$ are known as the *principal stretches* and the vectors $\{\mathbf{e}_i\}$ are the *principal directions*.

A.1.3 Stress Tensors

In this section we outline the standard stress tensors. The Cauchy stress tensor $\mathbf{T}$ is used to measure the stress in the current configuration. It is a second order contravariant tensor defined in the current configuration. As such, we understand it as a map $\mathbf{T} : T_x^*B_2 \to T_xB_2$, as explained in Section A.1.2. It is defined as follows. Consider a small area element in the deformed configuration of area da with unit normal $\mathbf{n}$. The unit normal transforms covariantly and so belongs to $T_x^*B_2$. The force experienced by the area element is the contravariant vector

$$da\mathbf{T}\mathbf{n}. \tag{A.38}$$

In order for there to be a local balance of torques on any particular segment of the deformed

configuration, it is necessary that the Cauchy stress tensor is symmetric [43], i.e.

$$\mathbf{T}^T = \mathbf{T}. \tag{A.39}$$

We define the first Piola-Kirchhoff stress tensor $\mathbf{P}$ as follows. Consider a small area element in the reference configuration with area dA and unit normal $\mathbf{N}$. Under the deformation ϕ it deforms to an area element in the deformed configuration with area da and unit normal $\mathbf{n}$. The first Piola-Kirchhoff stress tensor $\mathbf{P}$ is defined such that

$$\mathbf{P}\mathbf{N}dA = \mathbf{T}\mathbf{n}da. \tag{A.40}$$

That is, for an area element with normal $\mathbf{N}$ in the reference configuration, the Piola-Kirchhoff stress tensor gives the force it experiences in current configuration. The first Piola-Kirchhoff stress tensor may be expressed as the *Piola Transform* of the Cauchy stress tensor, i.e.,

$$\mathbf{P} = J\mathbf{T}\mathbf{F}^{-T}. \tag{A.41}$$

The second Piola-Kirchhoff stress tensor $\mathbf{S}$ is the pullback of $\mathbf{T}$, scaled by the factor J which accounts for the change in volume. It has no physical interpretation, but is of theoretical use; it is given by

$$\mathbf{S} = \mathbf{F}^{-1}\mathbf{P} = J\mathbf{F}^{-1}\mathbf{T}\mathbf{F}^{-T}. \tag{A.42}$$

The first Piola-Kirchhoff stress tensor is in general not symmetric. However it follows directly from (A.39) that the second Piola-Kirchhoff stress is symmetric, i.e.

$$\mathbf{S}^T = \mathbf{S}. \tag{A.43}$$

A.1.4 Hyperelasticity

After having described strains and stresses we now need to relate the two: the relationship between the two is known as *constitutive relations* and varies from material to material. A *hyperelastic* material is a material which possesses a strain-energy function $\psi(\mathbf{F})$, giving the energy density per unit volume in the reference configuration. For hyperelastic materials

the 1st Piola Kirchhoff stress tensor is given by

$$\mathbf{P} = \frac{\partial \psi}{\partial \mathbf{F}}. \tag{A.44}$$

Here the differentiation is performed componentwise, i.e.

$$P_{ij} = \frac{\partial \psi}{\partial F_{ij}}.$$

In order that ψ remains unchanged for rigid body motions, it is necessary and sufficient that ψ is expressible as a function of the Green strain tensor $\mathbf{C} = \mathbf{F}^T\mathbf{F}$. Such a material is said to be *objective*. If the elastic response of a material is the same in every direction, i.e.

$$\psi(\mathbf{FQ}) = \psi(\mathbf{F}), \tag{A.45}$$

then the material is *isotropic*. The *representation theorem for invariants* states that the strain energy functions of materials which are isotropic and invariant may be written as

$$\psi = \psi[I_1(\mathbf{C}), I_2(\mathbf{C}), I_3(\mathbf{C})], \tag{A.46}$$

where $\{I_j\}$ are the three matrix invariants of $\mathbf{C}$. These are $I_1 = tr(\mathbf{C})$, $I_2 = \frac{1}{2}\left[(tr(\mathbf{C})^2 - tr(\mathbf{C}^2)\right]$ and $I_3 = |\mathbf{C}| = J^2$ (where $J = |\mathbf{F}|$). The differentials are given by

$$\frac{\partial I_1}{\partial \mathbf{F}} = 2\mathbf{F}, \quad \frac{\partial I_2}{\partial \mathbf{F}} = 2I_1\mathbf{F} - 2\mathbf{F}\mathbf{F}^T\mathbf{F}, \quad \frac{\partial I_3}{\partial \mathbf{F}} = 2I_3\mathbf{F}^{-T}. \tag{A.47}$$

On differentiation, it may be shown that

$$\mathbf{T} = 2J^{-1}\left[\left(I_2\frac{\partial \psi}{\partial I_2} + I_3\frac{\partial \psi}{\partial I_3}\right)\mathbf{I} + \frac{\partial \psi}{\partial I_1}\mathbf{B} - I_3\frac{\partial \psi}{\partial I_2}\mathbf{B}^{-1}\right], \tag{A.48}$$

where $\mathbf{B} = \mathbf{F}\mathbf{F}^T$. The coefficients of $\{\mathbf{I}, \mathbf{B}, \mathbf{B}^{-1}\}$ are known as the response functions. Note that the invariants of $\mathbf{C}$ are the same as the invariants of $\mathbf{B}$.

We may take higher order derivatives of the strain energy. For example we define the fourth order tensor $\frac{\partial^2 \psi}{\partial \mathbf{F}^2}$ to be the multilinear map such that

$$\frac{\partial^2 \psi}{\partial \mathbf{F}^2} : \delta\mathbf{F}_1 : \delta\mathbf{F}_2$$

is the differential of

$$\frac{\partial^2 \psi}{\partial \mathbf{F}^2} : \delta \mathbf{F}_1$$

with respect to $\mathbf{F}$ in the direction of $\delta \mathbf{F}_2$. By the commutivity of partial derivatives,

$$\frac{\partial^2 \psi}{\partial \mathbf{F}^2} : \delta \mathbf{F}_1 : \delta \mathbf{F}_2 = \frac{\partial^2 \psi}{\partial \mathbf{F}^2} : \delta \mathbf{F}_2 : \delta \mathbf{F}_1.$$

Higher order derivatives are defined analogously. We may also employ Taylor's theorem to expand the strain energy about $\mathbf{F} = \mathbf{F}_0$. Consider a small perturbation $\mathbf{u}$ in the displacement, which induces the small perturbation $\nabla \mathbf{u}$ in the deformation gradient. Then the Taylor expansion in ψ is given by

$$\psi\left(\mathbf{F}_0 + \nabla \mathbf{u}\right) = \psi\left(\mathbf{F}_0\right) + \sum_{n=1}^{\infty} \frac{1}{n!} \frac{\partial \psi}{\partial \mathbf{F}} : \nabla \mathbf{u} : \ldots : \nabla \mathbf{u}. \tag{A.49}$$

It is crucial that the components of $\mathbf{F}_0$ and $\nabla \mathbf{u}$ are relative to the same basis. By convention we always use an orthonormal basis, so that the components of these tensors are the *physical* components.

The Second Piola-Kirchhoff stress tensor may be expressed as the derivative of the strain energy with respect to $\mathbf{E}$, i.e.

$$\mathbf{S} = \frac{\partial \psi}{\partial \mathbf{E}}. \tag{A.50}$$

Blatz-Ko Material

The Blatz Ko model was derived from experiments on compressible foamed elastomers and rubbers by Blatz and Ko. It is a strain energy function commonly used to model compressible, nonlinear hyperelastic materials. For an overview of the Blatz-Ko model and its properties refer to Beatty [17]. The strain energy for a Blatz-Ko material is [17]

$$\psi(I_1, I_2, I_3) = \frac{Gf}{2}\left(I_1 - 3 - \frac{2}{q}\left(I_3^{\frac{q}{2}} - 1\right)\right) + \frac{G(1-f)}{2}\left(\frac{I_2}{I_3} - 3 - \frac{2}{q}\left(I_3^{\frac{-q}{2}} - 1\right)\right), \tag{A.51}$$

where $\{I_1, I_2, I_3\}$ are the three principal invariants of $\mathbf{C}$, G is the shear modulus and $q < 0$ is a parameter. In order that a simple tension always produces an equibiaxial stretch it is

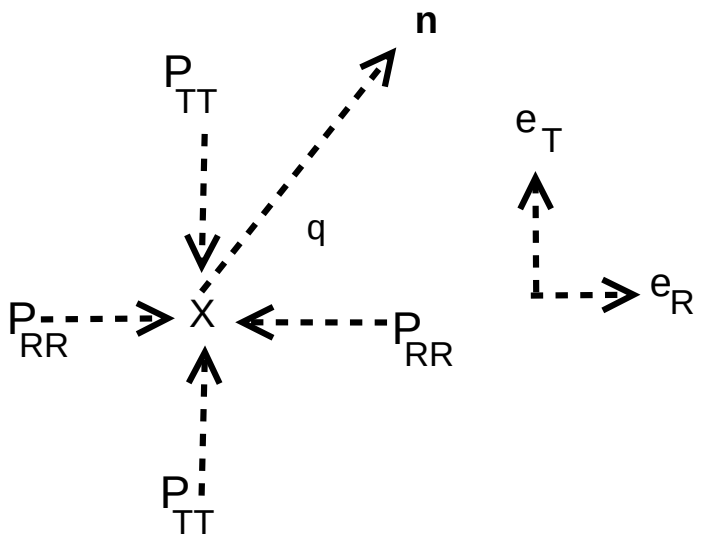

Figure A.2: The stress at a point X with normal $\mathbf{n}$. Here $\mathbf{e}_R$ and $\mathbf{e}_T$ are the cylindrical unit basis vectors. The angle between the normal and $\mathbf{e}_R$ is q.

sufficient that [17]

$$G > 0 \tag{A.52}$$

$$0 < f \leq 1. \tag{A.53}$$

The terms with q and $-q$ model the (hydrostatic pressure) response of the material to changes in volume. We insist that $q < 0$ in order that compressions produce compressive stress and expansions produce tensions.

A.1.5 Onset of Plasticity / Fracture

Some solids cease to behave elastically at high levels of deformation. An example is the bending of a paper clip. After the stress exceeds a critical threshold, irreversible flow occurs and the clip will not spring back to its original shape after the force is relaxed. We will not be modelling plastic flows in this thesis, however we wish to derive yield conditions so that we may have yield criteria governing when our elastic model ceases to be physically realistic.

Since the Cauchy stress tensor $\mathbf{T}$ is symmetric (a consequence of the material being in rotational equilibrium) it is diagonalisable. In fact, in this thesis the deformation is radially

symmetric (in cylindrical coordinates), so that the principal (i.e. diagonal) stresses are $\{T_{RR}, T_{\Theta\Theta}, T_{ZZ}\}$. At the point X in Figure A.1.5, the normal (parallel to $\mathbf{n}$) and shear (perpendicular to $\mathbf{n}$, in the direction with angle $\left(q + \frac{\pi}{2}\right)$) forces are respectively

$$\begin{aligned} N =& \mathbf{n} \cdot \mathbf{T} \cdot \mathbf{n} && \text{(A.54)} \\ =& \frac{1}{2}\left(T_{RR} + T_{\Theta\Theta}\right) + \frac{1}{2}\left(T_{RR} - T_{\Theta\Theta}\right)\cos(2q) && \text{(A.55)} \\ F =& \mathbf{n}^{\perp} \cdot \mathbf{T} \cdot \mathbf{n} && \text{(A.56)} \\ =& \frac{1}{2}\left(T_{\Theta\Theta} - T_{RR}\right)\sin(2q). && \text{(A.57)} \end{aligned}$$

The *Tresca* yield criterion states that yielding occurs when the shear force exceeds the critical stress τ. The maximal shear force occurs when $q = \pm\frac{\pi}{4}$, so that the yield criterion is

$$\frac{1}{2}\left(|T_{\Theta\Theta} - T_{RR}|\right) = \tau. \tag{A.58}$$

We obtain a similar yield criterion for the pairs $|T_{RR} - T_{ZZ}|$ and $|T_{\Theta\Theta} - T_{ZZ}|$.

A.1.6 Equations of Equilibrium

We now have all the machinery necessary to describe the state of a deformed body in mechanical equilibrium. In mechanical equilibrium acceleration and velocity is negligible. Suppose the current configuration is given by B_2, with boundary ∂B_2, and the reference configuration is given by B_0, with boundary ∂B_0. Suppose the body force density per unit volume in the current configuration B_2 is given by $\mathbf{f}^{\phi}$. Suppose a surface force of $\mathbf{g}^{\phi}$ acts on ∂B_2^{+}, and the displacement is fixed to zero on ∂B_2^{-}. For the tumour to be in equilibrium it is necessary and sufficient that

$$\begin{aligned} -\nabla \cdot \mathbf{T} &= \mathbf{f}^{\phi} \text{ in } B_2 \\ \mathbf{T}\mathbf{n} &= \mathbf{g}^{\phi} \text{ on } \partial B_2^{+}, \end{aligned} \tag{A.59}$$

where $\mathbf{n}$ is normal to ∂B_2^+. In the reference configuration (A.59) is equivalent to

$$\begin{aligned} -\nabla \cdot \mathbf{P} &= \mathbf{f} \text{ in } B_0 \\ \mathbf{P} \cdot \mathbf{N} &= \mathbf{g} \text{ on } \Gamma_0, \end{aligned} \tag{A.60}$$

where $\mathbf{N}$ is normal to ∂B_0^+ and $\mathbf{g}$ is the Piola Transform of $\mathbf{g}^\phi$. The body force $\mathbf{f}$ expresses the force per volume $\mathbf{f}^\phi$ scaled for the reference configuration, i.e. $\mathbf{f} = J\mathbf{f}^\phi$.

If there exist potentials for the body force and boundary force, then the equations of equilibrium are the Euler Lagrange equations which extremise the potential energy. To see this, suppose that $\hat{f}$ and $\hat{g}$ are potentials for $\mathbf{f}$ and $\mathbf{g}$, such that

$$\begin{aligned} \mathbf{f} &= -\frac{\partial \hat{f}}{\partial \mathbf{u}} \\ \mathbf{g} &= -\frac{\partial \hat{g}}{\partial \mathbf{u}}. \end{aligned} \tag{A.61}$$

It follows that the potential energy of the system is

$$W = \iiint_{B_0} \left(\psi + \hat{f} \right) dV + \oint_{\partial B_0} \hat{g} \cdot \mathbf{n} dA. \tag{A.62}$$

We let η be an *admissible* variation on the displacement. This means η must be suitably continuous and differentiable, and $\eta = \mathbf{0}$ on ∂B_0^-. The first variation of the potential energy in the direction of η is

$$\iiint_{B_0} \left(\frac{\partial \psi}{\partial \mathbf{F}} : \nabla \eta - \mathbf{f}.\eta \right) dV - \oint_{\partial B_0} \eta.\left(\mathbf{g} \cdot \mathbf{n} \right) dA. \tag{A.63}$$

We have made use of the fact that the displacement gradient is *linear* in the displacement, so that the first variation in $\mathbf{F}$ is just $\nabla \eta$. Applying the chain rule to the first integral, we find

$$\begin{aligned} &\iiint_{B_0} \left(-\eta.\left(\nabla \cdot \mathbf{P} \right) - \mathbf{f}.\eta + \nabla \cdot \left(\mathbf{P}^T \eta \right) \right) dV - \oint_{\partial B_0} \eta \cdot \mathbf{g} dA \\ &\quad = \iiint_{B_0} -\eta.\left(\nabla \cdot \mathbf{P} + \mathbf{f} \right) dV + \oint_{\partial B_0} \eta.\left(-\mathbf{g} + \mathbf{P} \cdot \mathbf{n} \right) dA. \end{aligned} \tag{A.64}$$

We obtain the equations of equilibrium by setting the coefficients of η to zero.

A.1.7 Incompressible Elasticity

Many collagenous materials are almost incompressible. Incompressible materials are such that $\det(\mathbf{F}) = 1$. To model this we introduce a Lagrange multiplier p to the strain energy, as follows

$$\psi = \psi^*(\mathbf{F}) - p(J-1), \tag{A.65}$$

where ψ^* is the strain energy function defining our constitutive relation. Differentiating this with respect to $\mathbf{F}$ we find

$$\mathbf{P} = \frac{\partial \psi^*}{\partial \mathbf{F}} - pJ\mathbf{F}^{-T}. \tag{A.66}$$

The equations of equilibrium retain their same definition, however we must also use the incompressibility equation

$$J - 1 = 0 \tag{A.67}$$

to solve for the displacement $\mathbf{u}$. We note that p is a function of position and in general will vary throughout the body.

A.1.8 Cylindrical Coordinates

Cylindrical coordinates $\{R, \Theta, Z\}$ are obtained through the coordinate functions

$$\begin{aligned} R &= \sqrt{x^2 + y^2}, \\ \Theta &= \tan^{-1} \frac{y}{x}, \\ Z &= z, \end{aligned} \tag{A.68}$$

where $\mathbf{X} = (x, y, z)^T$ in Cartesian coordinates and $\mathbf{X} \neq \mathbf{0}$. The natural basis vectors are

$$\begin{aligned} \mathbf{g}_R &= (\cos\Theta, \sin\Theta, 0)^T \\ \mathbf{g}_\Theta &= (-R\sin\Theta, R\cos\Theta, 0)^T \\ \mathbf{g}_Z &= (0, 0, 1)^T. \end{aligned} \tag{A.69}$$

The orthonormal cylindrical basis vectors are the scaled versions of the cylindrical basis vectors, i.e.

$$\mathbf{e}_R = \mathbf{g}_R \quad \mathbf{e}_\Theta = R^{-1}\mathbf{g}_\Theta \quad \mathbf{e}_Z = \mathbf{g}_Z. \tag{A.70}$$

The physical components of vectors and tensors are obtained by scaling by the magnitude of the basis vectors. For example, if $\mathbf{u} = u^\alpha \mathbf{g}_\alpha$ is a contravariant vector, then the physical components $\hat{u}^i$ are such that $\mathbf{u} = \hat{u}^i \mathbf{e}_i$, i.e. $\hat{u}^R = u^R$, $\hat{u}^\Theta = Ru^\Theta$ and $\hat{u}^Z = u^Z$. We obtain the physical components of the gradient of $\mathbf{u}$ by obtaining the gradient using the tensor components, and then substituting the physical components for the tensor components. In array form, we find

$$\nabla \mathbf{u} = \begin{pmatrix} \frac{\partial \hat{u}_r}{\partial R} & \frac{1}{R}\left(\frac{\partial \hat{u}_r}{\partial \Theta} - \hat{u}_\theta\right) & \frac{\partial u_r}{\partial Z} \\ \frac{\partial \hat{u}_\theta}{\partial R} & \frac{\hat{u}_r}{R} + \frac{1}{R}\frac{\partial \hat{u}_\theta}{\partial \Theta} & \frac{\partial u_\theta}{\partial Z} \\ \frac{\partial u_z}{\partial R} & \frac{1}{R}\frac{\partial u_z}{\partial \Theta} & \frac{\partial u_z}{\partial Z} \end{pmatrix}. \tag{A.71}$$

Suppose $\mathbf{P}$ is a second order tensor field[1], with physical components $\mathbf{P} = P_{\alpha\beta}\mathbf{e}_\alpha \otimes \mathbf{e}_\beta$. The divergence of $\mathbf{P}$ is

$$\begin{aligned} \nabla \cdot \mathbf{P} = &\left(\frac{1}{R}\frac{\partial (RP_{RR})}{\partial R} + \frac{1}{R}\frac{\partial P_{R\Theta}}{\partial \Theta} - \frac{1}{R}P_{\Theta\Theta} + \frac{\partial P_{RZ}}{\partial Z}\right)\mathbf{e}_R + \\ &+ \left(\frac{1}{R}\frac{\partial (RP_{\Theta R})}{\partial R} + \frac{1}{R}\frac{\partial P_{\Theta\Theta}}{\partial \Theta} + \frac{\partial P_{\Theta Z}}{\partial Z} + \frac{1}{R}P_{R\Theta}\right)\mathbf{e}_\Theta + \\ &\left(\frac{1}{R}\frac{\partial (RP_{ZR)}}{\partial R} + \frac{1}{R}\frac{\partial P_{Z\Theta}}{\partial \Theta} + \frac{\partial P_{ZZ}}{\partial Z}\right)\mathbf{e}_Z. \end{aligned} \tag{A.72}$$

In multiplying terms expressed in cylindrical coordinates, we make use of the following trigonometric identities

$$\begin{aligned} \cos\theta\cos\phi &= \frac{1}{2}\left(\cos(\theta-\phi) + \cos(\theta+\phi)\right) \\ \sin\theta\sin\phi &= \frac{1}{2}\left(\cos(\theta-\phi) - \cos(\theta+\phi)\right) \\ \sin\theta\cos\phi &= \frac{1}{2}\left(\sin(\theta+\phi) + \sin(\theta-\phi)\right) \\ \cos\theta\sin\phi &= \frac{1}{2}\left(\sin(\theta+\phi) - \sin(\theta-\phi)\right). \end{aligned} \tag{A.73}$$

[1]The expression in terms of physical components is the same regardless of whether $\mathbf{P}$ is (2,0), (1,1) or (0,2).

A.1.9 Area Enclosed By Deformed Capillary

We find the area of the deformed capillary wall. To find this we consider the area of a small radial segment. The vector defining one of its sides is merely the position vector in Eulerian coordinates, i.e.

$$\mathbf{x} = \begin{pmatrix} R + u_r \\ u_\theta \end{pmatrix}. \tag{A.74}$$

We parameterise the arc using the material coordinate Θ, writing the position vector as $\mathbf{X}(\Theta)$. In material coordinates, the incremental tangential vector to the curve is given by

$$\mathbf{X}(\Theta + d\Theta) \simeq \mathbf{X}(\Theta) + Rd\Theta\mathbf{e}_\Theta,$$

where we have weighted by the metric R. Under the deformation, the tangential vector transforms to

$$\mathbf{v}_2 = Rd\Theta\mathbf{F} \cdot \mathbf{e}_\Theta. \tag{A.75}$$

The area of the segment is given by $\frac{1}{2}|\mathbf{v}_2 \times \mathbf{x}|$. Writing

$$u_r = R + u_0 + \epsilon W_1 cos(n\Theta) + \frac{\epsilon^2}{2}\left(W_2 cos(2n\Theta) + W_{2,0}\right) \tag{A.76}$$

$$u_\Theta = \epsilon V_1 sin(n\Theta) + \frac{\epsilon^2}{2} V_2 sin(2n\Theta), \tag{A.77}$$

we find the area enclosed by the capillary is

$$\int_0^{2\pi} \frac{1}{2}|\mathbf{v}_2 \times \mathbf{x}|\, d\Theta = \pi\left((R+u_0)^2 + \frac{1}{2}\left(\epsilon^2 V_1^2 + \epsilon^2 W_1^2 + \frac{\epsilon^4}{4}V_2^2 + \frac{\epsilon^4}{4}\left(W_2^2 + 2W_{2,0}^2\right)\right)\right). \tag{A.78}$$

Appendix B

Model Parameters

We outline some values for the parameters. Most of the parameters outlined below vary widely amongst different tumour lines. Many vary widely within particular tumours. Accordingly, most values below should be understood to be estimates.

The distribution of intercapillary distances and capillary diameters in human colon adenocarcinomas is outlined in Table B.7. This data was obtained from Konerding *et al* [87]. We let the outer radius R_2 be the natural length scale of our problem. We assume all the different types of tumour have a similar distribution of intercapillary distances and capillary diameters. We use this data to determine approximate values for the parameters R_1/R_2 and h/R_1. It is interesting comparing this data with typical values for tumour cords. The typical radii of vessels in tumour cords range from 10 to 40 microns [21]. The distance from the vessel wall to the first layer of necrotic cells is typically 60 to 120 microns [21]. Thus it can be seen that the dimensions of our annular geometry are very similar to those of tumour cords. From Table 1.1 the range of values for h (the thickness of the basement membrane) is 50-100 nm.

We outline the parameters governing the nutrient distribution and rate of uptake. We calculate the oxygen distribution coefficients from the experiments on EMT6/Ro mouse mammary sarcoma spheroids by Freyer *et al* and Casciari *et al* [35, 34, 54]. These experiments calculated the rate of uptake of oxygen and glucose by the spheroids, and also the dependence of the growth on the oxygen level, glucose level and pH. The oxygen parameters thus vary according to the glucose distribution and pH. We calculate the maximum rate of

uptake λ_n by dividing the rate of uptake per cell by the cellular volume, after noting that the rate of uptake varies approximately linearly with cell volume. We find λ_n is approximately 0.006 to 0.05 mMs^{-1} depending on microenvironment factors such as the glucose concentration or the pH. We similarly find k_n is approximately 4.64×10^{-3} mM and k_c is approximately 8.3×10^{-3}mM [35]. The maximum doubling time varied from $10 - 600$ hours depending on the glucose and pH [54]. However most values were clustered at the lower end of this spectrum, so we take the doubling time to be approximately twice per day. We obtain the proliferation constant λ_c by dividing $ln(2)$ by the doubling time. The diffusion coefficient is approximately $1.5 \times 10^{-9} m^2 s^{-1}$ [122]. The partial pressure of the oxygen in the blood ranges from $40 - 100$ mmHG [24]. The lower limit corresponds to deoxygenated blood in the veins and the upper limit corresponds to freshly oxygenated blood in the arteries [24]. In normal tissues we expect the oxygen partial pressure to be approximately 80 mmHG, however we expect considerable variation in tumours due to their poor vasculature [137]. In particular, the lower limit of 40 mmHG is the threshold of the onset of hypoxia, where normal cell functioning is impaired through a lack of oxygen. We obtain the molarity of the oxygen in the blood by multiplying the oxygen partial pressure by the solubility $s = 0.0013$ mM/mmHG [24]. This is the solubility of oxygen in blood at normal body temperature. Thus the molarity of the oxygen in the blood ranges from approximately $0.05 - 0.13$mM.

We may obtain a crude order of magnitude for the parameter H^* giving the level of compression at which the rate of cell proliferation is half of its maximum using Helmlinger *et al* ([75]). Helmlinger *et al* grew human colon adenocarcinoma (LS174T) tumour spheroids in agarose gels of varying stiffness. Amongst other things they measured the cellular density and the cellular proliferation rate in unstressed spheroids, spheroids cultured in 0.7 per cent agarose and spheroids cultured in 1 per cent agarose. We assume that H (giving the inhibition due to compression of the cell proliferation) equals 1 for the unstressed spheroids. The respective proliferation rates of the spheroids in 0.7 per cent and 1 per cent agarose are approximately 0.58 and 0.40 those of the unstressed spheroids. Similarly the cell densities of the spheroids in agarose are respectively 1.57 and 2.01 of the unstressed spheroids. We

recall that relative cell densities are equal to $|\mathbf{F}_e|^{-1}$ in our constitutive relation

$$H = (1 + H^*)\frac{|\mathbf{F}_e|}{1 + H^*|\mathbf{F}_e|}. \tag{B.1}$$

Substituting these two sets of parameters into the above gives us a very crude fit for H^*. The parameters corresponding to the spheroids in 0.7 per cent agarose imply H^* is -0.22, and the parameters corresponding to the spheroids in 1 per cent agarose imply H^* is -0.33. This is an acceptable fit given the paucity of data and the simplicity of our model. We take H^* equal to -0.25.

B.0.10 Chemotherapy Parameters

The parameters governing the chemotherapy are outlined in Tables B.2 and B.3. We have obtained parameters for the chemotherapeutic drugs Cisplatin and Tirapazamine. For Cisplatin we assume $k_{met} = 0$. We determine the maximum rate of uptake through noting that the linearised rate of uptake equations are of the form

$$D_c\nabla^2 c = \frac{\lambda_d}{k_d}c, \tag{B.2}$$

so that

$$\lambda_d = gk_d, \tag{B.3}$$

where g is the initial linear rate of uptake given in Table B.2 and k_d is the Michaelis Constant. We estimate the Michaelis constant to be $25\mu M$ [48]. This gives us $\lambda_d = 4.5\mu M min^{-1}$.

The rate of cell death varies amongst cell lines. We estimate the maximum rate of cell death for cisplatin using data from Evans [48]. Evans immersed a layer of JB1 rat hepatoma cells for 2 hours in a solution containing cisplatin, measuring the number of cells in the layer after two days. He found the $10\mu M$ solution produced a layer 64 per cent the size of the control layer, and similarly the $25\mu M$ solution produced a layer 43 percent the size of the control layer and the $50\mu M$ solution produced a layer 32 percent the size of the control layer. On the assumption that the convergence is of the order of the inverse of the level of concentration (as implied by the Michaelis-Menten kinetics of our model), we expect that in the limit as the concentration of the drug heads to infinity the size of the drug layer

Parameter	Value	Unit
A	1557	nM
B	862	nM
C	261	nM
D	20	nM
k_1	41.6	min^{-1}
k_2	0.17	min^{-1}
k_3	1.3×10^{-2}	min^{-1}
k_4	5.9×10^{-4}	min^{-1}

Table B.1: Parameters Governing the Blood Concentration of Vinblastine after a single injection. These are taken from Shipley *et al* [125] and are calculated for a person with blood volume 44 litres given a single injection of 2700 nM. The last four parameters give the half-lives for each phase of the metabolism.

would be approximately 20 per cent. On fitting this to our constitutive relations, we find the ratio of the treated mass to the control mass is

$$exp\left(-\delta t \lambda_d p_1\right) = 0.2 \tag{B.4}$$

where δt is 2 hours. On substitution of these values we find that approximately

$$p_1 \times \lambda_d = 20 \text{ per day}, \tag{B.5}$$

to one significant figure. It needs to be emphasised that this is only a crude estimate. We expect the kill rate to vary from tumour to tumour. On substituting the above value for λ_d, we find $p_1 = 3.1 \times 10^{-3} \mu M^{-1}$.

Parameters governing the distribution and uptake of Tirapazamine are outlined in Table B.3. We could not find any parameters governing the clearance of Tirapazamine from the body. We therefore will use the (nondimensional) cisplatin clearance parameters. In converting a dosage in mgm^{-2} to a molar concentration, we note that there is approximately 2.7 litres of blood per body surface area for the average human adult, and the molecular weight of Tirapazamine is 0.178148 mg per mole. We find there are 2.08 mM per mgm^{-2}.

B.0.11 Radiotherapy Parameters

The parameters governing the radiotherapy are outlined in Table B.4. These parameters seem roughly constant for all types of tumour cell. We assume a low dose of 2 Gy applied

Parameter	Value	Unit	Description
g	0.18	min^{-1}	Rate of Uptake of Cisplatin [101]
D	17.5×10^{-8}	$cm^2 s^{-1}$	Diffusion Cf. for Cisplatin [101]
k_d	25	μM	Michaelis Constant for Cisplatin Uptake [48]
λ_d	4.5	$\mu M min^{-1}$	Maximum Rate of Uptake in Michaelis Term
$p_1 \times \lambda_d$	20	day^{-1}	Max Cell Kill Rate of Cisplatin [48]
p_1	$3.1e-3$	μM^{-1}	Cell Kill Rate of Cisplatin
V_c	9.41	m^{-2}	[47]
a	0.42	h^{-1}	[47]
b	5.1	h^{-1}	[47]
c	9.2×10^{-3}	h^{-1}	[47]
K_{21}	0.22	h^{-1}	[47]
K_{31}	1.87	h^{-1}	[47]
A	0.15	–	Inferred
B	0.66	–	Inferred
C	0.19	–	Inferred

Table B.2: Parameters Governing the Blood Concentration of Cisplatin. We note for the sake of conversion that 1 mole of Cisplatin weighs 290.105 grams. The last nine parameters govern the clearance of cisplatin from the body.

Parameter	Value	Units	Description
D	$0.049 - 1.7 \times 10^{-6}$	$cm^2 s^{-1}$	Diffusion Coefficient
λ_{drug}	0.159	$\mu M s^{-1}$	Maximum Uptake Rate
p_1	$8.02e-4$	$\mu M^{-1} min^{-1}$	Toxicity Rate
k_{met}	$0.38 - 35.3$	min^{-1}	Linear Metabolism Rate
KO	1.3	μM	Half-Kill Oxygen Concentration
k_d	1.14	μM	Michaelis Constant

Table B.3: Parameters Governing the Uptake of Tirapazamine analogs. For many parameters the drugs span a range of values. We have taken the maximum uptake rate and linear uptake rate per cell volume fraction and multiplied by the cell volume fraction 0.348. Takenfrom Hicks *et al* [77, 76].

Parameter	Description	Value	Unit	Reference
α_h	Linear	0.08	Gy^{-1}	[144]
β_h	Quadratic	0.01	Gy^{-2}	[144]
m	Maximum OER	2.9	-	[55]
K_m	O_2 Concentration at Point of Inflexion of Response Curve	0.0043	mM	[144]

Table B.4: Parameters Governing the Cell Death due to Radiotherapy.

Tumour Line	Description	$2G + \lambda$ (mmHG)
MCaIV	Murine Mammary Carcinoma	50
LS174T	Human Colon Adenocarcinoma	30
U87	Human Glioblastoma	200
HSTS26T	Human Soft Tissue Sarcoma	300
Mu89	Murine	7.4

Table B.5: Elastic Modulii of Various Tumours. The first four moduli are taken from Netti *et al* [106]. The last was calculated by myself using data provided by Dr Tiina Roose.

daily. The point of inflexion of the response curve is given by $K_m = 3.28$ mmHG [144]. We convert this to mM by multiplying by $0.0013mM(mmHG^{-1})$, which links the blood oxygen molarity to the oxygen partial pressure. We thus find $K_m = 0.0043mM$. The dosage D is taken to be $2Gy$ daily.

B.0.12 Elastic Parameters

We outline parameter values for the two elastic models of the tumour we have developed.

The tumour elastic properties were measured using the confined compression test by Netti *et al* [106]. In these experiments a small slice of tumour is placed in a confined chamber and compressed in one direction. The compression was increased approximately every 15 minutes. The stress (in the direction of the compression) was measured continuously over time. After each compression, the stress increased greatly before decaying over time. The decay in stress was caused by the poroelastic relaxation as the interstitial fluid

Parameter	Value	Units
λ_n	10^{-2}	$molm^{-3}s^{-1}$
λ_c	1.6×10^{-5}	s^{-1}
k_n	4.6×10^{-3}	$molm^{-3}$
k_c	8.3×10^{-3}	$molm^{-3}$

Table B.6: Parameters Governing the Uptake of the Nutrient (oxygen). They are taken from Roose *et al* [122]

Tumour Type	Mean I'vessel Dist	Min	Max	Mean Vessel Diam	Min	Max
Control Mucosa	101.5	41.7	181.2	12	6.4	20.9
Tumour Periphery	54.3	3.9	494.6	19.4	5.6	53.5
Luminal Tumour Surface	118.6	8.5	1181.5	18.3	2.2	84.5
Tumour Centre	177.7	19.3	1756.3	30.9	0.9	161.9

Tumour Type	Interbranch Distance	Min	Max
Control Mucosa	51.2	2.2	238.5
Tumour Periphery	50.2	5.7	336.3
Luminal Tumour Surface	78.5	6.6	920.8
Tumour Centre	131.9	9.18	896.1

Table B.7: In the top table is the distribution of intervessel distances and diameters in colorectal adenocarcinomas and mucosa. In the bottom are interbranch distances. All distances are in micrometers (10^{-6}m). The control mucosa is noncancerous and taken from the colon. This data is taken from Konerding [87].

Tumour Type	Average R_1/R_2	h/R_1
Control Mucosa	0.118	0.012
Tumour Periphery	0.357	0.0075
Luminal Tumour Surface		0.0083
Tumour Centre	0.174	0.0048

Table B.8: The range of possible values for the length ratios. The value for R_1/R_2 was found by dividing the mean vessel diameter by the mean intervessel distance, using data from Table B.7. It can be seen that generally R_1/R_2 is greater for tumoural tissue than the control tissue, particularly at the tumour periphery. In calculating h/R_1, we took h to be 75 nm.

Constant	Symbol	Expression
Bulk Modulus	K	$\frac{E}{3(1-2\nu)}$
Lame's Constant	λ	$\frac{E\nu}{(1+\nu)(1-2\nu)}$
Shear Modulus	G	$\frac{E}{2(1+\nu)}$

Table B.9: The various elastic constants, expressed in terms of the Young's Modulus and Poisson's Ratio.

was squeezed out of the tumour. The residual stress remaining in the tumour after the poroelastic relaxation is plotted in Figure B.1. We fitted a Blatz-Ko model to the results. The two carcinomas (MCaIV and LS174T) did not fit the elastic model well. Netti *et al* observes that the reason for this is probably that these two carcinomas have a relatively weak extracellular matrix compared to the other two. The collagen content of these two carcinomas is approximately 0.2 per cent, whereas the collagen content of the other tumour lines is approximately 0.5 to 1 per cent. Thus these two carcinomas exhibit viscoelastic behaviour and are less likely to sustain high levels of stress. We therefore do not expect our elastic model to apply to the two carcinomas. The fitted data is outlined in Table B.5 [106].

We recall the Cauchy Stress for a Blatz-Ko material is given by

$$\mathbf{T} = \frac{Gf}{J}\left(\mathbf{F}\mathbf{F}^T - J^q\mathbf{I}\right) - \frac{G(1-f)}{J}\left(\mathbf{F}^{-T}\mathbf{F}^{-1} - J^{-q}\mathbf{I}\right), \tag{B.6}$$

where G is the shear modulus, $J = det(\mathbf{F})$ and q and f are undetermined parameters. Thus for each tumour line, there are three parameters to be fitted for: $\{q, G, f\}$. We eliminate one parameter by fitting in the small strain (linear) limit as follows. In these experiments, $\mathbf{E}_{xx} \neq 0$ (where the x axis is in the direction of compression) and all other components of the strain are zero. In the linear limit we find

$$\begin{aligned} T_{xx} &= 2GE_{xx} + \left(K - \frac{2G}{3}\right)E_{xx} \\ &= \left(K + \frac{4G}{3}\right)E_{xx}. \end{aligned} \tag{B.7}$$

Thus in the confined compression experiments, the small strain ratio of the compressive stress to the compressive strain yields $\left(K + \frac{4G}{3}\right)$. The bulk modulus K may be expressed in terms of $q = \frac{-2\nu}{1-2\nu}$ and G. We may thus eliminate G from the Blatz-Ko model, and it remains for us to fit the remaining two parameters. We fit for q and f using nonlinear least squares. We confine our fit to the acceptable ranges $-\infty < q \leq 0$ and $0 \leq f \leq 1$. The results are in Table B.10.

We may infer $G = (2-q)^{-1}\left(K + \frac{4G}{3}\right)$. We find that $G = 23$ mmHG (3100 Pa) for

Tumour Line	$2G + \lambda$ (mmHG)	q	q^+	q^-	f	f^+	f^-
HSTS26T	300	-10.9	-8.5	-13.3	0.04	0.02	0.07
U87	200	-7.9	-6.4	-9.3	0.20	0.10	0.30
LS174T	30	-5.5	-4.9	-6.0	1	-	-
MCaIV	50	-4.6	-4.3	-4.8	1	-	-
Mu89	7.4	-11.3	-13.1	-9.4	0.27	0.41	0.13

Table B.10: The parameters obtained by fitting the stress-strain data to a Blatz-Ko model using nonlinear least squares. The data for q is to 1 decimal place, and the data for f to 2 decimal places. The + and − columns give 95 per cent confidence intervals. We cannot provide such confidence intervals when $f = 1$ because this is at the boundary of the region of permissible values for f.

HSTS26T and $G = 20$ mmHG (2700 Pa) for U87, using the fitted values. Similarly the values for the Young's Modulii are 9000 Pa and 7800 Pa respectively.

As explained at the start of this chapter, we know of no direct experimental measurements of the yield stress for tumours. We estimate the yield stress using the experimental measuring of the stretching and fracturing of brain tissue by Franceschini *et al* [52]. In these experiments segments of brain tissue were uniaxially stretched. As the stretch ratio λ increased the tissue behaved elastically, before beginning to damage (indicated by the curvature of the stress-strain curve inflecting from positive to negative) and then completely fracturing. The onset of damage occured at a mean stretch of 1.91, with a standard deviation of 0.42. Our model, using the above fitted parameters for U87 brain tumours, indicates a stress $\mathbf{T}$ of $24E_t$ corresponds to this stretch. The stress corresponding to a stretch of 1.49 (one standard deviation away from the mean) is $4.6E_t$ and the stress corresponding to a stretch of 1.07 (two standard deviations from the mean) is $0.25E_t$. There is clearly substantial variation in the elastic response and fracture of the brain samples, probably largely due to the fact that they used tissue take from all segments of the brain.

We estimate the Young's Modulus of the capillary basement membrane to be 2 MPa. On the assumption that the Poisson's Ratio is approximately 0.5 (since the basement membrane is approximately incompressible, we find the Shear Modulus is approximately 6.7×10^5 Pa. For $HSTS26T$ the ratio of the Basement Membrane Young's Modulus to the tumour Young's Modulus is approximately 220 to 1 (to 2 significant figures). For U87, the ratio is approximately 260 to 1 (to 2 significant figures). The range of values for the Young's

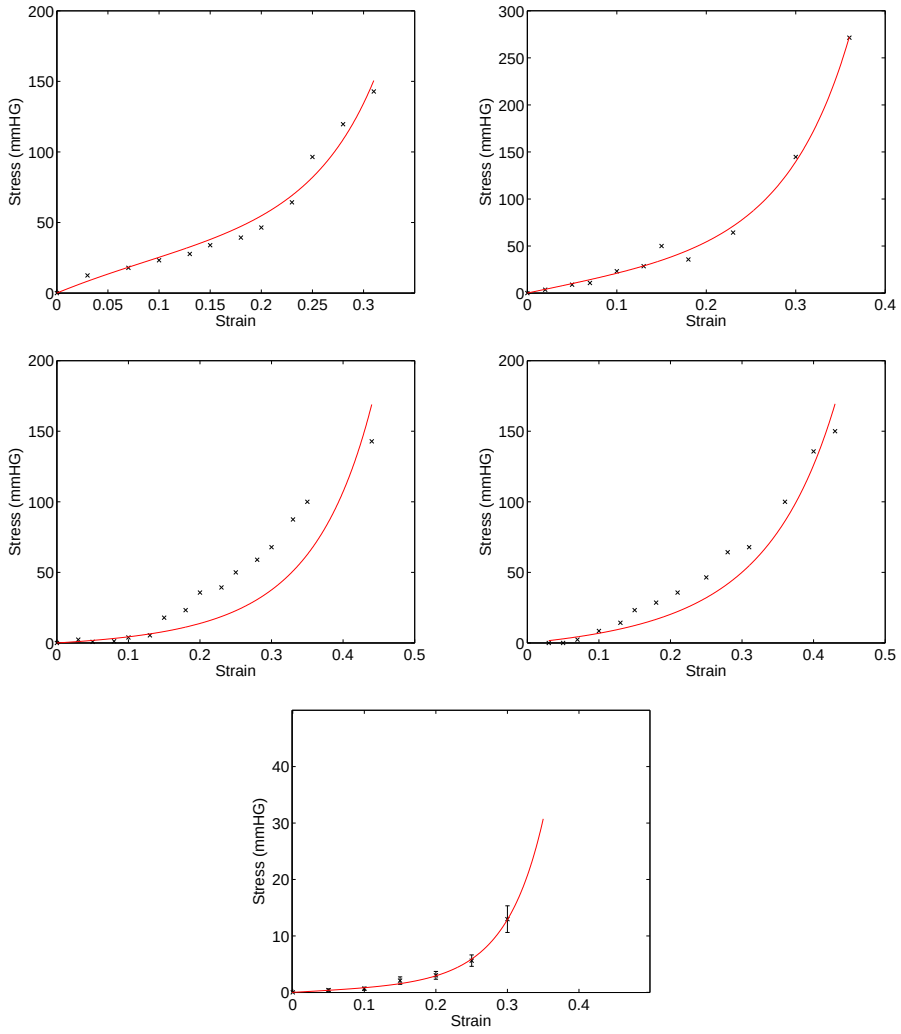

Figure B.1: The fitted curves giving the stress-strain relationship in HSTS26T (top left), U87 (top right), LS174T (bottom left) and MCaIV (bottom right) and Mu89(bottom). HSTS26T is human soft tissue sarcoma, U87 is human glioblastoma, LS174T is human colon adenocarcinoma, MCaIV is murine mammary carcinoma (grown in mice) and MU89 is melanoma.

Modulus of the basement membrane is given in Table 1.1. The default value we will use is 1 MPa.

Appendix C

Tumour Constitutive Identities

C.0.13 Blatz-Ko Incremental Equations For Anisotropic Growth

We outline some of the derivatives of the 'grown' Blatz-Ko strain energy function defined in (2.52). These derivatives are with respect to a base state with deformation gradient $\mathbf{F}_0$ and growth dilation tensor $\mathbf{F}_g$. The growth dilation tensor is diagonal, with principal components $\{\zeta_\alpha\}$, and $\eta_0 = \zeta_R\zeta_\Theta\zeta_Z = |\mathbf{F}_g|$.

$$\begin{aligned}\frac{\partial \mathbf{P}}{\partial \mathbf{F}} : \nabla\mathbf{u} = \eta_0 G_t f \left(\nabla\mathbf{u}\mathbf{F}_g^{-2} - q\eta_0^{-q}J_0^q\left(\mathbf{F}_0^{-T} : \nabla\mathbf{u}\right)\mathbf{F}_0^{-T} + \eta_0^{-q}J_0^q\mathbf{F}_0^{-T}\nabla\mathbf{u}^T\mathbf{F}_0^{-T}\right)\\ - \eta_0 G_t(1-f)\left(-\mathbf{F}_0^{-T}\nabla\mathbf{u}^T\mathbf{F}_0^{-T}\mathbf{F}_g^2\mathbf{F}_0^{-1}\mathbf{F}_0^{-T} - \mathbf{F}_0^{-T}\mathbf{F}_g^2\mathbf{F}_0^{-1}\nabla\mathbf{u}\mathbf{F}_0^{-1}\mathbf{F}_0^{-T}\right.\\ \left.-\mathbf{F}_0^{-T}\mathbf{F}_g^2\mathbf{F}_0^{-1}\mathbf{F}_0^{-T}\nabla\mathbf{u}^T\mathbf{F}_0^{-T} + q\eta_0^q J_0^{-q}\left(\mathbf{F}_0^{-T} : \nabla\mathbf{u}\right)\mathbf{F}_0^{-T} + \eta_0^q J_0^{-q}\mathbf{F}_0^{-T}\nabla\mathbf{u}^T\mathbf{F}_0^{-T}\right)\end{aligned} \tag{C.1}$$

It follows that if $P_{\alpha_1\alpha_2\alpha_3\alpha_4} = \frac{\partial P_{\alpha_1\alpha_2}}{\partial F_{\alpha_3\alpha_4}}$, then

$$P_{\alpha\alpha\alpha\alpha} = \eta_0 G_t f\left(\zeta_\alpha^{-2} + (1-q)\eta_0^{-q}J_0^q F_{0,\alpha\alpha}^{-2}\right) - \eta_0 G_t(1-f)\left(-3\zeta_\alpha^2 F_{0,\alpha\alpha}^{-4} + (q+1)\eta_0^q J_0^{-q}F_{0,\alpha\alpha}^{-2}\right) \tag{C.2}$$

$$P_{\alpha\alpha\beta\beta} = -q\eta_0^{1-q}G_t f J_0^q F_{0,\alpha\alpha}^{-1}F_{0,\beta\beta}^{-1} - q\eta_0^{q+1}G_t(1-f)J_0^{-q}F_{0,\alpha\alpha}^{-1}F_{0,\beta\beta}^{-1} \tag{C.3}$$

$$P_{\alpha\beta\alpha\beta} = \eta_0 G_t f\zeta_\beta^{-2} + \eta_0 G_t(1-f)F_{0,\alpha\alpha}^{-2}F_{0,\beta\beta}^{-2}\zeta_\alpha^2 \tag{C.4}$$

$$P_{\alpha\beta\beta\alpha} = \eta_0^{1-q}G_t f J_0^q F_{0,\alpha\alpha}^{-1}F_{0,\beta\beta}^{-1} + \eta_0 G_t(1-f)\left(F_{0,\alpha\alpha}^{-1}F_{0,\beta\beta}^{-3}\zeta_\beta^2 + F_{0,\beta\beta}^{-1}F_{0,\alpha\alpha}^{-3}\zeta_\alpha^2 - \eta_0^q J_0^{-q}F_{0,\alpha\alpha}^{-1}F_{0,\beta\beta}^{-1}\right), \tag{C.5}$$

where $\alpha \neq \beta$.

$$\frac{\partial \mathbf{P}}{\partial \zeta_\alpha}\zeta_\alpha = \eta G_t f\left(-2\mathbf{F}\mathbf{F}_g^{-3}\delta\mathbf{F}_g + q\eta^{-q-1}J_0^q\mathbf{F}_0^{-T}\delta\eta\right) + \delta\eta G_t f\left(\mathbf{F}\mathbf{F}_g^{-2} - \eta^{-q}J_0^q\mathbf{F}_0^{-T}\right)$$
$$- \eta G_t(1-f)\left(2\mathbf{F}_0^{-T}\mathbf{F}_g\delta\mathbf{F}_g\mathbf{F}_0^{-1}\mathbf{F}_0^{-T} - q\eta^{q-1}\delta\eta J_0^{-q}\mathbf{F}_0^{-T}\right)$$
$$- \delta\eta G_t(1-f)\left(\mathbf{F}_0^{-T}\mathbf{F}_g^2\mathbf{F}_0^{-1}\mathbf{F}_0^{-T} - \eta^q J_0^{-q}\mathbf{F}_0^{-T}\right), \quad \text{(C.6)}$$

where we sum over α.

$$\frac{\partial^2 \mathbf{P}}{\partial\zeta_\alpha\partial\mathbf{F}} : \nabla\mathbf{u}\delta\zeta_\alpha = \delta\eta G_t f\left(\nabla\mathbf{u}\mathbf{F}_g^{-2} - q\eta^{-q}J_0^q\left(\mathbf{F}_0^{-T} : \nabla\mathbf{u}\right)\mathbf{F}_0^{-T} + \eta^{-q}J_0^q\mathbf{F}_0^{-T}\nabla\mathbf{u}^T\mathbf{F}_0^{-T}\right)$$
$$+ \eta G_t f\left(-2\nabla\mathbf{u}\mathbf{F}_g^{-3}\delta\mathbf{F}_g + q^2\eta^{-q-1}\delta\eta J_0^q\left(\mathbf{F}_0^{-T} : \nabla\mathbf{u}\right)\mathbf{F}_0^{-T} - q\eta^{-q-1}\delta\eta J_0^q\mathbf{F}_0^{-T}\nabla\mathbf{u}^T\mathbf{F}_0^{-T}\right)$$
$$-\delta\eta G_t(1-f)\left(-\mathbf{F}_0^{-T}\nabla\mathbf{u}^T\mathbf{F}_0^{-T}\mathbf{F}_g^2\mathbf{F}_0^{-1}\mathbf{F}_0^{-T} - \mathbf{F}_0^{-T}\mathbf{F}_g^2\mathbf{F}_0^{-1}\nabla\mathbf{u}\mathbf{F}_0^{-1}\mathbf{F}_0^{-T} - \mathbf{F}_0^{-T}\mathbf{F}_g^2\mathbf{F}_0^{-1}\mathbf{F}_0^{-T}\nabla\mathbf{u}^T\mathbf{F}_0^{-T}\right.$$
$$\left. + q\eta^q J_0^{-q}\left(\mathbf{F}_0^{-T} : \nabla\mathbf{u}\right)\mathbf{F}_0^{-T} + \eta^q J_0^{-q}\mathbf{F}_0^{-T}\nabla\mathbf{u}^T\mathbf{F}_0^{-T}\right)$$
$$- \eta G_t(1-f)\left(-2\mathbf{F}_0^{-T}\nabla\mathbf{u}^T\mathbf{F}_0^{-T}\mathbf{F}_g\delta\mathbf{F}_g\mathbf{F}_0^{-1}\mathbf{F}_0^{-T} - 2\mathbf{F}_0^{-T}\mathbf{F}_g\delta\mathbf{F}_g\mathbf{F}_0^{-1}\nabla\mathbf{u}\mathbf{F}_0^{-1}\mathbf{F}_0^{-T}\right.$$
$$\left. -2\mathbf{F}_0^{-T}\mathbf{F}_g\delta\mathbf{F}_g\mathbf{F}_0^{-1}\mathbf{F}_0^{-T}\nabla\mathbf{u}^T\mathbf{F}_0^{-T} + q^2\eta^{q-1}\delta\eta J_0^{-q}\left(\mathbf{F}_0^{-T} : \nabla\mathbf{u}\right)\mathbf{F}_0^{-T} + q\eta^{q-1}\delta\eta J_0^{-q}\mathbf{F}_0^{-T}\nabla\mathbf{u}^T\mathbf{F}_0^{-T}\right), \quad \text{(C.7)}$$

where we sum over α. The second derivative is

$$\frac{\partial^2 \mathbf{P}}{\partial \mathbf{F}^2} = f\frac{\partial^2 \mathbf{P}_f}{\partial \mathbf{F}^2} + (1-f)\frac{\partial^2 \mathbf{P}_{1-f}}{\partial \mathbf{F}^2}, \quad \text{(C.8)}$$

where

$$\frac{\partial^2 \mathbf{P}_f}{\partial \mathbf{F}^2} : \nabla\mathbf{u} : \nabla\mathbf{v} = G_t \eta_0^{1-q} J_0^q \Big[-\mathbf{F}_0^{-T}\nabla\mathbf{u}^T\mathbf{F}_0^{-T}\nabla\mathbf{v}^T\mathbf{F}_0^{-T} - \mathbf{F}_0^{-T}\nabla\mathbf{v}^T\mathbf{F}_0^{-T}\nabla\mathbf{u}^T\mathbf{F}_0^{-T}$$
$$+q\left(\mathbf{F}_0^{-T} : \nabla\mathbf{v}\right)\mathbf{F}_0^{-T}\nabla\mathbf{u}^T\mathbf{F}_0^{-T} + q\left(\mathbf{F}_0^{-T} : \nabla\mathbf{u}\right)\mathbf{F}_0^{-T}\nabla\mathbf{v}^T\mathbf{F}_0^{-T}$$
$$-q^2\left(\mathbf{F}_0^{-T} : \nabla\mathbf{v}\right)\left(\mathbf{F}_0^{-T} : \nabla\mathbf{u}\right)\mathbf{F}_0^{-T} + q\left(\mathbf{F}_0^{-T}\nabla\mathbf{v}^T\mathbf{F}_0^{-T} : \nabla\mathbf{u}\right)\mathbf{F}_0^{-T}\Big]$$
$$\frac{\partial^2 \mathbf{P}_{1-f}}{\partial \mathbf{F}^2} : \nabla\mathbf{u} : \nabla\mathbf{v} =$$
$$-G_t\eta\mathbf{F}_0^{-T}\Big(\nabla\mathbf{u}^T\mathbf{F}_0^{-T}\nabla\mathbf{v}^T\mathbf{F}_0^{-T}\mathbf{F}_g^2\mathbf{F}_0^{-1} + \nabla\mathbf{u}^T\mathbf{F}_0^{-T}\mathbf{F}_g^2\mathbf{F}_0^{-1}\nabla\mathbf{v}\mathbf{F}_0^{-1} +$$
$$\nabla\mathbf{u}^T\mathbf{F}_0^{-T}\mathbf{F}_g^2\mathbf{F}_0^{-1}\mathbf{F}_0^{-T}\nabla\mathbf{v}^T + \mathbf{F}_g^2\mathbf{F}_0^{-1}\nabla\mathbf{v}\mathbf{F}_0^{-1}\nabla\mathbf{u}\mathbf{F}_0^{-1}$$
$$+\mathbf{F}_g^2\mathbf{F}_0^{-1}\nabla\mathbf{u}\mathbf{F}_0^{-1}\mathbf{F}_0^{-T}\nabla\mathbf{v}^T + \mathbf{F}_g^2\mathbf{F}_0^{-1}\mathbf{F}_0^{-T}\nabla\mathbf{v}^T\mathbf{F}_0^{-T}\nabla\mathbf{u}^T$$
$$\nabla\mathbf{v}^T\mathbf{F}_0^{-T}\nabla\mathbf{u}^T\mathbf{F}_0^{-T}\mathbf{F}_g^2\mathbf{F}_0^{-1} + \nabla\mathbf{v}^T\mathbf{F}_0^{-T}\mathbf{F}_g^2\mathbf{F}_0^{-1}\nabla\mathbf{u}\mathbf{F}_0^{-1} +$$
$$\nabla\mathbf{v}^T\mathbf{F}_0^{-T}\mathbf{F}_g^2\mathbf{F}_0^{-1}\mathbf{F}_0^{-T}\nabla\mathbf{u}^T + \mathbf{F}_g^2\mathbf{F}_0^{-1}\nabla\mathbf{u}\mathbf{F}_0^{-1}\nabla\mathbf{v}\mathbf{F}_0^{-1}$$
$$+\mathbf{F}_g^2\mathbf{F}_0^{-1}\nabla\mathbf{v}\mathbf{F}_0^{-1}\mathbf{F}_0^{-T}\nabla\mathbf{u}^T + \mathbf{F}_g^2\mathbf{F}_0^{-1}\mathbf{F}_0^{-T}\nabla\mathbf{u}^T\mathbf{F}_0^{-T}\nabla\mathbf{v}^T\Big)\mathbf{F}_0^{-T}$$
$$+\eta^{1+q}G_t\Big[qJ_0^{-q}\Big((\mathbf{F}_0^{-T} : \nabla\mathbf{v})\mathbf{F}_0^{-T}\nabla\mathbf{u}^T\mathbf{F}_0^{-T} + (\mathbf{F}_0^{-T} : \nabla\mathbf{u})\mathbf{F}_0^{-T}\nabla\mathbf{v}^T\mathbf{F}_0^{-T}\Big) +$$
$$J_0^{-q}\Big(\mathbf{F}_0^{-T}\nabla\mathbf{u}^T\mathbf{F}_0^{-T}\nabla\mathbf{v}^T\mathbf{F}_0^{-T} + \mathbf{F}_0^{-T}\nabla\mathbf{v}^T\mathbf{F}_0^{-T}\nabla\mathbf{u}^T\mathbf{F}_0^{-T}\Big) +$$
$$+q^2J_0^{-q}\left(\mathbf{F}_0^{-T} : \nabla\mathbf{u}\right)\left(\mathbf{F}_0^{-T} : \nabla\mathbf{v}\right)\mathbf{F}_0^{-T} + qJ_0^{-q}\left(\mathbf{F}_0^{-T}\nabla\mathbf{v}^T\mathbf{F}_0^{-T} : \nabla\mathbf{u}\right)\mathbf{F}_0^{-T}\Big]. \quad \text{(C.9)}$$

The third derivative is

$$\frac{\partial^3 \mathbf{P}}{\partial \mathbf{F}^3} = f\frac{\partial^3 \mathbf{P}_f}{\partial \mathbf{F}^3} + (1-f)\frac{\partial^3 \mathbf{P}_f}{\partial \mathbf{F}^3}, \quad \text{(C.10)}$$

where

$$\frac{\partial^3 \mathbf{P}_f}{\partial \mathbf{F}^3} : \nabla \mathbf{u} : \nabla \mathbf{u} : \nabla \mathbf{u} = q \left(\mathbf{F}_0^{-T} : \nabla \mathbf{u} \right) \frac{\partial^2 \mathbf{P}_f}{\partial \mathbf{F}^2} : \nabla \mathbf{u} : \nabla \mathbf{u} +$$

$$G_t \eta_0^{1-q} J_0^q \Big[6\mathbf{F}_0^{-T} \nabla \mathbf{u}^T \mathbf{F}_0^{-T} \nabla \mathbf{u}^T \mathbf{F}_0^{-T} \nabla \mathbf{u}^T \mathbf{F}_0^{-T} - 4q \left(\mathbf{F}_0^{-T} : \nabla \mathbf{u} \right) \mathbf{F}_0^{-T} \nabla \mathbf{u}^T \mathbf{F}_0^{-T} \nabla \mathbf{u}^T \mathbf{F}_0^{-T}$$

$$-3q \left(\left(\mathbf{F}_0^{-T} \nabla \mathbf{u}^T \mathbf{F}_0^{-T} \right) : \nabla \mathbf{u} \right) \mathbf{F}_0^{-T} \nabla \mathbf{u}^T \mathbf{F}_0^{-T} + 2q^2 \left(\left(\mathbf{F}_0^{-T} \nabla \mathbf{u}^T \mathbf{F}_0^{-T} \right) : \nabla \mathbf{u} \right) \left(\mathbf{F}_0^{-T} : \nabla \mathbf{u} \right) \mathbf{F}_0^{-T}$$

$$-2q \left(\left(\mathbf{F}_0^{-T} \nabla \mathbf{u}^T \mathbf{F}_0^{-T} \nabla \mathbf{u}^T \mathbf{F}_0^{-T} \right) : \nabla \mathbf{u} \right) \mathbf{F}_0^{-T} + \left(\mathbf{F}_0^{-T} : \nabla \mathbf{u} \right)^2 q^2 \mathbf{F}_0^{-T} \nabla \mathbf{u}^T \mathbf{F}_0^{-T} \Big]$$

$$\frac{\partial^3 \mathbf{P}_{1-f}}{\partial \mathbf{F}^3} : \nabla \mathbf{u} : \nabla \mathbf{u} : \nabla \mathbf{u} = 2\eta G_t \Big[3\mathbf{F}_0^{-T} \nabla \mathbf{u}^T \mathbf{F}_0^{-T} \nabla \mathbf{u}^T \mathbf{F}_0^{-T} \nabla \mathbf{u}^T \mathbf{F}_0^{-T} \mathbf{F}_g^2 \mathbf{F}_0^{-1} \mathbf{F}_0^{-T} +$$

$$\mathbf{F}_0^{-T} \nabla \mathbf{u}^T \mathbf{F}_0^{-T} \nabla \mathbf{u}^T \mathbf{F}_0^{-T} \mathbf{F}_g^2 \mathbf{F}_0^{-1} \nabla \mathbf{u} \mathbf{F}_0^{-1} \mathbf{F}_0^{-T} + \mathbf{F}_0^{-T} \nabla \mathbf{u}^T \mathbf{F}_0^{-T} \nabla \mathbf{u}^T \mathbf{F}_0^{-T} \mathbf{F}_g^2 \mathbf{F}_0^{-1} \mathbf{F}_0^{-T} \nabla \mathbf{u}^T \mathbf{F}_0^{-T} +$$

$$2\mathbf{F}_0^{-T} \nabla \mathbf{u}^T \mathbf{F}_0^{-T} \nabla \mathbf{u}^T \mathbf{F}_0^{-T} \mathbf{F}_g^2 \mathbf{F}_0^{-1} \nabla \mathbf{u} \mathbf{F}_0^{-1} \mathbf{F}_0^{-T} + \mathbf{F}_0^{-T} \nabla \mathbf{u}^T \mathbf{F}_0^{-T} \mathbf{F}_g^2 \mathbf{F}_0^{-1} \nabla \mathbf{u} \mathbf{F}_0^{-1} \nabla \mathbf{u} \mathbf{F}_0^{-1} \mathbf{F}_0^{-T}$$

$$+ \mathbf{F}_0^{-T} \nabla \mathbf{u}^T \mathbf{F}_0^{-T} \mathbf{F}_g^2 \mathbf{F}_0^{-1} \nabla \mathbf{u} \mathbf{F}_0^{-1} \nabla \mathbf{u} \mathbf{F}_0^{-1} \mathbf{F}_0^{-T} + \mathbf{F}_0^{-T} \nabla \mathbf{u}^T \mathbf{F}_0^{-T} \mathbf{F}_g^2 \mathbf{F}_0^{-1} \nabla \mathbf{u} \mathbf{F}_0^{-1} \mathbf{F}_0^{-T} \nabla \mathbf{u}^T \mathbf{F}_0^{-T} +$$

$$2\mathbf{F}_0^{-T} \nabla \mathbf{u}^T \mathbf{F}_0^{-T} \nabla \mathbf{u}^T \mathbf{F}_0^{-T} \mathbf{F}_g^2 \mathbf{F}_0^{-1} \mathbf{F}_0^{-T} \nabla \mathbf{u}^T \mathbf{F}_0^{-T} + \mathbf{F}_0^{-T} \nabla \mathbf{u}^T \mathbf{F}_0^{-T} \mathbf{F}_g^2 \mathbf{F}_0^{-1} \nabla \mathbf{u} \mathbf{F}_0^{-1} \mathbf{F}_0^{-T} \nabla \mathbf{u}^T \mathbf{F}_0^{-T} +$$

$$\mathbf{F}_0^{-T} \nabla \mathbf{u}^T \mathbf{F}_0^{-T} \mathbf{F}_g^2 \mathbf{F}_0^{-1} \mathbf{F}_0^{-T} \nabla \mathbf{u}^T \mathbf{F}_0^{-T} \nabla \mathbf{u}^T \mathbf{F}_0^{-T} + \mathbf{F}_0^{-T} \nabla \mathbf{u}^T \mathbf{F}_0^{-T} \mathbf{F}_g^2 \mathbf{F}_0^{-1} \mathbf{F}_0^{-T} \nabla \mathbf{u}^T \mathbf{F}_0^{-T} \nabla \mathbf{u}^T \mathbf{F}_0^{-T} +$$

$$\mathbf{F}_0^{-T} \nabla \mathbf{u}^T \mathbf{F}_0^{-T} \mathbf{F}_g^2 \mathbf{F}_0^{-1} \nabla \mathbf{u} \mathbf{F}_0^{-1} \nabla \mathbf{u} \mathbf{F}_0^{-1} \mathbf{F}_0^{-T} + 3\mathbf{F}_0^{-T} \mathbf{F}_g^2 \mathbf{F}_0^{-1} \nabla \mathbf{u} \mathbf{F}_0^{-1} \nabla \mathbf{u} \mathbf{F}_0^{-1} \nabla \mathbf{u} \mathbf{F}_0^{-1} \mathbf{F}_0^{-T}$$

$$+ \mathbf{F}_0^{-T} \mathbf{F}_g^2 \mathbf{F}_0^{-1} \nabla \mathbf{u} \mathbf{F}_0^{-1} \nabla \mathbf{u} \mathbf{F}_0^{-1} \mathbf{F}_0^{-T} \nabla \mathbf{u}^T \mathbf{F}_0^{-T}$$

$$\mathbf{F}_0^{-T} \nabla \mathbf{u}^T \mathbf{F}_0^{-T} \mathbf{F}_g^2 \mathbf{F}_0^{-1} \nabla \mathbf{u} \mathbf{F}_0^{-1} \mathbf{F}_0^{-T} \nabla \mathbf{u}^T \mathbf{F}_0^{-T} + 2\mathbf{F}_0^{-T} \mathbf{F}_g^2 \mathbf{F}_0^{-1} \nabla \mathbf{u} \mathbf{F}_0^{-1} \nabla \mathbf{u} \mathbf{F}_0^{-1} \mathbf{F}_0^{-T} \nabla \mathbf{u}^T \mathbf{F}_0^{-T} +$$

$$\mathbf{F}_0^{-T} \mathbf{F}_g^2 \mathbf{F}_0^{-1} \nabla \mathbf{u} \mathbf{F}_0^{-1} \mathbf{F}_0^{-T} \nabla \mathbf{u}^T \mathbf{F}_0^{-T} \nabla \mathbf{u}^T \mathbf{F}_0^{-T} + \mathbf{F}_0^{-T} \mathbf{F}_g^2 \mathbf{F}_0^{-1} \nabla \mathbf{u} \mathbf{F}_0^{-1} \mathbf{F}_0^{-T} \nabla \mathbf{u}^T \mathbf{F}_0^{-T} \nabla \mathbf{u}^T \mathbf{F}_0^{-T}$$

$$\mathbf{F}_0^{-T} \nabla \mathbf{u}^T \mathbf{F}_0^{-T} \mathbf{F}_g^2 \mathbf{F}_0^{-1} \mathbf{F}_0^{-T} \nabla \mathbf{u}^T \mathbf{F}_0^{-T} \nabla \mathbf{u}^T \mathbf{F}_0^{-T} + \mathbf{F}_0^{-T} \mathbf{F}_g^2 \mathbf{F}_0^{-1} \nabla \mathbf{u} \mathbf{F}_0^{-1} \mathbf{F}_0^{-T} \nabla \mathbf{u}^T \mathbf{F}_0^{-T} \nabla \mathbf{u}^T \mathbf{F}_0^{-T}$$

$$+ \mathbf{F}_0^{-T} \mathbf{F}_g^2 \mathbf{F}_0^{-1} \mathbf{F}_0^{-T} \nabla \mathbf{u}^T \mathbf{F}_0^{-T} \nabla \mathbf{u}^T \mathbf{F}_0^{-T} \nabla \mathbf{u}^T \mathbf{F}_0^{-T} \Big]$$

$$+ \eta^{1+q} G_t \Big[-3q^2 J_0^{-q} \left(\mathbf{F}_0^{-T} : \nabla \mathbf{u} \right)^2 \mathbf{F}_0^{-T} \nabla \mathbf{u}^T \mathbf{F}_0^{-T} - 3q J_0^{-q} \left(\mathbf{F}_0^{-T} \nabla \mathbf{u}^T \mathbf{F}_0^{-T} : \nabla \mathbf{u} \right) \mathbf{F}_0^{-T} \nabla \mathbf{u}^T \mathbf{F}_0^{-T}$$

$$- 6q J_0^{-q} \left(\mathbf{F}_0^{-T} : \nabla \mathbf{u} \right) \mathbf{F}_0^{-T} \nabla \mathbf{u}^T \mathbf{F}_0^{-T} \nabla \mathbf{u}^T \mathbf{F}_0^{-T} - 6J_0^{-q} \mathbf{F}_0^{-T} \nabla \mathbf{u}^T \mathbf{F}_0^{-T} \nabla \mathbf{u}^T \mathbf{F}_0^{-T} \nabla \mathbf{u}^T \mathbf{F}_0^{-T}$$

$$-3q^2 J_0^{-q} \left(\mathbf{F}_0^{-T} : \nabla \mathbf{u} \right) \left(\mathbf{F}_0^{-T} \nabla \mathbf{u}^T \mathbf{F}_0^{-T} : \nabla \mathbf{u} \right) \mathbf{F}_0^{-T} - 2q J_0^{-q} \left(\mathbf{F}_0^{-T} \nabla \mathbf{u}^T \mathbf{F}_0^{-T} \nabla \mathbf{u}^T \mathbf{F}_0^{-T} : \nabla \mathbf{u} \right) \mathbf{F}_0^{-T} \Big].$$

The instantaneous bulk modulus is

$$\frac{1}{9}P_{\alpha\alpha\beta\beta} = \frac{1}{9}G_t\Big[f\eta\zeta_\alpha^{-2} - f\eta^{-q}J_0^q(q-1)\left(F_{0,RR}^{-2}+F_{0,\Theta\Theta}^{-2}+F_{0,ZZ}^{-2}\right)$$
$$-2fq\eta^{1-q}J_0^q\left(F_{0,RR}^{-1}F_{0,\Theta\Theta}^{-1}+F_{0,RR}^{-1}F_{0,ZZ}^{-1}+F_{0,\Theta\Theta}^{-1}F_{0,ZZ}^{-1}\right)+$$
$$(1-f)\eta\Big(3\left(\zeta_R^2F_{0,RR}^{-4}+\zeta_\Theta^2F_{0,\Theta\Theta}^{-4}+\zeta_Z^2F_{0,ZZ}^{-4}\right)-\eta^qJ_0^{-q}(1+q)\left(F_{0,RR}^{-2}+F_{0,\Theta\Theta}^{-2}+F_{0,ZZ}^{-2}\right)$$
$$-2q\eta^{1+q}J_0^{-q}\left(F_{0,RR}^{-1}F_{0,\Theta\Theta}^{-1}+F_{0,RR}^{-1}F_{0,ZZ}^{-1}+F_{0,\Theta\Theta}^{-1}F_{0,ZZ}^{-1}\right)\Big)\Big],$$

where we sum over α and β. We use the following expressions to evaluate $\nabla\cdot\frac{\partial\mathbf{P}}{\partial\zeta_\alpha}\delta\zeta_\alpha$,

$$\frac{\partial}{\partial R}\left(\frac{\partial\mathbf{P}}{\partial\zeta_\alpha}\delta\zeta_\alpha\right)|_{RR} = \frac{\partial\eta}{\partial R}G_tf\left(-2F_{0,RR}\zeta_R^{-3}\delta\zeta_R+q\eta^{-q-1}J_0^qF_{0,RR}^{-1}\delta\eta\right)$$
$$+\eta G_tf\left(-2F_{0,RR}\zeta_R^{-3}\frac{\partial(\delta\zeta_R)}{\partial R}+6F_{0,RR}\zeta_R^{-4}\frac{\partial\zeta_R}{\partial R}\delta\zeta_R-2\frac{\partial^2u_0}{\partial R^2}\zeta_R^{-3}\delta\zeta_R-q(q+1)\eta^{-q-2}\frac{\partial\eta}{\partial R}J_0^qF_{0,RR}^{-1}\delta\eta\right.$$
$$\left.+q^2\eta^{-q-1}J_0^{q-1}\frac{\partial J_0}{\partial R}F_{0,RR}^{-1}\delta\eta-q\eta^{-q-1}J_0^qF_{0,RR}^{-2}\frac{\partial^2u_0}{\partial R^2}\delta\eta+q\eta^{-q-1}J_0^qF_{0,RR}^{-1}\frac{\partial\delta\eta}{\partial R}\right)$$
$$+G_tf\frac{\partial\delta\eta}{\partial R}\left(F_{0,RR}\zeta_R^{-2}-\eta^{-q}J_0^qF_{0,RR}^{-1}\right)$$
$$+G_tf\delta\eta\left(\frac{\partial^2u_0}{\partial R^2}\zeta_R^{-2}-2F_{0,RR}\zeta_R^{-3}\frac{\partial\zeta_R}{\partial R}+J^q\eta^{-q}F_{0,RR}^{-2}\frac{\partial^2u_0}{\partial R^2}-qJ^{q-1}\eta^{1-q}\frac{\partial(J/\eta)}{\partial R}F_{0,RR}^{-1}\right)$$
$$-\frac{\partial\eta}{\partial R}G_t(1-f)\left(2\zeta_R\delta\zeta_RF_{0,RR}^{-3}-q\eta^{q-1}\delta\eta J_0^{-q}F_{0,RR}^{-1}\right)$$
$$-\eta G_t(1-f)\left(2\frac{\partial\zeta_R}{\partial R}\delta\zeta_RF_{0,RR}^{-3}+2\zeta_R\frac{\partial\delta\zeta_R}{\partial R}F_{0,RR}^{-3}-6\zeta_R\delta\zeta_RF_{0,RR}^{-4}\frac{\partial^2u_0}{\partial R^2}-q(q-1)\eta^{q-2}\frac{\partial\eta}{\partial r}\delta\eta J_0^{-q}F_{0,RR}^{-1}\right.$$
$$\left.-q\eta^{q-1}\frac{\partial\delta\eta}{\partial R}J_0^{-q}F_{0,RR}^{-1}+q^2\eta^{q-1}\delta\eta J_0^{-q-1}\frac{\partial J_0}{\partial R}F_{0,RR}^{-1}+q\eta^{q-1}\delta\eta J_0^{-q}F_{0,RR}^{-2}\frac{\partial^2u_0}{\partial R^2}\right)$$
$$-G_t(1-f)\frac{\partial(\delta\eta)}{\partial R}\left(F_{0,RR}^{-3}\zeta_R^2-\eta^qJ_0^{-q}F_{0,RR}^{-1}\right)$$
$$-\delta\eta G_t(1-f)\left(-3F_{0,RR}^{-4}\frac{\partial^2u_0}{\partial R^2}\zeta_R^2+2F_{0,RR}^{-3}\zeta_R\frac{\partial\zeta_R}{\partial R}\right.$$
$$\left.+qJ_0^{-q-1}\eta^{q+1}\frac{\partial(J_0/\eta)}{\partial R}F_{0,RR}^{-1}+(J_0/\eta)^{-q}F_{0,RR}^{-2}\frac{\partial^2u_0}{\partial R^2}\right)\quad\text{(C.11)}$$

and

$$\left(\frac{\partial \mathbf{P}}{\partial \zeta_\alpha}\delta\zeta_\alpha\right)|_{RR} - \left(\frac{\partial \mathbf{P}}{\partial \zeta_\alpha}\delta\zeta_\alpha\right)|_{\Theta\Theta} = \eta G_t f\left(-2\left(F_{0,RR}\zeta_R^{-3}\delta\zeta_R - F_{0,\Theta\Theta}\zeta_\Theta^{-3}\delta\zeta_\Theta\right)\right.$$
$$\left.+q\eta^{-q-1}J_0^q\delta\eta\left(F_{0,RR}^{-1} - F_{0,\Theta\Theta}^{-1}\right)\right)+\delta\eta G_t f\left(F_{0,RR}\zeta_R^{-2} - F_{0,\Theta\Theta}\zeta_\Theta^{-2} - \eta^{-q}J_0^q\left(F_{0,RR}^{-1} - F_{0,\Theta\Theta}^{-1}\right)\right)$$
$$- \eta G_t(1-f)\left(2\left(F_{0,RR}^{-3}\zeta_R\delta\zeta_R - F_{0,\Theta\Theta}^{-3}\zeta_\Theta\delta\zeta_\Theta\right) - q\eta^{q-1}\delta\eta J_0^{-q}\left(F_{0,RR}^{-1} - F_{0,\Theta\Theta}^{-1}\right)\right)$$
$$- \delta\eta G_t(1-f)\left(\zeta_R^2 F_{0,RR}^{-3} - \zeta_\Theta^2 F_{0,\Theta\Theta}^{-3} - \eta^q J_0^{-q}\left(F_{0,RR}^{-1} - F_{0,\Theta\Theta}^{-1}\right)\right). \quad \text{(C.12)}$$

C.0.14 Incompressible Neo-Hookean Model

The strain energy function is

$$\psi = \frac{G_c}{2}(I_1 - 3) - p(J-1), \quad \text{(C.13)}$$

where p is a Lagrange Multiplier enabling the incompressibility constraint

$$J - 1 = 0 \quad \text{(C.14)}$$

and I_1 is the first invariant of $\mathbf{C} = \mathbf{F}^T \cdot \mathbf{F}$. We differentiate with respect to $\mathbf{F}$ to obtain the first Piola-Kirchhoff stress

$$\mathbf{P} = G_c\mathbf{F} - pJ\mathbf{F}^{-T}. \quad \text{(C.15)}$$

The increment in the incompressibility condition (C.14) is

$$\mathbf{F}_0^{-T} : \nabla\mathbf{u} = 0. \quad \text{(C.16)}$$

The increment in the Piola Kirchhoff Stress corresponding to an increment $\mathbf{u}$ in the displacment and the Lagrange Multiplier is

$$\frac{\partial \mathbf{P}}{\partial \mathbf{F}} : \nabla\mathbf{u} = G_c\nabla\mathbf{u} - pJ_0\left((\mathbf{F}_0^{-T} : \nabla\mathbf{u})\mathbf{F}_0^{-T} - \mathbf{F}_0^{-T}\nabla\mathbf{u}^T\mathbf{F}_0^{-T}\right),$$
$$\frac{\partial \mathbf{P}}{\partial p} = -J_0\mathbf{F}_0^{-T}. \quad \text{(C.17)}$$

We may thus write the increment in the first Piola-Kirchhoff stress, for a displacement satisfying (C.16), as

$$\left(\frac{\partial \mathbf{P}}{\partial \mathbf{F}} : \nabla \mathbf{u} + \frac{\partial \mathbf{P}}{\partial p}\delta p\right) \cdot \mathbf{e}_R = \begin{pmatrix} a\nabla \mathbf{u}_{RR} + b\nabla \mathbf{u}_{\Theta\Theta} + g\delta p \\ c\nabla \mathbf{u}_{\Theta R} + d\nabla \mathbf{u}_{R\Theta} \\ c\nabla \mathbf{u}_{ZR} + d\nabla \mathbf{u}_{RZ} \end{pmatrix}, \tag{C.18}$$

where $a = G_c$, $b = -p$, $c = G_c$, $d = p$, $g = -F^{-1}_{0,RR}$. The second increment in the Piola Kirchhoff Stress, corresponding to a second increment $\mathbf{v}$ in the displacement is

$$\begin{aligned}\frac{\partial^2 \mathbf{P}}{\partial \mathbf{F}^2} : \nabla \mathbf{u} : \nabla \mathbf{v} = -pJ_0 \Big[&(\mathbf{F}_0^{-T} : \nabla \mathbf{v})(\mathbf{F}_0^{-T} : \nabla \mathbf{u})\mathbf{F}_0^{-T} - (\mathbf{F}_0^{-T}\nabla \mathbf{v}^T\mathbf{F}_0^{-T} : \nabla \mathbf{u})\mathbf{F}_0^{-T} \\ &- (\mathbf{F}_0^{-T} : \nabla \mathbf{u})\mathbf{F}_0^{-T}\nabla \mathbf{v}^T\mathbf{F}_0^{-T} - (\mathbf{F}_0^{-T} : \nabla \mathbf{v})\mathbf{F}_0^{-T}\nabla \mathbf{u}^T\mathbf{F}_0^{-T} \\ &+\mathbf{F}_0^{-T}\nabla \mathbf{v}^T\mathbf{F}_0^{-T}\nabla \mathbf{u}^T\mathbf{F}_0^{-T} + \mathbf{F}_0^{-T}\nabla \mathbf{u}^T\mathbf{F}_0^{-T}\nabla \mathbf{v}^T\mathbf{F}_0^{-T}\Big].\end{aligned}$$

The second increment in the Piola Kirchhoff Stress is

$$\frac{\partial^2 \mathbf{P}}{\partial \mathbf{F}\partial p} : \nabla \mathbf{u} = J_0\left(-(\mathbf{F}_0^{-T} : \nabla \mathbf{u})\mathbf{F}_0^{-T} + \mathbf{F}_0^{-T}\nabla \mathbf{u}^T\mathbf{F}_0^{-T}\right).$$

For an incremental displacement $\mathbf{u}$ satisfying the incompressibility constraint (C.16), the third increment in the Piola-Kirchhoff stress is

$$\begin{aligned}\frac{\partial^3 \mathbf{P}}{\partial \mathbf{F}^3} : \nabla \mathbf{u} : \nabla \mathbf{u} : \nabla \mathbf{u} = -p\Big[&2\mathbf{F}_0^{-T}(\mathbf{F}_0^{-T}\nabla \mathbf{u}^T\mathbf{F}_0^{-T}\nabla \mathbf{u}^T\mathbf{F}_0^{-T}) : \nabla \mathbf{u} \\ &+3\left((\mathbf{F}_0^{-T}\nabla \mathbf{u}^T\mathbf{F}_0^{-T}) : \nabla \mathbf{u}\right)\mathbf{F}_0^{-T}\nabla \mathbf{u}^T\mathbf{F}_0^{-T} \\ &-6\mathbf{F}_0^{-T}\nabla \mathbf{u}^T\mathbf{F}_0^{-T}\nabla \mathbf{u}^T\mathbf{F}_0^{-T}\nabla \mathbf{u}^T\mathbf{F}_0^{-T}\Big], \\ \frac{\partial^3 \mathbf{P}}{\partial \mathbf{F}^2\partial p} : \nabla \mathbf{u} : \nabla \mathbf{u} = \Big[&\left((\mathbf{F}_0^{-T}\nabla \mathbf{u}^T\mathbf{F}_0^{-T}) : \nabla \mathbf{u}\right)\mathbf{F}_0^{-T} - 2\mathbf{F}_0^{-T}\nabla \mathbf{u}^T\mathbf{F}_0^{-T}\nabla \mathbf{u}^T\mathbf{F}_0^{-T}\Big].\end{aligned}$$

Appendix D

Supplement on Numerical Solution

D.1 Numerical Solution of First Order Incremental Equations

We outline the structure of some of the matrices defined in Section 7. The nonzero components of $\mathbf{L}_c^{n,\omega}$ are as follows,

$$L_{11} = -R^{-1}F_{0,RR}^2$$

$$L_{13} = -nR^{-1}F_{0,RR}^2$$

$$L_{15} = -F_{0,RR}\omega$$

$$G_c^{-1}F_{0,\Theta\Theta}L_{21} = -n^2R^{-2} - R^{-2} - G_c^{-1}R^{-1}\frac{\partial p_0}{\partial R} - \omega^2 - 2R^{-1}F_{0,RR}\frac{\partial^2 u_0}{\partial R^2} + R^{-2}F_{0,RR}^4$$

$$G_c^{-1}F_{0,\Theta\Theta}L_{23} = -2nR^{-2} - nG_c^{-1}R^{-1}\frac{\partial p_0}{\partial R} - 2nR^{-1}F_{0,RR}\frac{\partial^2 u_0}{\partial R^2} + nR^{-2}F_{0,RR}^4$$

$$G_c^{-1}F_{0,\Theta\Theta}L_{24} = -nR^{-1}F_{0,RR}^2$$

$$F_{0,\Theta\Theta}L_{25} = \omega\left(G_c + p_0F_{0,RR}^{-2}\right)\left(R^{-1}F_{0,RR}^3 - \frac{\partial^2 u_0}{\partial R^2}\right)$$

$$-\omega F_{0,RR}\left(\frac{\partial p_0}{\partial R}F_{0,RR}^{-2} - \frac{2p_0}{F_{0,RR}^3}\frac{\partial^2 u_0}{\partial R^2} + \frac{p_0}{R}F_{0,\Theta\Theta}^2 + GR^{-1}\right)$$

$$G_c^{-1}F_{0,\Theta\Theta}L_{26} = -\omega F_{0,RR}$$

$$L_{34} = 1$$

$$
\begin{aligned}
L_{41} &= n\left(2R^{-2} + G_c^{-1}R^{-1}\frac{\partial p_0}{\partial R}\right) \\
L_{42} &= -nF_{0,RR}R^{-1}G_c^{-1} \\
L_{43} &= n^2R^{-2} + R^{-2} + G_c^{-1}R^{-1}\frac{\partial p_0}{\partial R} + \omega^2 \\
L_{44} &= -R^{-1} \\
L_{56} &= 1 \\
L_{61} &= \omega G_c^{-1}\frac{\partial p}{\partial R}F_{0,\Theta\Theta} \\
L_{62} &= -\omega G_c^{-1} \\
L_{65} &= n^2R^{-2} + \omega^2 \\
L_{66} &= -R^{-1}.
\end{aligned} \tag{D.1}
$$

The matrices $\mathbf{P}_{inc}^{n,\omega,-}$ and $\mathbf{P}_{inc}^{n,\omega,+}$ are

$$\mathbf{P}_{inc}^{n,\omega,-} = \begin{pmatrix} -\frac{G_c}{R}F_{0,RR}^2 - \frac{p_0}{R} & -F_{0,\Theta\Theta} & -\frac{n}{R}\left(G_cF_{0,RR}^2 + p_0\right) & 0 & -\omega\left(F_{0,RR}G_c + p_0F_{0,RR}^{-1}\right) & 0 \\ -\frac{n}{R}p_0 & 0 & -\frac{p_0}{R} & G_c & 0 & 0 \\ -p_0\omega F_{0,RR}^{-1} & 0 & 0 & 0 & 0 & G_c \\ 1 & 0 & 0 & 0 & 0 & 0 \\ 0 & 0 & 1 & 0 & 0 & 0 \\ 0 & 0 & 0 & 0 & 1 & 0 \end{pmatrix} \tag{D.2}$$

$$\mathbf{P}_{n,\omega}^{(-)-1} = \begin{pmatrix} 0 & 0 & 0 & 1 & 0 & 0 \\ -F_{0,RR} & 0 & 0 & -\frac{F_{0,RR}}{R}(G_cF_{0,RR}^2 + p_0) & -\frac{n}{R}F_{0,RR}(G_cF_{0,RR}^2 + p_0) & -\omega(F_{0,RR}^2G_c + p_0) \\ 0 & 0 & 0 & 0 & 1 & 0 \\ 0 & G_c^{-1} & 0 & \frac{n}{RG_c}p_0 & \frac{p_0}{RG_c} & 0 \\ 0 & 0 & 0 & 0 & 0 & 1 \\ 0 & 0 & G_c^{-1} & \frac{p_0}{G_c}\omega F_{0,\Theta\Theta} & 0 & 0 \end{pmatrix} \tag{D.3}$$

$$\mathbf{P}_{inc}^{n,\omega,+} = \begin{pmatrix} R^{-1}P_{RR\Theta\Theta} & P_{RRRR} & nR^{-1}P_{RR\Theta\Theta} & 0 & \omega P_{RRZZ} & 0 \\ -nR^{-1}P_{\Theta RR\Theta} & 0 & -R^{-1}P_{\Theta RR\Theta} & P_{\Theta R\Theta R} & 0 & 0 \\ -\omega P_{ZRRZ} & 0 & 0 & 0 & 0 & P_{ZRZR} \\ 1 & 0 & 0 & 0 & 0 & 0 \\ 0 & 0 & 1 & 0 & 0 & 0 \\ 0 & 0 & 0 & 0 & 1 & 0 \end{pmatrix}. \tag{D.4}$$

D.2 Numerical Solution of Second Order Equations

We outline the method of solution of $\mathbf{u}_2^a$. We expect $\mathbf{u}_2^a$ to be highly unstable for large n or large ω because it is proportional to terms quadratic in $\nabla\mathbf{u}^{(n,\omega)}$, which we saw in Section

7 is highly unstable. We must therefore also employ the method of compound matrices to accurately solve for $\mathbf{u}_2^a$. We firstly recall the equations governing $\mathbf{u}_2^a$, i.e.

$$\nabla \cdot \frac{\partial \mathbf{P}}{\partial \mathbf{F}} : \nabla \mathbf{u}_2^a = -\nabla \cdot \frac{\partial^2 \mathbf{P}}{\partial \mathbf{F}^2} : \nabla \mathbf{u}^{(n,\omega)} : \nabla \mathbf{u}^{(n,\omega)}. \tag{D.5}$$

If we are employing a finite geometry with a null-displacement (models A and E) at R_2, then $\mathbf{u}_2^a = 0$ at $R = R_2$. For models B and D, the boundary condition at R_2 is

$$\left(\frac{\partial \mathbf{P}}{\partial \mathbf{F}} : \nabla \mathbf{u}_2^a + \frac{\partial^2 \mathbf{P}}{\partial \mathbf{F}^2} : \nabla \mathbf{u}^{(n,\omega)} : \nabla \mathbf{u}^{(n,\omega)} \right) \cdot \mathbf{n} = \mathbf{0}. \tag{D.6}$$

If the geometry is infinite, then $\mathbf{u}_2^a \to \mathbf{0}$ as $R \to \infty$.

For a vector $\mathbf{v}$, we define $\mathbf{v}|_{n,\omega}$ to be $(v_1^*, v_2^*, v_3^*)^T$, where

$$(v_1^* \cos n\Theta \cos \omega Z, v_2^* \sin n\Theta \cos \omega Z, v_3^* \cos n\Theta \sin \omega Z)^T$$

is the projection of $\mathbf{v}$ onto $U_{n,\omega}$. We decompose $\mathbf{u}_2^a$ into its components with azimuthal modes 0 and $2n$ and axial modes 0 and 2ω, i.e.

$$\tilde{\mathbf{u}}_{2,a,b} = \left(W_{2,a,b}, W'_{2,a,b}, V_{2,a,b}, V'_{2,a,b}, Z_{2,a,b}, Z'_{2,a,b}\right)^T \text{ where} \tag{D.7}$$

$$\mathbf{u}_2^a|_{a,b} = (W_{2,a,b}, V_{2,a,b}, Z_{2,a,b})^T. \tag{D.8}$$

Note that if $\omega = 0$ then $\tilde{\mathbf{u}}_{2,2n,2w} = \tilde{\mathbf{u}}_{2,2n,0}$ and $\tilde{\mathbf{u}}_{2,0,2\omega} = \tilde{\mathbf{u}}_{2,0,0}$, so that we need only solve for $\tilde{\mathbf{u}}_{2,2n,0}$ and $\tilde{\mathbf{u}}_{2,0,0}$. A similar result holds if $n = 0$. However throughout this section we assume $n \neq 0$ and $\omega \neq 0$ so that we may solve the system in its full generality.

We obtain the following four ordinary differential equations over V_m,

$$\tilde{\mathbf{u}}'_{2,0,0} = \mathbf{L}^{0,0} \cdot \tilde{\mathbf{u}}_{2,0,0} + \mathbf{f}_{0,0}, \tag{D.9}$$

$$\tilde{\mathbf{u}}'_{2,2n,0} = \mathbf{L}^{2n,0} \cdot \tilde{\mathbf{u}}_{2,2n,0} + \mathbf{f}_{2n,0}, \tag{D.10}$$

$$\tilde{\mathbf{u}}'_{2,0,2\omega} = \mathbf{L}^{0,2\omega} \cdot \tilde{\mathbf{u}}_{2,0,2\omega} + \mathbf{f}_{0,2\omega}, \tag{D.11}$$

$$\tilde{\mathbf{u}}'_{2,2n,2\omega} = \mathbf{L}^{2n,2\omega} \cdot \tilde{\mathbf{u}}_{2,2n,2\omega} + \mathbf{f}_{2n,2\omega}. \tag{D.12}$$

Elements $\{1,3,5\}$ of $\mathbf{f}_{a,b}$ are zero. The other elements are given by

$$\begin{pmatrix} f_{a,b,2} \\ f_{a,b,4} \\ f_{a,b,6} \end{pmatrix} = -\mathbf{T}^{-1} \cdot \left(\nabla \cdot \left(\frac{\partial^2 \mathbf{P}}{\partial \mathbf{F}^2} : \nabla \mathbf{u}^{(n,\omega)} : \nabla \mathbf{u}^{(n,\omega)} \right) \right) |_{a,b}, \tag{D.13}$$

where $\mathbf{T}$ is given in (4.31). The matrices $\{\mathbf{L}^{a,b} | a = 0, 2n \text{ and } b = 0, 2\omega\}$ are of the same form as $\mathbf{L}$ in (7.1), except $n \to a$ and $\omega \to b$.

It should be noted that the azimuthal component of $\mathbf{u}_{2,0,2\omega}$ is trivially zero, so we may regard $\tilde{\mathbf{u}}_{2,0,2\omega}$ as a vector of length 4. Also the axial component of $\mathbf{u}_{2,2n,0}$ is trivially zero, so we may also regard $\tilde{\mathbf{u}}_{2,2n,0}$ as a vector of length 4. Finally the axial and aximuthal components of $\mathbf{u}_{2,0,0}$ are both trivially zero, so we may regard $\tilde{\mathbf{u}}_{2,0,0}$ as a vector of length 2.

The equations over the capillary wall V_c have a very similar format. We write

$$\tilde{\mathbf{u}}_{2,a,b} = \left(W_{2,a,b}, X_{2,a,b}, V_{2,a,b}, V'_{2,a,b}, Z_{2,a,b}, Z'_{2,a,b} \right)^T \text{ where ,} \tag{D.14}$$

$$\mathbf{u}^a_2|_{a,b} = (W_{2,a,b}, V_{2,a,b}, Z_{2,a,b}), \tag{D.15}$$

$$p^a_2 = X_{2,0,0} + X_{2,2n,0} \cos 2n\Theta + X_{2,0,2\omega} \cos 2\omega Z + X_{2,2n,2\omega} \cos 2n\Theta \cos 2\omega\Theta. \tag{D.16}$$

The derivative of $W_{2,a,b}$ is obtained from the incompressibility condition; the derivative of $V'_{2,a,b}$ from the azimuthal component of the equation of equilibrium; the derivative of $X_{2,a,b}$ is obtained from the radial component of the equation of equilibrium, and the derivative of $Z_{2,a,b}$ is obtained from the axial component of the equation of equilibrium. We obtain explicit expressions for these equations as follows.

The increment in the incompressibility condition amounts to

$$\frac{\partial W_{2,a,b}}{\partial R} = -F^2_{0,RR} R^{-1} \left(a V_{2,a,b} + W_{2,a,b} \right) - b F_{0,RR} Z_{2,a,b} + \left(F_{0,RR} \left(\mathbf{F}_0^{-T} \left(\nabla \mathbf{u}^{(n,\omega)} \right)^T \mathbf{F}_0^{-T} \right) : \nabla \mathbf{u}^{(n,\omega)} \right) |_{a,b}. \tag{D.17}$$

We differentiate this and substitute $\frac{\partial W_{2,a,b}}{\partial R}$, obtaining

$$\frac{\partial^2 W_{2,a,b}}{\partial R^2} = -R^{-1}F_{0,RR}^2 a\frac{\partial V_{2,a,b}}{\partial R}+(aV_{2,a,b}+W_{2,a,b})\left(R^{-2}F_{0,RR}^2-2R^{-1}F_{0,RR}\frac{\partial^2 u_0}{\partial R^2}+R^{-2}F_{0,RR}^4\right)$$
$$+bR^{-1}\left(1+\frac{\partial u_0}{\partial R}\right)^3 Z_{a,b}-b\left(\frac{\partial^2 u_0}{\partial R^2}Z_{a,b}+\left(1+\frac{\partial u_0}{\partial R}\right)Z'_{a,b}\right)$$
$$-R^{-1}F_{0,RR}^3\left(\mathbf{F}_0^{-T}\left(\nabla\mathbf{u}^{(n,\omega)}\right)^T\mathbf{F}_0^{-T}\right):\nabla\mathbf{u}^{(n,\omega)}|_{a,b}+\frac{\partial}{\partial R}\left[F_{0,RR}\left(\mathbf{F}_0^{-T}\left(\nabla\mathbf{u}^{(n,\omega)}\right)^T\mathbf{F}_0^{-T}\right):\nabla\mathbf{u}^{(n,\omega)}\right]|_{a,b}. \tag{D.18}$$

The ordinary differential equations over the capillary are of the form

$$\tilde{\mathbf{u}}'_{2,0,0}=\mathbf{L}_c^{0,0}\cdot\tilde{\mathbf{u}}_{2,0,0}+\mathbf{f}|_{0,0}, \tag{D.19}$$
$$\tilde{\mathbf{u}}'_{2,2n,0}=\mathbf{L}_c^{2n,0}\cdot\tilde{\mathbf{u}}_{2,2n,0}+\mathbf{f}|_{2n,0}, \tag{D.20}$$
$$\tilde{\mathbf{u}}'_{2,0,2\omega}=\mathbf{L}_c^{0,2\omega}\cdot\tilde{\mathbf{u}}_{2,0,2\omega}+\mathbf{f}|_{0,2\omega}, \tag{D.21}$$
$$\tilde{\mathbf{u}}'_{2,2n,2\omega}=\mathbf{L}_c^{2n,2\omega}\cdot\tilde{\mathbf{u}}_{2,2n,2\omega}+\mathbf{f}|_{2n,2\omega}. \tag{D.22}$$

It can be seen that the structure of $\mathbf{L}_c^{a,b}$ is the same as in (7.2), except $n\to a$ and $\omega\to b$. The components of $\mathbf{f}$ (over the capillary) are

$$f_1=F_{0,RR}\left(\mathbf{F}_0^{-T}\left(\nabla\mathbf{u}^{(n,\omega)}\right)^T\mathbf{F}_0^{-T}\right):\nabla\mathbf{u}^{(n,\omega)}, \tag{D.23}$$
$$f_3=0, \tag{D.24}$$
$$f_5=0, \tag{D.25}$$
$$\begin{pmatrix}-G_c^{-1}F_{0,\Theta\Theta}f_2\\ f_4\\ f_6\end{pmatrix}=-G_c^{-1}\nabla\cdot\left(\frac{\partial^2\mathbf{P}}{\partial\mathbf{F}^2}:\nabla\mathbf{u}^{(n,\omega)}:\nabla\mathbf{u}^{(n,\omega)}+2\frac{\partial^2\mathbf{P}}{\partial\mathbf{F}^2}:\nabla\mathbf{u}^{(n,\omega)}p^{(n,\omega)}\right), \tag{D.26}$$
$$+\begin{pmatrix}R^{-1}F_{0,RR}^3\left(\mathbf{F}_0^{-T}\left(\nabla\mathbf{u}^{(n,\omega)}\right)^T\mathbf{F}_0^{-T}\right):\nabla\mathbf{u}^{(n,\omega)}-R^{-1}\frac{\partial}{\partial R}\left[RF_{0,RR}\left(\mathbf{F}_0^{-T}\left(\nabla\mathbf{u}^{(n,\omega)}\right)^T\mathbf{F}_0^{-T}\right):\nabla\mathbf{u}^{(n,\omega)}\right]\\ 0\\ 0\end{pmatrix} \tag{D.27}$$

For $a \in \{0, 2n\}$ and $b \in \{0, 2\omega\}$, the boundary condition at $R = R_1$ is

$$\tilde{\mathbf{u}}^{-}_{2,a,b} = \mathbf{Q}^{a,b}_{inc} \cdot \tilde{\mathbf{u}}_{2,a,b} + \left(\mathbf{P}^{a,b}_{capinc}\right)^{-1} \cdot \mathbf{p}_1|_{a,b}, \tag{D.28}$$

where the vector $\mathbf{p}_1$ is given by

$$\mathbf{p}_1 = \begin{pmatrix} -G_c F_{0,RR} \left(\mathbf{F}_0^{-T} \left(\nabla \mathbf{u}^{(n,\omega)}\right)^T \mathbf{F}_0^{-T}\right) : \nabla \mathbf{u}^{(n,\omega)} \\ 0 \\ 0 \\ 0 \\ 0 \\ 0 \end{pmatrix} + \begin{pmatrix} \left(\frac{\partial^2 \mathbf{P}}{\partial \mathbf{F}^2} : \nabla \mathbf{u}^{(n,\omega)} : \nabla \mathbf{u}^{(n,\omega)}|_+ - \frac{\partial^2 \mathbf{P}}{\partial \mathbf{F}^2} : \nabla \mathbf{u}^{(n,\omega)} : \nabla \mathbf{u}^{(n,\omega)}|_- - 2\frac{\partial^2 \mathbf{P}}{\partial \mathbf{F} \partial p} : \nabla \mathbf{u}^{(n,\omega)} p^{(n,\omega)}|_-\right) \cdot \mathbf{n} \\ 0 \\ 0 \\ 0 \end{pmatrix}. \tag{D.29}$$

The matrices $\mathbf{Q}^{a,b}_{inc}$ and $\mathbf{P}^{a,b}_{capinc}$ are both defined in Section 7. The boundary condition at R_0 is

$$\mathbf{P}^{a,b}_{inc} \cdot \tilde{\mathbf{u}}_{2,a,b} = \mathbf{p}_0|_{a,b}, \tag{D.30}$$

where

$$\mathbf{p}_0 = \begin{pmatrix} -G_c F_{0,RR} \left(\mathbf{F}_0^{-T} : \left(\nabla \mathbf{u}^{(n,\omega)}\right)^T \mathbf{F}_0^{-T}\right) : \nabla \mathbf{u}^{(n,\omega)} \\ 0 \\ 0 \end{pmatrix} - \left(\frac{\partial^2 \mathbf{P}}{\partial \mathbf{F}^2} : \nabla \mathbf{u}^{(n,\omega)} : \nabla \mathbf{u}^{(n,\omega)}|_- + 2\frac{\partial^2 \mathbf{P}}{\partial \mathbf{F} \partial p} : \nabla \mathbf{u}^{(n,\omega)} p^{(n,\omega)}|_-\right) \cdot \mathbf{n}. \tag{D.31}$$

The matrix $\mathbf{P}^{a,b}_{inc}$ is defined in Section 7.

Solution of $\mathbf{u}_{2,2n,2\omega}$ using Method of Compound Matrices

We use the method of compound matrices to solve the equations in (D.12). The reason we use this method is that $\mathbf{u}_{2,a,b}$ is even more unstable that $\mathbf{u}^{(n,\omega)}$ because it is proportional to the square of $\nabla\mathbf{u}^{(n,\omega)}$. We restrict ourselves to outlining the solution of $\mathbf{u}_{2,2n,2\omega}$ - the method of numerical solution of the other variables is very similar. We also restrict ourselves to outlining the method of solution for the composite model (with a distinct capillary wall structure with geometry V_c).

We may write the general solution of (D.12) as

$$\mathbf{u}_{2,2n,2\omega} = \mathbf{U}\cdot\mathbf{c} + \mathbf{g}, \tag{D.32}$$

where $\mathbf{g}$ satisfies (D.12) and the boundary condition at R_2 (in the case of an infinite annulus, $\mathbf{g}\to\mathbf{0}$ as $R\to\infty$). Here $\mathbf{U}$ is the 6×3 solution matrix satisfying

$$\mathbf{U}' = \mathbf{L}^{2n,2\omega}\cdot\mathbf{U}. \tag{D.33}$$

In the case of a finite geometry, $\mathbf{U}$ satisfies the boundary condition at R_2. If the geometry is infinite, $\mathbf{U}\to 0$ as $R\to\infty$. In this latter case we determine the behaviour of $\mathbf{U}$ for large R using the method outlined in Section 7.1.2.

Let $\{y_{ijk}|1\le i<j<k\le 6\}$ be the twenty minors of $\mathbf{U}$. Here y_{ijk} is the determinant of rows $\{i,j,k\}$ of $\mathbf{U}$. We let $\{z_{ijkl}\}$ be the fifteen minors of the form

$$z_{ijkl} = g_i y_{jkl} - g_j y_{kli} + g_k y_{lij} - g_l y_{ijk}. \tag{D.34}$$

The evolution of $\mathbf{y}$ and $\mathbf{z}$ is governed by equations of the form

$$\mathbf{y}' = \mathbf{B}\cdot\mathbf{u}, \tag{D.35}$$

$$\mathbf{z}' = \mathbf{C}\cdot\mathbf{z} + \mathbf{D}\cdot\mathbf{f}. \tag{D.36}$$

The structure of the matrices $\mathbf{B}$,$\mathbf{C}$ and $\mathbf{D}$ is given in [107]. We may also define the minors $\mathbf{y}_c$ and $\mathbf{z}_c$ over the capillary in an analogous way. Our method of solution is to integrate the minors from R_2 (R_u in the case of an infinite geometry) to R_0, and then use the minors

to determine $\tilde{\mathbf{u}}$ at R_0 and integrate this from R_0 back to R_2.

We write the boundary condition at R_1 (D.28) as

$$\left(\mathbf{g}^- - \mathbf{q}, \mathbf{U}\right) = \mathbf{Q}_{inc}^{2n,2\omega} \cdot \left(\mathbf{g}^+, \mathbf{U}\right), \tag{D.37}$$

where $\mathbf{q} = \left(\mathbf{P}_{capinc}^{2n,2\omega}\right)^{-1} \cdot \mathbf{p}_1|_{2n,2\omega}$. We use Laplace's determinant identity to write this in terms of $\mathbf{z}_c$ and $\mathbf{z}$ as follows. We let $\mathbf{Q}_{ijkl}$ be the 4×6 matrix composed of the (i, j, k, l) rows of $\mathbf{Q}_{inc}^{2n,2\omega}$. We write the fifteen minors of $\mathbf{Q}_{ijkl}$ as $\{Q_{ijkl,mnop}\}$, where the (m, n, o, p) minor is the determinant of columns (m, n, o, p) of $\mathbf{Q}_{ijkl}$. Applying Laplace's determinant identity to rows $\{i, j, k, l\}$ of (D.37) we find

$$z_{c,ijkl} - (q_i y_{c,jkl} - q_j y_{c,kli} + q_k y_{c,lij} - q_l y_{c,ijk}) = \sum_{1 \le m < n < o < p \le 6} Q_{ijkl,mnop} z_{mnop}, \tag{D.38}$$

at R_1. This allows us to determine $\mathbf{z}_c$ at R_1 using the values of $\mathbf{z}$ at R_1.

We continue the integration of y_c and z_c from R_1 to R_0 using the analogues of (D.35) and (D.36) over the capillary. Once we have obtained solutions for $\{\mathbf{y}, \mathbf{y}_c, \mathbf{z}, \mathbf{z}_c\}$ we use these to determine a solution for $\mathbf{u}_{2,2n,2\omega}$. Two of the boundary conditions we use to obtain the starting value of $\tilde{\mathbf{u}}_{2,2n,2\omega}$ at R_0 come from (D.30); the other two come from the identity [107]

$$\begin{pmatrix} y_{234} & -y_{134} & y_{124} & -y_{123} & 0 & 0 \\ 0 & y_{345} & -y_{245} & y_{235} & -y_{234} & 0 \\ 0 & 0 & y_{456} & -y_{356} & y_{346} & -y_{345} \end{pmatrix} \cdot \mathbf{u} = \begin{pmatrix} z_{1234} \\ z_{2345} \\ z_{3456} \end{pmatrix}. \tag{D.39}$$

The method used to obtain $\tilde{\mathbf{u}}_{2,2n,2\omega}$ is the same as in Section D.2. We integrate from R_0 to R_1 using the ordinary differential equation over the capillary (D.22). We use the value of $\tilde{\mathbf{u}}_{2,2n,2\omega}$ at R_1^- to obtain $\tilde{\mathbf{u}}_{2,2n,2\omega}$ at R_1^+ using the boundary condition at R_1. We may then integrate $\tilde{\mathbf{u}}_{2,2n,2\omega}$ from R_1 to R_2 (in the case of a finite geometry). If the geometry is infinite, we integrate $\tilde{\mathbf{u}}_{2,2n,2\omega}$ until it has decayed to a value below our error tolerance.

The original ordinary differential equation over V_m (D.12) is highly unstable, with three large positive eigenvalues for large R. This can be seen from the general solution of the linearised equation in Section 7.1.2. Since our required solution decays to zero, this means that if we use (D.12) to integrate $\tilde{\mathbf{u}}_{2,2n,2\omega}$ the required solution is quickly dominated by the

exponentially growing errors. We therefore use the following alternative governing equations derived in Ng [107] to reintegrate for $\tilde{\mathbf{u}}$, i.e.

$$y_{ijk}\tilde{u}_i' = L_{i\mu}\left(y_{\mu jk}\tilde{u}_i - y_{\mu ik}\tilde{u}_j + y_{\mu ij}\tilde{u}_k - z_{i\mu jk}\right) + y_{ijk}f_{2n,2\omega,i}, \tag{D.40}$$

$$y_{ijk}\tilde{u}_j' = L_{j\mu}\left(y_{\mu jk}\tilde{u}_i - y_{\mu ik}\tilde{u}_j + y_{\mu ij}\tilde{u}_k - z_{i\mu jk}\right) + y_{ijk}f_{2n,2\omega,j}, \tag{D.41}$$

$$y_{ijk}\tilde{u}_k' = L_{k\mu}\left(y_{\mu jk}\tilde{u}_i - y_{\mu ik}\tilde{u}_j + y_{\mu ij}\tilde{u}_k - z_{i\mu jk}\right) + y_{ijk}f_{2n,2\omega,k}, \tag{D.42}$$

where we sum over μ. These result in a system of the form

$$\tilde{\mathbf{u}}' = \mathbf{M}\cdot\tilde{\mathbf{u}} + \mathbf{m}. \tag{D.43}$$

For each row i of the above equation, we may choose j and k arbitrarily, as long as $i \neq j \neq k$. We make sure to choose j and k such that the eigenvalues of $\mathbf{M}$ are minimised. In doing this we are ensuring the governing equations are as stable as possible. In particular, we generally insist on minimising the largest eigenvalue of $\mathbf{M}$.

D.2.1 Solution of Other Components of $\mathbf{u}_2^a$

We may solve for $\{\mathbf{u}_{2,0,0}, \mathbf{u}_{2,2n,0}, \mathbf{u}_{2,0,2\omega}\}$ using the same method as for $\mathbf{u}_{2,2n,2\omega}$. Although this method is reliable, it is inefficient because these variables have a simpler structure than $\mathbf{u}_{2,2n,2\omega}$. For example the axial components of $\mathbf{u}_{2,2n,0}$ and the azimuthal components of $\mathbf{u}_{2,0,2\omega}$ are identically zero. After the elimination of these redundancies, the equations governing $\mathbf{u}_{2,2n,0}$ and $\mathbf{u}_{2,0,2\omega}$ can be put in a substantially more simple form. For example, the vector of minors $\mathbf{y}$ corresponding to these variables has only six elements instead of twenty. However because the method is almost identical to that of the previous section we do not outline the specific details.

After we eliminate the redundancies in $\mathbf{u}_{2,0,0}$ we find that it can be considered as a vector of dimension two. Its method of solution is almost exactly the same as the method of solution of $\mathbf{u}_2^p$ in Section D.2.2, except we swap the following variables

$$\frac{\partial \mathbf{P}}{\partial \zeta} \to \frac{\partial^2 \mathbf{P}}{\partial \mathbf{F}^2} : \nabla\mathbf{u}^{(n,\omega)} : \nabla\mathbf{u}^{(n,\omega)}. \tag{D.44}$$

D.2.2 Solution of Purely Radial Second Order Equation

In this section we outline our method for solving for $\mathbf{u}_2^p$. As with our solution of $\mathbf{u}^{(n,\omega)}$ and $\mathbf{u}_2^a$ we employ the method of compound matrices as the governing equations are highly unstable. The governing ordinary differential equation has one large positive and one large negative eigenvalue. Our numerical solution must resolve both eigenvalues, but this becomes very difficult to do when the R domain is large, because whichever direction we integrate one eigenvalue comes to dominate the other. We recall that the second order variable $\mathbf{u}_2^p$ is defined as

$$\begin{aligned} \nabla \cdot \left(\frac{\partial \mathbf{P}}{\partial \mathbf{F}} : \nabla \mathbf{u}_2^p \right) &= - \nabla \cdot \frac{\partial \mathbf{P}}{\partial \zeta_\alpha} \zeta_{\alpha,2}, \\ \left(\frac{\partial \mathbf{P}}{\partial \mathbf{F}} : \nabla \mathbf{u}_2^p + \frac{\partial \mathbf{P}}{\partial \zeta} \zeta_{\alpha,2} \right) \cdot \mathbf{n} &= \mathbf{0} \text{ at } R = R_1. \end{aligned} \tag{D.45}$$

The boundary condition at $R = R_2$ depends on the model variant. For the model variants with an infinite geometry, we stipulate the outer boundary condition to be

$$\left(\frac{\partial \mathbf{P}}{\partial \mathbf{F}} : \nabla \mathbf{u} \right) \cdot \mathbf{n} = \left(\frac{\partial \mathbf{P}}{\partial \mathbf{F}} : \nabla \mathbf{u}^{(l)} \right) \cdot \mathbf{n}, \tag{D.46}$$

$$\mathbf{u} = \mathbf{u}^{(l)}, \tag{D.47}$$

at a sufficiently large $R = R_g$. We choose R_g to be sufficiently large that the coefficients $\frac{\partial \mathbf{P}}{\partial \mathbf{F}}$ differ from the constants of linear elasticity by $\mathrm{O}(\epsilon_p)$ (where ϵ_p is our desired error tolerance) and the magnitude of the increments $\frac{\partial \mathbf{P}}{\partial \zeta_\alpha} \frac{\partial \zeta_\alpha}{\partial t}$ is also at most ϵ_p. Here $\mathbf{u}^{(l)}$ is the purely radial solution to the equations of linear elasticity which decays to zero.[1] In Section 3.2 we proved it is of the form

$$\mathbf{u}^l = CR^{-1}\mathbf{e}_R, \tag{D.48}$$

for some constant C. We substitute (D.48) into (D.46) and (D.47) and eliminate the constant C. This leaves us with single linear constraint on $\mathbf{u}$ at R_g.

[1] As we explained in Section 7.1.2 we could have equivalently equated the derivative of $\mathbf{u}_2^p$ to the derivative of $\mathbf{u}^{(l)}$ instead of the stress at $R = R_g$

In models A and D the boundary condition at R_2 is

$$\mathbf{u} = \mathbf{0}. \tag{D.49}$$

In models B and E the boundary condition at R_2 is

$$\left(\frac{\partial \mathbf{P}}{\partial \mathbf{F}} : \nabla \mathbf{u}_2^p + \frac{\partial \mathbf{P}}{\partial \zeta}\zeta_{\alpha,2}\right) \cdot \mathbf{n} = \mathbf{0}. \tag{D.50}$$

Solution using Method of Compound Matrices

We let

$$\mathbf{v} = \left(u_{2,R}^p, (u_{2,R}^p)'\right)^T. \tag{D.51}$$

be the solution vector. The field equation may be rearranged to be of the form

$$\mathbf{v}' = \mathbf{L}^0\mathbf{v} + \mathbf{f}, \tag{D.52}$$

where $f_1 = 0$ and f_2 is essentially the radial component of $-\nabla \cdot \frac{\partial \mathbf{P}}{\partial \mathbf{F}} : \nabla \mathbf{u}$. The matrix $\mathbf{L}^0$ is equal to the first two rows and columns of $\mathbf{L}$ in (7.1), except $n = 0$ and $\omega = 0$. Let $\mathbf{h}$ be a solution of the homogeneous equation, i.e.

$$\nabla \cdot \left(\frac{\partial \mathbf{P}}{\partial \mathbf{F}} : \nabla \mathbf{h}\right) = \mathbf{0}.$$

In the case of a finite geometry, $\mathbf{h}$ satisfies one of the boundary conditions

$$\mathbf{h} = \mathbf{0}, \quad \frac{\partial \mathbf{P}}{\partial \mathbf{F}} : \nabla \mathbf{h} \cdot \mathbf{n} = \mathbf{0} \tag{D.53}$$

at $R = R_2$ (depending on the model variant). In the case of an infinite geometry, $\mathbf{h}$ satisfies (D.47) at $R = R_g$. We may straightforwardly integrate from R_g to R_1 using a Runge-Kutta scheme to determine $\mathbf{h}$. We define $\mathbf{g}$ to be a particular solution satisfying the field equation in (D.45) and also the outer boundary condition. The outer boundary condition governing $\mathbf{g}$ is the same as that governing $\mathbf{h}$, except for models B and D, for which

$$\left(\frac{\partial \mathbf{P}}{\partial \mathbf{F}} : \nabla \mathbf{g} + \frac{\partial \mathbf{P}}{\partial \zeta_\alpha}\delta\zeta_\alpha\right) \cdot \mathbf{n} = \mathbf{0} \tag{D.54}$$

at $R = R_2$. Let

$$z = g_1 h_2 - g_2 h_1. \tag{D.55}$$

On substitution of (D.55) into (D.52) we find

$$z' = (L^0_{11} + L^0_{22})z - f_2 h_1 + f_1 h_2. \tag{D.56}$$

We may thus numerically integrate z from R_g (for an infinite geometry) or R_2 (for a finite geometry) to R_1 using a Runge-Kutta scheme. At R_1 we may solve for $\mathbf{v}$ using the following two conditions. One is the radial component of the null-stress condition

$$\left(\frac{\partial \mathbf{P}}{\partial \mathbf{F}} : \nabla \mathbf{v}\right) \cdot \mathbf{n} = \mathbf{0}, \tag{D.57}$$

and the other is obtained from the condition

$$\left|\mathbf{v} - \mathbf{g}\dot{:}\mathbf{h}\right| = 0, \tag{D.58}$$

which implies

$$v_1 h_2 - v_2 h_1 = z. \tag{D.59}$$

One option is now simply to integrate $\mathbf{v}$ from R_1 to R_2 using (D.52). However this method is potentially unstable because the solution we are seeking decays as R gets large, yet $\mathbf{L}^0$ has a large positive eigenvalue for large R. We derive an alternative ordinary differential equation governing $\mathbf{v}$ as follows. There exists a constant γ such that

$$v_i - g_i = \gamma h_i, \tag{D.60}$$

$$v_i' - g_i' = \gamma h_i', \tag{D.61}$$

where i equals 1 or 2. On elimination of γ we find

$$h_i v_j' = h_i g_j' + v_i h_j' - g_i h_j'. \tag{D.62}$$

After substituting z and h_j' we find

$$h_1 v_j' = -zA_{j2} + v_1 A_{j\mu} h_\mu + h_1 f_j, \tag{D.63}$$

$$h_2 v_j' = zA_{j1} + v_2 A_{j\mu} h_\mu + h_2 f_j. \tag{D.64}$$

We choose the equations which maximise the stability of the integration. For large R, when z and $\mathbf{g}$ are small, we assume $i = j$ in (D.62), so that the governing equation is of the form

$$v_j' = v_j \frac{h_j'}{h_j} - \frac{z}{h_j} A_{j2} + f_j. \tag{D.65}$$

This is now a one-dimensional ordinary differential equation in v_j. It is stable for large R and small f_j and z because $\frac{h_j'}{h_j} < 0$ for large R. This follows from the fact that $\mathbf{h}$ is of the same form as (D.48) for large R.

D.3 Solution of Incremental Nutrient Equation

We solve for the increment in the nutrient distribution using the method of compound matrices. We use this method because the increment in the nutrient is proportional to $\nabla \mathbf{u}^{(n,\omega)}$, and therefore it is unstable (as we explained in Section 7). The equation governing the increment in the nutrient distribution is given in (4.81) by

$$\begin{aligned}
&\left(1 + \frac{u_0}{R}\right)\left(1 + \frac{du_0}{dR}\right)^{-1} \frac{d^2 N_{n,\omega}}{dR^2} + R^{-1} \frac{dN_{n,\omega}}{dR}\left(1 - (R + u_0)\left(1 + \frac{du_0}{dR}\right)^{-2} \frac{d^2 u_0}{dR^2}\right) \\
&- n^2 R^{-2}\left(1 + \frac{du_0}{dR}\right)\left(1 + \frac{u_0}{R}\right)^{-1} N_{n,\omega} - J_0 \frac{\alpha}{k_n^*}\left(1 + \frac{n_0}{k_n^*}\right)^{-2} N_{n,\omega} - J_0\left(\mathbf{F}_0^{-T} : \nabla \mathbf{u}\right) \frac{\alpha n_0}{k_n^* + n_0} \\
&\qquad - \omega^2 J_0 N_{n,\omega} \\
&+ \nabla \cdot \Big(J(\mathbf{F}_0^{-T} : \nabla \mathbf{u}^{(n,\omega)}) \mathbf{F}_0^{-1} \mathbf{F}_0^{-T} \nabla n_0 - H_0 J_0 \mathbf{F}_0^{-1} \nabla \mathbf{u}^{(n,\omega)} \mathbf{F}_0^{-1} \mathbf{F}_0^{-T} \nabla n_0 - H_0 J_0 \mathbf{F}_0^{-1} \mathbf{F}_0^{-T} \nabla (\mathbf{u}^{(n,\omega)})^T \mathbf{F}_0^{-T} \nabla n_0 \Big) \\
&\qquad = 0.
\end{aligned} \tag{D.66}$$

The boundary condition at $R = R_1$ is $N_{n,\omega} = 0$. If the geometry is finite then the boundary condition at R_2 is $\frac{\partial N_{n,\omega}}{\partial R} = 0$. In the case of an infinite geometry, we divide the geometry into two regimes $R_1 \leq R \leq R_u$ and $R > R_u$, where R_u is given in Section 7. In the outer regime we linearise (D.66) and solve the linearised equations analytically. The linearisation

of (D.66) is

$$\frac{\partial^2 N_{n,\omega}}{\partial R^2} + R^{-1}\frac{\partial N_{n,\omega}}{\partial R} - n^2 R^{-2} N_{n,\omega} - \frac{\alpha}{k_n^*} N_{n,\omega} - \omega^2 N_{n,\omega} = 0. \tag{D.67}$$

We have considered the variables $\{u_0, n_0, \nabla \mathbf{u}^{(n,\omega)}, N_{n,\omega}\}$ to be 'small' in obtaining our linearisation. The solution of (D.67) which decays as $R \to \infty$ is

$$N_{n,\omega} = N_{n,\omega}^{(c)} K_n\left(\left(\sqrt{\frac{\alpha}{k_n^*} + \omega^2}\right) R\right) \tag{D.68}$$

$$N'_{n,\omega} = N_{n,\omega}^{(c)}\left[nR^{-1}K_n\left(\left(\sqrt{\frac{\alpha}{k_n^*} + \omega^2}\right) R\right) - K_{n+1}\left(\left(\sqrt{\frac{\alpha}{k_n^*} + \omega^2}\right) R\right)\left(\sqrt{\frac{\alpha}{k_n^*} + \omega^2}\right)\right]. \tag{D.69}$$

where $N_{n,\omega}^{(c)}$ is an undetermined constant. We insist that $N_{n,\omega}$ and its derivative is of this form as $R = R_u$. This gives us a linear constraint on $N_{n,\omega}$ and $N'_{n,\omega}$ at R_u when we eliminate the constant $N_{n,\omega}^{(c)}$. We may use the method outlined in Section D.2.1 to solve for $N_{n,\omega}$.

Bibliography

[1] P. W. Alford, J. D. Humphrey, and L. A. Taber, Growth and remodeling in a thick-walled artery model: effects of spatial variations in wall constituents, Biomechanical Modelling and Mechanobiology, 7 (2008), pp. 245–262.

[2] T. Alper and D. P. H. Flanders, Role of oxygen in modifying the radiosensitivity of e. coli b, Nature, 178 (1956), pp. 978–979.

[3] M. B. Amar and P. Ciarletta, Swelling instability of surface-attached gels as a model of soft tissue growth under geometric constraints, Journal of the Mechanics and Physics of Solids, 58 (2010), pp. 935–954.

[4] M. B. Amar and A. Gorely, Growth and instability in elastic tissues, Journal of the Mechanics and Physics of Solids, 53 (2005), pp. 2284–2319.

[5] D. Ambrosi and F. Guana, Stress-modulated growth, Mathematics and Mechanics of Solids, 12 (2005), p. 319.

[6] D. Ambrosi and F. Mollica, On the mechanics of a growing tumor, International Journal of Engineering Science, 40 (2001), pp. 1297–1316.

[7] ——, The role of stress in the growth of a multicell spheroid, Journal of Mathematical Biology, 48 (2004), pp. 477–499.

[8] D. Ambrosi and L. Preziosi, On the closure of mass balance models for tumor growth, Mathematical Models and Methods in the Applied Sciences, 12 (2002), pp. 737–754.

[9] D. Ambrosi and L. Preziosi, Cell adhesion mechanisms and stress relaxation in the mechanics of tumours, Biomechanics and Modelling in MechanoBiology, 8 (2009), pp. 397–413.

[10] S. Antman, Nonlinear Problems of Elasticity, Springer, 1995.

[11] R. Araujo and D. McElwain, A linear-elastic model of anisotropic tumour growth, European Journal of Applied Mathematics, 15 (2004), pp. 365–384.

[12] ——, New insights into vascular collapse and growth dynamics in solid tumours, Journal of Theoretical Biology, 228 (2004), pp. 335–346.

[13] R. Araujo and S. McElwain, A mixture theory for the genesis of residual stresses in growing tissues i: A general formulation, SIAM Journal of Applied Mathematics, 65 (2005), pp. 1261–1284.

[14] ——, A mixture theory for the genesis of residual stresses in growing tissues ii: Solutions to the biphasic equations for a multicell spheroid, SIAM Journal of Applied Mathematics, 66 (2005), pp. 447–467.

[15] V. Arumugam, M. Naresh, and R.Sanjeevi, Effect of strain rate on the fracture behaviour of skin, Journal of Bioscience, 19 (1994), pp. 307–313.

[16] A. L. Baldwin and R. Gore, Simulataneous measurement of capillary distensibility and hydraulic conductance, Microvascular Research, 38 (1989), pp. 1–22.

[17] M. Beatty, Introduction to Nonlinear Elasticity, Plenum Press, 1996, ch. 2, pp. 13–104.

[18] M. Beatty, Nonlinear Effects in Fluids and Solids, Plenum Press, 1996.

[19] A. Bertuzzi, A. D'Onofrio, A. Fasano, and A. Gandolfi, Regression and regrowth of tumour cords following single-dose anticancer treatment, Bulletin of Mathematical Biology, 65 (2003), pp. 903–931.

[20] A. Bertuzzi, A. Fasano, A. Gandolfi, and C. Sinisgalli, Tumour cords and their response to anticancer agents, in Selected Topics in Cancer Modeling, Birkhauser Boston, 2008.

[21] A. Bertuzzi and A. Gandolfi, Cell kinetics in a tumour cord, Journal of Theoretical Biology, 204 (2000), pp. 587–599.

[22] M. Biot, Surface instability of rubber in compression, Applied Scientific Research, 12 (1963), pp. 168–182.

[23] B. Boley and J. Weiner, Theory of Thermal Stresses, Wiley, 1960.

[24] W. F. Boron and E. L. Boulpaep, eds., Medical Physiology, Saunders, 2003.

[25] G. Bou-Gharios, M. Ponticos, V. Rajkumar, and D. Abraham, Extra-cellular matrix in vascular networks, Cell Proliferation, 37 (2004), pp. 207–220.

[26] Y. Boucher and R. Jain, Microvascular pressure is the principal driving force for interstitial hypertension in solid tumors: Implications for vascular collapse, Cancer Research, 52 (1992), pp. 5110–5114.

[27] F. Brau, H. Vandeparre, A. Sabbah, C. Poulard, A. Boudaoud, and P. Damman, Multiple-length-scale elastic instability mimics parametric resonance of nonlinear oscillators, Nature Physics, 7 (2011), pp. 56–60.

[28] C. Breward, H. Byrne, and C. Lewis, A multiphase model describing vascular tumour growth, Bulletin of Mathematical Biology, 1 (2004), pp. 1–28.

[29] J. M. Brown and W. R. Wilson, Exploiting tumour hypoxia in cancer treatment, Nature Reviews Cancer, 4 (2004), pp. 437–447.

[30] H. Byrne and L. Preziosi, Modelling solid tumour growth using the theory of mixtures, Mathematical Medicine and Biology, 20 (2003), pp. 341–366.

[31] J. Candiello, M. Balasubramani, E. Schreiber, G. Cole, U. Mayer, W. Falfter, and H. Lin, Biomechanical properties of native basement membranes, FEBS Journal, 274 (2007), pp. 2897–2908.

[32] E. Canetta, A. Duperray, A. Leyrat, and C. Verdier, Measuring cell viscoelastic properties using a force-spectrometer: influence of protein-cytoplasm interactions, Biorheology, 42 (2005), pp. 321–333.

[33] K. P. Carl-Henrik Heldin, Kristofer Rubin and A. Ostman, High interstitial fluid pressure - an obstacle in cancer therapy, Nature Review. Cancer, 4(10) (2004), pp. 806–13.

[34] J. Casciari, S. Sotirchos, and R. Sutherland, Mathematical modelling of microenvironment and growth in emt6/ro multicellular tumour spheroids, Cell Proliferation, 25 (1992), pp. 1–22.

[35] J. J. Casciari, S. V. Sotirchos, and R. M. Sutherland, Variations in tumor cell growth rates and metabolism with oxygen concentration, glucose concentration, and extracellular ph, Journal of Cellular Physiology, 151 (1992), pp. 386–394.

[36] U. Cavallaro, B. Schaffhauser, and G. Christofori, Cadherins and the tumour progression: is it all in a switch?, Cancer Letters, 176 (2002), pp. 123–128.

[37] M. Chaplain, L. Graziano, and L. Preziosi, Mathematical modelling of the loss of tissue compression responsiveness and its role in solid tumour development, Mathematical Medicine and Biology, (2006).

[38] C. Chen, M. Mrksich, S. Huang, G. M. Whitesides, and D. E. Ingber, Geometric control of cell life and death, Science, 276 (1997), pp. 1425–1428.

[39] C. S. Chen, J. Tan, and J. Tien, Mechanotransduction at cell-matrix and cell-cell contacts, Biomedical Engineering, 6 (2004), pp. 275–302.

[40] G. Cheng, J. Tse, R. Jain, and L. Munn, Micro-environment mechanical stress controls tumour spheroid size and morphology by suppressing proliferation and inducing apoptosis in cancer cells, PLOS One, 4 (2009), pp. 1–2.

[41] K. Christ and K. Turner, Methods to measure the strength of cell adhesion to substrates, Journal of Adhesion Science and Technology, 24 (2010), pp. 2027–2058.

[42] K. V. Christ, K. B. Williamson, K. S. Masters, and K. T. Turner, Measurement of single-cell adhesion strength using a microfluidic assay, Biomedical Microdevices, 3 (2010), pp. 443–455.

[43] Ciarlet, Mathematical Elasticity Volume 1: Three-Dimensional Elasticity, Elsevier Science, 1988.

[44] P. G. Ciarlet, Mathematical Elasticity Volume III: Theory of Shells, Elsevier Science, 2000.

[45] B. S. Croix, C. Sheehan, J. W. Rak, V. A. Florenes, J. M. Slingerland, and R. S. Kerbel, E-cadherin?dependent growth suppression is mediated by the cyclin-dependent kinase inhibitor p27, Journal of Cell Biology, 142 (1998), pp. 557–571.

[46] A. Davey, On the removal of the singularities from the riccati method, Journal of Computational Physics, 30 (1979), pp. 137–144.

[47] C. Erlichman, S. J. Soldin, J. J. Thiessen, J. F. G. Sturgeon, and S. Fine, Disposition of total and free cisplatin on two consecutive treatment cycles in patients with ovarian cancer, Cancer Chemotherapy Pharmacology, 19 (1987), pp. 75–79.

[48] D. Evans and C. Dive, Effects of cisplatin on the induction of apoptosis in proliferating hepatoma cells and nonproliferating immature thymocytes, Cancer Research, 53 (1993), pp. 2133–2139.

[49] J. E. Flaherty, J. B. Keller, and S. Rubinow, Post buckling behaviour of elastic tubes and rings with opposite sides in contact, SIAM Journal on Applied Mathematics, 23 (1972), pp. 446–455.

[50] G. Forgacs, R. A. Foty, Y. Shafrir, and M. S. Steinberg, Viscoelastic properties of living embryonic tissues: a quantitative study, Biophysical Journal, 74 (1998), p. 2227?2234.

[51] A. Fowler, Mathematical Models in the Applied Sciences, Cambridge University Press, 1997.

[52] G. Franceschini, D. Bigoni, P. Regitnig, and G. Holzapfel, Brain tissue deforms similarly to filled elastomers and follows consolidation theory, Journal of the Mechanics and Physics of Solids, 54 (2006), pp. 2592–2620.

[53] J. Freyer, Rates of oxygen consumption for proliferating and quiescent cells isolated from multicellular tumor spheroids, Advances in experimental medicine and biology, 345 (1994), pp. 335–342.

[54] J. Freyer and R. Sutherland, A reduction in the in situ rates of oxygen and glucose consumption of cells in emt6/ro spheroids during growth, Journal of Cellular Physiology, 124 (1985), pp. 516–524.

[55] J. P. Freyer, K. Jarrett, S. Carpenter, and M. R. Raju, Oxygen enhancement ratio as a function of dose and cell cycle phase for radiation-resistant and sensitive cho cells, Radiation Research, 127 (1991), pp. 97–107.

[56] Y. Fung, Biomechanics: Mechanical Properties of Living Tissues (2nd Edition), Springer, 2004.

[57] Y. Fung and P. Tong, Classical and Computational Solid Mechanics, World Scientific, 2001.

[58] A. M. P. S. G. Himpel, E. Kuhl, Computational modelling of isotropic multiplicative growth, CMES.

[59] J. Galle, M. Loeffler, and D. Drasdo, Modeling the effect of deregulated proliferation and apoptosis on the growth dynamics of epithelial cell populations in vitro, Biophysical Journal, 88 (2005), pp. 62–75.

[60] J. Galle, L. Preziosi, and A. Tosin, Contact inhibition of growth described by a multiphase and an individual cell-based models, Applied Mathematics Letters, 22 (2009), p. 1483.

[61] L. Gibson and M. Ashby, Cellular Solids: Structure and Properties, Cambridge University Press, 1997.

[62] R. Goldacre and B. Sylven, On the access of blood-borne dyes to various tumour regions, British Journal of Cancer, 16 (1962), pp. 306–321.

[63] M. Golubitsky and D. Schaeffer, Singularities and Groups in Bifurcation Theory: Volume 1, Springer, 1985.

[64] A. Goriely, M. Robertson-Tessi, M. Tabor, and R. Vandiver, Elastic growth models, (2008).

[65] A. Goriely and R. Vandiver, On the mechanical stability of growing arteries, IMA Journal of Applied Mathematics, 75 (2010), pp. 549–570.

[66] G. Griffon-Etienne, Y. Boucher, C. Brekken, H. D. Suit, and R. K. J. ', Taxane-induced apoptosis decompresses blood vessels and lowers interstitial fluid pressure in solid tumors: Clinical implications, Cancer Research, 59 (1999), pp. 3776–3782.

[67] Guyton, Textbook of Medical Physiology (Eighth Edition), W.B. Saunders Company, 1991.

[68] H.-C. Han, Nonlinear buckling of blood vessels: A theoretical study, Journal of Biomechanics, 41 (2008), pp. 2708–2713.

[69] ——, Blood vessel buckling within soft surrounding tissue generates tortuosity, Journal of Biomechanics, 42 (2009), pp. 2797–2801.

[70] ——, Determination of the critical buckling pressure of blood vessels using the energy approach, Annals of Biomedical Engineering, 39 (2010), pp. 1032–1040.

[71] D. Haughton and R. Ogden, Bifurcation of inflated circular cylinders of elastic material under axial loading - i. membrane theory for thin-walled tubes, Journal of the Mechanics and Physics of Solids, 27 (1979), pp. 179–212.

[72] ——, Bifurcation of inflated circular cylinders of elastic material under axial loading - ii. exact theory for thick-walled tubes, Journal of the Mechanics and Physics of Solids, 27 (1979), pp. 489–512.

[73] A. Hazel and M. Heil, Surface-tension-induced buckling of liquid-lined elastic tubes: A model for pulmonary airway closure, Proceedings of the Royal Society A: Mathematical, Physical and Engineering Sciences, 461 (2005), pp. 1847–1868.

[74] M. Heil and T. Pedley, Large post-buckling deformations of cylindrical shells conveying viscous flow, Journal of Fluids and Structures, 10 (1996), pp. 565–599.

[75] G. Helmlinger, P. Netti, H. Lichtenbeld, R. Melder, and R. Jain, Solid stress inhibits the growth of multicellular tumour spheroids, Nature Biotechnology, 15 (1997), pp. 778–783.

[76] K. O. HICKS, H. MYINT, A. V. PATTERSON, F. B. PRUIJN, B. G. SIIM, K. PATEL, and W. R. WILSON, Oxygen dependence and extravascular transport of hypoxia-activated prodrugs: Comparison of the dinitrobenzamide mustard pr-104a and tirapazamine, International Journal of Radiation Oncology, 69 (2007), pp. 560–571.

[77] K. O. Hicks, F. B. Pruijn, T. W. Secomb, M. P. Hay, R. Hsu, J. M. Brown, W. A. Denny, M. W. Dewhirst, and W. R. Wilson, Use of three-dimensional tissue cultures to model extravascular transport and predict in vivo activity of hypoxia-targeted anticancer drugs, Journal of the National Cancer Institute, 98 (2006), pp. 1118–1128.

[78] A. Hoger, T. V. Dyke, and V. Lubarda, Symmetrization of the growth deformation and velocity gradients in residually stressed biomaterials., Z. Angew. Math. Phys., 55 (2004), pp. 848–860.

[79] G. Holzapfel and T. Gasser, A new constitutive framework for arterial wall mechanics and a comparative study of material models, Journal of Elasticity, 61 (2000), pp. 1–48.

[80] D. Ingber, Cellular tensegrity: defining new rules of biological design that govern the cytoskeleton, Journal of Cell Science, 104 (1993), pp. 613–627.

[81] E. Jahde and M. Rajewsky, Tumor-selective modification of cellular microenvironment in vivo: Effect of glucose infusion on the ph in normal and malignant rat tissues, Cancer Research, 42 (1982), pp. 1505–1512.

[82] R. Jain, Barriers to drug delivery in solid tumours., Scientific American, 271 (1995), pp. 59–65.

[83] R. Jain, Taming vessels to treat cancer, Scientific American, (2008).

[84] A. Jones, H. Byrne, J. Gibson, and J. Dold, A mathematical model of the stress induced by avascular tumour growth, Journal of Mathematical Biology, 40 (2000), pp. 473–499.

[85] R. Kalluri, Basement membranes: Structure, assembly and role in tumour angiogenesis, Nature Reviews: Cancer, 3 (2003), pp. 422–433.

[86] W. Koiter, Elastic Stability of Solids and Structures, Cambridge University Press, 2009.

[87] M. Konerding, E. Fait, and A. Gaumann, 3d microvascular architecture of pre-cancerous lesions and invasive carcinomas of the colon, British Journal of Cancer, 84 (2001), pp. 1354–62.

[88] A. Lee and H.-C. Han, A nonlinear thin-wall model for vein buckling, Cardiovascular Engineering and Technology, 1 (2010), pp. 282–289.

[89] J. Lee and G. S. Schonbein, Biomechanics of skeletal muscle capillaries: Hemodynamic resistance, endothelial distensibility, and pseudopod formation, Annals of Biomedical Engineering, (1995), pp. 226–246.

[90] W. Legant, J. Miller, B. Blakely, D. Cohen, G. Genin, and C. Chen, Measurements of mechanical tractions exerted by cells in three-dimensional matrices, Nature Methods, (2010).

[91] A. J. Leu, D. A. Berk, A. Lymboussaki, K. Alitalo, and R. K. Jain, Absence of functional lymphatics within a murine sarcoma: A molecular and functional evaluation, Cancer Research, 60 (2000), pp. 4324–4327.

[92] B. Li, Y.-P. Cao, and X.-Q. Feng, Growth and surface folding of esophageal mucosa: A biomechanical model, Journal of Biomechanics, 44 (2011), pp. 182–188.

[93] B. Li, Y.-P. Cao, X.-Q. Feng, and H. Gao, Surface wrinkling of mucosa induced by volumetric growth: Theory, simulation and experiment, Journal of the Mechanics and Physics of Solids, 59 (2011), pp. 758–774.

[94] C. Lim, E. Zhou, and S. Quek, Mechanical models for living cells?a review, Journal of Biomechanics, 39 (2006), pp. 195–216.

[95] H. Lu, L. Y. Koo, W. M. Wang, D. A. Lauffenburger, L. G. Griffith, and K. F. Jensen, Microfluidic shear devices for quantitative analysis of cell adhesion, Analytical Chemistry, 76 (2004), pp. 5257–5264.

[96] V. Lubarda and A. Hoger, On the mechanics of solids with a growing mass, International Journal of Solids and Structures, 39 (2002), pp. 4627–4664.

[97] L. Mahadevan, Polymer science and biology: structure and dynamics at multiple scales, Royal Society of Chemistry Journal of Biomechanics, 139 (2008), pp. 9–19.

[98] J. E. Marsden and T. J. Hughes, Mathematical Foundations of Elasticity, Dover, 1983.

[99] A. Mathur, A. Collinsworth, W. Reichert, W. Kraus, and G. Truskey, Endothelial, cardiac muscle and skeletal muscle exhibit different viscous and elastic properties as determined by atomic force microscopy, Journal of Biomechanics, 34 (2001), pp. 1545–1553.

[100] A. Minchinton and I. Tannock, Drug penetration in solid tumours, Nature, 6 (2006), pp. 583–592.

[101] S. Modok, R. Scott, R. Alderden, M. Hall, H. Mellor, S. Bohic, T. Roose, T. Hambley, and R. Callaghan, Transport kinetics of four- and six-coordinate platinum compounds in the multicell layer tumour model, British Journal of Cancer, 97 (2007), pp. 194–200.

[102] F. Mollica, R. K. Jain, and P. A. Netti, A model for temporal heterogeneities of tumor blood flow, Microvascular Research, 65 (2003), pp. 56–60.

[103] A. Moreno, A. Katz, L. Gold, and R. Reddy, Mechanics of distension of dog veins and other very thin-walled tubular structures, Circulation Research, 27 (1970), pp. 1069–1080.

[104] D. Moulton and A. Goriely, Possible role of differential growth in airway wall remodeling in asthma, Journal of Applied Physiology, 110 (2011), pp. 1003–1012.

[105] J. Nagy, S. Chang, A. Dvorak, and H. Dvorak, Why are tumour blood vessels abnormal and why is it important to know?, British Journal of Cancer, 100 (2009), pp. 865–869.

[106] P. A. Netti, D. A. Berk, M. A. Swartz, A. J. Grodzinsky, , and R. K. Jain, Role of extracellular matrix assembly in interstitial transport in solid tumors, Cancer Research, 60 (2000), pp. 2497–2503.

[107] B. Ng and W. Reid, The compound matrix method for ordinary differential systems, Journal of Computational Physics, 58 (1985), pp. 209–228.

[108] F. Niordson, shell theory, North-Holland, 1985.

[109] J. Nowinski, Surface instability of a half-space under high two-dimensional compression, Department of Mechanical and Aerospace Engineering, (1974), pp. 364–376.

[110] R. Ogden, Non-Linear Elastic Deformations, Ellis Horwood Limited, 1984.

[111] T. P. Padera, B. R. Stoll, J. B. Tooredman, D. Capen, E. di Tomaso, and R. K. Jain, Cancer cells compress intratumour vessels, Nature Brief Communications, 427 (2004), p. 695.

[112] D. Pesen and J. H. Hoh, Micromechanical architecture of the endothelial cell cortex, Biophysical Journal, 88 (2005), pp. 670–679.

[113] D. Pioletti and L. Rakotomanana, Non-linear viscoelastic laws for soft biological tissues, European Journel of Mechanics and Solids, 19 (2000), pp. 749–759.

[114] C. Pozrikidis, Buckling and collapse of open and closed cylindrical shells, Journal of Engineering Mathematics, 42 (2002), pp. 157–180.

[115] W. H. Press, S. A. Teukolsky, W. T. Vetterling, and B. P. Flannery, Numerical Recipes in C++ Second Edition, Cambridge University Press, 1992.

[116] L. Preziosi and A. Tosin, Multiphase modelling of tumour growth and extracellular matrix interaction: mathematical tools and applications, Journal of Mathematical Biology, 58 (2009), pp. 625–656.

[117] Rayleigh, On waves propagated along the plane surface of an elastic solid, Proceedings of London Mathematical Society, (1885).

[118] D. Rischin, L. Peters, R. Fisher, A. Macann, J. Denham, M. Poulsen, M. Jackson, L. Kenny, M. Penniment, J. Corry, D. Lamb, and B. McClure, Tirapazamine, cisplatin, and radiation versus fluorouracil, cisplatin, and radiation in patients with locally advanced head and neck cancer: A randomized phase ii trial of the trans-tasman radiation oncology group (trog 98.02), Journal of Clinical Oncology, 23 (2006), pp. 79–87.

[119] E. Rodriguez, A. Hoger, and A. D. McCulloch, Stress-dependent finite growth in soft elastic tissues, Journal of Biomechanics, 27 (1994), pp. 455–467.

[120] B. Roeder, K. Kokini, and S. Voytik-Harbin, Fibril microstructure affects strain transmission within collagen extracellular matrices, Journal of Biomechanical Engineering, 131 (2009), pp. 1–11.

[121] T. Roose, J. Chapman, and P. Maini, Mathematical models of avascular tumour growth, SIAM Journal on Applied Mathematics, 49 (2007), pp. 179–208.

[122] T. Roose, P. Netti, L. Munn, Y. Boucher, and R. Jain, Solid stress generated by spheroid growth estimated using a linear poroelasticity model, Microvascular Research, 66 (2003), pp. 204–212.

[123] J. Rosenzweig and O. Jensen, Capillary-elastic instabilities of liquid-lined lung airways, Journal of Biomechanical Engineering, 124 (2002), pp. 650–655.

[124] H. Sato, N. Kataoko, F. Kajiya, M. Katano, T. Takigawa, and T. Masuda, Kinetic study on the elastic change of vascular endothelial cells on collagen matrices by atomic force microscopy, Colloids and Surfaces B: Biointerfaces, 34 (2004), pp. 141–146.

[125] R. Shipley, S. Chapman, and T. Roose, Multiscale model predictions of fluid and vinblastine distribution in dorsal skinfold chambers, Unpublished Thus Far.

[126] R. Skalak, S. Zargaryan, R. Jain, P. Netti, and A. Hoger, Compatibility and the genesis of residual stress by volumetric growth, Journal of Mathematical Biology, 34 (1996), pp. 889–914.

[127] L. Smaje, P. Fraser, and G. Clough, The distensibility of single capillaries and venules in the cat mesentery, Microvascular Research, (1980), pp. 358–370.

[128] J. Stoer and R. Bulirsch, Introduction to Numerical Analysis, Springer, 2002.

[129] B. Stoll, A Quantitative Analysis of the Development and Remodeling of Blood Vessels in Tumors: Contribution of Endothelial Progenitor Cells to Angiogenesis and Effect of Solid Stress on Blood Vessel Morphology, PhD thesis, Massachusetts Institute of Technology, 2003.

[130] L. Taber, Towards a unified theory for morphomechanics, Philosophical Transactions of the Royal Society: A, 367 (2009), pp. 3555–3583.

[131] L. Taber and D. Eggers, Theoretical study of stress-modulated growth in the aorta, Journal of Theoretical Biology, 180 (1996), pp. 343–357.

[132] Tadjbakhsh and Odeh, Equilibrium states of elastic rings, Journal of Mathematical Analysis and Applications, 18 (1967), pp. 59–74.

[133] I. Tannock, The relation between cell proliferation and the vascular system in a transplanted mouse mammary tumour, British Journal of Cancer, 1 (1965), pp. 258–273.

[134] I. Tannock, The relation between cell proliferation and the vascular system in a transplanted mouse mammary tumour, British Journal of Cancer, 22(2) (1968), pp. 258–273.

[135] Y. Tsukatani, K. Suzuki, and K. Takahashi, Loss of density-dependent growth inhibition and dissociation of a-catenin from e-cadherin, Journal of Cellular Physiology, 173 (1997), pp. 54–63.

[136] R. Vandiver and A. Goriely, Differential growth and residual stress in cylindrical elastic structures, Philosophical Transactions of the Royal Society, 367 (2009), pp. 3607–3630.

[137] P. Vaupel, F. Kallinowski, and P. Okunieff, Blood flow, oxygen and nutrient supply, and metabolic microenvironment of human tumors: A review, Cancer Research, 49 (1989), pp. 6449–6465.

[138] P. W. Vaupel, S. Frinak, and H. I. Bicher, Heterogeneous oxygen partial pressure and ph distribution in c3h mouse mammary adenocarcinoma, Cancer Research, 41 (1981), pp. 2008–2013.

[139] V. Vogel and G. Baneyx, The tissue engineering puzzle: A molecular perspective, Annual Review of Biomedical Engineering, 5 (2003), pp. 441–463.

[140] A. Voldina and O. Pozdnyakov, Investigation of the blood capillaries in the functioning diaphragm, Morphology and Pathomorphology, 77 (1974), pp. 84–87.

[141] K. Volokh, Stresses in growing soft tissues, Acta Biomaterials, 2 (2006), pp. 493–504.

[142] N. Wang, J. Butler, and D. Ingber, Mechanotransduction across the cell surface and through the cytoskeleton, Science, 260 (1993), pp. 1124–1127.

[143] J. Ward and J. King, Mathematical modelling of avascular-tumour growth, IMA Journal of Mathematics Applied in Medicine & Biology, 14 (1997), pp. 39–69.

[144] B. G. Wouters and J. M. Brown, Cells at intermediate oxygen levels can be more important than the 'hypoxic fraction' in determining tumor response to fractionated radiotherapy, Radiation Research, 147 (1997), pp. 541–550.

[145] C. Zhu, G. Bao, and N. Wang, Cell mechanics: Mechanical response, cell adhesion, and molecular deformation, Annual Review of Biomedical Engineering, (2000), pp. 189–226.